UNIVERSITÀ DEGLI STUDI DI MILANO-BICOCCA
Scuola di Dottorato di Scienze

Dottorato in Fisica e Astronomia, Ciclo XXII
Coordinatore: Prof. Claudio Destri

Next-to-Leading-Order QCD corrections to Shower Monte Carlo event generators: single vector-boson and single-top hadroproduction

Tutore: Prof. Paolo Nason

Tesi di: Emanuele Re
Matricola n. 040679

Anno Accademico 2008-2009

Contents

Introduction

Predictions for processes that will be studied accurately at present and future colliders (namely at the Tevatron and the LHC) are mainly based on Next-to-Leading-Order calculations. Total cross sections and more exclusive kinematical observables, such as transverse momentum or rapidity distributions, are often calculated with this level of accuracy. In particular, phase space regions where transverse momenta are large are described properly, since real corrections are fully included. However, despite of their accuracy, from a pratical point of view these calculations are not the best tool to perform simulations at the detector level, both because they rely on a non-trivial cancellation between divergent virtual and real contributions and because their outputs are a set of outgoing partonic momenta, instead of hadronic ones.

For these reasons, experimentalists often use Monte Carlo event generators to perform simulations. In addiction to produce events at the detector level, these tools are based on the Parton Shower formalism, that permits to achieve a good description of high-multiplicty final states in the collinear enhanced regions. Nevertheless, high transverse-momentum regions are poorly described, since the shower algorithm is based on the collinear approximation. Furthermore, inclusive observables (such as the total cross section) are accurate only at the leading order.

It is then clear that a method to include Next-to-Leading-Order QCD corrections to event generators is needed, especially in view of the beginning of running of the LHC. In this way a large amount of the acquired knowledge on QCD corrections would be made directly available to the experimentalists in a flexible form, that they could easily use for simulations.

In recent years, efforts have been done in this direction, yielding more than one proposal. At present, however, complete results have been obtained only within the Monte Carlo at Next-to-Leading-Order (`MC@NLO`) and the POsitive Weight Hardest Emission Generator (`POWHEG`) frameworks.

In this thesis, we describe the implementations of single vector boson and single top s- and t-channel hadroproduction in the `POWHEG` framework.

The thesis is organized as follows.

In chapter 1, we give an introduction to some basic aspects of perturbative QCD, relevant for this thesis. In particular, we describe how fixed order calculations are usually performed and how Monte Carlo event generators work.

In chapter 2, we point out the main differences of the two approaches, highlighting the benefits and drawbacks of both. The core of the chapter is devoted to the description of the `POWHEG` method, that permits to build an event generator that retains benefits both of NLO calculations and of Shower Monte Carlo programs.

In chapter 3 and 4 we describe the `POWHEG` implementation of single vector boson and single-top hadroproduction, respectivley. Corresponding results are presented, together with detailed comparisons with analogous results obtained with `MC@NLO` and with other Monte Carlo programs (`PYTHIA`). For the single vector boson case, comparisons with available Tevatron data are also shown.

Finally, we summarize our work and give our conclusions.

The introductive part of chapter 1 is based on textbooks and review articles, while sec. 1.2, 1.3 and chapter 2 are mainly based on refs. [1–3].

The content of chapter 3 and 4 is based on the following published papers, in collaboration with S. Alioli, P. Nason and C. Oleari:

- S. Alioli, P. Nason, C. Oleari and E. Re
  NLO vector-boson production matched with shower in POWHEG.
  Published in JHEP 0807:060,2008.
  e-Print: arXiv:0805.4802 [hep-ph]

- S. Alioli, P. Nason, C. Oleari and E. Re
  NLO single-top production matched with shower in POWHEG: s- and t-channel contributions.
  Published in JHEP 0909:111,2009.
  e-Print: arXiv:0907.4076 [hep-ph]

Chapter 1

QCD applications to collider Physics

In this chapter we give a brief introduction to the basics of perturbative Quantum Chromodynamics (QCD) and describe how the theory can be used to produce results relevant to collider Physics. The aim of this chapter is to illustrate how fixed order calculations and Shower Monte Carlo event generators work. This is needed to introduce the basic concepts that we use throughout the thesis.

The chapter is organized as follows.

In section 1.1 we give the Lagrangian of the theory and the Feynman rules that follow from it. We also describe briefly the concept of running coupling constant and its physical consequence, in particular the ones concerning the definition of the perturbative domain of the theory. A quick overview on the structure of squared amplitudes in the soft and collinear limits is also given.

In section 1.2 we give an introduction to fixed order perturbative calculations, and describe how these are practically performed, at the Next-to-Leading-Order, in the so-called *subtraction methods*. A description of the two methods that we used for the work presented in this thesis is also given.

Finally, in section 1.3 we describe how the factorization properties of QCD amplitudes allow to resum dominant contributions to a given cross section. From this feature, we describe the Parton Shower formalism and its role within event generators.

1.1 Basic aspects of QCD

The content of this introductory section is based on Quantum Field Theory and QCD textbooks [4–7] and on reviews [8, 9].

1.1.1 Lagrangian and Feynman rules

Quantum Chromodynamics is the quantum field theory that describes the interactions of quarks and gluons. It is a nonabelian gauge theory, with local $SU(N_c)$ symmetry, with $N_c = 3$. The elementary fields of the theory are the quark and the gluon fields, which will be denoted, respectively, ψ_i and A^a_μ. At the classical level, the Lagrangian density is given by

$$\mathcal{L}_{classical} = -\frac{1}{4} F^a_{\mu\nu} F^{a;\mu\nu} + \sum_{f=1}^{n_f} \left[\bar{\psi}^{(f)}_i \left(i \not{D}_{ij} - m_{(f)} \delta_{ij} \right) \psi^{(f)}_j \right] , \tag{1.1}$$

where the index f runs over all the quark flavours ($f = u, d, c, s, t, b$) and the field strength and the covariant derivative are given by

$$F^a_{\mu\nu} = \partial_\mu A^a_\nu - \partial_\nu A^a_\mu + g_s f^{abc} A^b_\mu A^c_\nu , \tag{1.2}$$

$$D^\mu_{ij} = \partial^\mu \delta_{ij} - i g_s t^a_{ij} A^{a;\mu} . \tag{1.3}$$

Quark (and antiquark) spinorial fields carry a color index i that runs from 1 to N_c. Gluon vector fields, instead, are labelled by the index a, that runs from 1 to $N_c^2 - 1$. With g_s we denote the coupling strength between colored quanta. We also introduce here the strong coupling constant α_s,

$$\alpha_s = \frac{g_s^2}{4\pi} , \tag{1.4}$$

since perturbative results are often expressed in terms of this quantity instead of g_s.

The matrices t^a are the generators of the fundamental representation and they satisfy the commutation rules of the $SU(N_c)$ algebra:

$$[t^a, t^b] = i f^{abc} t^c , \tag{1.5}$$

where f^{abc} are the group structure constants, that define implicitly the group algebra. These constants can always be chosen real and antisymmetric, and they obey the Jacoby identity

$$f^{ade} f^{bcd} + f^{bde} f^{cad} + f^{cde} f^{abd} = 0 . \tag{1.6}$$

Usually, the generators of the fundamental representation are written in terms of the eight Gell-Mann matrices as follows:

$$t^a_{ij} = \frac{\lambda^a_{ij}}{2} . \tag{1.7}$$

An explicit expression for the matrices λ^a can be found for example in [5]. With this

choice, the following normalization condition holds:

$$\mathrm{Tr}[t^a t^b] \equiv t^a_{ij} t^b_{ji} = T_{\mathrm{F}}\ \delta^{ab}\,, \quad T_{\mathrm{F}} = \frac{1}{2}\,. \tag{1.8}$$

Other useful identities are:

$$\sum_{a=1}^{N_{\mathrm{c}}^2-1} t^a_{ij} t^a_{jk} \;=\; C_{\mathrm{F}}\ \delta_{ik}\,, \quad C_{\mathrm{F}} = \frac{N_{\mathrm{c}}^2-1}{2N_{\mathrm{c}}}\,, \tag{1.9}$$

$$\sum_{a,\,b=1}^{N_{\mathrm{c}}^2-1} f^{abc} f^{abd} \;=\; C_{\mathrm{A}}\ \delta^{cd}\,, \quad C_{\mathrm{A}} = N_{\mathrm{c}}\,. \tag{1.10}$$

The Lagrangian density $\mathcal{L}_{classical}$ includes all the interactions among the fundamental fields of the theory, and it is invariant under a local $SU(N_{\mathrm{c}})$ transformation, which transforms the quark and the gluon fields as follows:

$$\psi(x) \;\rightarrow\; U(x)\ \psi(x)\,, \tag{1.11}$$

$$\left[t^a A^a_\mu(x)\right] \;\rightarrow\; U(x) \left[t^a A^a_\mu(x) - \frac{i}{g_{\mathrm{S}}} U^{-1}(x) \partial_\mu U(x)\right] U^{-1}(x)\,. \tag{1.12}$$

The U matrices belong to the group $SU(N_{\mathrm{c}})$ and depend functionally on x, since the $SU(N_{\mathrm{c}})$ symmetry has been gauged. They can be obtained by exponentiating the generators of the fundamental representation:

$$U(x) = \exp\left\{i\ \theta^a(x)\, t^a\right\}, \tag{1.13}$$

where $\theta^a(x)$ are real arbitrary functions, parameterizing a given local transformation.

To quantize the theory consistently, two other terms have to be added to the classical Lagrangian density. A first problem arises because $\mathcal{L}_{classical}$ is invariant when the gluon field change by a total derivative. When the theory is canonically quantized, this gauge freedom makes the timelike component of the gluon field conjugate momentum identically null, spoiling therefore the canonical commutation rules. This feature arises also in abelian theories and, to prevent this to happen, one has to introduce a term that brokes explicitly the full gauge invariance of the Lagrangian: for this reason, this term is usually called *gauge-fixing* term. There are several types of gauge-fixing terms, but, to keep the theory manifestly covariant, one needs to impose on the gluon fields a covariant constrain, such

as the Lorentz condition $\partial^\mu A^a_\mu = 0$. The corresponding gauge-fixing term reads then

$$\mathcal{L}_{gauge-fixing} = -\frac{1}{2\xi}(\partial^\mu A^a_\mu)^2 \,, \tag{1.14}$$

where ξ is a free parameter (several choices are possible), that does not enter in physical observables. The Lorentz gauge-fixing term lowers of one unity the number of degrees of freedom of the gauge boson fields. In abelian theories, as in QED, no other terms are needed, because the remaining nonphysical degrees of freedom of the photons cancels out in the calculation of physical quantities. In non abelian gauge theories with a covariant gauge fixing, instead, we need to cancel these nonphysical degrees of freedom explicitly. This is achieved by introducing a set of (nonphysical) complex scalar anticommuting fields, called ghosts, that interact with gluons. We have

$$\mathcal{L}_{ghosts} = \partial^\mu \eta^{a*} D^{ab}_\mu \eta^b \,, \tag{1.15}$$

where $D^{ab}_\mu = \delta^{ab}\partial_\mu - g_{\rm s} f^{abc} A^c_\mu$.

It is worthwhile to recall that ghosts are not needed if one works in an axial gauge, since in that case the number of degrees of freedom is already lowered of two units by the axial gauge-fixing term, which however is not covariant a constrain.

The full Lagrangian density is then given by

$$\mathcal{L}_{QCD} = \mathcal{L}_{classical} + \mathcal{L}_{gauge-fixing} + \mathcal{L}_{ghosts} \,. \tag{1.16}$$

From eq. (1.16), one can derive the QCD Feynman rules, that we reported in Appendix A.

1.1.2 Running of the coupling constant

In Quantum Field Theories, it is well known that results obtained including quantum corrections (loops) contain ultraviolet (UV) and infrared (IR) divergences. In the following of this thesis, we will see how one handles with the presence of IR divergences. UV divergences, instead, are removed by means of the renormalization procedure: after renormalization, amplitudes are free of UV poles, but the coupling constant becomes *running*. This means that the renormalized coupling constant depends on the energy scale at which the theory itself is probed. Since this feature has important phenomenological consequences, in this section we give a brief explanation of how this mechanism works, without entering into the technical details of the renormalization procedure.[1]

[1] In particular, here we follow [9].

The (one-loop) renormalization procedure consists basically in a redefinition of the fields and the parameters present in the original (*bare*) Lagrangian density, by means of renormalization constants. Renormalized amplitudes are free of UV poles, but a new, arbitrary, mass scale is introduced in the theory, the *renormalization scale*, that we denote here as μ.

For the purpose of this section, we just need the relation between the bare ($\alpha_{\rm S}^{(b)}$) and the renormalized ($\alpha_{\rm S}$) coupling constant, that, when dimensional regularization is used, reads

$$\alpha_{\rm S}^{(b)} = Z_g^2 \; \mu^{2\epsilon} \; \alpha_{\rm S} \,, \tag{1.17}$$

and the expression for the one-loop charge renormalization constant Z_g. One has:

$$Z_g = 1 - \frac{\alpha_{\rm S}}{\epsilon} \; \frac{b_0}{2} \,, \tag{1.18}$$

where

$$b_0 = \frac{11 C_{\rm A} - 4 n_{\rm f} T_{\rm F}}{12\pi} \,. \tag{1.19}$$

The scale μ in (1.17) is an arbitrary energy scale, needed to keep the renormalized coupling $g_{\rm S}$ dimensionless, after having defined the theory in $d = 4 - 2\epsilon$ dimensions. Since the initial Lagrangian does not depend upon this scale, then the bare coupling has to be scale independent too. From this simple consideration, it follows that the (logarithmic) derivative of $\alpha_{\rm S}^{(b)}$ with respect to μ has to vanish, so that $\alpha_{\rm S}$ has to be scale dependent:

$$\begin{aligned} 0 &= 2\, Z_g \alpha_{\rm S}\, \mu^2 \frac{dZ_g}{d\mu^2} + Z_g^2 \alpha_{\rm S}\, \epsilon + Z_g^2\, \mu^2 \frac{d\alpha_{\rm S}}{d\mu^2} \\ &= \beta(\alpha_{\rm S}) \left(2 Z_g \alpha_{\rm S} \frac{dZ_g}{d\alpha_{\rm S}} + Z_g^2 \right) + Z_g^2 \alpha_{\rm S}\, \epsilon \,, \end{aligned} \tag{1.20}$$

where we have introduced the beta–function, defined as usual as

$$\beta(\alpha_{\rm S}) = \mu^2 \, \frac{d\alpha_{\rm S}}{d\mu^2} \,. \tag{1.21}$$

From eq. (1.18) and (1.20), we obtain

$$\beta(\alpha_{\rm S}) = -b_0 \, \alpha_{\rm S}^2 \,. \tag{1.22}$$

The differential equation in (1.22) drives the running of the coupling constant. In fact,

one has:

$$-b_0 \int_{\mu_0^2}^{\mu^2} \frac{d\bar{\mu}^2}{\bar{\mu}^2} = \int_{\alpha_{\rm S}(\mu_0^2)}^{\alpha_{\rm S}(\mu^2)} \frac{d\alpha_{\rm S}}{\alpha_{\rm S}^2}\,, \tag{1.23}$$

which implies

$$\alpha_{\rm S}\left(\mu^2\right) = \frac{\alpha_{\rm S}\left(\mu_0^2\right)}{1+\alpha_{\rm S}\left(\mu_0^2\right) b_0 \log\left(\frac{\mu^2}{\mu_0^2}\right)}\,. \tag{1.24}$$

We are now in the position to comment the result. The fields content of QCD is such that the inequality $n_{\rm f} < \frac{11}{2} N_{\rm c}$ holds, so that $b_0 > 0$ and the beta–function is negative. We have then obtained that QCD exhibits the remarkable property of *asymptotic freedom*: this means that the renormalized coupling constant $\alpha_{\rm S}$ becomes smaller as the scale at which it is evaluated grows (eq. (1.24)).

Eq. (1.24) tells us how the coupling constant changes when the reference scale varies, but does not fix an absolute value for $\alpha_{\rm S}$. This has to be extracted from experimental data, by fitting them with the more accurate available calculations. If one measure the value of $\alpha_{\rm S}$ at a given reference scale $\bar{\mu}$, then it is possible to express the (one-loop) running of $\alpha_{\rm S}$ in a simple way:

$$\alpha_{\rm S}(\mu^2) = \frac{1}{b_0 \log(\mu^2/\Lambda_{QCD}^2)}\,, \tag{1.25}$$

where Λ_{QCD} is fixed by the condition

$$\alpha_{\rm S}(\bar{\mu}^2) = \frac{1}{b_0 \log(\bar{\mu}^2/\Lambda_{QCD}^2)}\,. \tag{1.26}$$

For consistency, to perform a calculation where other experimental inputs rather then $\alpha_{\rm S}$ are needed, it is important to use the same values of $\alpha_{\rm S}$ used to fit these inputs from data. Typically, this happens when dealing with hadronic processes, where one uses Parton Distribution Functions (PDF's) that are fitted from other data. For this reason, in this thesis we have used as a reference value for $\alpha_{\rm S}$ the value associated to the corresponding PDF set. In all the result presented, we used the CTEQ6M [10] set, where a two loop evolution for $\alpha_{\rm S}$ is assumed. We report here the relevant formulae.

The two loop expression for the beta function reads:

$$\beta(\alpha_{\rm S}) = -b_0\,\alpha_{\rm S}^2 - b_1\,\alpha_{\rm S}^3\,, \tag{1.27}$$

where b_1 is given by

$$b_1 = \frac{153 - 19\,n_{\rm f}}{24\,\pi^2}\,. \tag{1.28}$$

The corresponding two loop evolution used for $\alpha_{\rm S}$ reads [2]

$$\alpha_{\rm S}(\mu^2) = \frac{1}{b_0 \log(\mu^2/\Lambda^2_{\overline{\rm MS}})} \left[1 - \frac{b_1}{b_0^2} \frac{\log[\log(\mu^2/\Lambda^2_{\overline{\rm MS}})]}{\log(\mu^2/\Lambda^2_{\overline{\rm MS}})}\right] , \tag{1.29}$$

where the reference value associated with the CTEQ6M set is

$$\alpha_{\rm S}(M_Z^2) = 0.1189 \quad (\Lambda^{(5)}_{\overline{\rm MS}} = 0.2262 \text{ GeV}) . \tag{1.30}$$

We use the symbol $\Lambda_{\overline{\rm MS}}$ to remind that the beta–function has been calculated in the $\overline{\rm MS}$ scheme. Furthermore, the numerical value reported above corresponds to a calculation done with $n_{\rm f} = 5$, that is the correct choice as long as all quarks, apart from the top, are lighter than the scale μ. When the scale μ crosses a quark mass threshold, then the corresponding quark flavour decouples, and a more correct running equation can be obtained changing $n_{\rm f}$ accordingly, and matching the values of $\alpha_{\rm S}$ at the mass threshold.

It is worthwhile to remark that the values of Λ_{QCD} are always of the same order of magnitude, even if they change slightly when the order of the perturbative calculation (or the renormalization scheme) changes. Numerically, the values are in the range $100 - 400$ MeV. This means that results obtained within perturbative QCD are reliable when the relevant mass scale is (much) larger then Λ_{QCD}, the coupling constant being (much) smaller than 1. Finally, we notice that Λ_{QCD} gives also an estimate of the scale at which QCD becomes strongly coupled. Therefore, Λ_{QCD} gives also an estimate of the *hadronization* scale, i.e. the energy scale at which quarks and gluons bind together to form hadrons.

1.1.3 Infrared divergences and factorization of QCD amplitudes

Before describing the general formalism of NLO computations and Parton Showers, we give a description of the factorization properties of QCD amplitudes in the infrared region. Indeed, a lot of general and technical issues that are present both in fixed order Monte Carlo programs and in event generators based on Parton Showers, are related to the behavior of QCD squared amplitudes in this kinematic region. For this reason, we find useful to introduce this point before describing the two approaches separately.

For a general amplitude involving massless colored particles, there are two (overlapping) regions of the outgoing particles phase space, where the squared amplitude diverges: the collinear and the soft region.[3]

[2] Eq. (1.29) has to be interpreted as an expansion in inverse power of $\log(\mu^2/\Lambda^2_{\overline{\rm MS}})$.

[3] We recall that we use the word *infrared* when referring generically to both the two limits, without

As a guiding example, we consider a generic process with $n+1$ on-shell final state particles, where a quark of momentum k and a gluon of momentum l become collinear (i.e. their relative angle goes to zero). If the two particles come from the splitting of an internal quark line into a qg pair, then the corresponding squared amplitude is divergent, the internal propagator going on its mass shell. However, it can be shown that, in this singular region, the squared amplitude exactly factorizes, in terms of an n-body squared amplitude multiplied for a *splitting function*. In fig. 1.1 this factorization property is reported schematically.

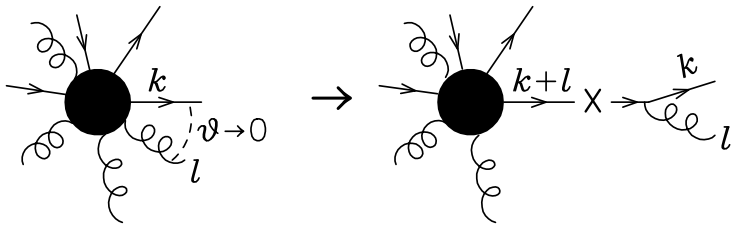

Figure 1.1: Pictorial representation of the factorization of a QCD squared amplitude.

When translated in equations, the meaning of fig. 1.1 corresponds to:

$$\begin{aligned} |\mathcal{M}_{n+1}(k_\oplus, k_\ominus; \ldots, k, \ldots, l, \ldots)|^2 d\Phi_{n+1} \;&\to\; |\mathcal{M}_n(k_\oplus, k_\ominus; \ldots, k+l, \ldots)|^2 d\Phi_n \\ &\times\; \frac{\alpha_S}{2\pi}\,\frac{dt}{t}\,P_{qq}(z)\,dz\,\frac{d\phi}{2\pi}\,, \end{aligned} \tag{1.31}$$

where $\mathcal{M}_{n+1}$ and $\mathcal{M}_n$ are respectively the amplitudes for the full $(n+1)$-body and the (underlying) n-body processes, which is represented as a blob in fig. 1.1, $P_{qq}(z)$ is the Altarelli-Parisi splitting function

$$P_{qq}(z) = C_{\text{F}}\,\frac{1+z^2}{1-z}\,, \tag{1.32}$$

and $d\Phi_n$ is the usual phase space integration, defined as

$$d\Phi_n = (2\pi)^4 \delta^4\left(\sum_{i=1}^{n} k_i - q\right) \prod_{i=1}^{n} \frac{d^3 k_i}{2k_i^0 (2\pi)^3}\,, \tag{1.33}$$

where $q = k_\oplus + k_\ominus$ is the total incoming momentum and k_i are the outgoing particles momenta. The parameters t, z and ϕ describe the kinematics of the splitting process: t is a variable with the dimension of a squared mass, vanishing in the collinear limit (for

distinguish them.

definiteness, we can think $t = (k+l)^2$), z a variable that, in the exact collinear limit, yields the momentum fraction of the outgoing quark relative to the momentum of the parent quark that has split

$$k \to z\,(k+l) \quad \text{for} \quad t \to 0, \tag{1.34}$$

and ϕ is the azimuth of the plane where $\vec{k}$ and $\vec{l}$ lie, around to the $\overrightarrow{k+l}$ direction.

To obtain (1.31), one uses the fact that, in the collinear limit, in addiction to the factorization properties of the squared amplitudes, also the full $(n+1)$-body phase space can be factorized in terms of the underlying n-body phase space and of an emission phase space:

$$d\Phi_{n+1} \to d\Phi_n \times \frac{1}{4(2\pi)^2}\, dt\, dz\, \frac{d\phi}{2\pi}\,. \tag{1.35}$$

Formulae similar to eq. (1.31) hold for the other possible splitting processes: $q \to gq$, $g \to gg$ and $g \to q\bar{q}$. They can be obtained from eq. (1.31) by replacing P_{qq} with the appropriate splitting kernels:

$$\begin{aligned} P_{qg}(z) &= C_{\rm F}\,\frac{1+(1-z)^2}{z}\,, \\ P_{gg}(z) &= 2C_{\rm A}\left[\frac{z}{1-z}+\frac{1-z}{z}+z(1-z)\right]\,, \\ P_{gq}(z) &= T_{\rm F}\left[z^2+(1-z)^2\right]\,. \end{aligned} \tag{1.36}$$

We point out that the (unregularized) Altarelli-Parisi splitting kernel suited for the splitting $i \to j,k$ is denoted by P_{ij}. By convention, the variable z (argument of the kernels) denotes the momentum fraction retained by the parton labelled with j, as implicitly defined in eq. (1.34). As a consequence, we distinguish between P_{qq} and P_{qg}.[4]

We also recall that, for the splittings $g \to gg$ and $g \to q\bar{q}$, a completely factorized formula, as eq. (1.31), holds only if the average over the polarization of the splitting gluon is taken. In fact, for these splittings, the factorization formula is more involved, since, at fixed helicities of the final state gg or $q\bar{q}$ partons, the parent gluon can have two helicities, and they can interfere. Exact formulae, expressed in terms of spin-dependent splitting kernels, can be found for example in sec. 4 of [11].

Another relevant effect is the correlation between the plane where the daughter partons lie and the polarization vector of the splitting gluon. This dependence, due again to spin effects, can be explicitly calculated and yields splitting kernels that depend upon an

[4]For the same reason, the P_{gg} kernel contains a factor 2, that will be omitted when no tagging of the outgoing partons will be assumed, as in sec. 1.3.

azimuthal angle. As in the previous case, this dependence cancels out when the integral over the azimuth is taken. A more careful discussion can be found in [5].[5]

In addiction to collinear regions, QCD amplitudes are singular when a final state gluon has a vanishing momentum. Hence, these divergences are called *soft*. Soft divergences are not necessarily related to collinear regions: in fact, the soft limit can be approached also when the gluon is emitted at large angle with respect to its parent parton. However, when an outgoing gluon is both collinear and soft, we expect to trace the soft divergences in the formulae we already presented. Indeed, the splitting kernels involving a final state gluon (P_{qq}, P_{qg} and P_{gg}) are singular in the limit $z \to 1$ (or $z \to 0$, for P_{qg}), that corresponds to the soft region.

In general, in the soft limit, squared amplitudes factorize in terms of color-correlated amplitudes, which we will introduce later, in sec. 1.2.3, when describing the FKS subtraction method.[6] A full factorization, in terms of the full n-body squared matrix element, holds only when in the n-body process there are no more than three color-connected particles.

As a conclusion of this quick review, we want to stress that both the soft and the collinear behaviors of QCD squared amplitudes are universal, since these limits are described by (quasi-) factorized formulae. This property is heavily used, both in performing NLO calculations and in defining the parton shower algorithm:

- In NLO calculations (see section 1.2), the universal structure of singular limits is used to regularize numerically the divergences of real squared amplitudes in $d = 4$ dimensions, as long as to subtract the infrared poles of the virtual contribution.

- In event generators, factorization is used to define a Markovian, recursive algorithm (the *Parton Shower*), to consistently describe processes with a large number of final state particles. We will see in section 1.3 that these dominant contributions are logarithmic enhanced, logarithms arising exactly from the collinear and soft behavior of squared amplitudes.

[5] We remind that this azimuthal correlation between the gluon polarization vector and the branching plane is present also in splittings initiated by a quark.

[6] General formulae for the soft limit of QCD squared amplitudes can be found, for example, in [11], and, for processes involving massive colored partons, in [12].

1.2 Fixed order calculations

In this section we describe the general features of NLO calculations for hadronic collision processes, fix the notation that we will be used throughout this thesis and describe how subtraction methods work.[7]

The content of this section is based on [2].

1.2.1 General formalism for NLO computation

We begin by considering $2 \to n$ processes at the leading order, i.e. at the lowest order at which the given process can take place. The momentum conservation reads

$$x_\oplus K_\oplus + x_\ominus K_\ominus = k_1 + \ldots + k_n \,, \tag{1.37}$$

where $x_{\circledast}$ are the momentum fractions of the incoming partons with respect to the four-momenta of the incoming hadrons, that we label as $K_{\circledast}$. Sometimes it is useful to denote the momenta of initial state partons with $k_{\circledast}$, so that we have:

$$k_\oplus = x_\oplus K_\oplus \,, \qquad\qquad k_\ominus = x_\ominus K_\ominus \,. \tag{1.38}$$

For ease of notation, the set of variables needed to define a unique n-body kinematic is denoted by $\mathbf{\Phi}_n$, and obviously it includes the final-state particles on-shell momenta and the two incoming momentum fractions:

$$\mathbf{\Phi}_n = \{x_\oplus, x_\ominus, k_1, \ldots, k_n\} \,. \tag{1.39}$$

We indicate with $\mathcal{B}$ the Born term, i.e. the squared matrix elements relevant to the Leading-Order (LO) contributions to our process.[8] At this order, the total cross section is then given by

$$\sigma_{\text{LO}} = \int d\mathbf{\Phi}_n \, \mathcal{L} \, \mathcal{B}(\mathbf{\Phi}_n) \,, \tag{1.40}$$

where $\mathcal{L}$ is the product of the incoming parton distribution functions

$$\mathcal{L} = \mathcal{L}(x_\oplus, x_\ominus) = f_\oplus(x_\oplus) \, f_\ominus(x_\ominus) \,, \tag{1.41}$$

[7] To make the notation easier, in this section we omit the parton flavours indexes and the scale dependences of the various contributions to the total NLO cross section.

[8] For simplicity, we restrict ourselves to processes where the Born contribution $\mathcal{B}$ is finite over the whole phase space $\mathbf{\Phi}_n$. Further details concerning this point can be found in [2].

and

$$d\mathbf{\Phi}_n = dx_\oplus \, dx_\ominus \, d\Phi_n \left(k_\oplus + k_\ominus; k_1, \ldots, k_n\right) \tag{1.42}$$

indicates the integration over the Born phase space Φ_n and the momentum fractions of incoming partons. As usual, the n-body phase space is defined as

$$d\Phi_n \left(q; k_1, \ldots, k_n\right) = (2\pi)^4 \, \delta^4 \left(q - \sum_{i=1}^{n} k_i \right) \prod_{i=1}^{n} \frac{d^3 k_i}{(2\pi)^3 \, 2k_i^0} \, . \tag{1.43}$$

At the NLO, we have to include real and virtual corrections, and factorization counterterms.

Real corrections are obtained integrating the tree-level squared amplitudes for the $2 \to n{+}1$ parton process, which we denote by $\mathcal{R}$, multiplied by the appropriate luminosity. The integral is done over the corresponding $(n+1)$-body phase space and the incoming partons momentum fractions. As for the n-body contribution, we denote with $\mathbf{\Phi}_{n+1}$ the whole set of variables that parameterize this space:

$$\mathbf{\Phi}_{n+1} = \{x_\oplus, x_\ominus, k_1, \ldots, k_{n+1}\} \, . \tag{1.44}$$

Real contributions are finite in the whole phase space $d\Phi_{n+1}$, except for the regions that correspond to soft and collinear emissions. There, the divergences are analytically integrable only in $d = 4 - 2\epsilon$ dimensions, and yield $1/\epsilon^2$ and $1/\epsilon$ poles.

Virtual corrections are given by the interference of the one-loop amplitudes with the LO ones. In general, these contributions contain both infrared and ultraviolet divergences. As we already mentioned in sec. 1.1.2, the renormalization procedure allows to remove systematically all the ultraviolet divergences, leaving UV- finite virtual contributions, that we denote by $\mathcal{V}_\mathrm{b}$. These terms are needed to be computed and expressed in $d = 4 - 2\epsilon$ dimensions, to explicitly expose the remaining IR divergences as $1/\epsilon^2$ and $1/\epsilon$ poles. The subscript b (for "bare") reminds us of the presence of infrared divergences in the amplitude.

The QCD infrared-divergences cancellation theorem, often referred to as Kinoshita-Lee-Nauenberg (KLN) theorem [13, 14], ensure that when the virtual contributions are summed up with the real ones (integrated over the radiation variables), then the poles coming from the integration over regions where an outgoing parton is soft or two outgoing partons are collinear cancel out, leaving an expression that contains only poles coming from configurations where an outgoing parton is collinear to the beam. The cancellation can not be completely achieved because when the outgoing parton is emitted from an incoming leg, then the momentum flowing inside the hard scattering process is different

from the one flowing inside the corresponding virtual contribution.

The full cancellation of these remaining singularities is achieved by adding two other counterterms ($\mathcal{G}_{\oplus,\mathrm{b}}$ and $\mathcal{G}_{\ominus,\mathrm{b}}$), one for each of the incoming partons ($\oplus$, $\ominus$), to the differential cross section. These factorizations counterterms are infrared divergent in four dimensions. Therefore, they are computed in $d = 4 - 2\epsilon$ dimensions, and the divergences appear as $1/\epsilon$ poles. To remind this fact, also in this case a subscript b has been included in the notation.

With all the above terms, we are now in the position of writing the total NLO cross section as

$$\begin{aligned}\sigma_{\mathrm{NLO}} &= \int d\mathbf{\Phi}_n \, \mathcal{L} \left[\mathcal{B}(\mathbf{\Phi}_n) + \mathcal{V}_{\mathrm{b}}(\mathbf{\Phi}_n) \right] + \int d\mathbf{\Phi}_{n+1} \, \mathcal{L} \, \mathcal{R}(\mathbf{\Phi}_{n+1}) \\ &+ \int d\mathbf{\Phi}_{n,\oplus} \, \mathcal{L} \, \mathcal{G}_{\oplus,\mathrm{b}}(\mathbf{\Phi}_{n,\oplus}) + \int d\mathbf{\Phi}_{n,\ominus} \, \mathcal{L} \, \mathcal{G}_{\ominus,\mathrm{b}}(\mathbf{\Phi}_{n,\ominus}) \; , \end{aligned} \tag{1.45}$$

where

$$d\mathbf{\Phi}_{n+1} = dx_\oplus \, dx_\ominus \, d\Phi_{n+1} \left(k_\oplus + k_\ominus ; k_1, \ldots, k_{n+1} \right) \; . \tag{1.46}$$

The factorization counterterms are integrated over the regions of the $(n+1)$-body phase space where the emitted parton is exactly collinear to one of the two incoming particles. These regions are labelled as $\mathbf{\Phi}_{n,\circledast}$, and we can write

$$\mathbf{\Phi}_{n,\oplus} = \{ x_\oplus, x_\ominus, z, k_1, \ldots, k_n \} \; , \quad z \, x_\oplus K_\oplus + x_\ominus K_\ominus = \sum_{i=1}^{n} k_i \; , \tag{1.47}$$

$$\mathbf{\Phi}_{n,\ominus} = \{ x_\oplus, x_\ominus, z, k_1, \ldots, k_n \} \; , \quad x_\oplus K_\oplus + z \, x_\ominus K_\ominus = \sum_{i=1}^{n} k_i \; , \tag{1.48}$$

where z is the fraction of momentum of the incoming parton after radiation, with respect to $k_{\circledast}$, the momentum of the parton extracted from the hadron. The integrals are defined as

$$d\mathbf{\Phi}_{n,\oplus} = dx_\oplus \, dx_\ominus \, dz \, d\Phi_n \left(z \, k_\oplus + k_\ominus ; k_1, \ldots, k_n \right) \; , \tag{1.49}$$

$$d\mathbf{\Phi}_{n,\ominus} = dx_\oplus \, dx_\ominus \, dz \, d\Phi_n \left(k_\oplus + z \, k_\ominus ; k_1, \ldots, k_n \right) \; . \tag{1.50}$$

Therefore, integrals are effectively performed over the n-body Born phase space and a further variable, that parameterizes the energy of the outgoing parton that is collinear to the beam. We can then associate with the phase-space configuration $\mathbf{\Phi}_{n,\circledast}$ an *underlying n-body configuration*, obtained by replacing the momenta of the incoming parton ($k_{\circledast}$) and of the outgoing collinear parton, with an incoming momentum having momentum

fraction $zx_{\textcircled{\pm}}$. Once this replacement has been done, from the momentum conservation constraints in (1.47) and (1.48) it follows that the variable $\bar{x}_{\textcircled{\pm}} = zx_{\textcircled{\pm}}$ does not depend on z anymore. The resulting underlying n-body phase space can be then fully identified with the Born phase-space $\mathbf{\Phi}_n$. However, we label this phase space with $\bar{\mathbf{\Phi}}_n$, to remind that it is a n-body configuration obtained after the aforementioned manipulation:

$$\bar{\mathbf{\Phi}}_n = \{\bar{x}_\oplus, \bar{x}_\ominus, k_1, \dots k_n\}\,, \qquad \bar{x}_{\textcircled{\pm}} = zx_{\textcircled{\pm}}\,, \qquad \bar{x}_{\textcircled{\mp}} = x_{\textcircled{\mp}}\,, \tag{1.51}$$

where, for future reference, we leave explicitly indicated the relation between $\bar{x}_{\textcircled{\pm}}$ and the integration variables $x_{\textcircled{\pm}}$ and z.

Although at this point all the terms needed to perform a NLO calculation have been formally described, a couple of points need a more careful attention:

- We already noticed that the r.h.s. of eq. (1.45) contains factors that are separately IR divergent, but whose sum is finite. However, we have to describe how this cancellation is achieved in practice.
- We want to calculate expectation values for observables that are more exclusive than the total cross section, but such that the cancellation of IR divergences still holds.[9]

In the following we address the latter issue, while the former will be dealt with in sec. 1.2.2, when we describe subtraction methods.

The expectation value of an observable O is obtained multiplying each integrand in eq. (1.45) for the value assumed by O in the corresponding phase space point:

$$\begin{aligned}
\langle O \rangle \;&=\; \int d\mathbf{\Phi}_n\, \mathcal{L}\, O_n(\mathbf{\Phi}_n)\, \Big[\mathcal{B}(\mathbf{\Phi}_n) + \mathcal{V}_{\rm b}(\mathbf{\Phi}_n)\Big] \\
&+\; \int d\mathbf{\Phi}_{n+1}\, \mathcal{L}\, O_{n+1}(\mathbf{\Phi}_{n+1})\, \mathcal{R}(\mathbf{\Phi}_{n+1}) \\
&+\; \int d\mathbf{\Phi}_{n,\oplus}\, \mathcal{L}\, O_{n+1}(\mathbf{\Phi}_{n,\oplus})\, \mathcal{G}_{\oplus,{\rm b}}(\mathbf{\Phi}_{n,\oplus}) + \int d\mathbf{\Phi}_{n,\ominus}\, \mathcal{L}\, O_{n+1}(\mathbf{\Phi}_{n,\ominus})\, \mathcal{G}_{\ominus,{\rm b}}(\mathbf{\Phi}_{n,\ominus})\,,
\end{aligned} \tag{1.52}$$

where O_n and O_{n+1} are the value assumed by the observable O in terms of n and $(n+1)$ final-state particle momenta. Eq. (1.52) is made of terms that are separately divergent. The cancellation of divergences is guaranteed if we restrict to perform predictions for observables that are *infrared-safe*. Such observables are required to be insensitive to soft (S), final state collinear (FSC) and initial state collinear (ISC) emissions.

[9] In this context, an observable is defined as a function of the final state momenta.

Formally, these requirements correspond to the following properties:

(S) When $k_j \to 0$, then

$$O_{n+1}\left(k_1, \ldots, k_j, \ldots, k_{n+1}\right) \to O_n\left(k_1, \ldots, \cdot, \ldots, k_{n+1}\right), \tag{1.53}$$

where with the notation in the r.h.s. we denote the value assumed by the observable O when it is calculated removing the momentum k_j. Momentum conservation still holds because we are in the soft limit.

(FSC) When $\vec{k}_i \parallel \vec{k}_j$, then

$$O_{n+1}\left(k_1, \ldots, k_i, \ldots, k_j, \ldots, k_{n+1}\right) \to O_n\left(k_1, \ldots, k, \ldots, k_{n+1}\right), \tag{1.54}$$

where $k = k_i + k_j$.

(ISC) When $\vec{k}_j \parallel \vec{k}_{\circledast}$, then

$$O_{n+1}\left(k_1, \ldots, k_j, \ldots, k_{n+1}\right) \to O_n(k_1, \ldots, k_n). \tag{1.55}$$

Observe that, from eq. (1.55), the argument of O in the last two terms on the right hand side of eq. (1.52) can be set exactly equal to $\bar{\mathbf{\Phi}}_n$ rather than $\mathbf{\Phi}_{n,\circledast}$. The final formula for the NLO expectation value of O becomes then:

$$\begin{aligned}
\langle O \rangle &= \int d\mathbf{\Phi}_n \, \mathcal{L} \, O_n(\mathbf{\Phi}_n) \left[\mathcal{B}(\mathbf{\Phi}_n) + \mathcal{V}_{\mathrm{b}}(\mathbf{\Phi}_n) \right] \\
&+ \int d\mathbf{\Phi}_{n+1} \, \mathcal{L} \, O_{n+1}(\mathbf{\Phi}_{n+1}) \, \mathcal{R}(\mathbf{\Phi}_{n+1}) \\
&+ \int d\mathbf{\Phi}_{n,\oplus} \, \mathcal{L} \, O_n\big(\bar{\mathbf{\Phi}}_n\big) \, \mathcal{G}_{\oplus,\mathrm{b}}(\mathbf{\Phi}_{n,\oplus}) + \int d\mathbf{\Phi}_{n,\ominus} \, \mathcal{L} \, O_n\big(\bar{\mathbf{\Phi}}_n\big) \, \mathcal{G}_{\ominus,\mathrm{b}}(\mathbf{\Phi}_{n,\ominus}) \, .
\end{aligned} \tag{1.56}$$

The integrals in eq. (1.56) are usually too difficult to be performed analytically (because of the involved functional form of O) and, being divergent, they are also not suited for numerical computations. Different strategies have been proposed to handle this problem. The common underlying idea is to rewrite the above formula (or eq. (1.45)) in such a way that the cancellation of divergences is manifest for each term. In the following, we describe the subtraction formalism, first introduced in ref. [15] for e^+e^- annhilation.

1.2.2 Subtraction formalism

The subtraction formalism is based on the idea that one can cancel numerically the divergences arising in the integration of the real contributions $\mathcal{R}$, by subtracting from them quantities, called *real counterterms*, that diverge as $\mathcal{R}$ when a singular region is approached. In this way, the integration of real terms is no longer divergent. Furthermore, by adding to $\mathcal{V}_{\rm b}$ the analytic expression of the integral of these counterterms over the full radiation phase space, the cancellation on IR poles is achieved, and the final result remains finite.

Before describing the technicalities, we remind that this formalism is very general and powerful. In fact, owing to the factorization properties of QCD amplitudes, the whole procedure is universal, in the sense that it does not depend on the detail of the process at hand. For this reason, once the building blocks are known, then they can be used for several processes.

As anticipated above, the subtraction formalism requires the definition of a set of functions $\mathcal{C}^{(\alpha)}$, called real counterterms. The index α labels a particular singular region, i.e. a $(n+1)$-body kinematics where either a final-state parton has vanishing momentum, or a final-state massless parton has momentum proportional to an initial-state or to another final-state massless parton. Furthermore, for each α, a mapping $\mathbf{M}^{(\alpha)}$ of an $(n+1)$-body configuration into a singular one is needed:

$$\tilde{\mathbf{\Phi}}^{(\alpha)}_{n+1} = \mathbf{M}^{(\alpha)}\left(\mathbf{\Phi}_{n+1}\right) \ , \quad \tilde{\mathbf{\Phi}}^{(\alpha)}_{n+1} = \left\{\tilde{x}^{(\alpha)}_{\oplus}, \tilde{x}^{(\alpha)}_{\ominus}, \tilde{k}^{(\alpha)}_{1}, \ldots, \tilde{k}^{(\alpha)}_{n+1}\,.\right\} \tag{1.57}$$

Since each singular region α is characterized by a different mapping, we use the superscript α on the tilded variables, .

As already pointed out, we want the mapping and the counterterms to let the quantity

$$\mathcal{R}(\mathbf{\Phi}_{n+1})\, O_{n+1}(\mathbf{\Phi}_{n+1}) - \sum_{\alpha} \mathcal{C}^{(\alpha)}(\mathbf{\Phi}_{n+1})\, O_{n+1}\left(\mathbf{M}^{(\alpha)}\left(\mathbf{\Phi}_{n+1}\right)\right) \tag{1.58}$$

with singularities at most integrable in the $\mathbf{\Phi}_{n+1}$ space. Hence, the mapping (1.57) must be smooth near the singular region, and it must become the identity there. For example, if α is associated with the FSC region where the particles i and j become collinear, we must have $\tilde{\mathbf{\Phi}}^{(\alpha)}_{n+1} = \mathbf{\Phi}_{n+1}$ for $\vec{k}_i \parallel \vec{k}_j$.

As in the case of the ISC configurations (eqs. (1.47) and (1.48)), we associate with each $\tilde{\mathbf{\Phi}}^{(\alpha)}_{n+1}$ configuration an n-body configuration $\bar{\mathbf{\Phi}}^{(\alpha)}_{n}$, that we will call again the *underlying n-body configuration*

$$\bar{\mathbf{\Phi}}^{(\alpha)}_{n} = \left[\left\{\bar{x}_{\oplus}, \bar{x}_{\ominus}, \bar{k}_1, \ldots, \bar{k}_n\right\}\right]_{\alpha} , \tag{1.59}$$

which is obtained as follows:

- If $\alpha \in$ S (i.e. it is a soft region), $\bar{\mathbf{\Phi}}_n^{(\alpha)}$ is obtained by deleting the soft parton.
- If $\alpha \in$ FSC (i.e. it is a final-state collinear region), $\bar{\mathbf{\Phi}}_n^{(\alpha)}$ is obtained by replacing the momenta of the two collinear partons with their sum.
- If $\alpha \in$ ISC (i.e. it is an initial state collinear region), $\bar{\mathbf{\Phi}}_n^{(\alpha)}$ is obtained with the same procedure that leads to eq. (1.51): the collinear parton is deleted, and the momentum fraction of the initial-state radiating parton is replaced with its momentum fraction after radiation.

In all the above cases, the final-state momenta are relabelled with an index that takes values in the range $1, \ldots, n$, and, for ease of notation, we have introduced the *context convention*: if an expression is enclosed in the subscripted squared brackets

$$\big[\ldots\big]_\alpha\,, \tag{1.60}$$

we mean that all variables appearing inside have, when applicable, the superscripts corresponding to the subscript of the bracket.

As a consequence of this mapping procedure, the variables in $\bar{\mathbf{\Phi}}_n^{(\alpha)}$ are constrained by momentum conservation

$$\bar{x}_\oplus K_\oplus + \bar{x}_\ominus K_\ominus = \sum_{j=1}^{n} \bar{k}_j\ . \tag{1.61}$$

Furthermore, for S or FSC regions, we have

$$\bar{x}_{\oplus\!\!\!\!\!\!\ominus} = \tilde{x}_{\oplus\!\!\!\!\!\!\ominus}\,, \tag{1.62}$$

whereas for ISC regions, we have

$$\bar{x}_\oplus < \tilde{x}_\oplus\,, \qquad \bar{x}_\ominus = \tilde{x}_\ominus\,, \tag{1.63}$$

for the $\oplus$ direction, and the analogous one for the case of ISC in the $\ominus$ direction.

In the subtraction method one rewrites the contribution to any observable O coming from real radiation in the following way

$$\begin{aligned}\int d\mathbf{\Phi}_{n+1}\,\mathcal{L}\,O_{n+1}(\mathbf{\Phi}_{n+1})\;\mathcal{R}(\mathbf{\Phi}_{n+1}) = \sum_\alpha \int d\mathbf{\Phi}_{n+1}\;\Big[\tilde{\mathcal{L}}\,O_n\big(\bar{\mathbf{\Phi}}_n\big)\;\mathcal{C}(\mathbf{\Phi}_{n+1})\Big]_\alpha\;+\\ \int d\mathbf{\Phi}_{n+1}\Big\{\mathcal{L}\,O_{n+1}(\mathbf{\Phi}_{n+1})\;\mathcal{R}(\mathbf{\Phi}_{n+1}) - \sum_\alpha\Big[\tilde{\mathcal{L}}\,O_n\big(\bar{\mathbf{\Phi}}_n\big)\;\mathcal{C}(\mathbf{\Phi}_{n+1})\Big]_\alpha\Big\},\end{aligned} \tag{1.64}$$

where $\tilde{\mathcal{L}} = \mathcal{L}(\tilde{x}_\oplus, \tilde{x}_\ominus)$. In this way, under the assumptions we have made about the counterterms, and the assumption that O is an infrared-safe observable (eq. (1.53)- (1.55)), the second term on the r.h.s. of eq. (1.64) is integrable in $d = 4$ dimensions.

The first term on the r.h.s. of eq. (1.64) contains instead the divergences that have to cancel against the poles in $\mathcal{V}_{\rm b}$ and $\mathcal{G}_{\circledast,{\rm b}}$. The choice of the counterterms in eq. (1.58) and of the mapping (1.57) is crucial, because it should be such that the integrals in the first term of the r.h.s of eq. (1.64) are easily performed analytically in d dimensions, yielding a set of terms where divergences appear as poles in ϵ.

For this purpose, by means of the mapping $\mathbf{M}^{(\alpha)}$, for each α we parameterize the $(n+1)$-phase space in terms of an n-body phase space (obtained as described earlier), plus (three) more variables that describe the radiation process:

$$d\mathbf{\Phi}_{n+1} = d\bar{\mathbf{\Phi}}_n^{(\alpha)}\, d\Phi_{\rm rad}^{(\alpha)}\,. \tag{1.65}$$

The range of the radiation variables in $\Phi_{\rm rad}^{(\alpha)}$ may depend upon $\bar{\mathbf{\Phi}}_n^{(\alpha)}$. Furthermore, eq. (1.65) implicitly defines a Jacobian, possibly dependent upon $\bar{\mathbf{\Phi}}_n^{(\alpha)}$, that is supposed to be included into $d\Phi_{\rm rad}^{(\alpha)}$.

To deal with the luminosity in the first term of eq. (1.64), we need to distinguish two cases: the FSC+S case and the ISC one. In the former case we have

$$\tilde{\mathcal{L}} = \mathcal{L}(\tilde{x}_\oplus, \tilde{x}_\ominus) = \mathcal{L}(\bar{x}_\oplus, \bar{x}_\ominus)\,. \tag{1.66}$$

Defining

$$\left[\bar{\mathcal{C}}\left(\bar{\mathbf{\Phi}}_n\right) = \int d\Phi_{\rm rad}\, \mathcal{C}(\mathbf{\Phi}_{n+1})\right]_{\alpha\in\{\rm FSC,S\}}, \tag{1.67}$$

we can write the generic term in the first sum on the r.h.s. of eq. (1.64) as follows

$$\left[\int d\mathbf{\Phi}_{n+1}\, \tilde{\mathcal{L}}\, O_n\big(\bar{\mathbf{\Phi}}_n\big)\; \mathcal{C}(\mathbf{\Phi}_{n+1}) = \int d\bar{\mathbf{\Phi}}_n\, \tilde{\mathcal{L}}\, O_n\big(\bar{\mathbf{\Phi}}_n\big)\, \bar{\mathcal{C}}\left(\bar{\mathbf{\Phi}}_n\right)\right]_{\alpha\in\{\rm FSC,S\}}. \tag{1.68}$$

In the ISC case, we cannot factor out the luminosity, since $\tilde{x}_\circledast \neq \bar{x}_\circledast$. Therefore, we define

$$\left[\bar{\mathcal{C}}\left(\bar{\mathbf{\Phi}}_n, z\right) = \int d\Phi_{\rm rad}\, \mathcal{C}(\mathbf{\Phi}_{n+1})\;\, z\,\delta\left(z - \bar{x}_\circledast/\tilde{x}_\circledast\right)\right]_{\alpha\in\left\{\rm ISC_\circledast\right\}}, \tag{1.69}$$

which formally introduces the momentum fraction z, and write

$$\left[\int d\mathbf{\Phi}_{n+1}\, \tilde{\mathcal{L}}\, O_n\big(\bar{\mathbf{\Phi}}_n\big)\; \mathcal{C}(\mathbf{\Phi}_{n+1}) = \int d\bar{\mathbf{\Phi}}_n \frac{dz}{z} \tilde{\mathcal{L}}\, O_n\big(\bar{\mathbf{\Phi}}_n\big)\, \bar{\mathcal{C}}\left(\bar{\mathbf{\Phi}}_n, z\right)\right]_{\alpha\in\{\rm ISC\}}. \tag{1.70}$$

Notice that, owing to the delta function in eq. (1.69) we have

$$\tilde{\mathcal{L}} = \mathcal{L}(\tilde{x}_\oplus, \tilde{x}_\ominus) = \begin{cases} \mathcal{L}(\bar{x}_\oplus/z, \bar{x}_\ominus) & \text{for} \quad \alpha \in \mathrm{ISC}_\oplus \\ \mathcal{L}(\bar{x}_\oplus, \bar{x}_\ominus/z) & \text{for} \quad \alpha \in \mathrm{ISC}_\ominus \end{cases} . \tag{1.71}$$

Now we can observe that the variables $\left\{\tilde{x}_\oplus, \tilde{x}_\ominus, z, \bar{k}_1, \ldots, \bar{k}_n\right\}$ in the ISC regions can be naturally identified with the $\mathbf{\Phi}_{n,\circledast}$ variables in eqs. (1.47) and (1.48). In fact, the $\bar{k}_i$'s are integration variables, and can be identified with the k_i's in eqs. (1.47) and (1.48). Furthermore, the $\tilde{x}_\circledast$ variables have to coincide with $x_\circledast$ in eqs. (1.47) and (1.48), since $x_\circledast$ refers to a singular ISC region and the mapping in eq. (1.57) becomes the identity there. Therefore, the z variables of eqs. (1.51) and (1.69) are identical, and from eqs. (1.49) and (1.50), we obtain

$$d\mathbf{\Phi}_{n,\circledast} = d\bar{\mathbf{\Phi}}_n \frac{dz}{z} , \tag{1.72}$$

where we have performed the change of variables $\bar{x}_\circledast \to \tilde{x}_\circledast$.

We now write eq. (1.56) as

$$\begin{aligned} \langle O \rangle \;=\; & \int d\mathbf{\Phi}_n \, \mathcal{L}\, O_n(\mathbf{\Phi}_n) \left[\mathcal{B}(\mathbf{\Phi}_n) + \mathcal{V}_\mathrm{b}(\mathbf{\Phi}_n)\right] \\ & + \int d\mathbf{\Phi}_{n+1} \left\{ \mathcal{L}\, O_{n+1}(\mathbf{\Phi}_{n+1}) \; \mathcal{R}(\mathbf{\Phi}_{n+1}) - \sum_\alpha \left[\tilde{\mathcal{L}}\, O_n\big(\bar{\mathbf{\Phi}}_n\big) \; \mathcal{C}(\mathbf{\Phi}_{n+1}) \right]_\alpha \right\} \\ & + \sum_{\alpha \in \{\mathrm{FSC,S}\}} \left[\int d\bar{\mathbf{\Phi}}_n \, \tilde{\mathcal{L}}\, O_n\big(\bar{\mathbf{\Phi}}_n\big) \; \bar{\mathcal{C}}\left(\bar{\mathbf{\Phi}}_n\right) \right]_\alpha + \sum_{\alpha \in \left\{\mathrm{ISC}_\circledast\right\}} \left[\int d\mathbf{\Phi}_{n,\circledast} \, \tilde{\mathcal{L}}\, O_n\big(\bar{\mathbf{\Phi}}_n\big) \; \bar{\mathcal{C}}\left(\mathbf{\Phi}_{n,\circledast}\right) \right]_\alpha \\ & + \int d\mathbf{\Phi}_{n,\oplus} \, \tilde{\mathcal{L}}\, O_n\big(\bar{\mathbf{\Phi}}_n\big) \; \mathcal{G}_{\oplus,\mathrm{b}}(\mathbf{\Phi}_{n,\oplus}) + \int d\mathbf{\Phi}_{n,\ominus} \, \tilde{\mathcal{L}}\, O_n\big(\bar{\mathbf{\Phi}}_n\big) \; \mathcal{G}_{\ominus,\mathrm{b}}(\mathbf{\Phi}_{n,\ominus}) \; . \end{aligned} \tag{1.73}$$

For uniformity of notation, in the last line we have substituted $\mathcal{L} \to \tilde{\mathcal{L}}$, since in the phase space $\mathbf{\Phi}_{n,\circledast}$ we have $x_\circledast = \tilde{x}_\circledast$.

It turns out that it is always possible to write

$$\mathcal{G}_{\circledast,\mathrm{b}}(\mathbf{\Phi}_{n,\circledast}) \; + \sum_{\alpha \in \left\{\mathrm{ISC}_\circledast\right\}} \bar{\mathcal{C}}^{(\alpha)}(\mathbf{\Phi}_{n,\circledast}) = \mathcal{G}_\circledast(\mathbf{\Phi}_{n,\circledast}) + \delta(1-z)\, \mathcal{G}^{\mathrm{div}}_\circledast\left(\bar{\mathbf{\Phi}}_n\right) \; , \tag{1.74}$$

where $\mathcal{G}_\circledast(\mathbf{\Phi}_{n,\circledast})$ is finite in $d = 4$ dimensions.[10] The collinear poles coming from ISC regions cancel in the sum between $\mathcal{G}_{\circledast,\mathrm{b}}$ and the $\bar{\mathcal{C}}^{(\alpha)}$'s. The only remaining poles in ϵ are included in the last term of eq. (1.74), and have soft origin. They are the poles

[10] We point out that $\mathcal{G}_\circledast$, although finite, may contain distributions associated with the soft region $z \to 1$.

associated to soft divergences in the ISC regions, and they cancel out together with the other integrated counterterms and the $\mathcal{V}_{\rm b}$ contribution, so that in the quantity

$$\mathcal{V}(\mathbf{\Phi}_n) = \mathcal{V}_{\rm b}(\mathbf{\Phi}_n) + \left[\sum_{\alpha\in\{\rm FSC,S\}} \bar{\mathcal{C}}^{(\alpha)}\big(\bar{\mathbf{\Phi}}_n\big) + \mathcal{G}^{\rm div}_{\oplus}\big(\bar{\mathbf{\Phi}}_n\big) + \mathcal{G}^{\rm div}_{\ominus}\big(\bar{\mathbf{\Phi}}_n\big) \right]^{\bar{\mathbf{\Phi}}_n=\mathbf{\Phi}_n} , \tag{1.75}$$

all poles in ϵ cancel. With the notation

$$\big[\dots\big]^{\bar{\mathbf{\Phi}}_n=\mathbf{\Phi}_n}, \tag{1.76}$$

we mean that the argument between the brackets is evaluated for values of the phase-space variables $\bar{\mathbf{\Phi}}_n$ equal to $\mathbf{\Phi}_n$.

Defining now the following abbreviations

$$R = \mathcal{L}\,\mathcal{R}, \qquad C^{(\alpha)} = \tilde{\mathcal{L}}^{(\alpha)}\,\mathcal{C}^{(\alpha)}, \qquad G_{\oplus} = \tilde{\mathcal{L}}\,\mathcal{G}_{\oplus}, \qquad B = \mathcal{L}\,\mathcal{B}, \qquad V = \mathcal{L}\,\mathcal{V}\,, \tag{1.77}$$

equation (1.73) becomes

$$\begin{aligned}
\langle O\rangle \;=\; & \int d\mathbf{\Phi}_n\; O_n(\mathbf{\Phi}_n)\,\Big[B(\mathbf{\Phi}_n) + V(\mathbf{\Phi}_n)\Big] \\
+ \; & \int d\mathbf{\Phi}_{n+1}\Big\{O_{n+1}(\mathbf{\Phi}_{n+1})\; R(\mathbf{\Phi}_{n+1}) - \sum_\alpha \big[O_n\big(\bar{\mathbf{\Phi}}_n\big)\; C(\mathbf{\Phi}_{n+1})\big]_\alpha\Big\} \\
+ \; & \int d\mathbf{\Phi}_{n,\oplus}\; O_n\big(\bar{\mathbf{\Phi}}_n\big)\; G_\oplus(\mathbf{\Phi}_{n,\oplus}) + \int d\mathbf{\Phi}_{n,\ominus}\; O_n\big(\bar{\mathbf{\Phi}}_n\big)\; G_\ominus(\mathbf{\Phi}_{n,\ominus})\;,
\end{aligned} \tag{1.78}$$

and it is now suited to be integrated numerically, since all the integrals that appear in it are separately finite and can be evaluated in 4 dimensions.

Results presented in this thesis have been obtained using two popular subtraction methods: the one by Frixione, Kunszt and Signer, proposed in refs. [16, 17], and the one by Catani and Seymour, first appeared in ref. [11]. In the following, we describe how the two methods work, leaving the technical details to the original papers or to their description given in ref. [2].

1.2.3 Frixione, Kunszt and Signer subtraction

In the approach by Frixione, Kunszt and Signer (FKS), the cross section for the real-emission is expressed as a sum of terms, each one having at most one collinear and one soft singularity associated with one parton (called the FKS parton). Furthermore, each of the

resulting terms is integrated over the full radiation phase space, with a parameterization suited to handle numerically and analytically the now-isolated singulariti(es).

Isolation of singular regions

The terms are classified as follows, according to the collinear behavior of the FKS parton:

- The singular region associated with the final-state parton i becoming collinear to the beam axis ($k_i \cdot k_{\circledast} \to 0$) or soft ($k_i \to 0$) is labeled by i.
- Regions associated with final-state parton i becoming collinear to a final-state parton j ($k_i \cdot k_j \to 0$) or soft ($k_i \to 0$) are labeled by the pair ij.

The separation of the real emission terms $\mathcal{R}$ is achieved by multiplying $\mathcal{R}$ with non-negative functions $\mathcal{S}$ of the $(n+1)$-body phase space such that[11]

$$\sum_i \mathcal{S}_i + \sum_{ij} \mathcal{S}_{ij} = 1\,. \tag{1.79}$$

The $\mathcal{S}$ functions are requested to have the following properties:

$$\lim_{k_m^0 \to 0} \left(\mathcal{S}_i + \sum_j \mathcal{S}_{ij} \right) = \delta_{im}\,, \tag{1.80}$$

$$\lim_{\vec{k}_m \| \vec{k}_{\circledast}} \mathcal{S}_i = \delta_{im}\,, \tag{1.81}$$

$$\lim_{\vec{k}_m \| \vec{k}_l} (\mathcal{S}_{ij} + \mathcal{S}_{ji}) = \delta_{im}\delta_{jl} + \delta_{il}\delta_{jm}\,, \tag{1.82}$$

$$\lim_{\vec{k}_m \| \vec{k}_{\circledast}} \mathcal{S}_{ij} = 0\,, \tag{1.83}$$

which are all consistent with the constrain in eq. (1.79). By a careful analysis of eqs. (1.80)-(1.83), it turns out that in a given soft region, i.e. if parton m is soft, all $\mathcal{S}_i$ and $\mathcal{S}_{ij}$ with $i \neq m$ vanish. Instead, for ISC regions, i.e. when parton m becomes collinear to an initial state parton, the only non-vanishing $\mathcal{S}$ function is $\mathcal{S}_m$, that equals one, while for a given FSC region, i.e. when partons i and j are collinear, only $\mathcal{S}_{ij}$ and $\mathcal{S}_{ji}$ can differ from zero, and their sum is one.

[11] Two options are allowed for the range of the indices in the sums in eq. (1.79). We can let them range from 1 to $(n+1)$ (excluding only the $i = j$ possibility in the second sum), or we can assume that the $\mathcal{S}_i$ and $\mathcal{S}_{ij}$ vanish if the corresponding regions are not singular. In this last case, they are excluded from the sum. For example, if i is a gluon and j is a quark, we may set to zero $\mathcal{S}_{ji}$, since there is no soft singularity associated to j becoming soft. Notice that if i and j are both gluons, both terms $\mathcal{S}_{ij}$ and $\mathcal{S}_{ji}$ appear in the sum, since both gluons can become soft.

We now write

$$\mathcal{R} = \sum_i \mathcal{R}_i + \sum_{ij} \mathcal{R}_{ij}\,, \tag{1.84}$$

where

$$\mathcal{R}_i = \mathcal{S}_i \mathcal{R}\,, \qquad \mathcal{R}_{ij} = \mathcal{S}_{ij} \mathcal{R}\,. \tag{1.85}$$

The $\mathcal{R}_i$ terms diverge only in the regions in which parton i is soft and/or collinear to one of the initial-state partons, since in these regions $\mathcal{R}_{ij}$ vanish. Hence, $\mathcal{R}_i$ terms need real counterterms only for these regions. Conversely, the $\mathcal{R}_{ij}$ terms are divergent only in the regions in which parton i is soft and/or collinear to final-state parton j.[12]

After the $(n+1)$-body cross section is decomposed as in eq. (1.84), in the FKS method one chooses a different parameterization of the $(n+1)$-body phase space for each term, in such a way that the singular limits are easily identified:

- In the parameterization associated with $\mathcal{S}_i$, the key variables are the energy of parton i (directly related to soft singularities), and the angle between parton i and one of the initial-state partons (directly related to initial-state collinear singularities).

- In the parameterization associated with $\mathcal{S}_{ij}$, the important variables are the energy of parton i and the angle between parton i and j (related to a final-state collinear singularity).

Obviously, in both cases, a further azimuthal variable is needed.

In the FKS method, the $\oplus$ and $\ominus$ collinear regions are both singled out by the $\mathcal{S}_i$ functions. If one needs to treat the two collinear regions separately,[13] the FKS decomposition can then be refined easily, by replacing $\mathcal{S}_i$ with two functions $\mathcal{S}_i^{\oplus}$ and $\mathcal{S}_i^{\ominus}$

$$\mathcal{S}_i = \mathcal{S}_i^{\oplus} + \mathcal{S}_i^{\ominus}\,, \tag{1.86}$$

with the properties

$$\lim_{\vec{k}_m \parallel \vec{k}_{\oplus}} \mathcal{S}_i^{\oplus} = \delta_{im}\,, \qquad \lim_{\vec{k}_m \parallel \vec{k}_{\oplus}} \mathcal{S}_i^{\ominus} = 0\,, \tag{1.87}$$

that refine eq. (1.81). Eqs. (1.84) and (1.85) are modified accordingly.

[12] Have we chosen the option of keeping all the possible $\mathcal{S}$ functions different from zero, then the $\mathcal{R}_i$ and $\mathcal{R}_{ij}$ functions corresponding to non-singular regions would be non-zero, but finite.

[13] In particular, sometimes in `POWHEG` one needs to distinguish between the $\oplus$ and the $\ominus$ regions. Furthermore, in the single-top implementation described in chapter 4, we have distinguished the two regions.

$\mathcal{S}$ functions

In the original formulation of the FKS subtraction, each real contribution was integrated by partitioning the phase space into non-overlapping regions. This was obtained by choosing for $\mathcal{S}$ sets of θ functions. More recently (see ref. [18]), the method has been applied using instead smooth $\mathcal{S}$ functions. In the following, we outline how to build $\mathcal{S}$ functions systematically.

We first introduce the functions d_i and d_{ij}, where $i, j = 1, \ldots, n+1$, with the following properties

$$\begin{array}{lllllll} d_i = 0 & \text{if and only if} & E_i = 0 & \text{or} & \vec{k}_i \parallel \vec{k}_\oplus & \text{or} & \vec{k}_i \parallel \vec{k}_\ominus \,, \\ d_{ij} = 0 & \text{if and only if} & E_i = 0 & \text{or} & E_j = 0 & \text{or} & \vec{k}_i \parallel \vec{k}_j \,, \end{array} \tag{1.88}$$

where energies and spatial-momenta are computed in the center-of-mass frame of the incoming partons. We now introduce the quantity

$$\mathcal{D} = \sum_k \frac{1}{d_k} + \sum_{kl} \frac{1}{d_{kl}} \,, \tag{1.89}$$

and define

$$\mathcal{S}_i = \frac{1}{\mathcal{D}\, d_i} \,, \tag{1.90}$$

$$\mathcal{S}_{ij} = \frac{1}{\mathcal{D}\, d_{ij}}\, h\!\left(\frac{E_i}{E_i + E_j}\right) \,, \tag{1.91}$$

where h is a function such that

$$\lim_{z\to 0} h(z) = 1 \,, \qquad \lim_{z\to 1} h(z) = 0 \,, \qquad h(z) + h(1-z) = 1 \,. \tag{1.92}$$

Notice that the h factor is necessary only if one considers both functions $\mathcal{S}_{ij}$ and $\mathcal{S}_{ji}$ (which is strictly necessary only if both i and j are gluons). The functions defined in eqs. (1.90) and (1.91) satisfy by construction the property (1.79) and have the requested properties (1.80)-(1.83) in the singular limits, due to the vanishing requirements of d_i's and d_{ij}'s.

If the separation among the $\oplus$ and $\ominus$ collinear regions is needed, we simply need to introduce the two terms $d_i^{(\pm)}$, with the properties

$$d_i^{(\pm)} = 0 \quad \text{if and only if} \quad E_i = 0 \quad \text{or} \quad \vec{k}_i \parallel \vec{k}_{(\pm)} \,. \tag{1.93}$$

In this case, instead of using d_i's, the definition of $\mathcal{D}$ in eq. (1.89) becomes

$$\mathcal{D} = \sum_k \left(\frac{1}{d_k^{\oplus}} + \frac{1}{d_k^{\ominus}} \right) + \sum_{kl} \frac{1}{d_{kl}} \,, \tag{1.94}$$

and $\mathcal{S}_i^{\oplus}$ are obtained as follows:

$$\mathcal{S}_i^{\oplus} = \frac{1}{\mathcal{D}\, d_i^{\oplus}} \,. \tag{1.95}$$

In ref. [2] explicit choices for all the d terms are given. We will specify our choices in chapter 4, where the `POWHEG` implementation of single-top production will be described.

NLO differential cross section

The FKS final formula for the expectation value of O is:

$$\begin{aligned} \langle O \rangle &= \int d\mathbf{\Phi}_n \; O_n(\mathbf{\Phi}_n) \left[B(\mathbf{\Phi}_n) + V(\mathbf{\Phi}_n) \right] \\ &+ \int d\mathbf{\Phi}_{n+1} \, O_{n+1}(\mathbf{\Phi}_{n+1}) \; \hat{R}(\mathbf{\Phi}_{n+1}) \\ &+ \int d\mathbf{\Phi}_{n,\oplus} \; O_n\big(\bar{\mathbf{\Phi}}_n\big) \; G_{\oplus}(\mathbf{\Phi}_{n,\oplus}) + \int d\mathbf{\Phi}_{n,\ominus} \; O_n\big(\bar{\mathbf{\Phi}}_n\big) \; G_{\ominus}(\mathbf{\Phi}_{n,\ominus}) \;. \end{aligned} \tag{1.96}$$

In the following we give just the final expressions for the above terms. More details on their derivation can be found in [2]. For a complete description, we refer to the original papers [16, 17], although the notation used there is quite different from the present one.

The second term of the r.h.s. of eq. (1.96) is defined as $\hat{R} = \mathcal{L}\,\hat{\mathcal{R}}$. As explained in the following, with the notation $\hat{\mathcal{R}}$ we indicate the real contribution $\mathcal{R}$, together with all its counterterms. For a generic real process $\mathcal{R}$, it has the structure

$$\hat{\mathcal{R}} = \sum_i \hat{\mathcal{R}}_i + \sum_{ij} \hat{\mathcal{R}}_{ij} \,, \tag{1.97}$$

where[14]

$$\hat{\mathcal{R}}_i = \frac{1}{\xi_i} \left\{ \frac{1}{2} \left(\frac{1}{\xi_i} \right)_+ \left[\left(\frac{1}{1-y_i} \right)_+ + \left(\frac{1}{1+y_i} \right)_+ \right] \left[(1-y_i^2) \; \xi_i^2 \, \mathcal{R}_i \right] \right\} \tag{1.98}$$

[14] In the description of the FKS method reported here, we assume for the parameters ξ_c and $\delta_{I,O}$ the values 1 and 2.

for terms associated with ISC regions, and

$$\hat{\mathcal{R}}_{ij} = \frac{1}{\xi_i}\left\{\left(\frac{1}{\xi_i}\right)_+ \left(\frac{1}{1-y_{ij}}\right)_+ \left[(1-y_{ij})\;\xi_i^2\,\mathcal{R}_{ij}\right]\right\} \tag{1.99}$$

for terms having FSC singularities. If we need to separate the $\oplus$ and $\ominus$ collinear regions, as discussed at the end of sec. 1.2.3, we have

$$\hat{\mathcal{R}} = \sum_i \left(\hat{\mathcal{R}}_i^{\oplus} + \hat{\mathcal{R}}_i^{\ominus}\right) + \sum_{ij} \hat{\mathcal{R}}_{ij}\,, \tag{1.100}$$

$$\hat{\mathcal{R}}_i^{\circledast} = \frac{1}{\xi_i}\left\{\left(\frac{1}{\xi_i}\right)_+ \left(\frac{1}{1\mp y_i}\right)_+ \left[(1\mp y_i)\;\xi_i^2\,\mathcal{R}_i^{\circledast}\right]\right\}. \tag{1.101}$$

The variables ξ_i, y_i in eqs. (1.98) and (1.101) and ξ_i, y_{ij} in eq. (1.99) are variables suited to parameterize the radiation kinematics of the FKS parton i, in case of initial or final state singularities respectively. Their exact definition is

$$\xi_i = \frac{2k_i^0}{\sqrt{s}}\,, \qquad y_i = \cos\theta_i\,, \qquad y_{ij} = \cos\theta_{ij}\,, \tag{1.102}$$

where θ_i is the angle of parton i with the incoming parton $\oplus$, and θ_{ij} is the angle of parton i with parton j.[15] The singular limits are then approached when $\xi_i \to 0$ (soft region), $y_i \to \pm 1$ (ISC region) and $y_{ij} \to 1$ (FSC region).

For sake of completeness, we report the expression for the $(n+1)$-body phase space, that, in both the ISC and FSC regions, can be written as

$$\begin{aligned} d\Phi_{n+1} &= (2\pi)^d\,\delta^d\!\left(k_\oplus + k_\ominus - \sum_{i=1}^{n+1} k_i\right)\left[\prod_{l\neq i}\frac{d^{d-1}k_l}{(2\pi)^{d-1}\,2k_l^0}\right] \\ &\times \frac{s^{1-\epsilon}}{(4\pi)^{d-1}}\,\xi_i^{1-2\epsilon}\left(1-y^2\right)^{-\epsilon} d\xi_i\,dy\,d\Omega^{d-2}\,, \end{aligned} \tag{1.103}$$

where y, Ω stands for either y_i, Ω_i or y_{ij}, Ω_{ij}. The transverse angular variables $d\Omega_i^{d-2}$ are relative to the collision axis, while $d\Omega_{ij}^{d-2}$ are relative to the direction of parton j.

The fundamental observation is that now the terms $[(1-y_i^2)\;\xi_i^2\,\mathcal{R}_i]$ and $[(1-y_{ij})\;\xi_i^2\,\mathcal{R}_{ij}]$ are finite in the ISC and FSC regions labelled by their subscripts. Hence, the action of

[15] We remind that all variables are computed in the center-of-mass frame of the incoming partons.

the plus distributions in eqs. (1.98) and (1.99), defined as

$$\int_0^1 d\xi\, f(\xi) \left(\frac{1}{\xi}\right)_+ = \int_0^1 d\xi\, \frac{f(\xi) - f(0)}{\xi}\,, \tag{1.104}$$

$$\int_{-1}^1 dy\, f(y) \left(\frac{1}{1 \mp y}\right)_+ = \int_{-1}^1 dy\, \frac{f(y) - f(\pm 1)}{1 \mp y}\,, \tag{1.105}$$

is well behaved.

Moreover, we also notice that each of the terms outlined above is also finite in the whole phase space, since each $\mathcal{S}$ has to vanish exactly in correspondence of all the other singular regions.

The final expression in eq. (1.97) (or eq. (1.100)) involves only non-divergent terms, so it can be safely integrated over the full radiation phase space.[16] The important point is that each real contribution has to be integrated using the phase space parameterization suited for its singular structure, so that divergences are subtracted by plus distributions. In the FKS method, therefore, we can say that real counterterms are automatically generated by the action of the plus distributions contained in $\hat{\mathcal{R}}$.

To write the final expression for the soft-virtual term $V(\mathbf{\Phi}_n)$ in eq. (1.96), we need to fix the notation and the convention for the divergent term $\mathcal{V}_{\rm b}$. The virtual contribution $\mathcal{V}_{\rm b}$ of eq. (1.73) can be expressed as

$$\mathcal{V}_{\rm b} = \mathcal{N}\, \frac{\alpha_{\rm S}}{2\pi} \left[-\sum_{i \in \mathcal{I}} \left(\frac{1}{\epsilon^2}\, C_{f_i} + \frac{1}{\epsilon}\, \gamma_{f_i} \right) \mathcal{B} + \frac{1}{\epsilon} \sum_{\substack{i,j \in \mathcal{I} \\ i \neq j}} \log \frac{2k_i \cdot k_j}{Q^2}\, \mathcal{B}_{ij} + \mathcal{V}_{\rm fin} \right], \tag{1.106}$$

where

$$\mathcal{N} = \frac{(4\pi)^\epsilon}{\Gamma(1-\epsilon)} \left(\frac{\mu^2}{Q^2}\right)^\epsilon. \tag{1.107}$$

With $\mathcal{I}$ we label the $n+2$-parton involved in an n-body process:

$$\mathcal{I} = \{\oplus, \ominus, 1, \ldots, n\}\,. \tag{1.108}$$

[16] Before proceeding, we remark that the integration can be performed over the $d = 4$ version of the phase space in eq. (1.103), as suggested in the original FKS papers. This is however not necessary. Any parameterization of the phase space that allows a simple handling of the distributions is acceptable. This freedom has been exploited in [2], in order to simplify the formulation of the `POWHEG` method in the case of the $\mathcal{R}_{ij}$ contributions, where the choice of the azimuthal variable is different from that of eq. (1.103).

The quantities $\mathcal{B}_{ij}$ are the so-called *color-correlated Born amplitudes*, defined as

$$\mathcal{B}_{ij} = -\frac{1}{2s}\frac{1}{N_{\rm sym} D_\oplus D_\ominus S_\oplus S_\ominus}\sum_{\substack{\text{spins}\\ \text{colors}}} \mathcal{M}_{\{c_k\}}\left(\mathcal{M}^\dagger_{\{c_k\}}\right)_{\substack{c_i\to c'_i\\ c_j\to c'_j}} T^a_{c_i,c'_i} T^a_{c_j,c'_j}\,. \tag{1.109}$$

Here $\mathcal{M}_{\{c_k\}}$ is the Born amplitude, with the color indexes of all the involved particles $\mathcal{I}$ left exposed, and collectively indicated as $\{c_k\}$. The suffix on the parentheses that enclose $\mathcal{M}^\dagger_{\{c_k\}}$ indicates that the color indices of partons $i,j\in\mathcal{I}$ are substituted with primed indices in $\mathcal{M}^\dagger_{\{c_k\}}$. Furthermore, $N_{\rm sym}$ is the symmetry factor for identical particles in the final state, $D_{\circledast}$ are the dimension of the color representations of the incoming partons (3 for quarks and 8 for gluons), and $S_{\circledast}$ are the number of spin states. The factor $1/(2s)$ is the flux factor. We assume summation over repeated color indexes (c_k for $k\in\mathcal{I}$, c'_i, c'_j and a) and spin indices. For gluons $T^a_{cb} = if_{cab}$, where f_{abc} are the structure constants of the $SU(3)$ algebra. For incoming quarks $T^a_{\alpha\beta} = t^a_{\alpha\beta}$, where t are the color matrices in the fundamental representation, normalized as in eq. (1.8). For antiquarks $T^a_{\alpha\beta} = -t^a_{\beta\alpha}$. It is easy to see that, from color conservation, $\mathcal{B}_{ij}$ satisfies

$$\sum_{i\in\mathcal{I},i\neq j}\mathcal{B}_{ij} = C_{f_j}\mathcal{B}\,. \tag{1.110}$$

The symbol f_i denotes the flavour of parton i, i.e. g for a gluon, q for a quark and $\bar{q}$ for an antiquark. We define

$$C_g = C_{\rm A}\,, \qquad C_q = C_{\bar{q}} = C_{\rm F}\,, \tag{1.111}$$

$$\gamma_g = \frac{11C_{\rm A} - 4T_{\rm F}\,n_{\rm f}}{6}\,, \qquad \gamma_q = \gamma_{\bar{q}} = \frac{3}{2}C_{\rm F}\,, \tag{1.112}$$

$$\gamma'_g = \left(\frac{67}{9} - \frac{2\pi^2}{3}\right)C_{\rm A} - \frac{23}{9}T_{\rm F}\,n_{\rm f}\,, \qquad \gamma'_q = \gamma'_{\bar{q}} = \left(\frac{13}{2} - \frac{2\pi^2}{3}\right)C_{\rm F}\,. \tag{1.113}$$

In case i is a colorless particle all the above quantities are zero.

Notice that, in the second sum on the r.h.s. of eq. (1.106), we sum over $i\neq j$, and thus, since $\mathcal{B}_{ij}$ is symmetric, each term appears twice in the sum. The definition of the finite part $\mathcal{V}_{\rm fin}$ depends upon the definition of the normalization factor $\mathcal{N}$, for which we have adopted the common choice of eq. (1.107), and from the regularization scheme, that we assume to be the standard conventional dimensional regularization (CDR).[17] Finally, in eq. (1.106), μ^2 is the renormalization scale, and Q^2 is an (arbitrary) physical scale

[17] When the dimensional reduction (DR) scheme is used, we have $\mathcal{V}_{\rm fin} = \mathcal{V}^{\rm DR}_{\rm fin} - \alpha_{\rm S}/(2\pi)\,\mathcal{B}\sum_{i\in\mathcal{I}}\tilde{\gamma}(f_i)$, where $\tilde{\gamma}(g) = N_{\rm c}/6$ and $\tilde{\gamma}(q) = (N_{\rm c}^2-1)/(4N_{\rm c})$.

that is factored out from the virtual amplitude, in order to make the normalization $\mathcal{N}$ dimensionless (thus $\mathcal{V}_{\text{fin}}$ depends upon μ^2 and Q^2).

The soft-virtual term in eq. (1.96), according to the FKS method, is given by

$$V = \mathcal{L}\,\mathcal{V}\,, \qquad \mathcal{V} = \frac{\alpha_{\text{S}}}{2\pi}\left(\mathcal{Q}\,\mathcal{B} + \sum_{\substack{i,j\in\mathcal{I}\\ i\neq j}} \mathcal{I}_{ij}\,\mathcal{B}_{ij} + \mathcal{V}_{\text{fin}}\right). \tag{1.114}$$

The quantities $\mathcal{Q}$ and $\mathcal{I}_{ij}$ depend on the flavours and momenta of the incoming and outgoing partons. If the couple ij refers to massless colored particles, then they are defined as follows:

$$\begin{aligned}\mathcal{Q} &= \sum_{i=1}^{n}\left[\gamma'_{f_i} - \log\frac{s}{Q^2}\left(\gamma_{f_i} - 2C_{f_i}\log\frac{2E_i}{\sqrt{s}}\right) + 2C_{f_i}\left(\log^2\frac{2E_i}{\sqrt{s}}\right) - 2\gamma_{f_i}\log\frac{2E_i}{\sqrt{s}}\right]\\ &\quad - \log\frac{\mu_{\text{F}}^2}{Q^2}\left[\gamma_{f_\oplus} + \gamma_{f_\ominus}\right], \qquad (1.115)\\ \mathcal{I}_{ij} &= \frac{1}{2}\log^2\frac{s}{Q^2} + \log\frac{s}{Q^2}\log\frac{k_j\cdot k_i}{2E_jE_i} - \text{Li}_2\left(\frac{k_j\cdot k_i}{2E_jE_i}\right)\\ &\quad + \frac{1}{2}\log^2\frac{k_j\cdot k_i}{2E_jE_i} - \log\left(1-\frac{k_j\cdot k_i}{2E_jE_i}\right)\log\frac{k_j\cdot k_i}{2E_jE_i}\,, \qquad (1.116)\end{aligned}$$

where $s = (k_\oplus + k_\ominus)^2$ and E_i is the energy of parton i in the partonic center-of-mass frame.

We finally report the expressions for the initial-state collinear remnants that appear in eq. (1.96). For each real process that has ISC singularities, we have a term $G_\oplus = \tilde{\mathcal{L}}\,\mathcal{G}_\oplus$ (and a corresponding term $G_\ominus = \tilde{\mathcal{L}}\,\mathcal{G}_\ominus$ for the $\ominus$ collinear region), where

$$\begin{aligned}\mathcal{G}_\oplus^{f_\oplus f_\ominus}(z) &= \frac{\alpha_{\text{S}}}{2\pi}\sum_{f'_\oplus}\left\{(1-z)\,P^{f_\oplus f'_\oplus}(z,0)\left[\left(\frac{1}{1-z}\right)_+\log\frac{s}{\mu_{\text{F}}^2} + 2\left(\frac{\log(1-z)}{1-z}\right)_+\right]\right.\\ &\quad \left. - \left[\frac{\partial P^{f_\oplus f'_\oplus}(z,\epsilon)}{\partial\epsilon}\right]_{\epsilon=0} - K^{f_\oplus f'_\oplus}(z)\right\}\mathcal{B}^{f'_\oplus f_\ominus}(z)\,,\end{aligned} \tag{1.117}$$

for a process in which an incoming parton $\oplus$ of flavour $f_\oplus$ splits into a parton $f'_\oplus$ (with fraction z of the incoming momentum) that enters the Born process $\mathcal{B}$. The superscripts on $\mathcal{B}$ denote the flavours of the incoming parton, and the z dependence is to remind that the incoming $\oplus$ momentum is rescaled. The distributions are defined as in eq. (1.104), with $\xi = 1 - z$. The functions $P(z,\epsilon)$ are the leading-order Altarelli-Parisi splitting

functions in $d = 4 - 2\epsilon$ dimensions, given by

$$P^{qq}(z,\epsilon) = C_{\rm F}\left[\frac{1+z^2}{1-z} - \epsilon(1-z)\right] , \tag{1.118}$$

$$P^{qg}(z,\epsilon) = C_{\rm F}\left[\frac{1+(1-z)^2}{z} - \epsilon z\right] , \tag{1.119}$$

$$P^{gq}(z,\epsilon) = T_{\rm F}\left[1 - \frac{2z(1-z)}{1-\epsilon}\right] , \tag{1.120}$$

$$P^{gg}(z,\epsilon) = 2\,C_{\rm A}\left[\frac{z}{1-z} + \frac{1-z}{z} + z(1-z)\right] . \tag{1.121}$$

The distributions $K^{ff'}$ control the change of scheme in the evolution of parton distribution functions. They are defined in ref. [16], and equivalently, with the notation $K^{ff'}_{\rm F.S.}$ in ref. [11]. They are identically zero in $\overline{\rm MS}$.

1.2.4 Catani and Seymour subtraction

In the subtraction method proposed by Catani and Seymour, the subtraction of real divergences is performed by adding to each real squared amplitude a set of counterterms, called *dipoles*. At variance with the FKS approach, in the Catani-Seymour (CS) formalism there is no need to separate a real contribution $\mathcal{R}$ into terms that have at most one collinear and one soft singularity. This is due to the fact that the set of dipoles, integrated together with the real term, contains all the counterterms needed to handle, numerically, with all the possible singular regions. In the following, we give a description of the method, focusing only on the aspects relevant for its application in the context of single vector-boson hadroproduction, which will be described in chapter 3. For a fully general description of the method, we refer to [11].

Dipoles and singular regions

A dipole is a function of the $(n+1)$-body phase space $\mathbf{\Phi}_{n+1}$, labelled by the indexes of three partons: the emitted, the emitter and the spectator parton (the last two forming the dipole). In the dipole formulation, each singular region (S, ISC or FSC) can be basically identified by the couple emitter-emitted. Hence, a singular region receives, in general, contributions by several dipoles, differing among each other by the spectator parton. The real counterterms $\mathcal{C}^{(\alpha)}$ introduced in sec. 1.2.2 are then more naturally associated with dipoles, rather than singular regions. Unfortunately, this feature makes the CS subtraction method less natural than the FKS one for `POWHEG` applications, for reasons that we will

briefly explain in sec. 2.3.5.

The maps $\mathbf{M}^{(\alpha)}$ of eq. (1.57) in the dipole formulation are constructed in such a way that, in most cases, they affect only the momenta of the dipole partons, and all other momenta remain unchanged, the only exception being when the emitter and the spectator are the two incoming partons.

For the purpose of this thesis, we need just to use dipoles associated to initial state singularities, with an initial state spectator. The relevant expressions for these dipoles and the corresponding phase space parameterizations are given in chapter 3, while a complete treatment of all the other possibilities can be found in [2]. Here we just mention that, in the CS approach, initial state singularities associated with emissions from the $\oplus$ and the $\ominus$ leg have to be treated separately, since two distinct phase space parameterizations are needed, the mappings being different. Other subtleties related to the use of the CS subtraction in the POWHEG framework will be described in the following (see chapter 2 and 3).

NLO differential cross section

The CS final formula for the expectation value of O is then formally identical to the one given in eq. (1.78), where $\mathcal{C}^{(\alpha)}$ are the relevant dipoles for the real subprocess at hand, and the index α runs over all the relevant dipoles, instead that over the singular regions. A concrete example of this will be given when describing the POWHEG implementation of the single vector-boson hadroproduction (see eq. (3.34)).

In the following, we give the relevant formulae for the soft-virtual term $\mathcal{V}$, and the collinear remnants $\mathcal{G}_{\oplus}$.

For the soft-virtual contribution, the relevant formulae can be found in eqs. (C.27) and (C.28) of the original paper [11]. When translated in the notation used throughout this thesis, for $\mathcal{V}$ we obtain the following expression:

$$\mathcal{V} = \frac{\alpha_{\mathrm{S}}}{2\pi}\left\{\mathcal{V}_{\mathrm{fin}} - \sum_{\substack{i,j\in\mathcal{I}\\ i\neq j}}\left[\frac{1}{2}\log^2\frac{Q^2}{2k_i\cdot k_j} + \frac{\gamma_{f_i}}{C_{f_i}}\log\frac{Q^2}{2k_i\cdot k_j}\right]\mathcal{B}_{ij} + \sum_{i\in\mathcal{I}}\left[-\frac{\pi^2}{3}C_{f_i} + \gamma_{f_i} + K_{f_i}\right]\mathcal{B}\right\}, \tag{1.122}$$

where the conventions for the virtual term $\mathcal{V}_{\mathrm{fin}}$ are the same of those described in the FKS case (see eq. (1.106)).

The collinear remnant for the $\oplus$ region, for incoming partons of flavours $f_\oplus$, $f_\ominus$, is given

by (see eq. (10.30) of ref. [11])

$$\begin{aligned}
\mathcal{G}_{\oplus}^{f_\oplus f_\ominus}(z) &= \frac{\alpha_{\rm S}}{2\pi}\sum_{f'_\oplus}\Bigg\{\left[\overline{K}^{f_\oplus f'_\oplus}(z) - K_{\rm F.S.}^{f_\oplus f'_\oplus}(z)\right]\mathcal{B}^{f'_\oplus f_\ominus}(z) \\
&- \delta^{f_\oplus f'_\oplus}\sum_{i=1}^{n}\frac{\gamma_{f_i}}{C_{f_i}}\left[\left(\frac{1}{1-z}\right)_+ + \delta(1-z)\right]\mathcal{B}_{i\oplus}^{f'_\oplus f_\ominus}(z) + \frac{1}{C_{f'_\oplus}}\tilde{K}^{f_\oplus f'_\oplus}(z)\,\mathcal{B}_{\ominus\oplus}^{f'_\oplus f_\ominus}(z) \\
&- P^{f_\oplus f'_\oplus}(z)\frac{1}{C_{f'_\oplus}}\sum_{\substack{i\in\mathcal{I}\\ i\neq\oplus}}\mathcal{B}_{i\oplus}^{f'_\oplus f_\ominus}(z)\log\frac{\mu_{\rm F}^2}{2\,z\,k_\oplus\cdot k_i}\Bigg\}\,,
\end{aligned} \tag{1.123}$$

where the superscripts in $\mathcal{B}$ (and $\mathcal{B}_{ij}$) single out a given flavour combination for the incoming partons in the Born amplitude and in its color-correlated components.

An analogous expression holds for $\mathcal{G}_\ominus$. The definition of the functions $\overline{K}$, $\tilde{K}$ and $K_{\rm F.S.}$ is given in appendix C of ref. [11], whereas $P^{f_\oplus f'_\oplus}(z)$ is the usual, four-dimensional Altarelli-Parisi splitting kernel.

1.3 Parton Showers and Monte Carlo event generators

In the previous section, we described the formalism used to perform fixed-order calculations. In particular, we have seen how the full inclusion of NLO corrections can be achieved, both for the total cross section and for more exclusive observables.

This section is instead devoted to the description of Monte Carlo event generators based on Parton Showers (PS). Often, we will refer to them also as Shower Monte Carlo programs (SMC). A discussion about the differences among the two approaches in describing high-energy processes at hadron colliders is postponed to the next chapter. The content of this section is based mainly on [3].

1.3.1 Generalities

Shower Monte Carlo programs are computer programs aimed to give a realistic description of hadronic collisions.[18] They work by describing, sequentially, the stages between the collision of the incoming hadrons and the hadronization of outgoing partons. The underlying idea is that each stage is assumed to be weakly dependent from the others, since each stage takes place at its own energy scale, which differs from the others' ones.[19]

We can summarize the various steps as follows, starting from the one that involves higher energy scales:

1. *Hard scattering generation*
   A Standard Model (or Beyond Standard Model) process is simulated by generating the momenta of the incoming and outgoing particles, according to low-multiplicity, tree-level, matrix elements.

2. *Parton Shower algorithm*
   After the generation of a partonic event, the dominant perturbative QCD effects are simulated by means of a Markovian algorithm, called shower algorithm. In this stage, multiple radiation off colored particles is generated, giving an accurate description of the radiation pattern in the logarithmic-enhanced regions.

[18] In this thesis, our perspective will be focused on collider Physics, although SMC programs are largely used also in the context of e^+e^- annhilation.

[19] The exact definition of this separation is to some extent arbitrary, since it does not come from first principles. Nevertheless, experience shows that the idea of describing processes with different typical scales separately is adequate also in this case.

3. *Hadronization model*
   The many-partons final state (generated according to the steps 1 and 2) is converted into a set of outgoing hadrons, according to a phenomenological model, tuned on real data.

4. *Underlying event generation - Unstable hadrons decay*
   An underlying event is superimposed onto the generated event, according to some reasonable principle. If at the end unstable hadron have been generated, then they are decayed, taking into account their branching ratios.

In the following, we focus mainly on the shower stage: we give a theoretical formulation of it, and we explain how the algorithm is pratically implemented. For this purpose, we begin by describing multiple emissions in the leading-logarithmic collinear approximation. This allows to find a recipe to associate a weight for each given final state, generated by dressing an elementary hard scattering process with further emissions.

1.3.2 Leading-Logarithm calculation of multiparticle production

Ideally, in order to describe exclusive, high-multiplicity final states, one has to sum the perturbative expansion to all orders in $\alpha_{\rm S}$. In practice, this is possible if we limit ourselves to the most singular terms of the perturbative expansion, that are related to the logarithmic enhancement due to collinear and soft singularities. The shower algorithm is basically a method for the computation of this potentially infinite set of logarithmic enhanced Feynman graphs

Multiple emissions

In section 1.1.3 we showed how QCD amplitudes factorize in the collinear limit. By multiplying both sides of eq. (1.31) for the same flux factor (and for symmetry factors, in case of indistinguishable final state particles), it is straightforward to derive the corresponding relation for the $(n+1)$-body partonic cross section:

$$d\sigma_{n+1} = d\sigma_n \frac{\alpha_S}{2\pi} \frac{dt}{t} P_{i\to jk}(z)\, dz \frac{d\phi}{2\pi}\,, \tag{1.124}$$

where $d\sigma_n$ denotes the partonic differential cross section for a n-body final state. We have also introduced the exclusive, unregularized Altarelli-Parisi splitting kernels $P_{i\to jk}$. They are defined, in terms of the standard Altarelli-Parisi splitting functions given in eq. (1.36),

as

$$\begin{aligned} P_{q,qg}(z) &= P_{qq}(z) = P_{qg}(1-z)\,, \\ P_{g,q\bar{q}}(z) &= P_{gq}(z)\,, \\ P_{g,gg}(z) &= \frac{1}{2}P_{gg}(z)\,. \end{aligned} \tag{1.125}$$

The factorization of eq. (1.124) holds as long as the angle (or, more generally, the t variable) between the collinear partons is the smallest in the whole amplitude. Thus, it follows that the factorization formula (1.124) can be applied recursively, if a strong ordering between the hardness variables holds. This is shown pictorially, for two $q \to qg$ splittings, in figure 1.2, where we assume that the two angles become small, maintaining the ordering relation, $\theta' \gg \theta \to 0$.

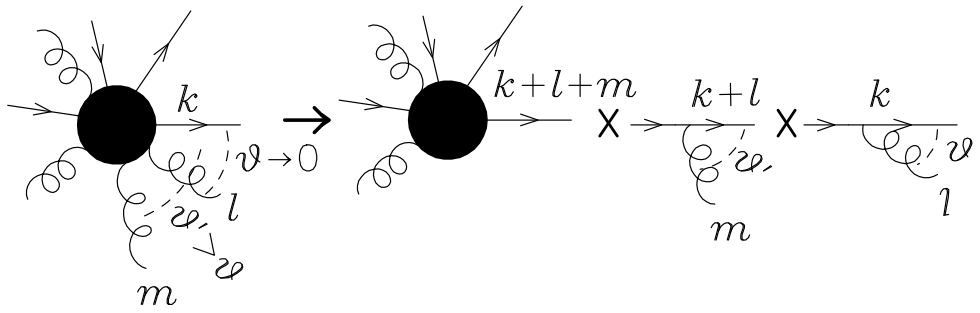

Figure 1.2: Strongly ordered multiple emissions.

For two collinear splittings, the $n+1$ cross section can then be written as

$$d\sigma_{n+1} \to d\sigma_{n-1} \left(\frac{\alpha_s}{2\pi}\frac{dt'}{t'}P_{i'\to j'k'}(z')dz'\frac{d\phi'}{2\pi}\right)\left(\frac{\alpha_s}{2\pi}\frac{dt}{t}P_{i\to jk}(z)dz\frac{d\phi}{2\pi}\right)\Theta(t'-t)\,, \tag{1.126}$$

where we have assumed two generic splittings $i \to jk$ and $i' \to j'k'$. At this point, it is easy to show that contributions coming from high-multiplicity QCD amplitudes, when integrated over the strong ordered region, are of the same order of magnitude of the (underlying) hard process they originated from (the blob in fig. 1.2), even if formally they are subleading by powers of the coupling constant $\alpha_{\rm s}$. In fact, by extending eq. (1.126) to n emissions and integrating the corresponding expression over a strong ordered region, we find that the cross section for emitting n extra partons goes as

$$\sigma_n \approx \sigma_0 \alpha_S^n \int \frac{dt_1}{t_1}\frac{dt_2}{t_2}\ldots\frac{dt_n}{t_n} \times \theta(Q^2 > t_1 > t_2 > \ldots > t_n > t_0) = \sigma_0 \frac{1}{n!}\alpha_S^n \log^n \frac{Q^2}{t_0}\,, \tag{1.127}$$

where σ_0 denotes the cross section for the hard scattering, Q is an upper limit for the virtualities in the splitting processes and t_0 is an infrared cutoff. In hadronic collisions, Q is of the same order of the typical energy scale of the hard process, while the natural choice for $\sqrt{t_0}$ is to use a scale of the order of the hadronization scale, which means of the same order of Λ_{QCD} (see sec. 1.1.2). The θ function here is defined to be equal to 1 if its argument is true, zero otherwise.

Before commenting on the above result, it is worthwile to recall the approximations that we made in deriving eq. (1.127):

- We have used as upper bound for the integration over t the scale Q. At this energy scale, however, the collinear approximation is no longer reliable.
- We have just kept track of logarithms coming from collinear splittings, neglecting all the other factors of order one, as long as spin correlations between different splittings.
- We have not discussed possible effects coming from the use of a running coupling constant evaluated at different energy scales for each splitting.
- We have also neglected the presence of soft divergences, which are however present in the splitting kernels. For the purpose of this section, we can assume that they are regularized by a tiny parameter δ, i.e. by the substitutions:

$$\frac{1}{1-z} \to \frac{1}{1-z+\delta}, \quad \frac{1}{z} \to \frac{1}{z+\delta}\,. \tag{1.128}$$

We will deal with all the above issues in the following. However, neither of them affects the leading-logarithm accuracy of the result. Hence, the above argument shows that $\sigma_n \approx \sigma_0$, since at the end of the calculation the natural choice for the renormalization scale is Q, and therefore $\alpha_{\rm s}(Q^2)\log(Q^2/t_0) \simeq 1$. This means that all the contributions corresponding to strong ordered emissions have to be treated on the same ground, irrespectively of the number of emissions: the Parton Shower algorithms are the pratical way to achieve this purpose.

We notice that this collinear approximation is sometimes called *Leading-Log* (LL) collinear approximation, since it yields contributions which go as $(\alpha_{\rm s}\log(Q^2/t_0))^n$, as we derived in eq. (1.127).

We also notice that, from eq. (1.124), it is straightforward to interpret the quantity

$$\frac{\alpha_{\rm s}(t)}{2\pi}\,\frac{dt}{t}\,P_{i\to jk}(z)\,dz\,\frac{d\phi}{2\pi} \tag{1.129}$$

as the differential probability for the splitting $i \to j, k$ to take place, with the emission of a particle of type j into the phase space volume $dt\, dz\, d\phi$. The use of a strong coupling evaluated at the scale t is reasonable, since this is the typical scale of the splitting process itself. More details on this point will be given in the following.

Counting logs

The leading-logarithmic approximation requires some more explanation, that can be easily understood by looking at the simplified factorization formula

$$d\sigma_1 \approx d\sigma_0 \frac{dt}{t}, \tag{1.130}$$

that holds when $t \ll Q^2$, Q being the typical scale of σ_0. We have

$$\int d\sigma_1 = \sigma_0 \int \frac{dt}{t} \theta(Q^2 > t > t_0) + \mathcal{O}(1) = \sigma_0 \log \frac{Q^2}{t_0} + \mathcal{O}(1)\,, \tag{1.131}$$

which follows from the fact that in the difference

$$\int d\sigma_1 - \sigma_0 \int \frac{dt}{t} \tag{1.132}$$

the singularity for small t cancels, and the difference must be of order 1. Therefore, even if we have said that the factorization formula holds for $t \ll Q^2$, we can integrate it for t up to Q^2, if we are interested in the leading-logarithm result. This is the reason why the first two approximations we listed above do not affect the validity of eq. (1.127). Furthermore, concerning the third approximation, it is easy to see that different choices for the argument of α_s would produce terms that are subleading with respect to the LL accuracy. In fact, one can always use eq. (1.24) to perform the expansion

$$\alpha_\mathrm{s}(Q'^2) = \alpha_\mathrm{s}(Q^2) \left(1 - b_0 \alpha_\mathrm{s}(Q^2) \log \frac{Q'^2}{Q^2} + \mathcal{O}(\alpha_\mathrm{s}^2)\right). \tag{1.133}$$

Hence, using different scales would produce terms $\sim \alpha_\mathrm{s}^2 \log$, which are subleading with respect to the collinear LL ones, that go as $\sim \alpha_\mathrm{s} \log$.

Splitting kinematics

From eq. (1.124), we see that the definition of t and z is to some extent arbitrary. In fact dt/t is invariant if we change t by some (possibly z dependent) scale factor, and for z the

only requirement is that eq. (1.34) is satisfied in the collinear limit. For the z variable we can define, for example,

$$z = \frac{k^0}{k^0 + l^0}\,, \tag{1.134}$$

or, more generally,

$$z = \frac{k \cdot \hat{n}}{k \cdot \hat{n} + l \cdot \hat{n}}\,, \tag{1.135}$$

that reduces to the definition (1.134) for $\hat{n} = (1, \vec{0})$, and is perfectly acceptable as long as $\hat{n}$ does not coincide with the collinear direction. Instead, for t the following three choices are all valid:

$$\text{virtuality}: \quad t = \quad (k+l)^2 \approx E^2\theta^2 z(1-z), \tag{1.136}$$

$$\text{transverse momentum}: \quad t = \quad k_\perp^2 = l_\perp^2 \approx E^2\theta^2 z^2(1-z)^2, \tag{1.137}$$

$$\text{angular variable}: \quad t = \quad E^2\theta^2\,, \tag{1.138}$$

where $E \approx (k+l)^0$, θ is the angle between $\vec{k}$ and $\vec{l}$ and the $\approx$ relations hold for small θ. The corresponding kinematics is illustrated in fig. 1.3.

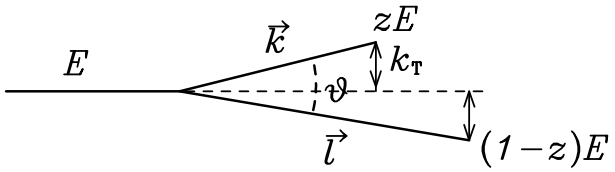

Figure 1.3: Kinematic variables for a splitting process.

Alternative choices in the definition of t and z make a difference in subleading terms in eq. (1.124), because these terms are non-singular when $t \to 0$. Therefore, the leading-log structure of collinear emissions is independent from this choice. However, when soft divergences are fully considered, i.e. when the cutoff δ in eq. (1.128) approaches zero, then the choice of t and z affects the double-log structure of multiple emissions. We discuss this issue in sec. 1.3.7.

The shower recipe

In what we discussed so far, we have not mentioned virtual contributions. However, in sec. 1.2, we showed that, in fixed order calculations, they are responsible for the cancellation of divergences coming from real contributions. Hence, order by order, they yield terms comparable with the corresponding radiative counterpart. For consistency, we need

to include also them in the description of multiparticle radiation, at least with the same accuracy of the real contributions.

In the following, we give the recipe for the calculation of multiparticle cross section, with the inclusion of virtual corrections, at the leading-log level. This brings to the definition of the Parton Shower algorithm.

We begin by specifying how to construct all possible event structures, for a given hard process (the Born process):

i. We choose a Born kinematics.

ii. For each colored parton produced in the hard interaction, we build all possible tree-level graphs that can arise from it. These are obtained by letting each quark to split into a qg pair and each gluon to split into a gg or $q\bar{q}$ pair.

iii. We associate to each splitting vertex in the graph the corresponding t, z, and ϕ values.

iv. We impose that the t variables are ordered: the t for splittings near the hard process must be less than the hard process scale Q^2, and all subsequent t's are in decreasing order as we go toward the branches of the tree-graph.

v. Given the initial hard parton momenta, and the t, z and ϕ variables at each splitting vertex, all the momenta in the tree graph are reconstructed.

We now specify the weight to be assigned to the given configuration:

a) The hard process has weight equal to its differential (Born level) cross section.

b) Each vertex has the weight

$$\theta(t - t_0) \quad \frac{\alpha_S(t)}{2\pi} \frac{dt}{t} P_{i,jk}(z)\, dz \frac{d\phi}{2\pi}\,, \tag{1.139}$$

where the one-loop evolution (1.25) for the strong coupling is assumed.[20] In order not to reach unphysical values of the running coupling constant, we inserted a θ function in eq. (1.139), where the infrared cutoff t_0 is assumed to be larger than Λ^2_{QCD}. We already mentioned the physical meaning of this cutoff: it is associated with the hadronization scale, i.e. the scale at which the perturbative approach fails, and some hadronization model is needed. The upper bound is determined by the t ordering of point (iv).

[20] More details on this point will be given later.

c) Each line in the graph has weight $\Delta_i(t', t'')$, where t' is the t value associated with the upstream vertex, t'' with the downstream vertex, and

$$\Delta_i(t', t'') = \exp\left[-\sum_{(jl)} \int_{t''}^{t'} \frac{dt}{t} \int_0^1 dz \;\; \frac{\alpha_S(t)}{2\pi} \;\; P_{i,jl}(z) \right] . \tag{1.140}$$

In case the line is a final one, t'' is replaced by the infrared cutoff t_0. The weights $\Delta_i(t', t'')$ are called *Sudakov form factors*. They represent all the dominant (leading-log) virtual corrections to the tree graph.

Before going on, we find useful to make here a couple of comments:

- At the end of this procedure, some hadronization model will be invoked, in order to convert the showered final state partons into hadrons. For the purpose of this section, we can neglect the hadronization stage, which we will discuss briefly in sec. 1.3.9. Therefore, here we consider initial and final states as made of partons.

- The final momentum assignemnt of step (v) is ambiguous, since a parton line acquires a positive virtuality larger than its mass, if it is followed by a splitting. Hence, to enforce energy and momentum conservation at each splitting, the momenta of the splitting parton has to be slightly changed. The common procedure implemented in SMC programs to take these effects into account is commonly known as *momentum reshuffling*, and it does not affect the leading-logarithmic structure of the result.

We stated that Sudakov form factors are needed to include virtual corrections in the shower algorithm. This is better understood when one interprets them in a probabilistic way: as we will see later, $\Delta_i(t', t'')$ corresponds to the probability that no emissions off the particle i takes place, between the two scales t' and t'' (see eq. (1.153)). Here, we limit ourselves to notice that kinematic configurations containing lines with very large differences between upstream and downstream hardness variables are suppressed. In fact, using eq. (1.25), we can estimate

$$\Delta_i(t', t'') \approx \exp\left[-C \int_{t''}^{t'} \frac{dt}{t} \;\; \frac{1}{\log \frac{t}{\Lambda^2_{QCD}}} \right] = \left(\frac{\log \frac{t''}{\Lambda^2_{QCD}}}{\log \frac{t'}{\Lambda^2_{QCD}}} \right)^C , \tag{1.141}$$

which becomes very small if $t' \gg t''$. Hence, Sudakov form factors suppress configurations that have no radiation down to very small scales. The typical behaviour of $\Delta(t', t'')$ as a function of t'' is reported in fig. 1.4.

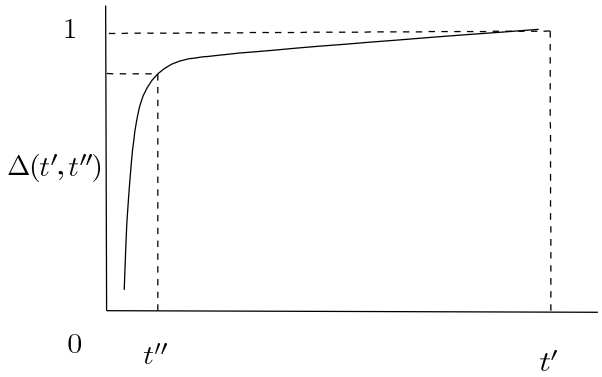

Figure 1.4: Typical behaviour of the Sudakov form factor $\Delta(t', t'')$. Here the independent variable is t'', while t' is to be considered fixed.

1.3.3 Formal representation of a shower

In this section we give a theoretical formulation of the Parton Shower algorithm and derive some of the fundamental properties that Parton Showers have.

For ease of notation, we introduce the symbol

$$\mathcal{S}_i(t, E) = \quad , \tag{1.142}$$

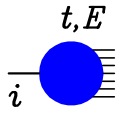

to represent the ensemble of all possible showers originating from parton i at a scale t. We can think of $\mathcal{S}_i(t, E)$ as a function defined on the set $\mathcal{F}$ of all final states (by final state we mean here a set of partons with specific momentum assignments), yielding the weight of the shower for that particular final state. The notation $\mathcal{S}_i^{\text{inc}}(t, E)$ is a shortcut to indicate the total weight of the shower attached to parton i, that means

$$\mathcal{S}_i^{\text{inc}}(t, E) = \sum_{\mathcal{F}} \mathcal{S}_i(t, E), \tag{1.143}$$

wher we mean sum over all possible final states $\mathcal{F}$ that can be originated from the parton i. Of course, $\mathcal{F}$ is not a discrete set, so, rather than a sum we should have a sum over the number and type of final state particles and an integral over their momenta. Alternatively we may imagine to divide the phase space into small cells, so that $\mathcal{F}$ can be thought as a discrete set, and the sum notation is appropriate.

Shower equation

The rules given in items (i-v) imply a recursive equation, that is illustrated in the following graphical equation

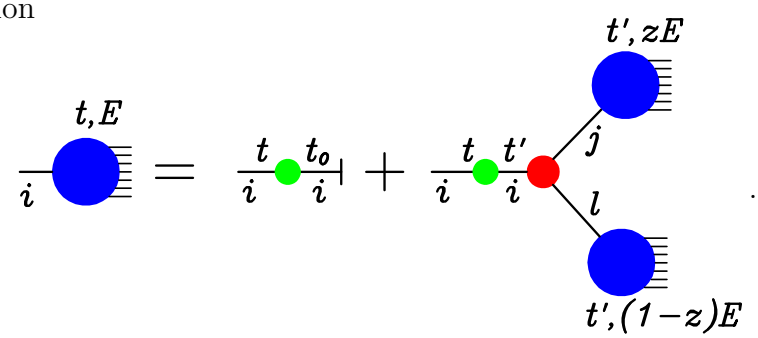

(1.144)

The meaning is quite intuitive: the set of all possible shower histories is obtained by adding the case in which no branching takes place to the case where one branching occurs, followed recursively by two showers starting at smaller energies and scales. Sudakov form factors are represented by the small blobs along the lines, while the blob connecting the i, j, l partons is the splitting probability. Notice that the phase spaces of the two independent showers, after the splitting, do not overlap in our collinear approximation, because of the strong ordering among subsequent t variables.

The mathematical translation of eq. (1.144) is given by the equation

$$\mathcal{S}_i(t,E) = \Delta_i(t,t_0)\mathcal{S}_i(t_0,E) +$$

$$\sum_{(jl)} \int_{t_0}^{t} \frac{dt'}{t'} \int_0^1 dz \int_0^{2\pi} \frac{d\phi}{2\pi} \frac{\alpha_S(t')}{2\pi} P_{i,jl}(z) \;\Delta_i(t,t')\mathcal{S}_j(t',zE)\mathcal{S}_l(t',(1-z)E)\,, \tag{1.145}$$

where the two terms correspond to the terms in the figure: no branching, plus one branching followed by two showers. Hence, $\mathcal{S}_i(t_0,E)$ represents a final state made by the incoming particle i alone, since no branching is possible below t_0.

By deriving eq. (1.145), we can easily see that $\mathcal{S}$ satisfies the differential equation

$$\begin{aligned} t\frac{\partial \mathcal{S}_i(t,E)}{\partial t} &= \sum_{(jl)} \int_0^1 dz \int_0^{2\pi} \frac{d\phi}{2\pi} \frac{\alpha_S(t)}{2\pi} P_{i,jl}(z)\; \mathcal{S}_j(t,zE)\mathcal{S}_l(t,(1-z)E) \\ &+ \left[-\sum_{(jl)} \int_0^1 dz \;\frac{\alpha_S(t)}{2\pi} P_{i,jl}(z) \right] \mathcal{S}_i(t,E)\,. \end{aligned} \tag{1.146}$$

Eq. (1.146) has the following meaning: if we raise the scale of the process by an infinitesimal amount, the shower has a larger probability to split into two subshowers (the first

term on the right hand side), and a smaller probability to remain the same (the second term). By summing eq. (1.146) over all possible final state, we see that $\mathcal{S}_i^{\rm inc}(t,E)$ obeys the equation

$$\begin{aligned} t\frac{\partial S_i^{\rm inc}(t,E)}{\partial t} &= \sum_{(jl)}\int_0^1 dz \;\; \frac{\alpha_S(t)}{2\pi}\, P_{i,jl}(z) S_j^{\rm inc}(t,zE) S_l^{\rm inc}(t,(1-z)E) \\ &+ \left[-\sum_{(jl)}\int_0^1 dz \;\; \frac{\alpha_S(t)}{2\pi}\, P_{i,jl}(z) \right] S_i^{\rm inc}(t,E). \end{aligned} \tag{1.147}$$

We immediately see that $S_i^{\rm inc}(t,E)=1$ satisfies the above equation, and is also consistent with the obvious initial condition $S_i^{\rm inc}(t_0,E)=1$. We thus state the *shower unitarity* property:

$$\mathcal{S}_i^{\rm inc}(t,E)=1. \tag{1.148}$$

This property is at the basis of the formulation of Shower Monte Carlo algorithms. It implies that *the total cross section computed at the Born level is equal to the total multi-particle cross section.* Of course, this statement holds in the approximation we are working with, and is obviously non-true in general: for example, in fixed-order calculations, the Born cross section is not equal to the full NLO cross section, which contains also the real term, where the contribution of one extra emission is fully included. Here, instead, we are only considering collinear-enhanced corrections, so we should state more precisely that the net effect of collinear-enhanced processes is one, when we sum over all processes. It is also instructive to check unitarity by expanding the shower order by order in α_S. For example, at the first order in α_S, we may have at most a single splitting. When we sum over all final states reached by parton i, we should thus consider only final states with one or two partons. For the one parton final state, the shower weight is given by the first order Taylor expansion of the Sudakov form factor:

$$\Delta_i(Q,t_0) = 1 - \sum_{(jl)}\int_{t_0}^{Q}\frac{dt}{t}\int_0^1 dz \;\; \frac{\alpha_S}{2\pi}\, P_{i,jl}(z) + \mathcal{O}(\alpha_S^2)\,. \tag{1.149}$$

The total weight for a two parton final state is instead given by

$$\int_{t_0}^{Q} \frac{dt}{t} \Delta_i(Q,t) \left[\sum_{(jl)} \int_0^{2\pi} \frac{d\phi}{2\pi} \int_0^1 dz \;\; \frac{\alpha_S}{2\pi} \, P_{i,jl}(z) \right] \Delta_j(t,t_0) \Delta_l(t,t_0)$$
$$= \int_{t_0}^{Q} \frac{dt}{t} \sum_{(jl)} \int_0^1 dz \;\; \frac{\alpha_S}{2\pi} \, P_{i,jl}(z) + \mathcal{O}(\alpha_S^2) \,, \tag{1.150}$$

and the sum of the two weights yields 1, as expected. From the above argument, one can see that the exact form for the integrand in the Sudakov form factor is dictated by the fact that collinear singularities, according to the KLN theorem, must cancel order by order.

From the shower unitarity property, it follows that the sequence of branching processes can be implemented with a Markovian algorithm, since the total weight of two subshowers initiated after a given splitting is one. Hence, each of the two showers evolves independently from the other one, and without affecting the branching process it originated from, which is clearly the basic requirement needed to build a Markovian algorithm.

1.3.4 Shower algorithm for final state radiation

It is apparent now that the development of the shower can be computed numerically using a simple probabilistic algorithm. We already interpreted the expression

$$\frac{\alpha_S(t')}{2\pi} \, \frac{dt'}{t'} \, P_{i,jl}(z) \, dz \, \frac{d\phi}{2\pi} \tag{1.151}$$

as the elementary probability for the branching $i \to jl$. Thus,

$$d\mathcal{P}_i^{\text{emiss}}(t') = \frac{\alpha_S(t')}{2\pi} \, \frac{dt'}{t'} \, \sum_{(jl)} \int dz P_{i,jl}(z) \tag{1.152}$$

is the probability for the parton i to undergo a branching in the dt' interval.

The expression for the Sudakov form factor can be easily recovered by calculating the probability of having no emissions at all between two scales t and t'. In fact, dividing the $[t,t']$ interval into N small subintervals of width δt, and calling t_k the center of each

subinterval, we have

$$\mathcal{P}_i^{\text{no emiss}}(t \to t') \simeq \prod_{k=1}^{N} \left(1 - d\mathcal{P}_i^{\text{emiss}}(t_k)\right) = \prod_{k=1}^{N} \left(1 - \frac{\alpha_S(t_k)}{2\pi} \frac{\delta t}{t_k} \sum_{(jl)} \int P_{i,jl}(z)\, dz\, \frac{d\phi}{2\pi}\right), \tag{1.153}$$

that reduces to the Sudakov form factor $\Delta_i(t, t')$ in the continuum limit $N \to +\infty$. Indeed, we can state that, in Parton Showers, virtual corrections are included in a probabilistic way: a Sudakov form factor corresponds to the probability of having non-resolvable emissions in a given $[t, t']$ interval.

As a obvious consequence of the probabilistic interpretation, the probability that, starting at the scale t, the first branching from the parton i is in the phase space element $dt'\, dz\, d\phi$, is then

$$d\mathcal{P}_i^{\text{1st}}(t \to t') = \Delta_i(t, t') \sum_{(jl)} \frac{\alpha_S(t')}{2\pi} \frac{dt'}{t'} P_{i,jl}(z)\, dz\, \frac{d\phi}{2\pi}, \tag{1.154}$$

i.e. it is the product of the no-branching probability from the scale t down to t' times the branching probability in the interval $dt'\, dz\, d\phi$. This is precisely equivalent to our shower recipe, if we remember that, because of unitarity, the total weight associated to further branchings of partons j and l is 1.

At this point, it is fundamental to notice that the r.h.s. of eq. (1.154), when integrated over z and ϕ, can be expressed as the exact differential of the Sudakov form factor, where the differential is assumed to be taken with respect to t':

$$d\mathcal{P}_i^{\text{1st}}(t \to t') = d\Delta_i(t, t')\,. \tag{1.155}$$

Hence, for a given leg of flavour i and virtuality t, one can obtain the value t' at which the next splitting happens by simply pick a random number, equal it to the Sudakov factor $\Delta_i(t, t')$ and solve the equation for t'. Indeed, the general algorithm for process generation goes as follows:

a) Generate a hard process configuration, with a probability that is proportional to its parton-level Born cross section. In this case, the scale Q has to be the typical scale of the hard process at hand.

b) For each final state colored parton, generate a shower in the following way:

   i. Set $t = Q$.

ii. Generate a random number $0 < r < 1$ and solve the equation $r = \Delta_i(t, t')$ for t'. In this way, t' is the value at which the following splitting has to take place.

iii. If $t' < t_0$, then no further branching is generated, the shower stops and the hadronization algorithm can be applied.

iv. If $t' \geqslant t_0$, then a splitting has to be generated: jl and z have to be generated with a distribution proportional to $P_{i,jl}(z)$, and the azimuth ϕ can be cast uniformly in the interval $[0, 2\pi]$. Energies of partons j and l are assigned as $E_j = zE_i$ and $E_l = (1-z)E_i$. The angle between j and l momenta is fixed by the value of t'. Given the angle, the azimuth ϕ and the spatial momentum lenght, the directions of j and l are fully reconstructed.

v. For each of the branched partons j and l, set $t = t'$ and go back to step (b-ii).

1.3.5 Initial state radiation in parton showers

In our description of Parton Showers, so far we have considered in detail only final state collinear emissions. However, in the context of fixed-order calculations, we discussed also how to deal with the presence of divergences associated to ISC configurations. Similarly to FSC emissions, these kinematic configurations are logarithmic enhanced, and give rise to *initial state showers*, that we describe in the following.

The kinematic configuration for an emission off an incoming leg is depicted in fig. 1.5. In this case, after the parton with momentum fraction $(1-z)$ is emitted off the incoming

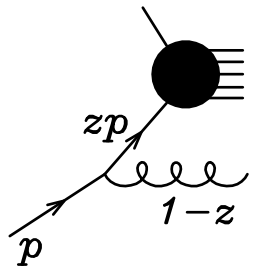

Figure 1.5: Emission off an incoming leg.

leg, then the initial state, that enters in the hard scattering blob with momentum fraction z, acquires a spacelike virtuality, limited in magnitude by the scale of the hard process. In this case, factorization holds as long as the virtuality of the parton entering the hard scattering is negligible with respect to all the other scales entering the hard scattering amplitude. Hence, in analogy with the previous case, the correct recipe to order the hardness variables is to generate multiple initial-state radiation with internal legs' virtuality

ordered from small (absolute) values (near the initial state parton) to large values (near the hard scattering). For the last splitting before the hard scatttering, the virtuality is limited by the hardness of the scattering process itself, that we labelled as Q.

Once an initial state emission is generated, then a further final state parton (the radiated one) is present in the event. This parton can obviously split again, giving rise to a final state shower. The resulting picture of this chain of emissions has then the structure reported in fig. 1.6, where the intermediate lines between t_1 and t_2 and between t_2 and the hard scattering are spacelike, whereas all other intermediate lines are timelike. The ordering is such that $t_1 < t_2 < Q$, and $t_1 > t'$, $t_2 > t'' > t'''$. In the following, for ease of notation, we always label the ordering variables as if they were positive, although this is not the case when virtuality is used as ordering variable. In that case, an absolute value is understood for negative virtualities.

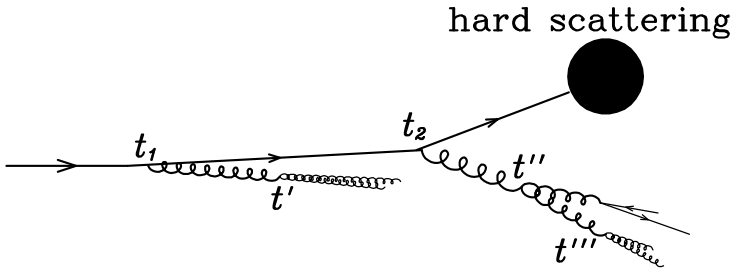

Figure 1.6: Schematical description of a shower involving initial state emissions.

In the following, we formally describe initial state showers and then give the shower recipe for processes involving initial state hadrons. We recall that the splitting functions and the Sudakov form factors needed to implement spacelike showers are the same ones used for final state radiation process, since differences arise only at the Next-to-Leading level.

Formal representation of initial state showers

An initial state shower is labelled as $\mathcal{S}_i(m, x, t, E)$ and the corresponding graphical representation is reported in the following:

$$\mathcal{S}_i(m, x, t, E) = \quad . \tag{1.156}$$

$\mathcal{S}_i(m, x, t, E)$ is a function on all possible states having a spacelike parton of type m with energy between xE and $(x+\delta x)E$, and scale t, originating from a parton i. Thus, it gives the weight of the shower for such states.

The initial state shower equation can be represented with the following graphical equation

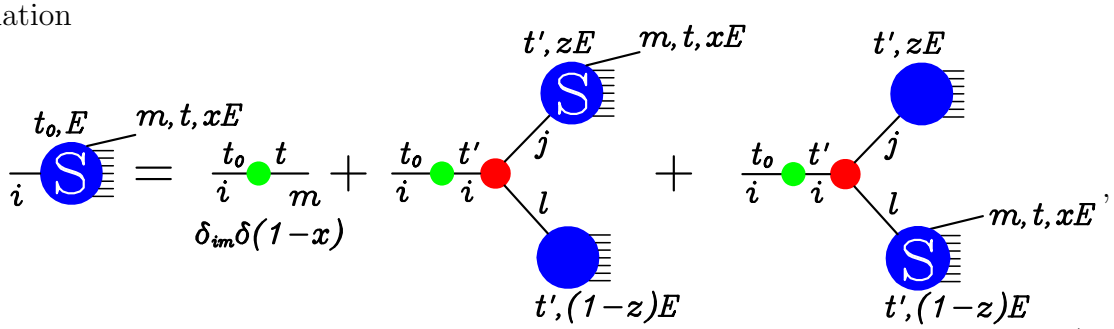

(1.157)

where the blobs marked with S represent spacelike showers, while the solid blob represents the timelike showers discussed previously. Solving eq. (1.157) corresponds to the so called forward evolution, since the recursive procedure would start from the low scale t_0. This technique was found to be inefficient from a pratical point of view, since most of the time one would end up with the two partons entering the hard scattering having an invariant mass not close to the correct one, that corresponds to Q, i.e. the relevant scale for the partonic cross section of the process at hand.[21] Hence, in modern Monte Carlo programs, it is preferred to solve the evolution equation in the opposite direction, according to the backward evolution method [19, 20]. In this way, the algorithm starts from the high-scale Q, so that a good efficency is guaranteed. The backward evolution is obtained by rewriting the shower equation as follows:

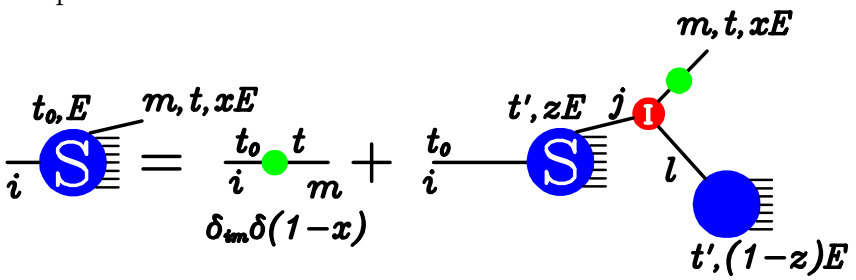

(1.158)

where the recursive procedure starts now at the high scale t instead of the low scale t_0. In this case, the red blob marked with I at the splitting vertex stands for the inclusive splitting kernel P_{jm}, instead of the exclusive one $P_{j,ml}$. The procedures depicted in the graphical equations (1.157) and (1.158) represent the same object, with a different

[21] For example, for a Drell-Yan process, this scale would be the mass of the produced vector boson.

recursion rule.

To obtain the probability for the first branching to take place, we have to sum over all final states in the graphical equation (1.158). As we discussed before, this sums yields 1 for timelike blobs, since they are associated with final state showers . For spacelike blobs, instead, one has

$$\sum_{\mathcal{F}} \mathcal{S}_i(m,x,t,E) = f_m^{(i)}(x,t), \tag{1.159}$$

where $f_m^{(i)}$ is the (scale dependent) parton density function.[22] When the sum over all final states is taken, the graphical equation (1.158) yields

$$f_m^{(i)}(x,t) = \delta_{mi}\delta(1-x)\Delta_m(t,t_0) + \int_{t_0}^{t}\frac{dt'}{t'}\int_x^1\frac{dz}{z}\sum_j f_j^{(i)}(z,t')\frac{\alpha_S(t')}{2\pi}P_{jm}\left(x/z\right)\Delta_m(t,t'), \tag{1.160}$$

and, by taking the derivative of both sides with respect to t, one has

$$\begin{aligned} t\frac{\partial f_m^{(i)}(x,t)}{\partial t} &= \frac{\alpha_S(t)}{2\pi}\sum_j\int_x^1\frac{dz}{z}\,P_{jm}(x/z)\,f_j^{(i)}(z,t) \\ &+ \left[-\sum_{(jl)}\int_0^1 dz\;\;\frac{\alpha_S(t)}{2\pi}\,P_{m,jl}(z)\right] f_m^{(i)}(x,t)\,. \end{aligned} \tag{1.161}$$

The previous equation is the ordinary Altarelli-Parisi [21–24] equation for the parton densities

$$t\frac{\partial f_m^{(i)}(x,t)}{\partial t} = \frac{\alpha_S(t)}{2\pi}\sum_j\int_x^1\frac{dz}{z}\,\hat{P}_{jm}(x/z)\,f_j^{(i)}(z,t)\,, \tag{1.162}$$

where $\hat{P}_{jm}$ are the regularized inclusive splitting kernels. They are given by

$$\begin{aligned} \widehat{P}_{qq}(z) &= C_F\left[\frac{1+z^2}{(1-z)_+}+\frac{3}{2}\delta(1-z)\right], \\ \widehat{P}_{qg}(z) &= P_{qg}(z), \\ \widehat{P}_{gq}(z) &= P_{gq}(z), \\ \widehat{P}_{gg}(z) &= 2C_A\left[\frac{z}{(1-z)_+}+\frac{1-z}{z}+z(1-z)+\left(\frac{11}{12}-\frac{n_f T_f}{3C_A}\right)\delta(1-z)\right]. \end{aligned} \tag{1.163}$$

[22] At this level, we are not considering hadrons yet. Therefore the parton density $f_m^{(i)}$ represents the probability to find a parton of type m in a parton of type i.

The probability distribution for the first backward branching of the parton m can be obtained from eq. (1.158) and (1.159). It reads

$$d\mathcal{P}_m^{1^{\rm st}}(t') = \sum_j f_j^{(i)}(z,t')\frac{\alpha_S(t')}{2\pi}P_{jm}(x/z)\Delta_m(t,t')\frac{dt'}{t'}\frac{dz}{z}\frac{d\phi}{2\pi}. \tag{1.164}$$

In order to generate the first branching, we must express eq. (1.164) as a differential in t'. Using the Altarelli-Parisi equation, we get

$$\begin{aligned}\frac{d\mathcal{P}_m^{1^{\rm st}}(t')}{dt'} &= \frac{\partial f_m^{(i)}(t',x)}{\partial t}\Delta_m(t,t') + \left[\frac{1}{t'}\sum_{(jl)}\int_0^1 dz \quad \frac{\alpha_S(t')}{2\pi}\, P_{m,jl}(z)\right] f_m^{(i)}(t',x)\Delta_m(t,t') \\ &= \frac{d}{dt'}\left[f_m^{(i)}(t',x)\Delta_m(t,t')\right]. \end{aligned}\tag{1.165}$$

We have obtained that the probability distribution for the first branching is uniform in $f_m^{(i)}(t',x)\Delta_m(t,t')$. Hence, to find t', we just need to generate a random number $0 < r < 1$, and then solve the equation

$$r = \frac{f_m^{(i)}(t',x)\Delta_m(t,t')}{f_m^{(i)}(t,x)} \tag{1.166}$$

for t'. The factor $f_m^{(i)}(t,x)$ in the denominator is introduced to normalize the right hand side to 1 when $t' = t$. Since the Sudakov form factor $\Delta_m(t,t')$ becomes very small when t' become small, then the right hand side of eq. (1.166) reaches its smallest value when $t' = t_0$. If the generated random number r is below the smallest possible value, then no branching takes place.

For reference, we also notice that sometimes the equivalent formula

$$\frac{f_m^{(i)}(t',x)\Delta_m(t,t')}{f_m^{(i)}(t,x)} = \exp\left[-\sum_j\int_{t'}^t\frac{dt''}{t''}\frac{\alpha_S(t'')}{2\pi}\int_x^1\frac{dz}{z}P_{jm}(z)\frac{f_j^{(i)}(t'',x/z)}{f_m^{(i)}(t'',x)}\right] \tag{1.167}$$

is used, that is the formula appearing in the original paper where backward evolution was introduced [19].

1.3.6 Shower algorithm for processes with incoming hadrons

We can now formulate the full recipe for the generation of a process where incoming hadrons are present. The algorithm is:

a) Generate a hard process configuration with a probability proportional to its parton

level cross section. This cross section includes also the parton density functions, evaluated at the typical scale Q of the process.

b) For each final state colored parton, generate a shower in the following way:

   i. Set $t = Q$.

   ii. Generate a random number $0 < r < 1$ and solve the equation $r = \Delta_i(t, t')$ for t'.

   iii. If $t' < t_0$ then no further branching is generated, and the shower stops.

   iv. If $t' \geqslant t_0$ then generate jl and z with a distribution proportional to $P_{i,jl}(z)$, and a value for the azimuth ϕ, with uniform probability in the interval $[0, 2\pi]$. Assign energies $E_j = zE_i$ and $E_l = (1-z)E_i$ to partons j and l. The angle between their momenta is fixed by the value of t'. Given the angle and the azimuth ϕ (together with the fact that the sum of their momenta must equal to the momentum of i) the directions of j and l are fully reconstructed.

   v. For each of the branched partons j and l, set $t = t'$ and go back to step bii.

c) For each initial state colored parton, generate an initial shower in the following way:

   i. Set $t = Q$.

   ii. Generate a random number $0 < r < 1$.

   iii. Solve for t' the equation

$$r = \frac{f_i^{(h)}(t', x)\Delta_i(t, t')}{f_i^{(h)}(t, x)},$$

   where $f^{(h)}$ is the parton density for the hadron where parton i is found, and $x = E_i/E_h$ is the momentum fraction of the parton.

   iv. If $t' < t_0$ then no further branching is generated, and the shower stops.

   v. If $t' \geqslant t_0$ then generate j and z with a distribution proportional to $P_{ij}(z)$, and a value for the azimuth ϕ, with uniform probability in the interval $[0, 2\pi]$. Call l the radiated parton, and assign energies $E_j = zE_i$ and $E_l = (1-z)E_i$ to partons j and l. The angle between their momenta is fixed by the value of t'. Given the angle and the azimuth ϕ (together with the fact that the sum of their momenta must equal to the momentum of i) the directions of j and l are fully reconstructed.

   vi. For parton j, set $t = t'$ and go back to step (c-ii). For parton l, set $t = t'$ and go back to step (b-ii).

1.3.7 Soft divergences

In all the previous discussion, we have only considered collinear singularities. In particular, we did not discuss the fact that the $z \to 1$ and $z \to 0$ limits are special, since (some of) the splitting kernels have soft divergences in these limits, and we supposed to have regularized them with a small cutoff (eq. (1.128)). Furthermore, we have still to discuss what is the best ordering variable to use. We will see that this is related to the treatment of soft divergences, which we describe in this section.

As a starting point, let us assume that the t variable is the virtuality, and let us focus upon a splitting at a scale t, with a given value of z, assumed to be defined as energy fraction with respect to the energy E of the splitting parton (eq. (1.134)). Under these assumptions, the two splitting partons have energies zE and $(1-z)E$, so they form a system with virtuality given by

$$2z(1-z)E^2(1-\cos\theta), \tag{1.168}$$

where θ is the angle between the two partons. Thus, we must have

$$z(1-z)E^2 \geq t/4, \tag{1.169}$$

in order for the splitting to be kinematically possible, the inequality being saturated when $\theta \to \pi$. Hence, the z integration is limited by

$$\frac{t}{4E^2} \leq z \leq 1 - \frac{t}{4E^2}. \tag{1.170}$$

If no soft singularities were present, effects coming from these nested integration limits could be neglected, because $t \ll E^2$ at any stage of the branching. In fact, at the beginning of the shower $E \approx \sqrt{Q}$, and after each branching E is reduced by a factor of order 1, since z is typically a number of order 1, if soft singularities were not present. Instead, $\sqrt{t}$ is reduced by a factor of order α_S at each branching.

However, in presence of soft singularities, the above argument is no longer applicable: for example, splittings with large (or small) values of z are enhanced, and one can no longer conclude that the energy of the partons is reduced by a factor of order 1 for each branching. It turns out that these regions of subleading logarithmic size can give contributions of order 1, in the same way we described for the colllinear case (sec. 1.3.2). Hence, to achieve logarithmic accuracy, soft divergences should be accounted for in a proper way. In particular, we want to describe accurately the soft emission pattern in the double logarithmic region, i.e. in the regions where emissions are both soft and collinear.

Double logarithmic structure

In the following, we want to show that the choice of the hardness parameter t affects the treatment of soft divergences. This is best seen by looking at the differences appearing in the exponent of the Sudakov form factor before integrating in t, when the three definitions of the ordering parameter given in eqs. (1.136), (1.137) and eq. (1.138) are used. In all the following approximations, we will neglect multiplicative factors of order 1 in front of each term, and we will neglect the exact form of the splitting kernel, retaining just the logarithmic-divergent structure $dz/(1-z)$. Inequalities are obtained by assuming $\theta < 1$ as a reliable range of validity for the collinear approximation to hold.

1. If t is assumed to be the virtuality of the incoming line, then we have $t \lesssim E^2 z(1-z)$ (see eq. (1.136)). This yields a double logarithmic integral of the form

$$\int \frac{dt}{t} \int_{t/E^2}^{1-t/E^2} \frac{dz}{1-z} \approx \frac{1}{2} \log^2 \frac{t}{E^2} \,. \tag{1.171}$$

2. If instead t is interpreted as the squared transverse momentum, then $t \lesssim E^2 z^2 (1-z)^2$, and we get

$$\int \frac{dt}{t} \int_{\sqrt{t}/E}^{1-\sqrt{t}/E} \frac{dz}{1-z} \approx \frac{1}{4} \log^2 \frac{t}{E^2} \,. \tag{1.172}$$

3. If t is interpreted as the squared angle, the result is

$$\int \frac{dt}{t} \int_0^1 \frac{dz}{1-z} \approx \log \frac{t}{t_0} \log \frac{E}{\Lambda}. \tag{1.173}$$

   It is worthwhile to observe that, if the ordering variable is proportional to the square of the angle, the value of z is not constrained by it. Then we have to impose a cutoff on z, in such a way that the energy of the final state particles cannot become smaller than some typical hadronic scale, which we call here Λ, and which is of the same order of Λ_{QCD}.

Angular ordering

We have seen that the three choices for the ordering variables yield different results for the Sudakov form factors, in particular in the double logarithmic region. It has been shown that this region is treated correctly if one uses as ordering parameter the angular variable θ. More precisely, angular ordering is necessary to take into account QCD coherence effects in a Markovian algorithm, such as the Parton Shower [25–31]. An argument to

explain this resut can be found for example in [5]. Here we limit ourselves to give just an explanation, that is based on known coherence effects.

We start by supposing that we order the emissions in decreasing virtuality. Since soft emissions always yield small virtualities, at the end of the shower one has a large number of soft gluons, unrestricted in angle if no angular ordering is imposed. But soft gluons emitted at large angles from final state partons add up coherently. This means that a soft gluon emitted from a bunch of partons sees all the emitting partons as a single entity, i.e. it sees the total color charge of the bunch, if its emission angle is larger than the angular separation of the bunch (see fig. 1.7). One can reinterpret this by saying that

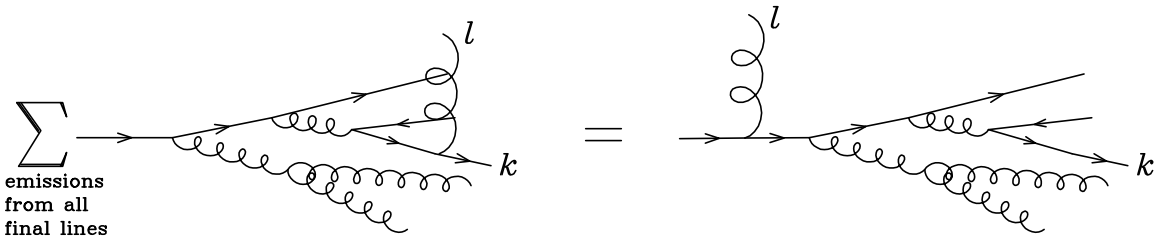

Figure 1.7: Soft emissions at large angle add coherently, i.e. they behave as if the emitter was the parton that originates the rest of the shower.

large-angle soft gluons are emitted before than small-angle ones, since the latters see the charge of each emitter while the formers just feel the total charge. It is then clear that angular ordering is the pratical way to obtain this result in a probabilistic algorithm.

Argument of the running coupling constant

Before concluding this section, focused on the treatment of soft singularities, we need to briefly describe a couple of subtleties concerning the choice of the scale at which α_s is evaluated in the Sudakov form factors, since this choice is related to the inclusion of higher-order logarithmic effects in the soft-collinear enhanced regions. In the following we simply limit ourselves to report the relevant results. More comments and references to the original papers can be found in [32].

In sec. 1.3.2 we already argued that the exact choice of the argument of α_s does not affect the leading-log collinear accuracy of the Parton Shower. However, it can be shown that, by choosing the argument of α_s equal to the maximum virtuality available for the outgoing gluon in the splitting at hand, one recovers almost exactly the soft behaviour of the two loop splitting kernel, yielding an improvement of the shower accuracy in these regions. More precisely, by using the one loop splitting kernels and expanding the one-loop α_s expression evaluated at the aforementioned scale, one generates the soft-enhanced

logarithmic terms ($\sim \alpha_{\rm S}^2 \log(1-z)/(1-z)$) present in the two-loop splitting kernels, as if their couplings were evaluated at a scale equal to the virtuality of the splitting parton, which we denote here as $\tilde{q}^2$. In particular, this corresponds to use the scale $(1-z)\tilde{q}^2$ for a splitting $q \to gq$, or $z(1-z)\tilde{q}^2$ for a splitting $g \to gg$.[23] In the collinear limit, the expression $z(1-z)\tilde{q}^2$ equals the transverse momentum of the emitted gluon with respect to the splitting parton (see eq. (1.136)- (1.138)). Hence, by choosing $k_{\rm T}$ as the argument of $\alpha_{\rm S}$, these logarithms are authomatically reproduced by the expansion of $\alpha_{\rm S}$.

With this choice, one still misses a term relevant when the $z \to 1$ limit of the two-loop splitting kernels P_{qq} and P_{gg} is taken, which goes as $\sim \alpha_{\rm S}^2/(1-z)$ (cfr. eq. (4.123) of [5]). This term can be taken into account by simply changing the value of Λ_{QCD} used to run the $\alpha_{\rm S}$ coupling constant present in the Sudakov form factors [33]. This new scale is traditionally called $\Lambda_{\rm MC}$ and its value is equal to

$$\Lambda_{\rm MC} = \Lambda_{\overline{\rm MS}} \exp\left(\frac{K_g}{4\pi b_0}\right), \tag{1.174}$$

where

$$K_g = C_{\rm A}\left(\frac{67}{18} - \frac{\pi^2}{6}\right) - T_{\rm F} n_{\rm f} \frac{10}{9}. \tag{1.175}$$

Its numerical value, for $n_{\rm f} = 5$, is

$$\Lambda_{\rm MC} = 1.569\, \Lambda^{(5)}_{\overline{\rm MS}}. \tag{1.176}$$

So, by adopting $\Lambda_{\rm MC}$ as the strong scale and using the transverse momentum as the argument of the running coupling $\alpha_{\rm S}$, we improve the leading-log accuracy, by including also next-to-leading logarithms, except those coming from wide-angle soft emissions, that can not be properly included in the quasi-collinear approximation we are working with.

1.3.8 HERWIG and PYTHIA

At present, the three more used SMC event generators are `HERWIG` [34], `PYTHIA` [35] and `SHERPA` [36, 37]. The formers, originally written in Fortran, have been used since the late 80's and are now being rewritten and upgraded in C++. The latter, instead, is more recent and it has been coded from the beginning in C++. Since the work presented in this thesis has been carried out with the use of the Fortran version of `PYTHIA` and `HERWIG`, in the following we report quickly the main features of them.

[23] Technically, the scale choice for a splitting $g \to gg$ should be $\mathrm{Min}\{z, 1-z\}\,\tilde{q}^2$, but for simplicity the symmetrized choice is often used.

The HERWIG shower is angular ordered [30,38], the ordering variable being defined such that it reduces to $t = E^2\theta^2/2$ in the collinear limit, where E is the energy of the incoming parton and θ is the angle between the two branched partons, carrying energies zE and $(1-z)E$. The Sudakov form factor is defined as

$$\Delta_i(t', t'') = \exp\left[-\sum_{(jl)} \int_{t''}^{t'} \frac{dt}{t} \int_0^1 dz\, \theta(tz^2(1-z)^2 - t_0)\ \frac{\alpha_S\left(tz^2(1-z)^2\right)}{2\pi}\ P_{i,jl}(z)\, dz\right]. \tag{1.177}$$

From the above equation, we see that, for the running of α_S, HERWIG uses a renormalization scale of the order of the the transverse momentum, and the Λ_{QCD} scale is chosen to be equal to $\Lambda_{\rm MC}$. Therefore, the HERWIG Sudakov form factor is correct at the NLL, as explained at the end of the previous section. The infrared cutoff, needed for the infrared divergent integration over z, is expressed by means of the θ function, that also acts as a lower cutoff for the argument of $\alpha_{\rm S}$. As usual, t_0 is a scale of the order of Λ_{QCD}. After a splitting characterized by a given value for z, one is left with two partons of energies zE and $(1-z)E$. Angular ordering is achieved by choosing as the initial condition for subsequent branchings the scales tz^2 and $t(1-z)^2$.

The traditional PYTHIA shower is based on virtuality ordering. Apparently this choice is more natural, since in a chain of consecutive splittings, virtuality ordering follows from considerations based on kinematics. However, in this way, coherence effects can not be taken into full account, and historically this yielded an unphysical increase in the number of soft partons, so that in PYTHIA the particle multiplicity in e^+e^- annihilation processes did not have the correct growth with energy. Furthermore, sizeable effects due to the lack of a consistent inclusion of coherence were also observed in hadronic collisions [39]. In the Fortran version of PYTHIA, the remedy was to introduce a procedure to veto branchings that violate angular ordering. This scheme (virtuality ordering with angular ordering imposed by veto) yields results in good agreement with observed data, both in e^+e^- and in hadronic collisions.

Recently, new showering schemes have become available in PYTHIA and HERWIG. In HERWIG++ [32], new showering variables have been introduced, to improve the boost invariance properties of the shower. Recent versions of PYTHIA also offer an alternative showering scheme, ordered in transverse momentum [40], that implements a variant of the so called *dipole shower* approach, first implemented in the ARIADNE [41] Monte Carlo. In this thesis, comparisons of POWHEG results with PYTHIA have been carried out using this $p_{\rm T}$–ordered shower.

1.3.9 Flavour, color, hadronization and underlying event

In this final section we quickly describe how hadronization models work, without entering into technical details. Before discussing hadronization, we need to discuss how flavour and color flows are treated at each splitting.

Flavour and color flows

At each splitting, in the collinear approximation we are working with, the flavour flow is well defined. Hence, at the end of the shower, we find quarks and antiquarks with a given flavour, together with gluons. Thus, the flavour content of the generated hadrons will depend on how the hadronization model treats the flavour content of these outgoing partons.

The color flow is not followed exactly in the collinear approximation, since the factorization formula is valid for color averaged squared amplitudes. However, we know that final state hadrons are color singlets, and hadronization models implemented in modern SMC comply with this by looking at the color structure of the outgoing partons at the end of the shower. Hence, we need a recipe to handle in a deterministic way the color flow at each splitting. In parton showers based on collinear factorization, this is achieved by working in the planar limit (also known as large N_c limit). The rules for the color assignment at each splitting are given in fig. 1.8. The only ambiguity is in the color assignment

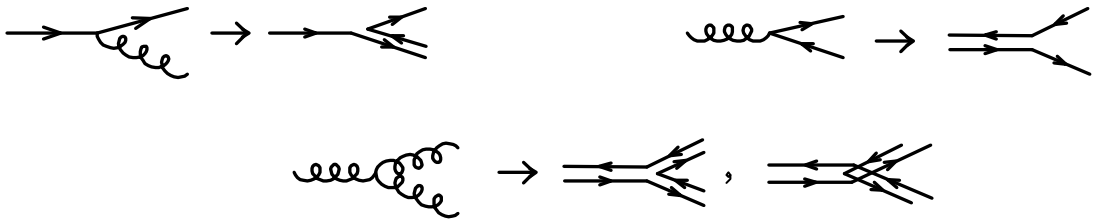

Figure 1.8: Planar rules for the assignment of color flow at each splitting.

for the slitting $g \to gg$. In this case, one chooses one of the two assignments with a 50% probability. In this way, at the end of the shower, one is left with a set of partons whose color connections are fully known.

Cluster and string based fragmentation models

The cluster and string fragmentation models are both based upon the assignments of color connections illustrated above. The former is the model implemented in `HERWIG`, whilst the latter is included in `PYTHIA`.

In the cluster model, final state gluons are forced to split into quark-antiquark pairs. Then each pair of color connected quark-antiquark is treated independently. If the invariant mass of the color connected pair is low enough, one matches mass and flavour with a corresponding hadronic two-body system (or with a resonance) with the same flavour. In this way, hadronization is carried out. We also notice that, in angular ordered showers, at the end of the shower color connected pairs are naturally close, i.e. configurations with large invariant-mass color-connected pairs are Sudakov suppressed (an effect known as *preconfinement*).

In the string fragmentation model, color connected partons are collected in a system consisting of a quark, several intermediate gluons, and an antiquark. One then imagines that a color flux tube, called *string*, is stretched from the quark to the antiquark of the color connected system, going through each intermediate gluon.

In the simplest case, the string is stretched between a quark and an antiquark, and the hadronic system is generated by pair creation by quantum tunneling inside the string. In practice, starting from each string end, one has a fragmentation function to describe the probability to generate a hadron carrying away a given fraction of the longitudinal momentum of the string. For example, if a string end has flavour f, then a hadron will be generated with flavour $f\overline{f'}$, and the left over string will have a flavour f' at his end. In this way, color and flavours are treated consistently. In the general case, with intermediate gluons in the color connected system, a similar procedure is adopted, with some care for the treatment of the kinks in the string associated to the intermediate gluons.

As a final remark, we recall that fragmentation models are one of the most complex aspects of Shower Monte Carlo, even if, at this level, the underlying theory (which is always QCD, but in the strong regime) is only used as a reasonable source of hints on certain features that the models should have. Nevertheless, models have unavoidably a large number of parameters, that are needed in order to represent faithfully the many final state features that are observed in strong interactions.

Underlying event

We have seen that the hadronization model deals with final state partons, turning them into hadrons. Initial state partons require some treatment too, in order to give a realistic description of the physics of the hadronic remnants.

First we need to discuss briefly how partons are extracted from incoming hadrons in SMC programs. In our shower description, we have introduced the parton densities to find a parton in a parton (eq. (1.159)). These objects should now be interpreted as the probabilities to find a parton in the incoming hadron. In the forward evolution scheme,

this would require to introduce an initial parton density at the scale t_0. In the backward evolution scheme, instead, this is not needed: one computes the cross section with the full PDF at the scale of the process (Q). However, when the backward shower stops, one is left with the problem of treating the structure of the remaining part of the incoming hadron. There are different models to handle this. Here we do not want to enter into details, and hence we refer to the original manuals of the codes for a deeper description.

Finally, it is worthwhile to notice that in SMC programs underlying event models are also implemented, by letting the remnants of the incoming hadrons to undergo relatively hard collisions. Also for these aspects, we refer to manuals for further details.

Chapter 2

Matching Next-to-Leading-Order calculations with Parton Showers

In this chapter we focus our attention in describing how to merge Next-to-Leading-Order calculations with Parton Showers, in order to build an event generator that aims to keep the good features of both the two approaches together.

From the description of NLO calculations and Parton Showers that we gave in the previous chapter, it is apparent that the main problem we need to deal with is essentially the possible overcounting of emissions, that can happen because SMC programs already implement NLO corrections, in the collinear (or soft) approximation.

Among many other proposals appeared in literature to achieve this goal, both for e^+e^- and hadron collisions,[1] two of them have been exploited to fully implement processes relevant for the Tevatron and the LHC experiments: the `MC@NLO` [42] and the `POWHEG` [1] methods. In this chapter we describe the latter approach, which is the method used to obtain the original results contained in this thesis.

The chapter is organized as follows.

Since we find useful to collect all the advantages and drawbacks of (leading-order[2]) Parton Showers and NLO calculations, we devote section 2.1 to this purpose. A quick description of the methods to merge Matrix Elements generators and Parton Showers is also given.

In section 2.2 we describe the main problems occurring when NLO contributions are included in SMC programs. In particular, we discuss in detail how the problem of double-counting arises. We also explain briefly how these issues are addressed in the `MC@NLO`

[1] See references contained in [2].

[2] Here we mean SMC programs where the matrix element for the hard process is accurate only at the tree level.

framework, since some of the results that will be presented are basically comparisons with analogous results obtained with that approach.

Section 2.3 will be devoted to an accurate description of the POWHEG method.

2.1 Next-to-Leading-Order calculations vs. Parton Showers

In this section we want to compare various aspects of NLO computations and SMC event generators, in order to summarize the advantages and the drawbacks of both. To highlight some of these differences, we find useful to compare the HERWIG and PYTHIA predictions for the transverse momentum spectrum and the rapidity of a W boson, together with the same curves calculated with NLO accuracy. In particular, we consider the Drell-Yan process $pp \to W^-(\to e^-\bar{\nu}_e)$ as the leading-order process.

1. In fig. 2.1 we show predictions for the W-boson transverse momentum.

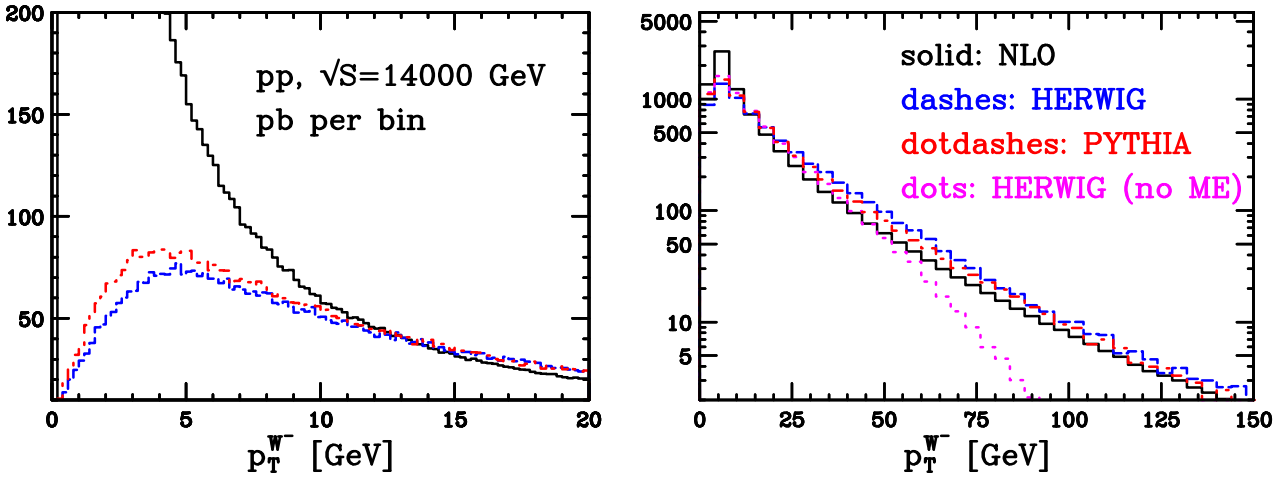

Figure 2.1: Transverse momentum of a W^- boson produced at the LHC. In the left panel, a zoom of the low-p_T region is reported. No K-factors have been included.

In the low transverse-momentum region, the NLO result exhibits a very pronounced enhancement. This is due to the fact that, in the low-p_T region, real corrections are approaching the collinear divergence, and the cancellation with virtual corrections affects only the first bin of the plot. Hence, at fixed order, there is nothing to prevent

the W-boson transverse-momentum to be arbitrarily small, the W-boson momentum being exactly balanced with the emitted parton that is becoming collinear to the beam axis. In SMC results, instead, low-p_{T} configurations are disfavored. In fact, as we have seen in chapter 1, the probability that no emission takes place between two very different scales is strongly suppressed, as we showed in eq. (1.141). In this case, the hard scale of the process is M_W^2, whereas the scale associated with no-emission is of the same order of the lower cut-off t_0. Hence, we have two very different scales, and a suppression is expected. This suppression is often called *Sudakov suppression*, and real data exhibit it, as we will see in chapter 3. Therefore, we want to preserve this feature when including NLO corrections in SMC generators.

2. In the right panel of fig. 2.1, it is visible that the high-p_{T} shape of the `HERWIG` result is damped when Matrix Element (ME) corrections are turned off. In this case, a more detailed explanation is needed.

   In general, one does not expect that SMC's describe high transverse-momentum regions with good accuracy, since emissions are performed in the collinear approximation. Despite of this, for processes simple enough, modern SMC event generators implement methods that permit to describe high-p_{T} tails with good accuracy. These techniques are commonly called *Matrix Element corrections*, and basically work by re-weighting the SMC hardest emission with the exact real matrix element for the process at hand. Moreover, a phase space region that would not be filled by the shower first emission variables (a *dead-zone*, in the PS jargon) can be populated according to the $(n+1)$-body exact matrix element.[3] More details can be found for example in the `HERWIG` [34, 43] or `PYTHIA` [44] manuals, or in the original papers where these methods have been first introduced and discussed [45, 46]. Here, we just want to recall that ME corrections are implemented for $2 \to 1$ processes, such as $pp \to \{W, Z\}$ or $pp \to H$. Predictions for more complicated processes may then exhibit a lack of high-p_{T} events, such as in the purple curve in fig. 2.1, which has been obtained by explicitly turn off ME corrections in `HERWIG`. In fact, such an effect has been observed in the context of single-top hadroproduction, and it will be discussed in more detail in the Results section of chapter 4. From the above description, it is then apparent that we aim to merge NLO calculations and SMC in such a way that the full real matrix-element accuracy is exactly retained.[4] In this way, high-k_{T}

[3] In the language adopted in `HERWIG`, these two corrections are called *soft* and *hard* ME corrections, respectively.

[4] Technically, we want that the $\mathcal{O}(\alpha_{\mathrm{S}})$ expansion of the matched approach coincides with the fixed-order one. Only differences that are subleading with respect to the NLO are admitted, i.e. they have to be NNLO effects.

emissions will be described without the need of ME corrections.

3. Another important difference between NLO and SMC results is the accuracy of inclusive observables. Here, we call "inclusive" the quantities that are affected both by real and virtual corrections. Apart from the total cross section, other more exclusive quantities have this property: a typical example is the W-boson rapidity y_W in Drell-Yan processes. In fig. 2.2 we show the NLO and SMC results for y_W,

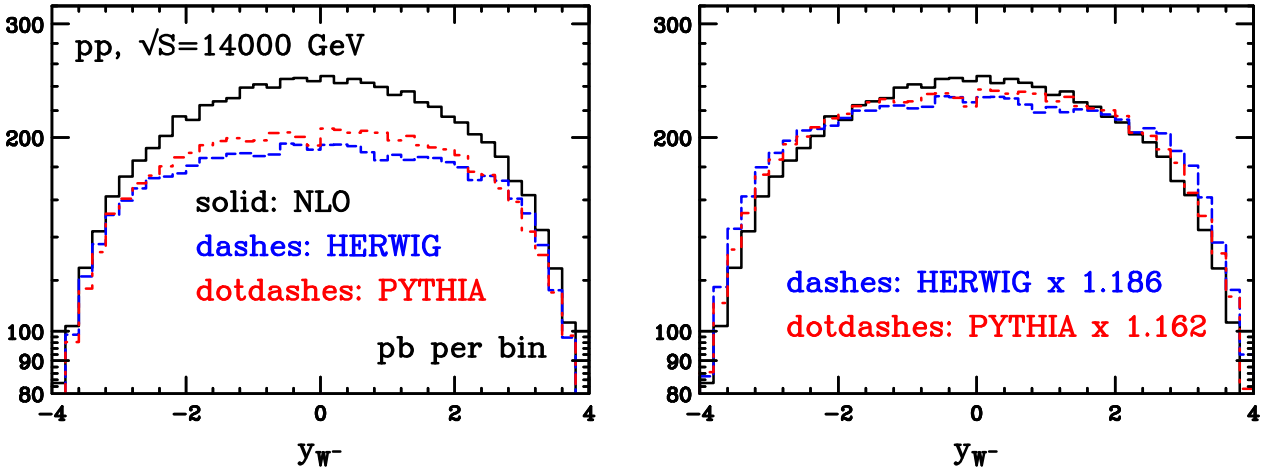

Figure 2.2: Rapidity of a W^- boson produced at the LHC. In the right panel, results obtained with Shower Monte Carlo event generators have been rescaled to the full NLO cross section.

with and without the inclusion of a K-factor: SMC results are in good agreement with the full NLO ones only when the K-factor is included. Hence, in a merged approach, we want to generate events with the correct overall normalization from the very beginning, so that K-factors are not needed anymore. Moreover, the obtained result will also be typically closer in shape to the NLO one, as it can be noticed by comparing fig. 2.2 with the `POWHEG` plot in fig. 3.28.

4. Next-to-Leading-Order results are more stable than LO ones, having a reduced dependence from the value used for the renormalization and factorization scales. In fact, the scale dependence of virtual and collinear remnant contributions compensate for terms that are generated by a change of μ_R and μ_F in the expression of the strong coupling and in the evaluation of partonic densities. In a merged approach, this feature would be inherited from the inclusion of these NLO terms.

5. It is also worthwhile to notice that, in SMC generators, high-multiplicity events are generated, although within the collinear approximation. Hence, some phase space regions that, for kinematic reasons, can not be filled with fixed order calculations, are instead described, at least with LL accuracy, when SMC's are used. An example of this effect will be discussed in chapter 4 (see fig. 4.2-panel (h), and the associated comment in the text).

6. Unlike NLO programs, SMC event generators produce unweighted events, i.e. events having all the same weight and distributed according to their relative differential cross section. Hence, it is straightforward to obtain a prediction for a generic observable, also when this is not infrared-safe. When matching the two approaches, we want to preserve this feature of SMC programs.

7. Finally, we want to recall that SMC programs generate events at the hadron level, so that simulations where detector effects are taken into account can be performed easily. In fact, SMC event generators are often used as "black-boxes". This means that the user can run the program and perform a simulation without knowing all the details of the program, but just implementing his own analysis procedure.

From the above list, it should be clear that both NLO calculations and SMC programs have desirable properties, that we want to preserve when merging the two approaches. The formulation of the `MC@NLO` and `POWHEG` methods is such that all the above features are obtained. The rest of this chapter will be dedicated to a description of the main problems to face in order to include NLO corrections in Parton Showers and obtaining all the above benefits. A description of the two methods cited above will be given, with particular attention on `POWHEG`, since it was the method used to obtain the results presented in this thesis.

2.1.1 Matching Matrix Elements and Parton Showers

For sake of completeness, before going on we want to recall that, besides to the `MC@NLO` and the `POWHEG` methods, there are algorithms to merge consistently tree-level Matrix Element generators (ME) and Parton Showers: the CKKW [47,48] and the MLM [49–51] approach. The main goal of these approaches, that we will denote as ME+PS, is to simulate processes with an arbitrary large number of extra emissions, by producing (with the ME generator) samples of weighted events with different multiplicities, and showering them, in order to include soft/collinear corrections and hadronization. Since ME generators can produce partonic events with high final-state multiplicity according to their exact tree level cross

section, by merging ME and PS's one gains good accuracy for the shape of multijet distributions *and* Sudakov suppression in the infrared region, thanks to the PS algorithm. Therefore, with these methods, multiple hard radiation is included more accurately than in `MC@NLO` and `POWHEG`, because, as we shall see, the latters include only the exact ME for the hardest emission (the real term in the NLO language). On the other hand, NLO accuracy for inclusive observables will not be achieved with the CKKW-MLM approaches, since virtual corrections are not included. Thus, we can say that NLO+SMC approaches (as `MC@NLO` and `POWHEG`) and ME+PS methods are two complementary tools, the formers being adequate to include all the NLO corrections exactly, as we shall show, while the latters being more reliable in describing multijet events.

2.2 Including NLO corrections into Shower Monte Carlo programs

In this section we will describe (some of) the technical problems occurring when merging NLO calculations and SMC programs. From the content of the previous section (in particular from items 1, 2 and 3 of the list therein), it is clear that we want a merging procedure with the following properties:

- The hardest generated emission has the correct NLO distribution also far from the collinear directions.
- The NLO accuracy for inclusive observables is retained. Hence, quantities integrated around the soft and collinear directions have NLO accuracy.
- At least the leading-logarithmic accuracy of the shower approach is maintained.

In this section we will proceed by first concentrating on the first requirement.

We also stress here that we call *hardest emission* the one having the highest transverse momentum. In particular, for radiation off incoming legs, the transverse momentum is assumed to be taken with respect to the beam axis. For final state radiation, instead, the definition of the transverse momentum is to some extent ambiguous. We will assume to use the transverse component of the momentum of the emitted parton with respect to the splitting direction, as measured in the partonic center-of-mass frame.

2.2.1 The double-counting problem

The main problem to face when merging NLO calculations with parton shower simulations is basically that of avoiding overcounting of emissions. This can happen because

SMC programs implement NLO corrections in an approximate way, through the shower algorithm. More precisely, according to [42], we say that a merging method is affected by *double-counting* if, after expanding all the contributions to the first order in the coupling constant $\alpha_{\rm S}$, it produces expectation values which are not equal to the exact NLO results.

In the following, we show this by calculating the SMC expectation value for an exclusive observable, expanding it at order $\alpha_{\rm S}$ and comparing it to the exact NLO result. We will proceed through a simplified example, similar to the 'toy model' of the original `MC@NLO` paper [42]. In particular, for this subsection (2.2.1):

- We assume a $p_{\rm T}$-ordered SMC. From this, it follows that the first emission generated by the SMC corresponds to the hardest one.
- We suppose that an n-body event is an event without radiation.[5]

Further complications, such as the presence of many singular regions and the role of collinear remnants, will be dealt with only in the description of the `POWHEG` method (sec. 2.3).

We begin by calculating the SMC cross section for the hardest emission, that according to our assumptions corresponds to the one generated first. Following the recipes given in sec. 1.3, we have

$$d\sigma_{\rm SMC}^{\rm hardest} = B(\mathbf{\Phi}_n)\, d\mathbf{\Phi}_n \Delta^{\rm MC}(t_{max}, t) \frac{\alpha_s}{2\pi}\frac{1}{t} P(z) d\Phi_{\rm rad}^{\rm MC}\,, \tag{2.1}$$

where B is the Born differential cross section,

$$\Delta^{\rm MC}(t_{max}, t) = \exp\left\{ -\int_t^{t_{max}} \frac{dt'}{t'} \int dz' \frac{\alpha_s}{2\pi} P(z') \right\} \tag{2.2}$$

is the SMC Sudakov form factor, t_{max} is the maximum allowed transverse momentum for the first emission,[6] and $d\Phi_{\rm rad}^{\rm MC} = dt\, dz\, d\phi/(2\pi)$. The presence of the Sudakov form factor in eq. (2.1) is responsible for the suppression of low-$p_{\rm T}$ radiation. In this section, we label the ordinary Sudakov form factor with the superscript MC, since in the following we will need to introduce another form factor, the `POWHEG`'s one.

In NLO calculations, when the subtraction method is used, the NLO differential cross section can be written as

$$d\sigma_{\rm NLO} = d\mathbf{\Phi}_n \Big\{ B(\mathbf{\Phi}_n) + V(\mathbf{\Phi}_n) + \left[R(\mathbf{\Phi}_{n+1}) - C(\mathbf{\Phi}_{n+1}) \right] d\Phi_{\rm rad} \Big\}\,, \tag{2.3}$$

[5] For example, we can think to a leading-order Drell-Yan process.

[6] We have assumed a $p_{\rm T}$-ordered shower.

which is the analogous of eq. (1.78), without specifying the expectation values for O and after a choice of the parameterization of the $(n+1)$-body phase space such that $d\mathbf{\Phi}_{n+1} = d\mathbf{\Phi}_n \, d\Phi_{\rm rad}$. The notation has already been introduced in sec. 1.2, and we do not report here further details. We just recall that V is finite, and contains one more power of $\alpha_{\rm S}$ with respect to B.

Now we calculate the expectation value for an exclusive observable. In particular, we assume to calculate the distribution of the transverse momentum of the hardest radiation. According to our assumptions, each point of this distribution (away from the zero value) is calculated by taking the expectation value of an observable that is nonvanishing only if the final state has more than n outgoing particles (i.e. we need at least one QCD emission). We denote this observable $\tilde{O}$, and we calculate its expectation value, according to the SMC and to the NLO cross section for the hardest emission:

$$\begin{aligned}
\langle \tilde{O} \rangle_{\rm SMC} &= \int d\mathbf{\Phi}_n \Delta^{\rm MC}(t_{max}, t) B(\mathbf{\Phi}_n) \frac{\alpha_s}{2\pi} \frac{1}{t} P(z) \, d\Phi^{\rm MC}_{\rm rad} \tilde{O}(\mathbf{\Phi}_{n+1}) \\
&= \int d\mathbf{\Phi}_n B(\mathbf{\Phi}_n) \frac{\alpha_s}{2\pi} \frac{1}{t} P(z) \, d\Phi^{\rm MC}_{\rm rad} \tilde{O}(\mathbf{\Phi}_{n+1}) + \mathcal{O}(\alpha_{\rm S}^2) \,, \qquad (2.4) \\
\langle \tilde{O} \rangle_{\rm NLO} &= \int d\mathbf{\Phi}_{n+1} R(\mathbf{\Phi}_{n+1}) \, \tilde{O}(\mathbf{\Phi}_{n+1}) \,. \qquad (2.5)
\end{aligned}$$

The double-counting problem arises when one tries to naively shower n and $(n+1)$-body partonic events generated after a reorganization of eq. (2.3). We write symbolically this naive procedure as follows:

$$\begin{aligned}
d\sigma_{\rm naive} &= d\mathbf{\Phi}_n \left[B(\mathbf{\Phi}_n) + V(\mathbf{\Phi}_n) - \int d\Phi_{\rm rad} C(\mathbf{\Phi}_{n+1}) \right] \mathcal{F}_{\rm SMC}\left(\mathbf{\Phi}_n\right) \\
&+ d\mathbf{\Phi}_{n+1} R(\mathbf{\Phi}_{n+1}) \, \mathcal{F}_{\rm SMC}\left(\mathbf{\Phi}_{n+1}\right) \,. \qquad (2.6)
\end{aligned}$$

With the symbol $\mathcal{F}_{\rm SMC}\left(\mathbf{\Phi}_n\right)$ we denote the SMC *generating functional* for a shower originated from an n-body configuration: it corresponds to the sum of all the possible kinematic configurations in which the shower originated from $\mathbf{\Phi}_n$ can end, each one weighted with its own probability, as obtained according to the recipes given in sec. 1.3. In practice, when an expectation value is taken, this functional returns the sum of the values assumed by the observable O in each of the aforementioned kinematic regions, each one weighted by the corresponding shower probability. For the following argument, we need just to assume that the shower generated by $\mathcal{F}_{\rm SMC}\left(\mathbf{\Phi}_n\right)$ works in the standard way, since the event to be showered is Born-like.

Double-counting is immediately manifest when calculating, at order $\alpha_{\rm S}$, and using (2.6),

the expectation value for $\tilde{O}$. In fact we have[7]

$$\langle \tilde{O} \rangle = \underbrace{\int d\mathbf{\Phi}_n B(\mathbf{\Phi}_n) \, \frac{\alpha_s}{2\pi} \frac{1}{t} P(z) \, d\Phi_{\rm rad}^{\rm MC} \tilde{O}(\mathbf{\Phi}_{n+1})}_{\text{SMC } 1^{\rm st} \text{ emission}} + \underbrace{\int d\mathbf{\Phi}_{n+1} R(\mathbf{\Phi}_{n+1}) \, \tilde{O}(\mathbf{\Phi}_{n+1})}_{\text{exact NLO}} + \mathcal{O}(\alpha_{\rm S}^2) \, . \tag{2.7}$$

The obtained value does not coincide, at order $\alpha_{\rm S}$, with the exact NLO result, and therefore this naive procedure is affected by double-counting. In particular, events generated according to eq. (2.6) will contain an excess of low-$p_{\rm T}$ radiation. In fact, in the collinear limit $t \to 0$ we have

$$R(\mathbf{\Phi}_{n+1}) \;\; d\Phi_{\rm rad} \to B(\mathbf{\Phi}_n) \left(\frac{\alpha_s}{2\pi} \frac{1}{t} P(z) \right) d\Phi_{\rm rad}^{\rm MC} \, , \tag{2.8}$$

and we are generating events in the same kinematic region twice.

At this point, another important comment is due . In addiction to produce double-counting, it would also be dificult to generate unweighted events using eq. (2.6). In fact, even if the total integral is finite, the two terms are separately divergent. Hence, also by using a small cutoff to avoid the exact singularity, the unweightening efficency to produce n and $(n+1)$-body kinematics would be very low.

In the following we describe how the double-counting problem is solved within the `MC@NLO` method.

2.2.2 The `MC@NLO` method

The `MC@NLO` proposal [42] was the first one to give an acceptable solution to the overcounting problem. The generality of the method has been explicitly proven by its application to processes of increasing complexity, such as heavy-flavour-pair [52] and single-top [18, 53] production. Here, we just want to give a simplified description of the way the method works, trying to use a notation similar to the one introduced previously. The exact formulation can be found in the original papers, together with the technical details.

The basic idea of `MC@NLO` is that of avoiding the overcounting by subtracting from the exact NLO cross section its approximation, as implemented in the SMC program to which

[7] Eq. (2.7) is the analogous of eq. (3.30) of [42]. Here we are neglecting the subtleties of eq. (3.28) and (3.29) of that paper, since we are interested only to keep the order $\alpha_{\rm S}$ contributions. However, in this $p_{\rm T}$-ordered toy model, the natural initial value of the ordering variable t for the shower generated by $\mathcal{F}_{\rm SMC}(\mathbf{\Phi}_{n+1})$ would correspond to the transverse momentum associated to the $(n+1)$-body kinematics. If that value is used, $(n+1)$-body events showered with $\mathcal{F}(\mathbf{\Phi}_{n+1})$ contribute to the hardest radiation with weight exactly equal to real matrix element, since harder radiation would be prevented by the shower ordering.

the NLO computation is matched. Such approximated cross section has to be computed analytically, and it is obviously SMC dependent. On the other hand, these subtraction terms are process-independent, and thus for a given SMC they can be computed once and for all. In the current version of the MC@NLO code, the MC subtraction terms have been computed for the Fortran version of HERWIG [34]. Some MC@NLO implementations have also been coded within HERWIG++ [54, 55].

The aforementioned subtraction is essentially introduced by adding and subtracting to eq. (2.3) the $\mathcal{O}(\alpha_{\rm S})$ expansion of the result that one would obtain by running the SMC. This procedure can be expressed by means of the MC@NLO generating functional:

$$\begin{aligned}\mathcal{F}_{\texttt{MC@NLO}} \;=\; & \int d\mathbf{\Phi}_{n+1}\Big\{\mathcal{F}_{\rm SMC}(\mathbf{\Phi}_{n+1})\Big[R(\mathbf{\Phi}_{n+1})-R^{\rm MC}(\mathbf{\Phi}_{n+1})\Big] \\ & +\mathcal{F}_{\rm SMC}(\mathbf{\Phi}_{n})\Big[\frac{B(\mathbf{\Phi}_{n})+V(\mathbf{\Phi}_{n})}{\mathcal{I}_{n}}+R^{\rm MC}(\mathbf{\Phi}_{n+1})-C(\mathbf{\Phi}_{n+1})\Big]\Big\}\,, \qquad (2.9)\end{aligned}$$

where $R^{\rm MC}$ corresponds to the ($\mathcal{O}(\alpha_{\rm S})$-expanded) weight assigned by the shower to an emission with kinematics given by $\mathbf{\Phi}_{n+1}$, whereas $\mathcal{F}_{\rm SMC}$ are the generating functionals of the SMC used. The factor $\mathcal{I}_n$ is defined as

$$\mathcal{I}_{n}=\frac{\int d\mathbf{\Phi}_{n+1}}{\int d\mathbf{\Phi}_{n}}\,, \qquad (2.10)$$

and it guarantees that the Born and soft-virtual terms are correctly normalized when the integration over $\mathbf{\Phi}_{n+1}$ is performed.

In equation (2.9), a mismatch between the coefficient that multiplies the $-R_{\rm MC}$ and $+R_{\rm MC}$ terms is introduced, the latter being multiplied by the generating functional $\mathcal{F}_{\rm SMC}(\mathbf{\Phi}_n)$ instead of $\mathcal{F}_{\rm SMC}(\mathbf{\Phi}_{n+1})$. Nevertheless, the difference between these two generating functionals is of order $\alpha_{\rm S}$, and each of the two multiplies $R^{\rm MC}$, which is of order $\alpha_{\rm S}$ too. Therefore NLO accuracy for both inclusive and exclusive observables is retained, since this mismatch manifests at order $\alpha_{\rm S}^2$. This proves the fact that double-counting is avoided.

To calculate the subtraction term $R^{\rm MC}$, and to evaluate the n-body contributions in the second term of the r.h.s. of eq. (2.9), one needs a mapping $\mathbf{\Phi}_{n+1}\to\mathbf{\Phi}_n$, whose exact properties are dictated by the shower details. Moreover, the shower has to treat both the collinear and the soft limits consistently, since the $R^{\rm MC}(\mathbf{\Phi}_{n+1})$ term itself acts as a local counterterm in the integration of the full real matrix element R, as it can be seen

in the first line of eq. (2.9).[8] If this last property is satisfied, then both the two terms in the square brackets of the r.h.s. of (2.9) have a finite integral, and the generation of unweighted events can be performed.

In practice, the MC@NLO algorithm works in two steps:

1. Generate a set of $\mathbb{H}$ and $\mathbb{S}$ events, obtained by integrating separately the two terms

$$\int d\mathbf{\Phi}_{n+1} \left[R(\mathbf{\Phi}_{n+1}) - R^{\rm MC}(\mathbf{\Phi}_{n+1}) \right] \tag{2.11}$$

and

$$\int d\mathbf{\Phi}_{n+1} \left[\frac{B(\mathbf{\Phi}_n) + V(\mathbf{\Phi}_n)}{\mathcal{I}_n} + R^{\rm MC}(\mathbf{\Phi}_{n+1}) - C(\mathbf{\Phi}_{n+1}) \right] , \tag{2.12}$$

and generating unweighted events accordingly. Events generated according to eq. (2.11) are called *Hard* ($\mathbb{H}$) events, and have $(n+1)$-body kinematics. Instead, kinematic configurations generated using eq. (2.12) are projected onto n-body ones, according to the mapping discussed above. In the MC@NLO jargon, these events are called *Standard* ($\mathbb{S}$) events.

2. Apply the shower algorithm to the generated partonic events.

In the above discussion we have just outlined how the MC@NLO method works, focusing only on some points. In the following we summarize the main benefits of the method, that are discussed with great accuracy in the original papers:

- Both inclusive and exclusive infrared-safe observables have NLO accuracy.
- Collinear emissions are resummed at the leading-logarithmic level.
- The double-logarithmic region is treated correctly if the SMC code used for showering has this capability.

Since MC@NLO uses the HERWIG shower, this last requirement is satisfied, owing to the fact that this shower is based upon angular-ordered branchings. Hence, in eq. (2.9), the generating functionals are the HERWIG ones.

As already stated, the MC@NLO method has been largely tested with success in a sequence of increasingly complicated processes. However, the method has some drawbacks, that we list in the following:

[8] Therefore, in the collinear limit, for example, the subtraction term has the property

$$R^{\rm MC}(\mathbf{\Phi}_{n+1})\; d\Phi_{\rm rad} \simeq B(\mathbf{\Phi}_n)\; \frac{\alpha_{\rm S}}{2\pi} \frac{1}{t} P(z)\; d\Phi^{\rm MC}_{\rm rad}\,.$$

- The differential cross sections for $\mathbb{H}$ and $\mathbb{S}$ events (eq. (2.11) and (2.12)) are not strictly positive. Therefore, MC@NLO can generate negative-weighted events. For the processes implemented so far, negative-weighted events are about 10–15% of the total. Their presence does not imply a negative cross section, since at the end physical distributions turn out to be positive. However, this requires, in general, a number of events higher than those required for an ordinary SMC to produce smooth distributions.
- The method is obviously SMC dependent, due to the presence of the shower subtraction term.

Furthermore, there are other minor issues. For example, in MC@NLO, medium-high-p_T emissions do not come entirely from $\mathbb{H}$ events, but sometimes also from $\mathbb{S}$ events, when the shower generates an hard emission. Although this is a subleading effect, it can turn out to be numerically relevant. In fact, we attribute the presence of dips in some MC@NLO distributions exactly to this feature. More details will be given in chapter 3 and 4.

2.3 The POWHEG method

In this section, we describe in detail the POWHEG method, first introduced in [1]. The method can be seen as an alternative to MC@NLO. In fact, while keeping the same features listed above, it overcomes the problem of negative-weighted events and, moreover, it is not SMC specific.

The basic idea of the method is to generate the hardest radiation of each event with NLO accuracy, by using always the exact NLO matrix elements, in a framework that does not depend upon the shower algorithm. For this reason, the method is fully independent from the SMC: the shower is only requested to implement vetoed emissions, which is a standard requirement for modern SMC generators. This corresponds to impose that all the following emissions have lower transverse momenta, and thus the accuracy of infrared-safe observables is possibly affected only by terms that are of Next-to-Next-to-Leading-Order (NNLO). In this way, the matching problem is considerably simplified, since a detailed examination of the shower properties used in the SMC is no longer needed. Furthermore, at variance with MC@NLO, POWHEG generates only positive-weighted events, as the acronym suggests.

In the following we give a detailed description of the method, which parallels the one given in [2]. We will concentrate only on the aspects relevant for the implementations described in this thesis. More advanced issues can be found in the aforementioned paper and in ref. [1].

2.3.1 The POWHEG master formula

In this first subsection, we give a simple illustration of the method, ignoring, for the moment, the complications due to the presence of several singular regions and of collinear remnants terms in the NLO cross section. This will allow to understand easily what are the main differences of this approach with respect to the MC@NLO one.

We begin by defining the $\bar{B}$ function, that is the inclusive cross section at fixed underlying Born variables. It is defined as follows:

$$\bar{B}(\mathbf{\Phi}_n) = B(\mathbf{\Phi}_n) + V(\mathbf{\Phi}_n) + \left[\int d\Phi_{\rm rad}\left[R(\mathbf{\Phi}_{n+1}) - C(\mathbf{\Phi}_{n+1})\right]\right]^{\bar{\mathbf{\Phi}}_n=\mathbf{\Phi}_n}, \tag{2.13}$$

where we have assumed that $d\mathbf{\Phi}_{n+1} = d\bar{\mathbf{\Phi}}_n d\Phi_{\rm rad}$, which is admissible as long as adequate variables are chosen to parametrize the $\mathbf{\Phi}_{n+1}$ phase space. We notice that, to calculate this function, one needs to integrate the (subtracted) real term by keeping the underlying n-body kinematics $\bar{\mathbf{\Phi}}_n$ fixed and equal to the Born one ($\mathbf{\Phi}_n$). This procedure is exactly the opposite of the one adopted to build real counterterms from $(n+1)$-body kinematics, when performing NLO calculations in the subtraction scheme, according to the mapping procedure of eq. (1.59). For this reason, in the POWHEG language, this procedure is often called *inverse construction*.

Next we introduce the (POWHEG) Sudakov form factor[9]

$$\Delta\left(\mathbf{\Phi}_n, p_{\rm T}\right) = \exp\left\{-\int \frac{\left[d\Phi_{\rm rad}\, R(\mathbf{\Phi}_{n+1})\, \theta(k_{\rm T}\left(\mathbf{\Phi}_{n+1}\right) - p_{\rm T})\,\right]^{\bar{\mathbf{\Phi}}_n=\mathbf{\Phi}_n}}{B(\mathbf{\Phi}_n)}\right\}. \tag{2.14}$$

The function $k_{\rm T}\left(\mathbf{\Phi}_{n+1}\right)$ should be equal, near the singular limit, to the transverse momentum of the emitted parton relative to the emitting one. Further details on the exact properties of the function $k_{\rm T}\left(\mathbf{\Phi}_{n+1}\right)$ will be discussed later. The POWHEG cross section for the generation of the hardest event is then

$$d\sigma = \bar{B}(\mathbf{\Phi}_n)\, d\mathbf{\Phi}_n \left\{\Delta\left(\mathbf{\Phi}_n, p_{\rm T}^{\rm min}\right) + \Delta\left(\mathbf{\Phi}_n, k_{\rm T}\left(\mathbf{\Phi}_{n+1}\right)\right)\, \frac{R\left(\mathbf{\Phi}_{n+1}\right)}{B(\mathbf{\Phi}_n)} d\Phi_{\rm rad}\right\}_{\bar{\mathbf{\Phi}}_n=\mathbf{\Phi}_n}, \tag{2.15}$$

where it is assumed that values of $k_{\rm T}\left(\mathbf{\Phi}_{n+1}\right) < p_{\rm T}^{\rm min}$ are not allowed. Equation (2.15) is

[9] We recall that a similar Sudakov form factor is also used in PYTHIA for weak vector-bosons and for Higgs via gluon fusion production, in order to implement a matrix-element matching for the first emission in the shower [45,56]. This is the reason why, in single vector-boson production, the high-$p_{\rm T}$ tail of PYTHIA result is in good agreement with the POWHEG one (see sec. 3.3).

the reference equation of the POWHEG method, and, together with the recipes to shower a partonic configuration accordingly generated (which will be described later), it can be considered the analogous of the MC@NLO formula given in eq. (2.9). From the above cross section, we can trace the main properties of the method:

- At large k_{T}, the cross section in eq. (2.15) coincides with the NLO one, up to NNLO terms.
- Infrared-safe observables are correctly described at the NLO. In fact, also the integral of eq. (2.15) around the small k_{T} region has the requested NLO accuracy.
- At small k_{T}, formula (2.15) behaves no worse than standard SMC generators. Hence, the leading-logarithm accuracy of the shower will be kept when events generated according to eq. (2.15) are fed to a p_{T}-vetoed shower.

The basic requirements listed at the beginning of section 2.2, for the inclusion of NLO corrections in a SMC, are then fulfilled. Explicit proofs of the first two properties will be given later, in sec. 2.3.4. Concerning the last point, more details are given in the following subsection.

Before going on, from eq. (2.13) and (2.15) we can also easily understand the reason why the POWHEG method generates only positive-weighted events. Each event generated according to (2.15) has a weight given by the value assumed by the $\bar{B}$ function in the n-body kinematic point $\mathbf{\Phi}_n$, since the term in the curly bracket of eq. (2.15) does not change this weight, being just a sum of emission probabilities. Therefore, events are positive-weighted if the $\bar{B}$ function is non-negative, which is a condition that has to hold: a negative value would mean that the $\mathcal{O}(\alpha_{\mathrm{S}})$ terms are negative, and larger than the Born term in magnitude, which is clearly something that can not happen in a meaningful perturbative series.

2.3.2 Showering the POWHEG events

The POWHEG formula (2.15) can be used to generate n or $(n+1)$-body partonic events. Then, these events have to be showered by a SMC program, in such a way that all the subsequent emissions are softer with respect to the one generated with POWHEG.

For a p_{T}-ordered shower, we simply require that the shower is started with an upper limit on the evolution variable equal to the transverse momentum of the POWHEG event. For showers ordered differently, we have to explicitly suppress emissions harder than the POWHEG one. This can be easily obtained by imposing a p_{T}-veto on the shower, which is a feature implemented in modern SMC generators. In this way, for *non* angular-ordered

showers, the accuracy of the final result in the soft and collinear regions corresponds to the shower's one. Thus, when POWHEG is interfaced to shower programs that use transverse-momentum ordering, results have double-log accuracy if the SMC is double-log accurate.[10]

Instead, when interfacing POWHEG to angular-ordered SMC programs, such as HERWIG, the double-log accuracy of the SMC is not sufficient to guarantee the double-log accuracy of the whole result, because some extra soft radiation must also be included. In fact, angular ordered SMC programs may generate soft radiation before generating the radiation with the largest p_{T}, while POWHEG works by generating it first. To recover the full double-log accuracy, one should add back this soft, wide-angle radiation by implementing a *vetoed-truncated* shower, whose properties have been described in ref. [1].

At present, the effect of the inclusion of vetoed-truncated showers has been studied only in the POWHEG implementations included in the HERWIG++ code. Although some improvements of the results have been observed for e^+e^- collisions, at present there is no evidence that the effect of not-including vetoed-truncated showers may have a significant impact on final results. Results reported in this thesis have been obtained without using truncated showers, in case of POWHEG interfaced with HERWIG.

In the following, we will give the exact formulation of the POWHEG method.

2.3.3 Detailed description of the POWHEG method

Flavours and singular regions separation

In order to implement the POWHEG method, the separation of the real terms into singular regions and the kinematics that associates a given $(n+1)$-body singular region with an n-body one have to be specified.

Furthermore, flavours should be carefully tracked, since in SMC programs different flavour structures always give rise to different events. We thus distinguish the contributions to the cross section also by their flavour structures, which are determined by the flavours of the incoming and outgoing partons. The index f_b labels the flavour structure of the n-body processes: hence we write B^{f_b} and V^{f_b} to distinguish among the various Born and soft-virtual contributions.

Contributions to the real cross section have to be distinguished both for the flavour structure and for the singular region on which they are projected. We use the index α_{r} to label both these properties: hence a given value of α_{r} labels a particular contribution to the real cross section that diverges in only one singular region of integration and has a

[10] For example, for the new showering formalism implemented in PYTHIA 6.4 [35], accurate soft resummation should be achieved at least in the large N_{c} limit.

specific flavour structure. We then write

$$R = \sum_{\alpha_r} R^{\alpha_r} . \tag{2.16}$$

A similar separation also holds for the counterterms, so that they are labelled by an index α_r, too.

In the FKS case, for example, the α_r contributions are obtained by first separating the real contribution R into the sum of all its flavour components. For each flavour component, one constructs the $\mathcal{S}$ functions, according to the procedure outlined in section 1.2.3, and then multiplies it by the factors $\mathcal{S}_i$ or $\mathcal{S}_{ij}$.

In the CS case, for each flavour component of the real contribution, one can define

$$\mathcal{S}_{\alpha_r} = \frac{\mathcal{D}_{\alpha_r}}{\sum_{\alpha_r'} \mathcal{D}_{\alpha_r'}} , \tag{2.17}$$

where α_r identifies one of the dipoles needed to integrate the given real contribution, once that a flavour structure has been fixed. The sum runs over all the dipoles needed for that "flavor-projected" real term. Notice that, by doing so, one can have more than one term associated to the same kinematic singular region, since dipoles are labelled also by the spectator index, as we already noticed in 1.2.4.[11]

At this point, there is only one underlying n-body process, with a specific flavour structure, in correspondence to each real contribution labelled by α_r. In fact, if the singular region is collinear, the index f_b is found by merging together the two collinear particles, by conserving the flavour. If the singular region is soft, f_b is found by removing the soft gluon.[12] A flavour structure has to be defined for collinear remnants too, which we label by the index $\alpha_{\circledast}$. The underlying n-body flavour structure is given in this case by the structure of the n-body matrix element that enters in the collinear remnant itself, as can be easily noticed by looking to eqs. (1.117) and (1.123). In the following, we denote $\{\alpha_r | f_b\}$ and $\{\alpha_{\circledast} | f_b\}$ the set of all values of the indices α_r and $\alpha_{\circledast}$ that have the flavour structure of the underlying n-body-configuration equal to f_b.

When the full flavour structure is taken in consideration, according to the notation

[11] We note here that, despite of the simplicity of eq. (2.17), when the CS subtraction scheme is used in POWHEG for processes whose Born cross section can diverge, such as $Z + 1$ jet, the isolation of singular regions can require a more careful treatment with respect to this quick example. Further details will be given in sec. 2.3.5.

[12] It is worthwhile to observe that, for non singular limits, the flavour structure of the underlying n-body process is undefined.

just introduced, eq. (1.78) can be written as

$$\langle O\rangle = \sum_{f_b}\left[\langle O\rangle_B^{f_b} + \sum_{\alpha_{\rm r}\in\{\alpha_{\rm r}|f_b\}}\langle O\rangle_R^{\alpha_{\rm r}} + \sum_{\alpha_\oplus\in\{\alpha_\oplus|f_b\}}\langle O\rangle_{G_\oplus}^{\alpha_\oplus} + \sum_{\alpha_\ominus\in\{\alpha_\ominus|f_b\}}\langle O\rangle_{G_\ominus}^{\alpha_\ominus}\right] \tag{2.18}$$

$$\langle O\rangle_B^{f_b} = \int d\mathbf{\Phi}_n\, O_n(\mathbf{\Phi}_n)\,\Big[B\left(\mathbf{\Phi}_n\right) + V\left(\mathbf{\Phi}_n\right)\Big]_{f_b}\,, \tag{2.19}$$

$$\langle O\rangle_{G_{\circledast}}^{\alpha_{\circledast}} = \int d\mathbf{\Phi}_{n,\circledast}\, O_n\big(\bar{\mathbf{\Phi}}_n\big)\; G_{\circledast}^{\alpha_{\circledast}}(\mathbf{\Phi}_{n,\circledast})\;, \tag{2.20}$$

$$\langle O\rangle_R^{\alpha_{\rm r}} = \int d\mathbf{\Phi}_{n+1}\Big[O_{n+1}(\mathbf{\Phi}_{n+1})\,R(\mathbf{\Phi}_{n+1}) - O_n\big(\bar{\mathbf{\Phi}}_n\big)\,C(\mathbf{\Phi}_{n+1})\Big]_{\alpha_{\rm r}}\,. \tag{2.21}$$

where we used a straightforward extension of the context square brackets (eq. (1.60)). According to ref. [1], we now perform the following manipulation

$$\langle O\rangle_R^{\alpha_{\rm r}} = \langle O\rangle_{R,n}^{\alpha_{\rm r}} + \langle O\rangle_{R,n+1}^{\alpha_{\rm r}}\,, \tag{2.22}$$

$$\langle O\rangle_{R,n}^{\alpha_{\rm r}} = \left[\int d\mathbf{\Phi}_{n+1}\, O_n\big(\bar{\mathbf{\Phi}}_n\big)\,\Big\{R\left(\mathbf{\Phi}_{n+1}\right) - C\left(\mathbf{\Phi}_{n+1}\right)\Big\}\right]_{\alpha_{\rm r}}\,, \tag{2.23}$$

$$\langle O\rangle_{R,n+1}^{\alpha_{\rm r}} = \left[\int d\mathbf{\Phi}_{n+1}\, R\left(\mathbf{\Phi}_{n+1}\right)\,\Big\{O_{n+1}(\mathbf{\Phi}_{n+1}) - O_n\big(\bar{\mathbf{\Phi}}_n\big)\Big\}\right]_{\alpha_{\rm r}}\,. \tag{2.24}$$

All the term that have n-body kinematics should be treated together, by putting them into an n-body kinematics term, that is called $\bar{B}$. We already introduced this function in eq. (2.13). Here, we just carefully distinguish the contributions to $\bar{B}$ according to their flavour structure. We start by rewriting eqs. (2.20), (2.23) and (2.24) as

$$\langle O\rangle_{G_{\circledast}}^{\alpha_{\circledast}} = \int d\bar{\mathbf{\Phi}}_n\, O_n\big(\bar{\mathbf{\Phi}}_n\big)\;\frac{dz}{z}\,G_{\circledast}^{\alpha_{\circledast}}\left(\mathbf{\Phi}_{n,\circledast}\right)\;, \tag{2.25}$$

$$\langle O\rangle_{R,n}^{\alpha_{\rm r}} = \left[\int d\bar{\mathbf{\Phi}}_n\, O_n\big(\bar{\mathbf{\Phi}}_n\big)\;d\Phi_{\rm rad}\,\left\{R\left(\mathbf{\Phi}_{n+1}\right) - C\left(\mathbf{\Phi}_{n+1}\right)\right\}\right]_{\alpha_{\rm r}}\,, \tag{2.26}$$

$$\langle O\rangle_{R,n+1}^{\alpha_{\rm r}} = \left[\int d\bar{\mathbf{\Phi}}_n\, d\Phi_{\rm rad}\, R\left(\mathbf{\Phi}_{n+1}\right)\left\{O_{n+1}\left(\mathbf{\Phi}_{n+1}\right) - O_n\big(\bar{\mathbf{\Phi}}_n\big)\right\}\right]_{\alpha_{\rm r}}\,. \tag{2.27}$$

Then, we write the $\bar{B}$ functions, one for each flavour configuration, as

$$\begin{aligned}\bar{B}^{f_b}(\mathbf{\Phi}_n) &= \left[B\left(\mathbf{\Phi}_n\right)+V\left(\mathbf{\Phi}_n\right)\right]_{f_b}+\sum_{\alpha_{\mathrm{r}}\in\{\alpha_{\mathrm{r}}|f_b\}}\int\left[d\Phi_{\mathrm{rad}}\left\{R\left(\mathbf{\Phi}_{n+1}\right)-C\left(\mathbf{\Phi}_{n+1}\right)\right\}\right]_{\alpha_{\mathrm{r}}}^{\bar{\mathbf{\Phi}}_n^{\alpha_{\mathrm{r}}}=\mathbf{\Phi}_n}\\ &+\sum_{\alpha_\oplus\in\{\alpha_\oplus|f_b\}}\int\frac{dz}{z}\,G_\oplus^{\alpha_\oplus}\left(\mathbf{\Phi}_{n,\oplus}\right)+\sum_{\alpha_\ominus\in\{\alpha_\ominus|f_b\}}\int\frac{dz}{z}\,G_\ominus^{\alpha_\ominus}\left(\mathbf{\Phi}_{n,\ominus}\right)\,,\end{aligned}\tag{2.28}$$

so that

$$\int d\mathbf{\Phi}_n\,O_n(\mathbf{\Phi}_n)\;\bar{B}^{f_b}(\mathbf{\Phi}_n)=\langle O\rangle_B^{f_b}+\sum_{\alpha_{\mathrm{r}}\in\{\alpha_{\mathrm{r}}|f_b\}}\langle O\rangle_{R,n}^{\alpha_{\mathrm{r}}}+\sum_{\alpha_\oplus\in\{\alpha_\oplus|f_b\}}\langle O\rangle_{G_\oplus}^{\alpha_\oplus}+\sum_{\alpha_\ominus\in\{\alpha_\ominus|f_b\}}\langle O\rangle_{G_\ominus}^{\alpha_\ominus}\,.\tag{2.29}$$

The exact NLO expression for the expectation value of O reads then

$$\begin{aligned}\langle O\rangle &= \sum_{f_b}\int d\mathbf{\Phi}_n\,O_n(\mathbf{\Phi}_n)\;\bar{B}^{f_b}(\mathbf{\Phi}_n)\\ &+ \sum_{\alpha_{\mathrm{r}}}\left[\int d\bar{\mathbf{\Phi}}_n\;d\Phi_{\mathrm{rad}}\,R\left(\mathbf{\Phi}_{n+1}\right)\left\{O_{n+1}\left(\mathbf{\Phi}_{n+1}\right)-O_n\left(\bar{\mathbf{\Phi}}_n\right)\right\}\right]_{\alpha_{\mathrm{r}}}.\end{aligned}\tag{2.30}$$

In sec. 2.3.4 we will show that the $\mathcal{O}(\alpha_{\mathrm{S}})$ expansion of the full POWHEG formula that we introduce in the following gives the same expression of eq. (2.30) for a generic infrared-safe observable.

POWHEG formula

The POWHEG Sudakov form factors have to be labelled with the underlying Born flavour index f_b:

$$\Delta^{f_b}(\mathbf{\Phi}_n,p_{\mathrm{T}})=\exp\left\{-\sum_{\alpha_{\mathrm{r}}\in\{\alpha_{\mathrm{r}}|f_b\}}\int\frac{\left[d\Phi_{\mathrm{rad}}\,R\left(\mathbf{\Phi}_{n+1}\right)\,\theta\left(k_{\mathrm{T}}(\mathbf{\Phi}_{n+1})-p_{\mathrm{T}}\right)\right]_{\alpha_{\mathrm{r}}}^{\bar{\mathbf{\Phi}}_n^{\alpha_{\mathrm{r}}}=\mathbf{\Phi}_n}}{B^{f_b}\left(\mathbf{\Phi}_n\right)}\right\}.\tag{2.31}$$

Notice that the identification $\bar{\mathbf{\Phi}}_n^{\alpha_{\mathrm{r}}}=\mathbf{\Phi}_n$ is a sensible one only if the underlying n-body-process flavour structure of α_{r} is equal to f_b. In eq. (2.31), $k_{\mathrm{T}}^{\alpha_{\mathrm{r}}}$ is a function of the kinematics variables that depends upon the particular singular region we are considering:

- For ISC singularities, k_{T} has to be proportional to the transverse momentum of the emitted parton with respect to the beam axis in the collinear limit, and coincide

with it in the soft *and* collinear limit.

- For FSC singularities, if the partons that are becoming collinear have momenta k_i and k_j, a proper choice for k_{T} is the (spatial) component of k_i (or equivalently k_j) orthogonal to the sum $\vec{k}_i+\vec{k}_j$. Other choices are possible, the important requirement being always that the soft and collinear limit has to be approached exactly by the function chosen for k_{T}. We will come back on this point later, in sec. 2.3.4. For these FSC regions, it is also important that the transverse momentum is computed in the CM frame of the colliding partons, so that unnaturally small or big values, possibly generated by longitudinal boosts, are avoided.

The final formula for the full POWHEG cross section is

$$\begin{aligned} d\sigma &= \sum_{f_b} \bar{B}^{f_b}(\mathbf{\Phi}_n)\, d\mathbf{\Phi}_n \Bigg\{ \Delta^{f_b}\left(\mathbf{\Phi}_n, p_{\mathrm{T}}^{\min}\right) \\ &\quad + \sum_{\alpha_{\mathrm{r}}\in\{\alpha_{\mathrm{r}}|f_b\}} \frac{\left[d\Phi_{\mathrm{rad}}\; \theta\left(k_{\mathrm{T}}\left(\mathbf{\Phi}_{n+1}\right) - p_{\mathrm{T}}^{\min}\right) \Delta^{f_b}(\mathbf{\Phi}_n, k_{\mathrm{T}})\; R\left(\mathbf{\Phi}_{n+1}\right) \right]_{\alpha_{\mathrm{r}}}^{\bar{\mathbf{\Phi}}_n^{\alpha_{\mathrm{r}}}=\mathbf{\Phi}_n}}{B^{f_b}(\mathbf{\Phi}_n)} \Bigg\}. \end{aligned} \tag{2.32}$$

The $p_{\mathrm{T}}^{\min}$ value introduced here is a lower cut-off on the transverse momentum, that is needed in order to avoid to reach unphysical values of the strong coupling constant and of the parton-density functions.

The POWHEG cross section (eq. (2.32)) looks very complex. Nevertheless, to handle with it numerically, one needs to use few well-known Monte Carlo techniques. We devote the last section of this chapter (sec. 2.3.6) to describe in some detail these techniques.

Interfacing to Parton Showers

The POWHEG algorithm generates the kinematics and flavour configuration of the hardest-emission event. The event should be fed into a SMC using the *Les Houches Interface for User Processes* [57] (LHIUP from now on), which specifies how to pass these informations to the SMC. As already discussed, one asks also that no events harder than the one generated by POWHEG are generated by the SMC. This is achieved by setting the variable SCALUP of the LHIUP equal to the k_{T} of the POWHEG event.

The LHIUP also requires that the color connections of the hard event (in the large N_c limit) should be specified. As it stands, POWHEG formula does not generate these large-N_c color structures, which are however really needed only to reach large-N_{c} NLL accuracy for

processes with more than three color connected partons at the Born level.[13] For processes with a simpler leading order color structure, the generation of the color configuration can be performed after the POWHEG event has been generated. A possible approach goes as follows:

- Generate the POWHEG event in the standard way.
- Compute the different (planar) color contributions to the Born cross section, at the kinematics of the generated underlying Born configuration.
- Pick an underlying Born color configuration, with a probability proportional to its weight with respect to all the other configurations.
- If no radiation has been generated, this is the color structure of the event.
- If radiation has been generated, POWHEG has also generated an $\alpha_{\rm r}$ index, specifying a singular region. In this case, we always assume that the emitted parton is (planar) color-connected to the emitter. This fully specifies the planar color structure of the generated event.

We notice that this method only requires the calculation of the planar color-structures of the Born term. For the implementations presented in this thesis, this was even not needed, since the Born terms were exactly planar, due to their electroweak nature. Therefore, color connections have been assigned just according to the generated index $\alpha_{\rm r}$.

Another method (which is usually implemented in MC@NLO) works by computing all the planar color contributions to R, and choosing one of them in proportion to its relative weight. If a Born-like event is generated, the same procedure has to be carried out for B.

2.3.4 Accuracy of the POWHEG method

This subsection is dedicated to comment the accuracy of the POWHEG method. We first give the explicit, general proof of the NLO accuracy of the POWHEG formula, that is valid both for inclusive and exclusive observables. Some remarks on the logarithmic accuracy achievable in the soft/collinear regions will be given later.

[13] In [2] a modification of the POWHEG Sudakov form factor has been also formulated, in order to generate these structures consistently.

NLO accuracy of the POWHEG formula

In the following, we want to prove that formula (2.32), when used to compute an infrared-safe observable, yields the correct NLO accuracy. For ease of notation, we omit the $\theta\left(k_{\mathrm{T}}-p_{\mathrm{T}}^{\min}\right)$ factor, always assuming that this factor is present when real radiation is generated.
If we apply formula (2.32) to an infrared-safe observable O, we have

$$\begin{aligned}
\langle O\rangle &= \sum_{f_b}\int d\mathbf{\Phi}_n\,\bar{B}^{f_b}(\mathbf{\Phi}_n)\Bigg\{\Delta^{f_b}\left(\mathbf{\Phi}_n,p_{\mathrm{T}}^{\min}\right)O_n(\mathbf{\Phi}_n)\\
&\quad+\sum_{\alpha_{\mathrm{r}}\in\{\alpha_{\mathrm{r}}|f_b\}}\frac{\left[\int d\Phi_{\mathrm{rad}}\;\Delta^{f_b}(\mathbf{\Phi}_n,k_{\mathrm{T}})\;R\left(\mathbf{\Phi}_{n+1}\right)O_{n+1}(\mathbf{\Phi}_{n+1})\right]_{\alpha_{\mathrm{r}}}^{\bar{\mathbf{\Phi}}_n^{\alpha_{\mathrm{r}}}=\mathbf{\Phi}_n}}{B^{f_b}(\mathbf{\Phi}_n)}\Bigg\}\\
&= \sum_{f_b}\int d\mathbf{\Phi}_n\bar{B}^{f_b}(\mathbf{\Phi}_n)\\
&\quad\times\Bigg\{\left[\Delta^{f_b}\left(\mathbf{\Phi}_n,p_{\mathrm{T}}^{\min}\right)+\sum_{\alpha_{\mathrm{r}}\in\{\alpha_{\mathrm{r}}|f_b\}}\frac{\left[\int d\Phi_{\mathrm{rad}}\;\Delta^{f_b}(\mathbf{\Phi}_n,k_{\mathrm{T}})\;R\left(\mathbf{\Phi}_{n+1}\right)\right]_{\alpha_{\mathrm{r}}}^{\bar{\mathbf{\Phi}}_n^{\alpha_{\mathrm{r}}}=\mathbf{\Phi}_n}}{B^{f_b}(\mathbf{\Phi}_n)}\right]O_n(\mathbf{\Phi}_n)\\
&\quad+\sum_{\alpha_{\mathrm{r}}\in\{\alpha_{\mathrm{r}}|f_b\}}\frac{\left[\int d\Phi_{\mathrm{rad}}\;\Delta^{f_b}(\mathbf{\Phi}_n,k_{\mathrm{T}})\;R\left(\mathbf{\Phi}_{n+1}\right)\left(O_{n+1}(\mathbf{\Phi}_{n+1})-O_n(\mathbf{\Phi}_n)\right)\right]_{\alpha_{\mathrm{r}}}^{\bar{\mathbf{\Phi}}_n^{\alpha_{\mathrm{r}}}=\mathbf{\Phi}_n}}{B^{f_b}(\mathbf{\Phi}_n)}\Bigg\},
\end{aligned}\tag{2.33}$$

where, in the second equality, we have simply added and subtracted the same term proportional to $R\left(\mathbf{\Phi}_{n+1}\right)O_n(\mathbf{\Phi}_n)$. We now show that the term in the large squared bracket in the third member of eq. (2.33) is equal to 1. In fact

$$\begin{aligned}
&\sum_{\alpha_{\mathrm{r}}\in\{\alpha_{\mathrm{r}}|f_b\}}\frac{\left[\int d\Phi_{\mathrm{rad}}\;\Delta^{f_b}(\mathbf{\Phi}_n,k_{\mathrm{T}})\;R\left(\mathbf{\Phi}_{n+1}\right)\right]_{\alpha_{\mathrm{r}}}^{\bar{\mathbf{\Phi}}_n^{\alpha_{\mathrm{r}}}=\mathbf{\Phi}_n}}{B^{f_b}(\mathbf{\Phi}_n)}\\
&\qquad=\int_{p_{\mathrm{T}}^{\min}}^{\infty}dp_{\mathrm{T}}\sum_{\alpha_{\mathrm{r}}\in\{\alpha_{\mathrm{r}}|f_b\}}\frac{\left[\int d\Phi_{\mathrm{rad}}\;\delta(k_{\mathrm{T}}-p_{\mathrm{T}})\,\Delta^{f_b}(\mathbf{\Phi}_n,p_{\mathrm{T}})\;R\left(\mathbf{\Phi}_{n+1}\right)\right]_{\alpha_{\mathrm{r}}}^{\bar{\mathbf{\Phi}}_n^{\alpha_{\mathrm{r}}}=\mathbf{\Phi}_n}}{B^{f_b}(\mathbf{\Phi}_n)}\\
&\qquad=-\int_{p_{\mathrm{T}}^{\min}}^{\infty}dp_{\mathrm{T}}\;\Delta^{f_b}(\mathbf{\Phi}_n,p_{\mathrm{T}})\frac{d}{dp_{\mathrm{T}}}\sum_{\alpha_{\mathrm{r}}\in\{\alpha_{\mathrm{r}}|f_b\}}\frac{\left[\int d\Phi_{\mathrm{rad}}\;\theta(k_{\mathrm{T}}-p_{\mathrm{T}})\;R\left(\mathbf{\Phi}_{n+1}\right)\right]_{\alpha_{\mathrm{r}}}^{\bar{\mathbf{\Phi}}_n^{\alpha_{\mathrm{r}}}=\mathbf{\Phi}_n}}{B^{f_b}(\mathbf{\Phi}_n)}\\
&\qquad=\int_{p_{\mathrm{T}}^{\min}}^{\infty}dp_{\mathrm{T}}\;\frac{d}{dp_{\mathrm{T}}}\Delta^{f_b}(\mathbf{\Phi}_n,p_{\mathrm{T}})=1-\Delta^{f_b}\left(\mathbf{\Phi}_n,p_{\mathrm{T}}^{\min}\right)\;,
\end{aligned}\tag{2.34}$$

where we have used the fact that $\Delta^{f_b}(\mathbf{\Phi}_n,\infty)=1$. Furthermore, in the last term in the

large curly bracket of eq. (2.33), small k_{T} values in the integral are suppressed by the $O_{n+1}(\mathbf{\Phi}_{n+1}) - O_n(\mathbf{\Phi}_n)$ factor, and therefore we can replace $\Delta^{f_b} \to 1$ and $B \to \bar{B}$ up to higher orders in α_{S}. Equation (2.33) thus reduces to

$$\begin{aligned}\langle O \rangle &= \sum_{f_b} \int d\mathbf{\Phi}_n \Bigg\{ \bar{B}^{f_b}(\mathbf{\Phi}_n)\, O_n(\mathbf{\Phi}_n) \\ &+ \sum_{\alpha_{\mathrm{r}} \in \{\alpha_{\mathrm{r}} | f_b\}} \left[\int d\Phi_{\mathrm{rad}}\, R\left(\mathbf{\Phi}_{n+1}\right) \left(O_{n+1}(\mathbf{\Phi}_{n+1}) - O_n(\mathbf{\Phi}_n)\right) \right]_{\alpha_{\mathrm{r}}}^{\bar{\mathbf{\Phi}}_n^{\alpha_{\mathrm{r}}} = \mathbf{\Phi}_n} \Bigg\}, \end{aligned} \tag{2.35}$$

up to NNLO corrections. The restriction $\theta(k_{\mathrm{T}} - p_{\mathrm{T}}^{\mathrm{min}})$ can now be dropped from the $d\Phi_{\mathrm{rad}}$ integration, its effect being suppressed by powers of $p_{\mathrm{T}}^{\mathrm{min}}$, and eq. (2.35) is immediately found to agree with eq. (2.30), thus concluding our proof.

We notice that the above argument shows also that the POWHEG method is not affected by double-counting, because at order α_{S} the expectation value of an observable calculated according to the POWHEG formula is equal to the NLO value.

Scale choices and POWHEG logarithmic accuracy

The POWHEG method deals only with the generation of the hardest emission. Subsequent radiation is generated by the SMC to which POWHEG is interfaced, and therefore, in general, only LL accuracy will be achieved. However, for exclusive observables that are sensitive to the hardest radiation, an improvement of the accuracy of the POWHEG Sudakov form factor can produce benefits. In the following we describe how this can be obtained.

The factorization (μ_{F}) and renormalization (μ_{R}) scales adopted in the definition of $\bar{B}$, eq. (2.28), and in the definition of the Sudakov form factors, eq. (2.31), are different. In the choice of the scales entering in $\bar{B}$, there is the usual freedom, typical of NLO calculations: scales have to be of the same order of the typical momentum scale of the process. In the Sudakov exponents, instead, one must adopt a scale of the order of the radiation transverse-momentum k_{T}. In fact, in [2, 58] it has been shown that, with this choice, the POWHEG Sudakov form factor in eq. (2.31) is equal to the DDT [59] Sudakov form factor, at least to the leading-logarithmic level.

Furthermore, if the number of colored particle in the Born term is less or equal than three, then, with the same prescription described in sec. 1.3.7 for the running of the α_{S} coupling in the Sudakov form factor (eq. (1.174)), one can reach NLL accuracy, provided that the functional form of k_{T} is such that it reduces to the exact value of the transverse momentum in the soft *and* collinear limit.

Finally, if the number of color-connected legs in the Born term is more than three,

then, with the above rules, NLL accuracy can be reached only in the large N_c limit, by generalizing the POWHEG Sudakov form factor given in eq. (2.31), following the recipes given in sec. 4.4 of [2].

2.3.5 The POWHEG method in the FKS and the CS subtraction methods

In this section, we summarize the recipes to build a POWHEG implementation of a process calculated in the FKS or in the CS subtraction scheme. More details will be given in the following chapters, since both these two subtraction approaches have been used.

POWHEG and the FKS subtraction scheme

Despite the technical complication introduced by the presence of plus distributions, the use of the FKS subtraction scheme in POWHEG is quite natural, since, at variance with the CS approach, *each* collinear region is singled out by one (and only one) $\mathcal{S}$ function.

The inverse construction, i.e. the procedure to build the emission variables starting from a point in the Born phase space ($\mathbf{\Phi}_n \to \mathbf{\Phi}_{n+1}$), is described in sec. 5.1-5.2 of [2]. Since we used it for the single-top implementation, we summarize it in sec. 4.1.2. Here we just remark that the FKS method allows also to use the same phase space parameterization, and hence the same inverse construction procedure, for both the $\oplus$ and the $\ominus$ regions.

Moreover, for each singular region, the subtraction terms generated by the action of plus distributions do contain only Born squared amplitude to be evaluated in the same kinematic point of the Born term. Stated otherwise, when POWHEG is used with the FKS approach, there is no need to use underlying-Born kinematics different from the Born one.

POWHEG and the CS subtraction scheme

The use of the CS subtraction method within the POWHEG framework requires more attention. Basically, this is due to the fact that a singular region is not entirely characterized by one single dipole. This immediately leads to separate singular regions by using dipoles, as we did in eq. (2.17). A R^{α_r} contribution would be defined as

$$R^{\alpha_r} = \frac{\mathcal{D}_{\alpha_r}}{\sum_{\alpha'_r} \mathcal{D}_{\alpha'_r}} R \,. \tag{2.36}$$

For complicated processes, this leads to a combinatorics that is much heavier than the one requested in the FKS approach.

Furthermore, since dipoles are not guaranteed to be positive, then it may happen that the sum in the denominator of eq. (2.36) vanishes. This can be solved by using the expression

$$R^{\alpha_r} = \frac{\mathcal{D}^2_{\alpha_r}}{\sum_{\alpha'_r} \mathcal{D}^2_{\alpha'_r}} R\,, \tag{2.37}$$

instead of (2.36) .

Moreover, (some of) the dipoles present in the sum in the denominator contain Born amplitudes to be evaluated in (n-body) kinematic points different from the Born configuration we have started with. In principle this is not a problem. However, for processes which are divergent at the Born level (such as $Z + 1$-jet), it can happen that some of the n-body configurations used to evaluate the dipoles contained in the sum collaps onto a n-body singular configuration, even if the original phase space point $\mathbf{\Phi}_n$ was far from that region.

In standard NLO calculation, an infrared-safe observable O, that vanishes when two singular regions are approached at the same time, would suppress the singular regions of the underlying Born process in the counterterm. In POWHEG instead, this can be solved by writing

$$R^{\alpha_r} = \frac{H\left(\bar{\mathbf{\Phi}}_n^{(\alpha_r)}\right)\mathcal{D}_{\alpha_r}}{\sum_{\alpha'_r} H\left(\bar{\mathbf{\Phi}}_n^{(\alpha'_r)}\right)\mathcal{D}_{\alpha'_r}} R\,, \tag{2.38}$$

where H is a positive function that vanishes when its argument approaches an n-body singular configuration. In this way, we have again

$$\sum_{\alpha_r} R^{\alpha_r} = R\,, \tag{2.39}$$

and now R^{α_r} is singular only in the α_r region.

From the above discussion, despite the fact that the first problems arising with the CS approach can be easily solved, it emerges that the use of the FKS approach seems at least easier than the CS one to implement NLO calculations in the POWHEG scheme.

2.3.6 Generation of the Born and the hardest radiation variables in POWHEG

As anticipated, we conclude this chapter by giving a description of the pratical way to generate partonic events according to the POWHEG master formula given in eq. (2.32).

Generation of the Born variables

As a first step, we need to generate Born-like configurations (points in the $\mathbf{\Phi}_n$ space) and values for the index f_b, distributed according to $\bar{B}^{f_b}(\mathbf{\Phi}_n)\, d\mathbf{\Phi}_n$. To obtain this, normally one would use the hit-and-miss procedure, which is a standard Monte Carlo technique. In practice, one finds an upper bound to the cross section, generates randomly the phase-space point, and accepts it with a probability equal to the ratio of the value of the cross section at the given point over the upper bound value, by comparing this ratio with a random number. In the POWHEG case, however, this is not possible, since each evaluation of the $\bar{B}$ function would require to integrate over the radiation variables, keeping the point in $\mathbf{\Phi}_n$ fixed.

Therefore, we use a slightly different technique: for each singular region, we parametrize the radiation variables $\Phi_{\rm rad}$ in terms of a set of three variables in the unit cube, that we call $X_{\rm rad} = \left\{X^{(1)}_{\rm rad}, X^{(2)}_{\rm rad}, X^{(3)}_{\rm rad}\right\}$. The collinear remnants phase space has an extra variable too (z, in our notation), which we parametrize in terms of one of these three variables, say $X^{(1)}_{\rm rad}$. We then introduce the $\tilde{B}^{f_b}$ function, defined as

$$\begin{aligned}
\tilde{B}^{f_b}(\mathbf{\Phi}_n, X_{\rm rad}) &= \left[B\left(\mathbf{\Phi}_n\right) + V\left(\mathbf{\Phi}_n\right)\right]_{f_b} \\
&+ \sum_{\alpha_{\rm r}\in\{\alpha_{\rm r}|f_b\}} \left[\left|\frac{\partial \Phi_{\rm rad}}{\partial X_{\rm rad}}\right| \left\{R\left(\mathbf{\Phi}_{n+1}\right) - C\left(\mathbf{\Phi}_{n+1}\right)\right\}\right]_{\alpha_{\rm r}}^{\bar{\mathbf{\Phi}}_n^{\alpha_{\rm r}}=\mathbf{\Phi}_n} \\
&+ \sum_{\alpha_\oplus\in\{\alpha_\oplus|f_b\}} \frac{1}{z}\left|\frac{\partial z}{\partial X^{(1)}_{\rm rad}}\right| G^{\alpha_\oplus}_{\oplus}\left(\mathbf{\Phi}_{n,\oplus}\right) + \sum_{\alpha_\ominus\in\{\alpha_\ominus|f_b\}} \frac{1}{z}\left|\frac{\partial z}{\partial X^{(1)}_{\rm rad}}\right| G^{\alpha_\ominus}_{\ominus}\left(\mathbf{\Phi}_{n,\ominus}\right) .
\end{aligned} \tag{2.40}$$

The integral of the $\tilde{B}^{f_b}$ function over the unitary cube corresponds then to $\bar{B}^{f_b}$:

$$\bar{B}^{f_b}(\mathbf{\Phi}_n) = \int_0^1 dX^{(1)}_{\rm rad} \int_0^1 dX^{(2)}_{\rm rad} \int_0^1 dX^{(3)}_{\rm rad}\; \tilde{B}^{f_b}(\mathbf{\Phi}_n, X_{\rm rad})\,. \tag{2.41}$$

We also define

$$\tilde{B}(\mathbf{\Phi}_n, X_{\rm rad}) = \sum_{f_b} \tilde{B}^{f_b}(\mathbf{\Phi}_n, X_{\rm rad})\,. \tag{2.42}$$

The bottleneck is now the generation of $(\mathbf{\Phi}_n,\, X_{\rm rad})$ points distributed as $\tilde{B}(\mathbf{\Phi}_n, X_{\rm rad})$. In fact, to generate according to $\bar{B}^{f_b}(\mathbf{\Phi}_n)$, one first integrates the $\tilde{B}(\mathbf{\Phi}_n, X_{\rm rad})$ function in the full $(\mathbf{\Phi}_n,\, X_{\rm rad})$ space, and then generates $(\mathbf{\Phi}_n,\, X_{\rm rad})$ points distributed as $\tilde{B}(\mathbf{\Phi}_n, X_{\rm rad})$. Then, for each generated phase-space point, one chooses an f_b value with a probability

equal to $\tilde{B}^{f_b}(\mathbf{\Phi}_n, X_{\rm rad})/\tilde{B}(\mathbf{\Phi}_n, X_{\rm rad})$. At this point, the $X_{\rm rad}$ values are discarded, and one has generated the $(\mathbf{\Phi}_n,\, f_b)$ values with probability proportional to $\bar{B}^{f_b}(\mathbf{\Phi}_n)$. In this way, by doing a single $(n+1)$-body phase-space integration, one is able to generate the Born configuration with reasonable efficiency.[14]

The generation of points in $(\mathbf{\Phi}_n,\, X_{\rm rad})$, distributed according to the integrand function $\tilde{B}(\mathbf{\Phi}_n, X_{\rm rad})$, can be performed by using computer programs that, after performing a single integration of a given function (typically with an adaptive method), can efficiently generate according to the function itself, i.e. generate unweighted events, in our language. One such popular program is the `BASES/SPRING` package [60]. More recently, another package, called `MINT` [61], has become available, and this is the package that we use in our `POWHEG` implementations.

Generation of the hardest-radiation variables

Given the Born kinematics $(\mathbf{\Phi}_n,\, f_b)$, we must now generate the hardest-radiation configuration, characterized by $(\alpha_{\rm r},\, \Phi_{\rm rad}^{\alpha_{\rm r}})$, with $\alpha_{\rm r} \in \{\alpha_{\rm r}|f_b\}$, with probability

$$\left[\frac{R\left(\mathbf{\Phi}_{n+1}\right)}{B^{f_b}(\mathbf{\Phi}_n)}\,\Delta^{f_b}(\mathbf{\Phi}_n, k_{\rm T}\left(\mathbf{\Phi}_{n+1}\right))\right]_{\alpha_{\rm r}}^{\bar{\mathbf{\Phi}}_n^{\alpha_{\rm r}}=\mathbf{\Phi}_n} d\Phi_{\rm rad}^{\alpha_{\rm r}}\,. \tag{2.43}$$

The Sudakov form factor can be written as

$$\Delta^{f_b}(\mathbf{\Phi}_n, p_{\rm T}) = \prod_{\alpha_{\rm r}\in\{\alpha_{\rm r}|f_b\}} \Delta_{\alpha_{\rm r}}^{f_b}(\mathbf{\Phi}_n, p_{\rm T})\,, \tag{2.44}$$

where

$$\Delta_{\alpha_{\rm r}}^{f_b}(\mathbf{\Phi}_n, p_{\rm T}) = \exp\left\{-\left[\int d\Phi_{\rm rad}\,\frac{R\left(\mathbf{\Phi}_{n+1}\right)}{B^{f_b}\left(\mathbf{\Phi}_n\right)}\,\theta\left(k_{\rm T}(\mathbf{\Phi}_{n+1}) - p_{\rm T}\right)\right]_{\alpha_{\rm r}}^{\bar{\mathbf{\Phi}}_n^{\alpha_{\rm r}}=\mathbf{\Phi}_n}\right\}. \tag{2.45}$$

The problem of generating the radiation variables according to eq. (2.43) can be reduced to the problem of generating them with probabilities

$$\left[\frac{R^{\alpha_{\rm r}}\left(\mathbf{\Phi}_{n+1}\right)}{B^{f_b}(\mathbf{\Phi}_n)}\,\Delta_{\alpha_{\rm r}}^{f_b}(\mathbf{\Phi}_n, k_{\rm T}\left(\mathbf{\Phi}_{n+1}\right))\right]^{\bar{\mathbf{\Phi}}_n^{\alpha_{\rm r}}=\mathbf{\Phi}_n} d\Phi_{\rm rad}^{\alpha_{\rm r}}\,, \tag{2.46}$$

[14] In this way, by "sampling" the $(n+1)$-body integrand in one point only for each point in $\mathbf{\Phi}_n$, it can happen that the $\tilde{B}$ value is negative. If this happens too frequently, one can perform a "folded" integration, i.e. one samples the $(n+1)$-body integrand in more than one point and takes the average value. In this way, it is very likely that the resulting $\tilde{B}$ value is positive, being the probability of picking more than one critical point in a multiple sampling very small.

by using the highest-bid method, which is illustrated in appendix B of [2]. We are thus left with the problem of generating radiation variables according to eq. (2.46) for a fixed value of $\alpha_{\rm r}$. This problem can be dealt with using the veto technique, explained in appendix A of [2]. To use this technique, we need a sufficiently simple upper bounding function

$$\left[\frac{R^{\alpha_{\rm r}}\left(\mathbf{\Phi}_{n+1}\right)}{B^{f_b}(\mathbf{\Phi}_n)}\right]^{\bar{\mathbf{\Phi}}_n^{\alpha_{\rm r}}=\mathbf{\Phi}_n} \leq F(\Phi_{\rm rad}^{\alpha_{\rm r}}, \mathbf{\Phi}_n). \tag{2.47}$$

This F function can be found by looking to the singular limit of the left hand side of eq. (2.47), that has, in general, a form suggested by the factorization theorem, and by elementary properties of the parton densities in the case of initial-state singular regions. Once the functional form of F is guessed, its normalization is found by scanning the $\mathbf{\Phi}_{n+1}$ phase space. We will give more details when describing the single vector-boson and the single-top implementations.

Chapter 3

NLO vector-boson production matched with shower in POWHEG

Although $W^{\pm}$ and Z vector bosons were discovered more than twenty years ago, weak vector-boson production in hadronic collisions is still one of the more studied process at present and future hadron colliders. For example, on the theoretical side, an accurate measurement of the W mass is important to check the internal consistency of the Standard Model. Moreover, owing to their large production rates, W and Z signals will be used at the LHC as "standard candles" to measure the collider luminosity, as well as to constrain inputs used for other predictions, such as parton distribution functions.

In this chapter we present an implementation of the W and Z hadroproduction cross section in the `POWHEG` framework, using the Catani-Seymour (CS) subtraction formalism. At present, this is the only full `POWHEG` implementation of a process in the CS approach. In ref. [2] an outline of the implementation of the Drell-Yan production cross section in `POWHEG` in the CS scheme was given. In the present chapter, we depart slightly from that approach. In particular, we use a more appropriate form of the hardness variable used for the generation of radiation. As a further point, for the case of W production, if angular correlations in decay products are correctly taken into account, a new problem arises. In fact, the Born-level W cross section vanishes when the fermion decay products are exactly in the opposite direction of the incoming quark-antiquark pair, which causes a problem in the generation of radiation within the `POWHEG` method. We show that this problem has a simple solution, that can be easily generalized to all cases in which the Born cross section vanishes.

The chapter is organized as follows.

In sec. 3.1 we describe how we performed the calculation for the NLO W and Z cross section.

In sec. 3.2 we discuss the POWHEG implementation and how to deal with vanishing Born cross sections.

In sec. 3.3 we show our results for several kinematic variables and compare them with MC@NLO [42] and PYTHIA 6.4 [35]. Sec. 3.3.3 is dedicated to a more careful analysis of the presence of rapidity dips in some MC@NLO distributions.

Finally, in sec. 3.4, we give our conclusions.

The content of this chapter is mainly based on the work published in [62]. Part of the content of sec. 3.3.3 is based on [63].

3.1 Description of the calculation

3.1.1 Kinematics

Born kinematics

We begin by considering the Born process for the annihilation of a quark and an antiquark into a lepton-antilepton pair[1] $q + \bar{q} \to l + \overline{l}$. As in sec. 1.2.1, we denote by $k_\oplus$ and $k_\ominus$ the incoming quark momenta, and by k_1 and k_2 the outgoing fermion momenta. We call $K_\oplus$ and $K_\ominus$ the incoming hadron momenta and define the momentum fractions $x_{\circledpm}$ as

$$k_{\circledpm} = x_{\circledpm} K_{\circledpm} \ . \tag{3.1}$$

We choose our reference frame with the z axis along the $k_\oplus$ direction. We introduce the following variables

$$M^2 = (k_1 + k_2)^2, \qquad Y = \frac{1}{2} \log \frac{(k_1 + k_2)^0 + (k_1 + k_2)^3}{(k_1 + k_2)^0 - (k_1 + k_2)^3}, \tag{3.2}$$

that characterize the invariant mass and rapidity of the virtual vector boson.[2] We also introduce the angle θ_l that represents the angle between the outgoing lepton and the $k_\oplus$ momentum, in the centre-of-mass frame of the lepton pair. The azimuthal orientation of the decay products is irrelevant here, since the cross sections do not depend upon it. We thus fix it to zero. At the end of the generation of the event, we perform a uniform, random azimuthal rotation of the whole event, in order to cover all final-state phase space. The set of variables M^2, Y and θ_l fully parametrize our Born kinematics. From them we

[1] In case of W production the quark-antiquark and lepton-antilepton pairs have different flavour. We focus here for simplicity on leptonic decays of the vector bosons. Hadronic decays are treated similarly.

[2] The virtuality of the lepton pair M^2 will be distributed according to a Breit-Wigner formula around the squared mass of the vector boson M_V^2 (where V stands for either the $W^\pm$ or the Z).

can reconstruct

$$x_\oplus = \sqrt{\frac{M^2}{S}} e^Y, \qquad x_\ominus = \sqrt{\frac{M^2}{S}} e^{-Y}, \tag{3.3}$$

where $S = (K_\oplus + K_\ominus)^2$. The leptons' momenta are first reconstructed in the longitudinal rest frame of the lepton pair, where each lepton has energy equal to $M/2$ and where the lepton momentum forms an angle θ_l with the $\oplus$ direction and has zero azimuth (i.e. it lies in the z, x plane and has positive x component). The leptons' momenta are then boosted with boost angle Y.

The Born phase space in terms of these variables is written as

$$d\mathbf{\Phi}_2 = dx_\oplus\, dx_\ominus (2\pi)^4 \delta^4(k_\oplus + k_\ominus - k_1 - k_2) \frac{d^3k_1}{(2\pi)^3 2k_1^0} \frac{d^3k_2}{(2\pi)^3 2k_2^0} = \frac{1}{S}\frac{1}{16\pi} dM^2\, dY\, d\cos\theta_l\, \frac{d\phi_l}{2\pi}\,. \tag{3.4}$$

Real-emission kinematics

The real emission process is described by the final-state momenta k_1, k_2 and k_3, where k_1 and k_2 have the same meaning as before, and k_3 is the momentum of the radiated light parton. In the POWHEG framework, applied in the context of the CS subtraction method, one introduces a different real phase-space parametrization for each CS dipole. In the present case, we have two CS dipoles, with the two incoming partons playing the role of the emitter and the spectator. We consider the case of the $\oplus$ collinear direction. Thus, the emitter is the incoming parton with momentum $k_\oplus$. We introduce the variable

$$x = 1 - \frac{(k_\oplus + k_\ominus)\cdot k_3}{k_\oplus \cdot k_\ominus}, \tag{3.5}$$

and the momenta

$$K = k_1 + k_2 = k_\oplus + k_\ominus - k_3 \tag{3.6}$$

$$\bar{K} = x\, k_\oplus + k_\ominus\,. \tag{3.7}$$

Observe that $K^2 = \bar{K}^2$, which is the condition that fixes the value of x. When k_3 is collinear to $k_\oplus$ we have

$$x k_\oplus = k_\oplus - k_3, \tag{3.8}$$

and $K = \bar{K}$. Following ref. [64], we introduce the boost tensor

$$\Lambda^\mu{}_\nu(K, \bar{K}) = g^\mu{}_\nu - \frac{2(K+\bar{K})^\mu (K+\bar{K})_\nu}{(K+\bar{K})^2} + \frac{2\bar{K}^\mu K_\nu}{K^2}\,, \tag{3.9}$$

the barred momenta

$$\bar{k}_r^\mu = \Lambda^\mu{}_\nu(K, \bar{K})\, k_r^\nu \qquad\qquad r = 1, 2, \tag{3.10}$$

the barred-momentum fractions

$$\bar{x}_\oplus = x\, x_\oplus, \qquad\qquad \bar{x}_\ominus = x_\ominus\,, \tag{3.11}$$

and the barred incoming momenta

$$\bar{k}_\oplus = x k_\oplus = \bar{x}_\oplus K_\oplus, \qquad\qquad \bar{k}_\ominus = k_\ominus = \bar{x}_\ominus K_\ominus\,. \tag{3.12}$$

The barred momenta characterize the underlying-Born kinematics. We define then

$$\bar{M}^2 = (\bar{k}_1 + \bar{k}_2)^2 = (k_1 + k_2)^2, \qquad\qquad \bar{Y}_\oplus = \frac{1}{2} \log \frac{(\bar{k}_1 + \bar{k}_2)^0 + (\bar{k}_1 + \bar{k}_2)^3}{(\bar{k}_1 + \bar{k}_2)^0 - (\bar{k}_1 + \bar{k}_2)^3}, \tag{3.13}$$

and the angle $\bar{\theta}_l$ is defined as in the Born case, but in term of the momenta $\bar{k}_\oplus$, $\bar{k}_\ominus$, $\bar{k}_1$ and $\bar{k}_2$.

The radiation variables are given by

$$x, \qquad\qquad v = \frac{k_\oplus \cdot k_3}{k_\oplus \cdot k_\ominus}, \qquad\qquad \phi, \tag{3.14}$$

where ϕ is the azimuth of k_3 around the z direction.

From the set of variables $\bar{M}^2$, $\bar{Y}_\oplus$, x, v and ϕ we can reconstruct the full production kinematics for the real-emission cross section. We summarize the reconstruction procedure from ref. [2]. From $\bar{M}^2$ and $\bar{Y}$ we reconstruct the barred momenta, as for the Born kinematics case. Then we reconstruct immediately

$$k_\oplus = \frac{\bar{k}_\oplus}{x}, \qquad k_\ominus = \bar{k}_\ominus, \tag{3.15}$$

and then

$$k_3 = v k_\ominus + (1 - x - v) k_\oplus + k_T, \tag{3.16}$$

where k_T has only transverse components. Its magnitude is determined by the on shell condition $k_3^2 = 0$, which yields

$$k_T^2 = 2 k_\oplus \cdot k_\ominus (1 - x - v) v \tag{3.17}$$

and its azimuth is ϕ. We then construct the vectors

$$K = k_\oplus + k_\ominus - k_3, \qquad \bar{K} = x k_\oplus + k_\ominus, \tag{3.18}$$

and the inverse boost

$$\Lambda^{-1}_{\mu\nu}(K, \bar{K}) = g_{\mu\nu} - \frac{2(K+\bar{K})_\mu (K+\bar{K})_\nu}{(K+\bar{K})^2} + \frac{2K_\mu \bar{K}_\nu}{K^2}, \tag{3.19}$$

from which we can compute the leptons' momenta

$$k_r = \Lambda^{-1}(K, \bar{K})\, \bar{k}_r, \qquad r = 1, 2. \tag{3.20}$$

The real-emission phase space can be expressed in a factorized form in terms of the underlying Born kinematics phase space and of the radiation variables

$$d\mathbf{\Phi}_3 = d\bar{\mathbf{\Phi}}_2\, d\Phi_{\rm rad}, \tag{3.21}$$

with

$$d\Phi_{\rm rad} = \frac{\bar{M}^2}{16\pi^2}\, \frac{d\phi}{2\pi}\, dv\, \frac{dx}{x^2}\, \theta(v)\, \theta\left(1 - \frac{v}{1-x}\right) \theta(x(1-x))\, \theta(x - \bar{x}_\oplus) \tag{3.22}$$

and

$$d\bar{\mathbf{\Phi}}_2 = \frac{1}{S}\, \frac{1}{16\pi}\, d\bar{M}^2\, d\bar{Y}\, d\cos\bar{\theta}_l\,. \tag{3.23}$$

The kinematic variables corresponding to the $\ominus$ collinear direction are reconstructed in full analogy. Observe that the underlying-Born variables and the radiation variables depend in general upon the collinear region that we are considering.

In the present case, while $\bar{M}$, x and ϕ are obviously independent of the region we are considering, $\bar{Y}$, $\bar{\theta}_l$ and v do depend upon it. In order to avoid a too heavy notation, we have refrained from appending $\oplus$ or $\ominus$ indices to the underlying Born and radiation variables. When necessary, we will put a $[\ ]_{\oplus}$ "context" bracket around a formula, meaning that the underlying Born and radiation variables inside it should refer to the $\oplus$ direction.

3.1.2 Cross sections

We have used the helicity amplitude method of refs. [65,66] in order to compute the cross sections including the vector-boson decay products. For the W-boson propagator we have taken

$$\frac{-g_{\mu\nu} + q_\mu q_\nu / M_W^2}{q^2 - M_W^2 + i\Gamma_W M_W} \tag{3.24}$$

and for the Z/γ-boson propagators, multiplied by the corresponding couplings,

$$g_l\, g_q\, \frac{-g_{\mu\nu} + q_\mu q_\nu / M_Z^2}{q^2 - M_Z^2 + i\Gamma_Z M_Z} + e_l\, e_q\, \frac{-g_{\mu\nu}}{q^2}, \tag{3.25}$$

where g_l, g_q are the lepton and quark couplings to the Z (for given helicities), and e_l, e_q are their electric charges.

As explained in sec. 2.3, we introduce the Born $\mathcal{B}_{q\bar{q}}$ and the real-emission cross sections $\mathcal{R}_{q\bar{q},g}$, $\mathcal{R}_{g\bar{q},q}$ and $\mathcal{R}_{qg,\bar{q}}$, that represent the contributions for quark-antiquark, gluon-antiquark and quark-gluon initiating processes. Notice that the flavour of the outgoing particle in the subscript of $\mathcal{R}$ is also taken to be incoming. In the case of Z production, q and $\bar{q}$ are conjugate in flavour. For $W^\pm$ production, because of flavour mixing, q and $\bar{q}$ may refer to different flavour species. We thus assume that, in general, q and $\bar{q}$ may both represent any flavour, but, in general, if q is a quark, $\bar{q}$ is an antiquark, and viceversa. $\mathcal{B}$ and $\mathcal{R}$ are obtained by taking the absolute value squared of the corresponding helicity amplitude, summing over the helicities and colors of the outgoing particles, averaging over the helicities and colors of the initial partons, and multiplying by the flux factor $1/(2s)$ (see eq. (3.27)). The soft-virtual term in the CS approach is given by (see eq. (2.107) in ref. [2])

$$\mathcal{V}_{q\bar{q}} = \frac{\alpha_S}{\pi} C_F \mathcal{B}_{q\bar{q}}\,. \tag{3.26}$$

Defining

$$s = (k_\oplus + k_\ominus)^2, \qquad u = (k_\oplus - k_3)^2 = -s\,v, \qquad t = (k_\ominus - k_3)^2 = -(1-x-v)\,s, \tag{3.27}$$

the CS subtraction terms are given by

$$\mathcal{C}^{\oplus}_{q\bar{q},g} = \left[-\frac{1}{u} 2\, g_s^2\, C_{\text{F}} \left\{ \frac{2}{1-x} - (1+x) \right\} \mathcal{B}_{q\bar{q}}(\bar{M}, \bar{Y}, \bar{\theta}_l) \right]_\oplus, \tag{3.28}$$

for gluon radiation from a $q\bar{q}$ initial-state, and

$$\mathcal{C}_{g\bar{q},q} = \left[-\frac{1}{u} 2\, g_s^2\, T_{\text{F}} \left\{ 1 - 2\,x\,(1-x) \right\} \mathcal{B}_{q\bar{q}}(\bar{M}, \bar{Y}, \bar{\theta}_l) \right]_\oplus, \tag{3.29}$$

for the $g\bar{q}$. Analogous formulae apply for the $q\bar{q}$ and the qg counterterms in the $\ominus$ collinear direction.

The collinear remnants are given by

$$\begin{aligned}\mathcal{G}_{\oplus}^{q\bar{q},g}(\mathbf{\Phi}_{2,\oplus}) &= \frac{\alpha_{\rm S}}{2\pi}C_{\rm F}\Bigg[\left(\frac{2}{1-z}\log\frac{(1-z)^2}{z}\right)_+ - (1+z)\log\frac{(1-z)^2}{z} + (1-z) \\ &\quad + \left(\frac{2}{3}\pi^2-5\right)\delta(1-z) + \left(\frac{1+z^2}{1-z}\right)_+\log\frac{M^2}{\mu_{\rm F}^2}\Bigg]\left[\mathcal{B}_{q\bar{q}}(\bar{M},\bar{Y},\bar{\theta}_l)\right]_{\oplus}, \qquad (3.30)\\ \mathcal{G}_{\oplus}^{g\bar{q},q}(\mathbf{\Phi}_{2,\oplus}) &= \frac{\alpha_{\rm S}}{2\pi}T_{\rm F}\left\{\left[z^2+(1-z)^2\right]\left[\log\frac{(1-z)^2}{z}+\log\frac{M^2}{\mu_{\rm F}^2}\right]+2z(1-z)\right\}\left[\mathcal{B}_{q\bar{q}}(\bar{M},\bar{Y},\bar{\theta}_l)\right]_{\oplus}. \qquad (3.31)\end{aligned}$$

The $\mathbf{\Phi}_{2,\oplus}$ notation, according to ref. [2], represents the set of variables

$$\mathbf{\Phi}_{2,\oplus} = \{x_\oplus, x_\ominus, z, k_1, k_2\}, \qquad z\,x_\oplus K_\oplus + x_\ominus K_\ominus = k_1 + k_2\,. \qquad (3.32)$$

We also associate an underlying Born configuration $\bar{\mathbf{\Phi}}_2$ to the $\mathbf{\Phi}_{2,\oplus}$ kinematics, defined by

$$\bar{k}_\oplus = z\,x_\oplus K_\oplus, \qquad \bar{k}_\ominus = x_\ominus K_\ominus, \qquad \bar{k}_1 = k_1, \quad \bar{k}_2 = k_2\,. \qquad (3.33)$$

The other two collinear remnants, $\mathcal{G}_{\ominus}^{q\bar{q},g}(\mathbf{\Phi}_{2,\ominus})$ and $\mathcal{G}_{\ominus}^{qg,\bar{q}}(\mathbf{\Phi}_{2,\ominus})$, are equal to $\mathcal{G}_{\oplus}^{q\bar{q},g}(\mathbf{\Phi}_{2,\oplus})$ and $\mathcal{G}_{\oplus}^{g\bar{q},q}(\mathbf{\Phi}_{2,\oplus})$ respectively, with $\left[\mathcal{B}_{q\bar{q}}(\bar{M},\bar{Y},\bar{\theta}_l)\right]_\oplus$ replaced by $\left[\mathcal{B}_{q\bar{q}}(\bar{M},\bar{Y},\bar{\theta}_l)\right]_\ominus$. We then introduce the notation B, V, R, C, G, to stand for $\mathcal{B}$, $\mathcal{V}$, $\mathcal{R}$, $\mathcal{C}$, $\mathcal{G}$, each multiplied by its appropriate parton densities. The differential cross section, multiplied by some infrared safe observable O, can then be written as

$$\begin{aligned}\langle O\rangle &= \sum_{q\bar{q}}\Bigg\{\int d\mathbf{\Phi}_2\left[B_{q\bar{q}}(\mathbf{\Phi}_2)+V_{q\bar{q}}(\mathbf{\Phi}_2)\right]O(\mathbf{\Phi}_2) \\ &+ \int d\mathbf{\Phi}_3\left\{R_{q\bar{q},g}(\mathbf{\Phi}_3)O(\mathbf{\Phi}_3) - C^{\oplus}_{q\bar{q},g}(\mathbf{\Phi}_3)\left[O(\bar{\mathbf{\Phi}}_2)\right]_\oplus - C^{\ominus}_{q\bar{q},g}(\mathbf{\Phi}_3)\left[O(\bar{\mathbf{\Phi}}_2)\right]_\ominus\right\} \\ &+ \int d\mathbf{\Phi}_3\left\{R_{g\bar{q},q}(\mathbf{\Phi}_3)O(\mathbf{\Phi}_3) - C_{g\bar{q},q}(\mathbf{\Phi}_3)\left[O(\bar{\mathbf{\Phi}}_2)\right]_\oplus\right\} \\ &+ \int d\mathbf{\Phi}_3\left\{R_{qg,\bar{q}}(\mathbf{\Phi}_3)O(\mathbf{\Phi}_3) - C_{qg,\bar{q}}(\mathbf{\Phi}_3)\left[O(\bar{\mathbf{\Phi}}_2)\right]_\ominus\right\} \\ &+ \int d\mathbf{\Phi}_{2,\oplus}\left[G^{q\bar{q},g}_{\oplus}(\mathbf{\Phi}_{2,\oplus})+G^{g\bar{q},q}_{\oplus}(\mathbf{\Phi}_{2,\oplus})\right]\,O(\mathbf{\Phi}_{2,\oplus}) \\ &+ \int d\mathbf{\Phi}_{2,\ominus}\left[G^{q\bar{q},g}_{\ominus}(\mathbf{\Phi}_{2,\ominus})+G^{qg,\bar{q}}_{\ominus}(\mathbf{\Phi}_{2,\ominus})\right]\,O(\mathbf{\Phi}_{2,\ominus})\Bigg\}\,. \qquad (3.34)\end{aligned}$$

3.2 POWHEG implementation

The starting point of a POWHEG implementation is the inclusive cross section at fixed underlying-Born flavour and kinematics. For the soft-virtual and Born contributions the underlying Born kinematics is obviously given by the Born kinematics itself. For the collinear remnant, for example, in the $\oplus$ direction (see eq. 3.32) the underlying Born kinematics is given by

$$\bar{\mathbf{\Phi}}_2 = \{z x_\oplus, x_\ominus, k_1, k_2\}\,. \tag{3.35}$$

For the CS counterterms, the underlying Born kinematics is given by the corresponding $\bar{\mathbf{\Phi}}_2$ variables defined in eqs. (3.11) and (3.12). In order to assign an underlying Born kinematics to the real term, one has to decompose it into contributions that are singular in only one kinematic region. Since $R_{g\bar{q},q}$ and $R_{qg,\bar{q}}$ are only singular in the $\oplus$ and $\ominus$ direction respectively, we assign their underlying Born to be the same of the corresponding CS subtraction term. For $R_{q\bar{q},g}$, on the other hand, we separate:

$$R_{q\bar{q},g} = R^{\oplus}_{q\bar{q},g} + R^{\ominus}_{q\bar{q},g}, \qquad R^{\circledast}_{q\bar{q},g} = R_{q\bar{q},g}\frac{C^{\circledast}_{q\bar{q},g}}{C^{\oplus}_{q\bar{q},g} + C^{\ominus}_{q\bar{q},g}}\,, \tag{3.36}$$

and assign to $R^{\circledast}_{q\bar{q},g}$ the same underlying Born kinematics of the corresponding CS counterterm $C^{\circledast}_{q\bar{q},g}$. The underlying Born flavour, on the other hand, is always $q\bar{q}$ in the notation we have adopted.

3.2.1 Generation of the Born variables

The primary ingredient for a POWHEG implementation is the $\bar{B}$ function, that is the inclusive cross section at fixed underlying Born variables. In our case, it is given by

$$\bar{B} = \sum_{q\bar{q}} \bar{B}_{q\bar{q}}, \tag{3.37}$$

$$\begin{aligned}\bar{B}_{q\bar{q}} &= B_{q\bar{q}}(\mathbf{\Phi}_2) + V_{q\bar{q}}(\mathbf{\Phi}_2) + \sum_{\circledast}\int \left[d\Phi_{\rm rad}\left\{R^{\circledast}_{q\bar{q},g}(\mathbf{\Phi}_3) - C^{\circledast}_{q\bar{q},g}(\mathbf{\Phi}_3)\right\}\right]^{\bar{\mathbf{\Phi}}_2=\mathbf{\Phi}_2}_{\circledast} \\ &+ \int \left[d\Phi_{\rm rad}\left\{R_{g\bar{q},q}(\mathbf{\Phi}_3) - C_{g\bar{q},q}(\mathbf{\Phi}_3)\right\}\right]^{\bar{\mathbf{\Phi}}_2=\mathbf{\Phi}_2}_{\oplus} + \int \left[d\Phi_{\rm rad}\left\{R_{qg,\bar{q}}(\mathbf{\Phi}_3) - C_{qg,\bar{q}}(\mathbf{\Phi}_3)\right\}\right]^{\bar{\mathbf{\Phi}}_2=\mathbf{\Phi}_2}_{\ominus} \\ &+ \int_{\bar{x}_\oplus}^1 \frac{dz}{z}\left[G^{q\bar{q},g}_{\oplus}(\mathbf{\Phi}_{2,\oplus}) + G^{g\bar{q},q}_{\oplus}(\mathbf{\Phi}_{2,\oplus})\right]^{\bar{\mathbf{\Phi}}_2=\mathbf{\Phi}_2} + \int_{\bar{x}_\ominus}^1 \frac{dz}{z}\left[G^{q\bar{q},g}_{\ominus}(\mathbf{\Phi}_{2,\ominus}) + G^{qg,\bar{q}}_{\ominus}(\mathbf{\Phi}_{2,\ominus})\right]^{\bar{\mathbf{\Phi}}_2=\mathbf{\Phi}_2}\end{aligned} \tag{3.38}$$

It is worthwhile to observe that, when integrating the $R^{\circledast}_{q\bar{q},g}(\mathbf{\Phi}_3)$ terms, only the dipole

corresponding to the region at hand will be evaluated with kinematics equal to the Born's one. Hence, when we integrate $R^{\oplus}_{q\bar{q},g}(\mathbf{\Phi}_3)$ over $[d\Phi_{\rm rad}]_{\oplus}$, the term $C^{\ominus}_{q\bar{q},g}$ in the denominator of eq. (3.36) is evaluated in a kinematical configuration which is not equal to the argument of $\bar{B}$, i.e. $\mathbf{\Phi}_2$. In this implementation, this does not cause any problem, since no dangerous kinematical configurations can be generated in this way. However, as outlined in sec. 2.3.5, in more complicated processes this may require special attention.

The radiation variables $\Phi_{\rm rad}$ are parametrized in terms of three variables that span the unit cube, $X_{\rm rad} = \{X^{(1)}_{\rm rad}, X^{(2)}_{\rm rad}, X^{(3)}_{\rm rad}\}$, while the z variable is parametrized in term of a single variable $X^{(1)}_{\rm rad}$ that ranges between 0 and 1. We then define the $\tilde{B}$ function

$$\begin{aligned}
\tilde{B}_{q\bar{q}} &= B_{q\bar{q}}(\mathbf{\Phi}_2) + V_{q\bar{q}}(\mathbf{\Phi}_2) + \sum_{\circledast} \left[\left| \frac{\partial \Phi_{\rm rad}}{\partial X_{\rm rad}} \right| \left\{ R^{\circledast}_{q\bar{q},g}(\mathbf{\Phi}_3) - C^{\circledast}_{q\bar{q},g}(\mathbf{\Phi}_3) \right\} \right]^{\bar{\mathbf{\Phi}}_2=\mathbf{\Phi}_2}_{\circledast} \\
&+ \left[\left| \frac{\partial \Phi_{\rm rad}}{\partial X_{\rm rad}} \right| \{ R_{g\bar{q},q}(\mathbf{\Phi}_3) - C_{g\bar{q},q}(\mathbf{\Phi}_3) \} \right]^{\bar{\mathbf{\Phi}}_2=\mathbf{\Phi}_2}_{\oplus} + \left[\left| \frac{\partial \Phi_{\rm rad}}{\partial X_{\rm rad}} \right| \{ R_{qg,\bar{q}}(\mathbf{\Phi}_3) - C_{qg,\bar{q}}(\mathbf{\Phi}_3) \} \right]^{\bar{\mathbf{\Phi}}_2=\mathbf{\Phi}_2}_{\ominus} \\
&+ \left[\frac{1}{z} \frac{\partial z}{\partial X^{(1)}_{\rm rad}} \left\{ G^{q\bar{q},g}_{\oplus}(\mathbf{\Phi}_{2,\oplus}) + G^{g\bar{q},q}_{\oplus}(\mathbf{\Phi}_{2,\oplus}) \right\} \right]^{\bar{\mathbf{\Phi}}_2=\mathbf{\Phi}_2}_{\oplus} \\
&+ \left[\frac{1}{z} \frac{\partial z}{\partial X^{(1)}_{\rm rad}} \left\{ G^{q\bar{q},g}_{\ominus}(\mathbf{\Phi}_{2,\ominus}) + G^{qg,\bar{q}}_{\ominus}(\mathbf{\Phi}_{2,\ominus}) \right\} \right]^{\bar{\mathbf{\Phi}}_2=\mathbf{\Phi}_2}_{\ominus} ,
\end{aligned} \tag{3.39}$$

so that defining $\tilde{B} = \sum_{q\bar{q}} \tilde{B}_{q\bar{q}}$, we have

$$\bar{B} = \int d^3 X_{\rm rad}\, \tilde{B} \,. \tag{3.40}$$

In practice, the $\tilde{B}$ function is integrated numerically over all $\mathbf{\Phi}_2, X_{\rm rad}$ integration variables, using an integration program that can generate the set of kinematic variables $\mathbf{\Phi}_2, X_{\rm rad}$, with a probability proportional to $d\mathbf{\Phi}_2\, d^3X_{\rm rad}\, \tilde{B}$ in the $d\mathbf{\Phi}_2\, d^3X_{\rm rad}$ kinematic cell (see, for example, refs. [60, 61]). Once the $\mathbf{\Phi}_2, X_{\rm rad}$ point is generated, the flavour $q\bar{q}$ is chosen with a probability proportional to the value of $\tilde{B}_{q\bar{q}}$ at that specific $\mathbf{\Phi}_2, X_{\rm rad}$ point. At this stage, the radiation variables are disregarded, and only the underlying Born ones are kept. This corresponds to integrate over the radiation variables, as explained in sec. 2.3.6.

3.2.2 Generation of the radiation variables

Radiation kinematics is instead generated using the POWHEG Sudakov form factor

$$\Delta^{q\bar{q}}(\mathbf{\Phi}_2, p_{\rm T}) = \prod_{\circledast} \Delta^{q\bar{q}}_{\circledast}\,, \tag{3.41}$$

where

$$\Delta^{q\bar{q}}_{\oplus}(\mathbf{\Phi}_2, p_{\rm T}) \;=\; \exp\left\{ -\left[\int d\Phi_{\rm rad}\, \frac{R^{\oplus}_{q\bar{q},g}(\mathbf{\Phi}_3) + R_{g\bar{q},q}(\mathbf{\Phi}_3)}{B_{q\bar{q}}(\mathbf{\Phi}_2)}\, \theta\left(k_{\rm T}(\mathbf{\Phi}_3) - p_{\rm T}\right) \right]_{\oplus}^{\bar{\mathbf{\Phi}}_2=\mathbf{\Phi}_2} \right\} \tag{3.42}$$

$$\Delta^{q\bar{q}}_{\ominus}(\mathbf{\Phi}_2, p_{\rm T}) \;=\; \exp\left\{ -\left[\int d\Phi_{\rm rad}\, \frac{R^{\ominus}_{q\bar{q},g}(\mathbf{\Phi}_3) + R_{qg,\bar{q}}(\mathbf{\Phi}_3)}{B_{q\bar{q}}(\mathbf{\Phi}_2)}\, \theta\left(k_{\rm T}(\mathbf{\Phi}_3) - p_{\rm T}\right) \right]_{\ominus}^{\bar{\mathbf{\Phi}}_2=\mathbf{\Phi}_2} \right\} \tag{3.43}$$

The function $k_T(\mathbf{\Phi}_3)$ measures the hardness of radiation in the real event. It is required to be of the order of the transverse momentum of the radiation in the collinear limit, and to become equal to it in the soft-collinear limit. In principle, the choice of $k_T(\mathbf{\Phi}_3)$ can differ in the two singular regions ($\oplus$ and $\ominus$) that we are considering. The choice adopted in the Examples section of ref. [2] had in fact this feature. We have found, however, that for practical reasons[3] it is better to adopt a different choice, namely to take $k_T(\mathbf{\Phi}_3)$ to coincide with that of eqs. (3.16) and (3.17).

The generation of radiation is performed individually for $\Delta^{q\bar{q}}_{\oplus}$ and $\Delta^{q\bar{q}}_{\ominus}$, and the highest generated k_T is retained. The upper bounding function for the application of the veto method is chosen to be[4]

$$\frac{R^{\oplus}_{q\bar{q},g} + R_{g\bar{q},q}}{B_{q\bar{q}}} \leq \frac{16\pi^2}{M^2}\, N^{\oplus}_{q\bar{q}}\, \frac{\alpha_s(k_T^2)}{2v}\, \frac{x^2}{1-x-v}\,, \tag{3.44}$$

and the analogous one for the $\ominus$ direction. The procedure used to generate radiation events according to this upper bounding function is described in Appendix B.

After the radiation generation, events are then passed to the Shower Monte Carlo program, using the LHIUP interface. No ambiguities can arise for color connections, since there are at most three colored particles, and hence there is only one possible way to

[3] The choice discussed in [2] is $k_T^2 = M^2(1-x)v$, and is such that k_T^2 is always bound to be smaller than M^2. Since the factorization and renormalization scales are taken equal to k_T, for vector-boson production at transverse momenta much larger than the vector-boson mass the coupling does not properly decrease.

[4] This upper bounding function differs from the ones of eqs. (7.163)–(7.166) in ref. [2], but is in fact equivalent to the bound of eq. (7.234) in the same reference, once the change of variables $\xi = 1 - x$, $y = (1 - 2v - x)/(1 - x)$ is performed, and the different definitions of $d\Phi_{\rm rad}$ are properly taken into account.

color-connect them. For Born-like events, there is only one line connecting the incoming quark-antiquark pair. For real-like events, instead, each of the two gluon lines is connected properly to one of the two quarks.

3.2.3 Born zeros

In case the Born cross section vanishes in particular kinematics points, a problem arises in the POWHEG expression for the Sudakov form factor (3.42) and (3.43). It happens, in fact, that although B vanishes, $\bar{B}$ may differ from zero. Born kinematics configurations with a vanishing Born cross section may thus be generated and, at the stage of radiation generation, one would find very large ratios of the real-emission cross section over the Born cross section. It would thus prove difficult to find a reasonable upper bound for this ratio. If one tries to neglect the problem, radiation events with a vanishing underlying Born configuration would never be generated. We observe that, in the limit of small hardness parameter, the real cross also exhibit the same vanishing behaviour of the Born cross section. Loosely speaking, the problem arises when the distance of the underlying Born configuration from the zero configuration is smaller than the distance of the real emission cross section from the singular (i.e. zero hardness) configuration. In order to solve this problem, in a completely general way, we further decompose the real cross section contribution as

$$R^{\alpha_r} = R^{\alpha_r,s} + R^{\alpha_r,r}, \tag{3.45}$$

where

$$R^{\alpha_r,s} = R^{\alpha_r}\,\frac{Z}{Z+H}, \qquad R^{\alpha_r,r} = R^{\alpha_r}\,\frac{H}{Z+H}. \tag{3.46}$$

The suffixes s and r stand for "singular" and "regular" respectively, and Z is a function of the kinematics that vanishes like the Born cross section, evaluated at the underlying Born kinematics of the given term. H is the hardness of radiation and it must vanish for vanishing transverse momentum of the radiation. The simplest possible choice would be

$$Z = \mathcal{B}\,\frac{k_{T,\max}^2}{\mathcal{B}_{\max}}, \qquad H = k_T^2\,, \tag{3.47}$$

where k_T is some definition of the transverse momentum of the radiation. Notice now that $R^{\alpha_r,s}$ vanishes as fast as the Born term when its underlying Born kinematics approaches the Born zero. It can thus be used in the expression for the Sudakov form factor (eqs. (3.42) and (3.43)) without problems. The $R^{\alpha_r,r}$ is instead non-vanishing, but, on the other hand, it does not have collinear or soft singularities because of the H factor, and thus it can be computed directly, without any Sudakov form factor. In the case of

W production, the Born zero is associated to $\bar{\theta}_l = 0$ if q is an antiquark, and $\bar{\theta}_l = \pi$ if it is a quark. We choose then

$$Z = M^2 \left(1 + s_q \cos\bar{\theta}_l\right)^2, \qquad H = k_T^2, \tag{3.48}$$

with k_T^2 given by formula (3.17) and the factor s_q equals 1 for quark, and -1 for antiquark. The angle $\bar{\theta}_l$ is chosen according to the $\oplus$ parametrization (for $R^{\oplus}$) or the $\ominus$ parametrization (for $R^{\ominus}$) of the real-emission phase space.

In addition, all the R^{α_r} terms in eq. (3.37) are replaced by the corresponding $R^{\alpha_r,s}$ and the $R^{\alpha_r,r}$ terms are generated in a way similar to what was done for eq. (3.39). In other words one defines

$$\begin{aligned}\tilde{B}^r = \sum_{q\bar{q}} \tilde{B}^r_{q\bar{q}} = \sum_{q\bar{q}} \quad & \left\{ \left[\left| \frac{\partial \Phi_{\rm rad}}{\partial X_{\rm rad}} \right| R^{\oplus,r}_{q\bar{q},g}(\mathbf{\Phi}_3) \right]_{\oplus}^{\bar{\mathbf{\Phi}}_2=\mathbf{\Phi}_2} + \left[\left| \frac{\partial \Phi_{\rm rad}}{\partial X_{\rm rad}} \right| R^{\ominus,r}_{q\bar{q},g}(\mathbf{\Phi}_3) \right]_{\ominus}^{\bar{\mathbf{\Phi}}_2=\mathbf{\Phi}_2} \right. \\ & \left. + \left[\left| \frac{\partial \Phi_{\rm rad}}{\partial X_{\rm rad}} \right| R^{r}_{g\bar{q},q}(\mathbf{\Phi}_3) \right]_{\oplus}^{\bar{\mathbf{\Phi}}_2=\mathbf{\Phi}_2} + \left[\left| \frac{\partial \Phi_{\rm rad}}{\partial X_{\rm rad}} \right| R^{r}_{qg,\bar{q}}(\mathbf{\Phi}_3) \right]_{\ominus}^{\bar{\mathbf{\Phi}}_2=\mathbf{\Phi}_2} \right\},\end{aligned} \tag{3.49}$$

and integrates over the whole $\mathbf{\Phi}_2, X_{\rm rad}$ phase space with the same method used for $\tilde{B}$. In order to generate an event, one chooses $\tilde{B}$ or $\tilde{B}^r$, with a probability proportional to their respective total integral. In case $\tilde{B}^r$ is chosen, one generates a kinematic configuration according to it. This kinematic configuration is a full 3-body configuration. The flavour $q\bar{q}$ is chosen with a probability proportional the the value of $\tilde{B}^r_{q\bar{q}}$ for the particular kinematic point that has been generated, and the event is sent to the output. In case $\tilde{B}$ is chosen, a kinematic configuration and an underlying Born flavour is chosen in the same way.

3.3 Results

The `MC@NLO` program provides an implementation of vector-boson production at the NLO level in a shower Monte Carlo framework. It should therefore be comparable to our calculation, and we thus begin by comparing `MC@NLO` and `POWHEG` distributions. In this comparison, the `POWHEG` code is interfaced to `HERWIG` [34, 43], in order to minimize differences due to the subsequent shower in the two approaches. We choose as our default parton-density functions the CTEQ6M [10] package, and the corresponding value of Λ_{QCD}. The factorization and renormalization scales are taken equal to $M_V^2 + (p_T^V)^2$ in the calculation of the $\bar{B}$ function, where $V = W$ or Z. In the generation of radiation, the factorization and renormalization scales are taken equal to the transverse momentum of the vector boson V. We also account properly for the heavy-flavour thresholds, when

the transverse momentum of the vector boson approaches the bottom and charm quark threshold. That is to say, when the renormalization scale crosses a heavy-flavour mass threshold, the QCD evolution of the running coupling is accordingly changed to the new number of active flavours. The other relevant parameters for our calculation are

M_z (GeV)	Γ_Z (GeV)	M_W (GeV)	Γ_W (GeV)	$\sin^2\theta_W^{\rm eff}$	$\alpha_{\rm em}^{-1}(M_Z)$
91.188	2.49	80.419	2.124	0.23113	127.934

.

The above values of masses and widths are used in eqs. (3.24) and (3.25). The W and Z couplings are given by

$$g = \frac{e}{\sin\theta_W^{\rm eff}}\,, \quad g_{l/q} = \frac{e}{\sin\theta_W^{\rm eff}\cos\theta_W^{\rm eff}}\left[T_3^{(l/q)} - q_{l/q}\sin^2\theta_W^{\rm eff}\right], \quad e = \sqrt{4\pi\alpha_{\rm em}(M_Z)}\,, \quad (3.50)$$

where l/q denotes the given left or right component of a lepton or a quark. For W production we used the following absolute values for the CKM matrix elements

ud	us	ub	cd	cs	cb	td	ts	tb
0.9748	0.2225	0.0036	0.2225	0.9740	0.041	0.009	0.0405	0.9992

.

In all figures shown in the following we do not impose any acceptance cut.

3.3.1 *Z* production at the Tevatron

In fig. 3.1 we show a comparison of the lepton transverse momentum and rapidity, and of the transverse momentum of the reconstructed lepton-antilepton pair at the Tevatron. We notice a larger cross section in `POWHEG`, when the Z transverse momentum becomes large. This is not unexpected, since for large momenta the `POWHEG` result is larger than the standard NLO result by a factor $\bar{B}/B$ (this feature has also some impact upon the transverse-momentum distribution of the lepton). Once this fact is accounted for, the transverse-momentum distribution of the Z is in fair agreement, although we find observable shape differences at low transverse momenta. We also notice a peak at $p_T = 0$ in the `MC@NLO` distribution, that is not present in the `POWHEG` result. We expect this distribution to be affected by low transverse-momentum power-suppressed effects. In fact, the peak at zero transverse momentum in `MC@NLO` disappears if the primordial transverse momentum of the partons (the `PTRMS` variable in `HERWIG`) is set to a non-zero value. In fig. 3.2 we compare the rapidity distribution of the reconstructed Z, its invariant mass, the azimuthal distance of the e^+e^- pair coming from Z decays, and the transverse momentum of the radiated jet at the Tevatron. The jet is defined using the `SISCONE` algorithm [67] as implemented in the `FASTJET` package [68], using $R = 0.7$. We find again fair agreement.

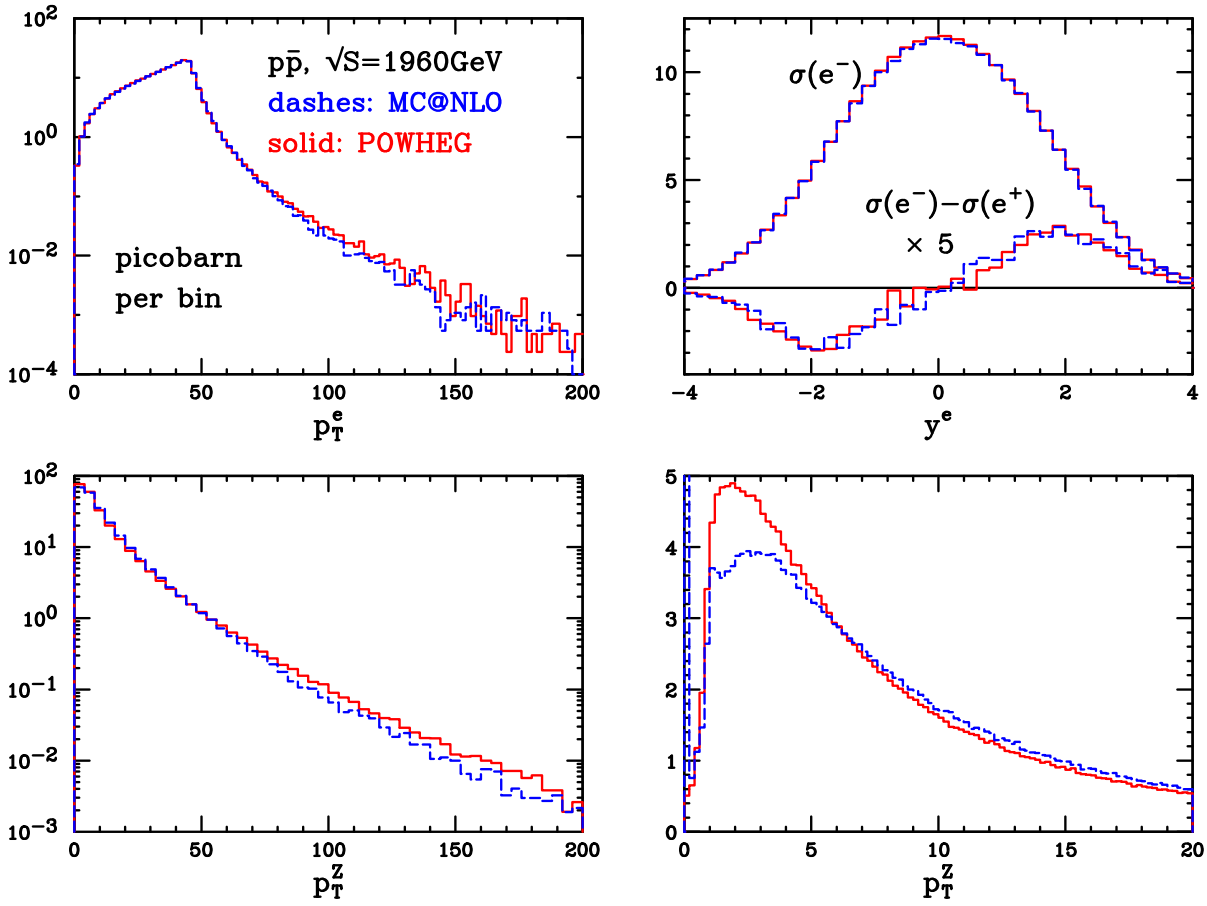

Figure 3.1: Comparison between POWHEG and MC@NLO results for the transverse momentum and rapidity of the lepton coming from the decay of the Z boson, and for the transverse momentum of the Z, as reconstructed from its decay products. The lepton-rapidity asymmetry is also shown. Plots done for the Tevatron $p\bar{p}$ collider.

In ref. [69], a discrepancy was found in the rapidity distribution of the hardest radiated jet as computed in MC@NLO and ALPGEN, for the case of top pair production at the Tevatron. The MC@NLO calculation shows there a dip at zero rapidity, not present in ALPGEN. In fact, the POWHEG calculation of this quantity does not display any dip. We thus examine the transverse momentum of the radiated jet in this case. Furthermore, we also plot the rapidity difference between the Z and the hardest radiated jet. The results are displayed in fig. 3.3. We have chosen different cuts for the minimum transverse momentum of the radiated jet, i.e. 10, 20, 40, 60 and 80 GeV. We observe noticeable differences in the rapidity distribution of the hardest jet in the two approaches. The MC@NLO result displays a dip at zero $y_{\rm jet} - y_Z$. We will come back on this feature in sec. 3.3.3.

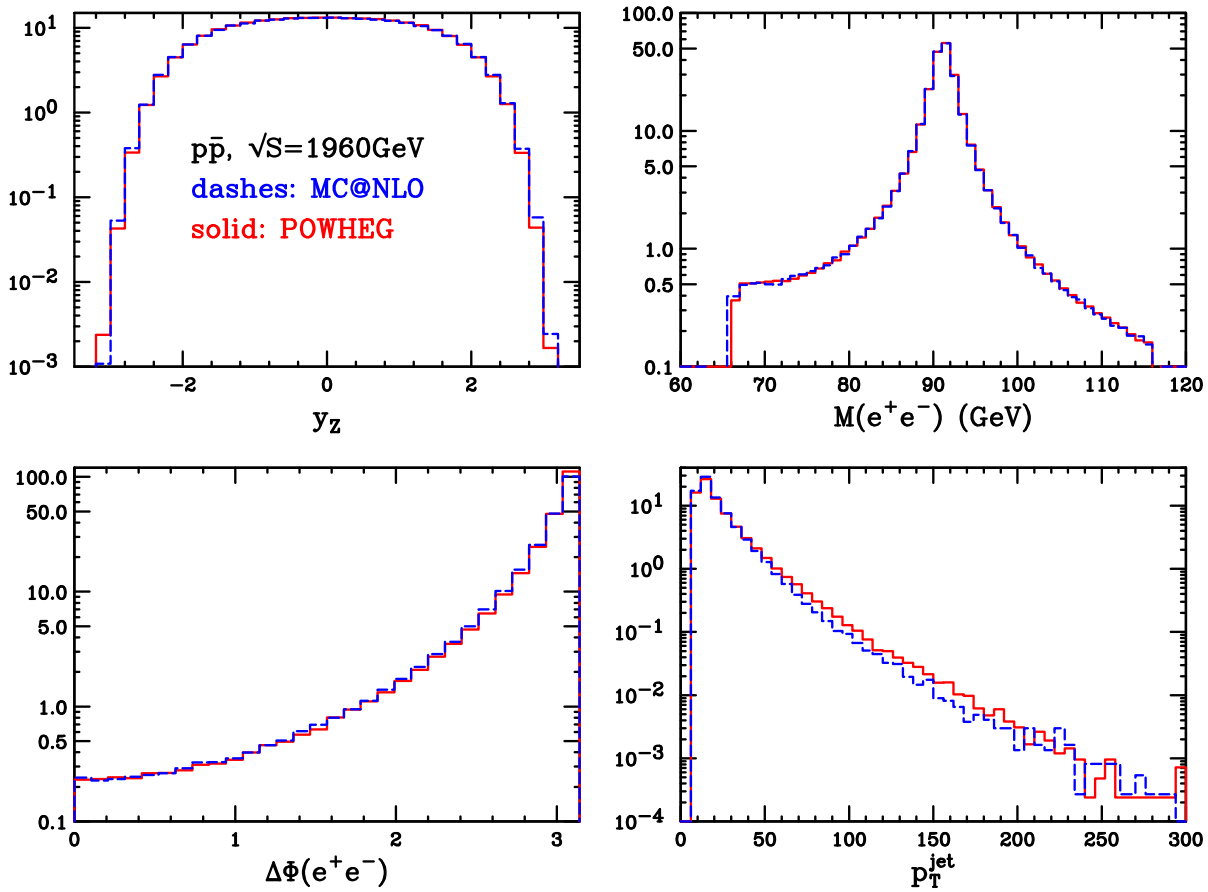

Figure 3.2: Comparison between POWHEG and MC@NLO for the reconstructed Z rapidity, its invariant mass, the lepton-pair azimuthal distance and the transverse momentum of the reconstructed jet, above a 10 GeV minimum value.

3.3.2 Z production at the LHC

Similar results are reported for the LHC in fig. 3.4 through 3.6. We notice less pronounced differences (with respect to the Tevatron case) in the p_T spectrum of the Z boson. The discrepancy in the $y_{\rm jet}$ distribution is still evident, although the dip is barely noticeable in this case.

The same set of plots are also shown for a PYTHIA-POWHEG comparison in fig. 3.7 through 3.10. In this case the POWHEG code was interfaced with PYTHIA. Photon radiation from final-state leptons was switched off (MSTJ(41)=3), in order to simplify the analysis. Furthermore, the new transverse-momentum ordered shower was used (i.e. the PYEVNW routine), since transverse-momentum ordering should be more appropriate in conjunction with POWHEG. In the plots, the PYTHIA output is normalized to the POWHEG total

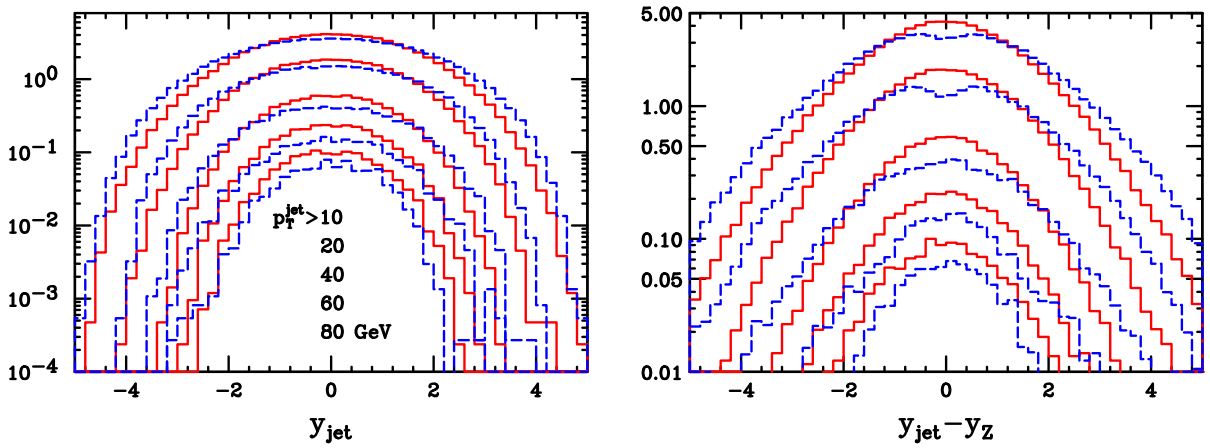

Figure 3.3: Rapidity distribution of the hardest jet with different transverse-momentum cuts, and the rapidity distance between the hardest jet and the reconstructed Z boson.

cross section. From fig. 3.7 through 3.8, we can see a remarkable agreement between the two calculations for the Tevatron results, the only visible discrepancy being given by the transverse-momentum distribution of the Z boson at small transverse momenta. We also notice that, unlike the case of the MC@NLO-POWHEG comparison, the transverse-momentum distribution of the Z is slightly harder in PYTHIA than in POWHEG. The rapidity distributions of the hardest jet are also in remarkable agreement.

In fig. 3.10 through 3.11, we carry out the same comparison in the LHC case. We notice here few important differences in the rapidity distribution of the Z boson, and, probably related to that, of the electron, the PYTHIA distribution being flatter in the central region. Both MC@NLO and POWHEG do not show this feature. As already pointed out in dec. 2.3.1, the generation of vector bosons in PYTHIA is not very different from the POWHEG generation. Radiation is generated with a very similar method [45, 56]. There are however differences. In PYTHIA the Born inclusive cross section is used rather than our $\bar{B}$ function. Furthermore, our choice of scales is constrained by the requirement of next-to-leading logarithmic accuracy in the Sudakov form factor. The discrepancy in the transverse-momentum distribution of the Z may be due to different requirements for the choice of the scale in the generation of radiation in the two algorithms. In particular, one possible explanation for the low-p_T difference is the fact that PYTHIA does not use the scale Λ_{MC} in the evaluation of the coupling constant present in the Sudakov form factor.[5] The discrepancy in the rapidity distribution may be due to the lack of NLO corrections in PYTHIA, i.e. to the use of the Born cross section (rather than the $\bar{B}$ function) and LO

[5] In fact, this option was included only from version 6.4.19, while results presented here were obtained with version 6.4.16.

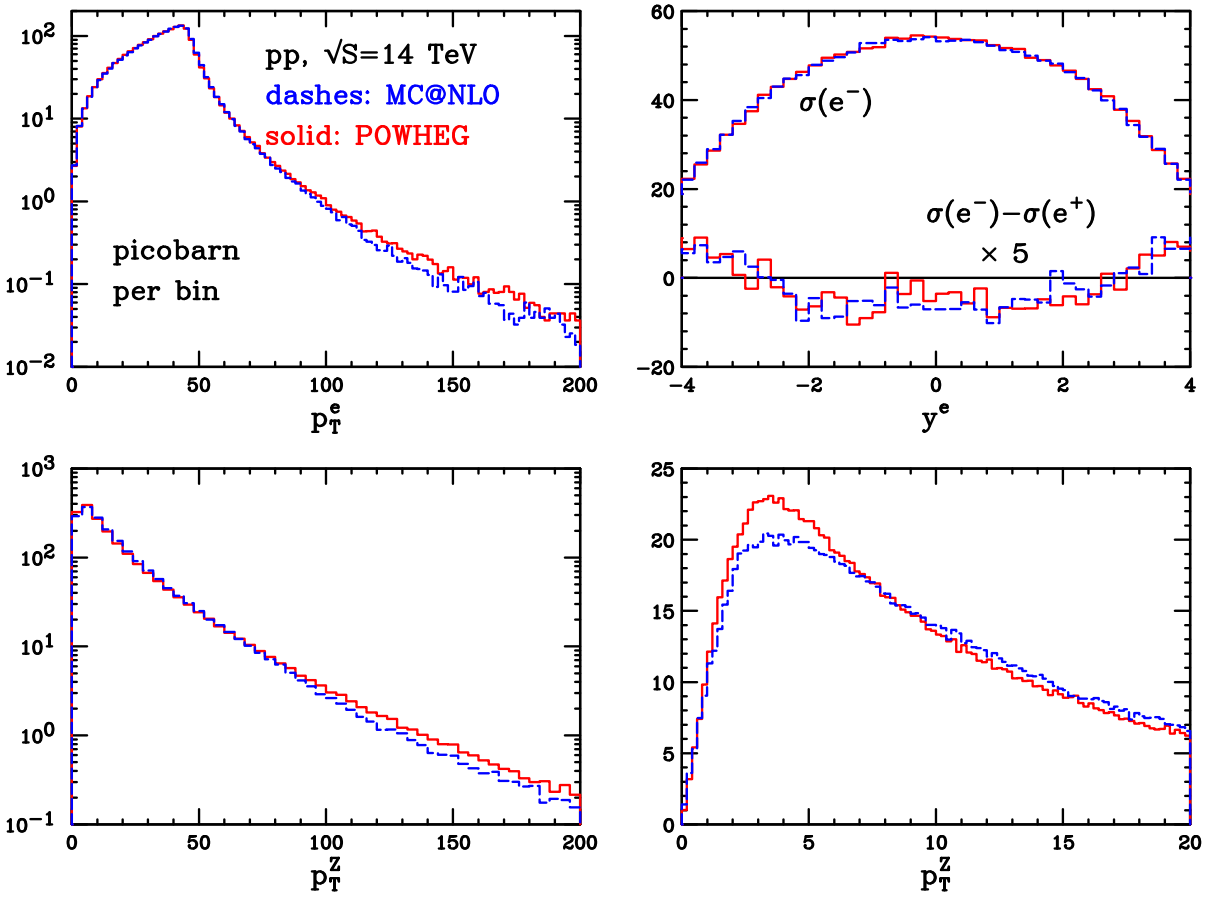

Figure 3.4: Same as fig. 3.1 for the LHC at 14 TeV.

parton densities. In fact, in fig. 3 of ref. [70], a comparison in the rapidity distribution of the Z at LO, NLO and NNLO, is shown for the LHC. One can notice from that figure that there is a difference in the LO and NLO shape of the distribution, the former being flatter. In order to elucidate this point, we show in fig. 3.13 the rapidity distribution of the Z boson computed at fixed order in QCD, at LO and NLO. With the LO calculation, we also show the result obtained using the same LO parton-distribution function (pdf) set used in `PYTHIA`, that is CTEQ5L. The figure leads to the conclusion that the use of the LO parton-density set CTEQ5L is the primary cause of this shape difference. We find, in fact, no difference in shape between the LO and NLO result if the same pdf set is used instead. We thus conclude that also the effect observed in fig. 3 of ref. [70] is due to the use of a LO parton-density set together with the LO result.

The predictions for the transverse-momentum distribution of the Z boson are summarized in fig. 3.14, in comparison with data from ref. [71], at $\sqrt{S} = 1960$ GeV and from

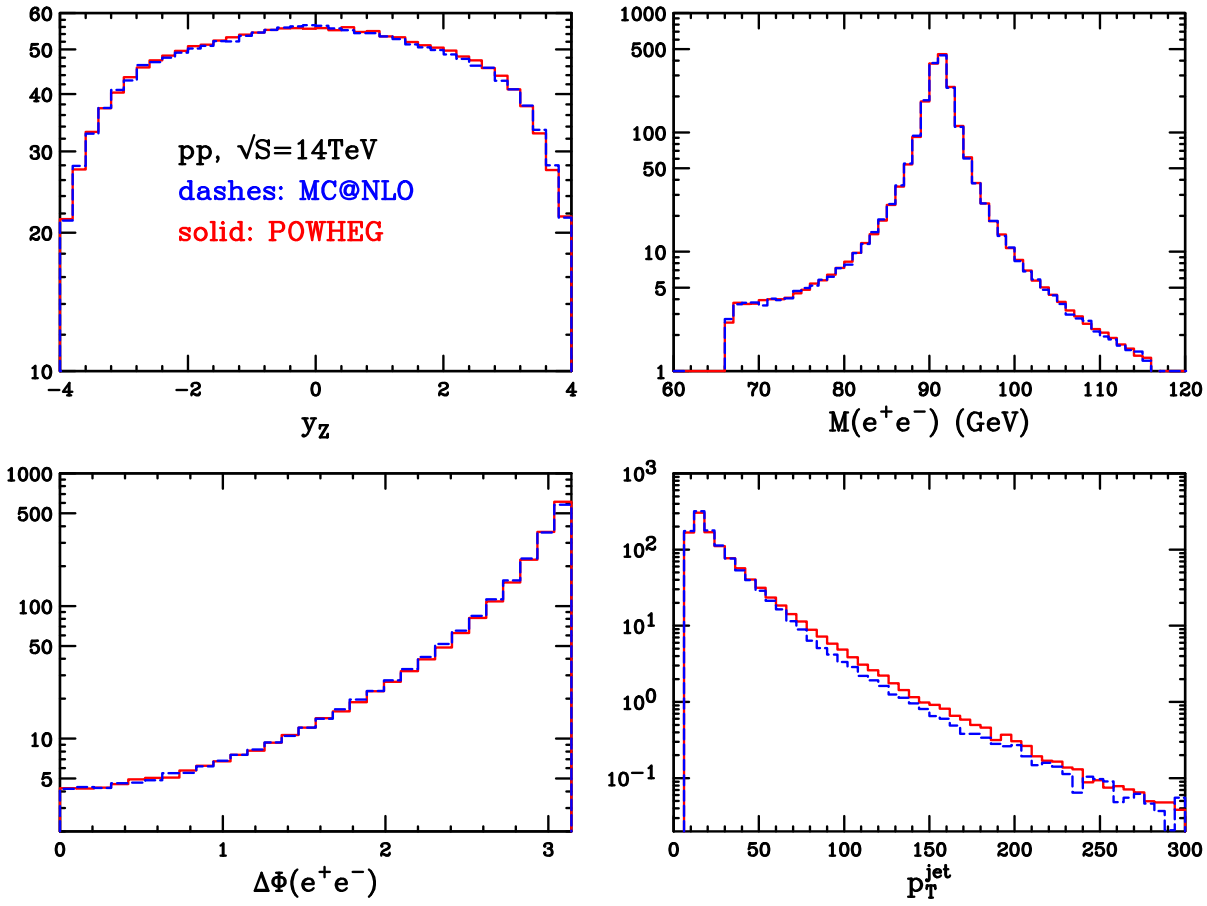

Figure 3.5: Same as fig. 3.2 for the LHC at 14 TeV.

refs. [72–74] at $\sqrt{S} = 1800$ GeV. The POWHEG+HERWIG and the MC@NLO output are obtained with an intrinsic transverse momentum of the incoming partons equal to 2.5 GeV (HERWIG's PTRMS parameter). Both data and predictions are normalized to 1. The difference in the shape of the distributions at 1960 and 1800 GeV are only minimal. We see that POWHEG with PYTHIA is in remarkable agreement with the MC@NLO result. On the other hand, standalone PYTHIA is closer to the output of POWHEG with HERWIG. In all cases, the agreement with data is fair, but not optimal. It is thus clear that this distributions is sensitive to long distance effects like hadronization and transverse-momentum smearing, and good agreement with data may only achieved by suitable tuning of the non-perturbative parameters of the shower Monte Carlo.

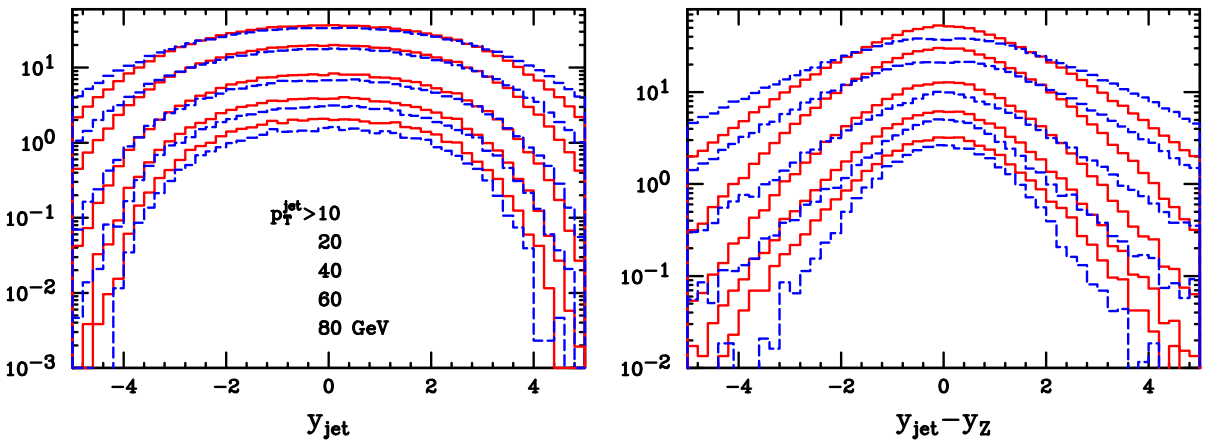

Figure 3.6: Same as fig. 3.3 at the LHC at 14 TeV.

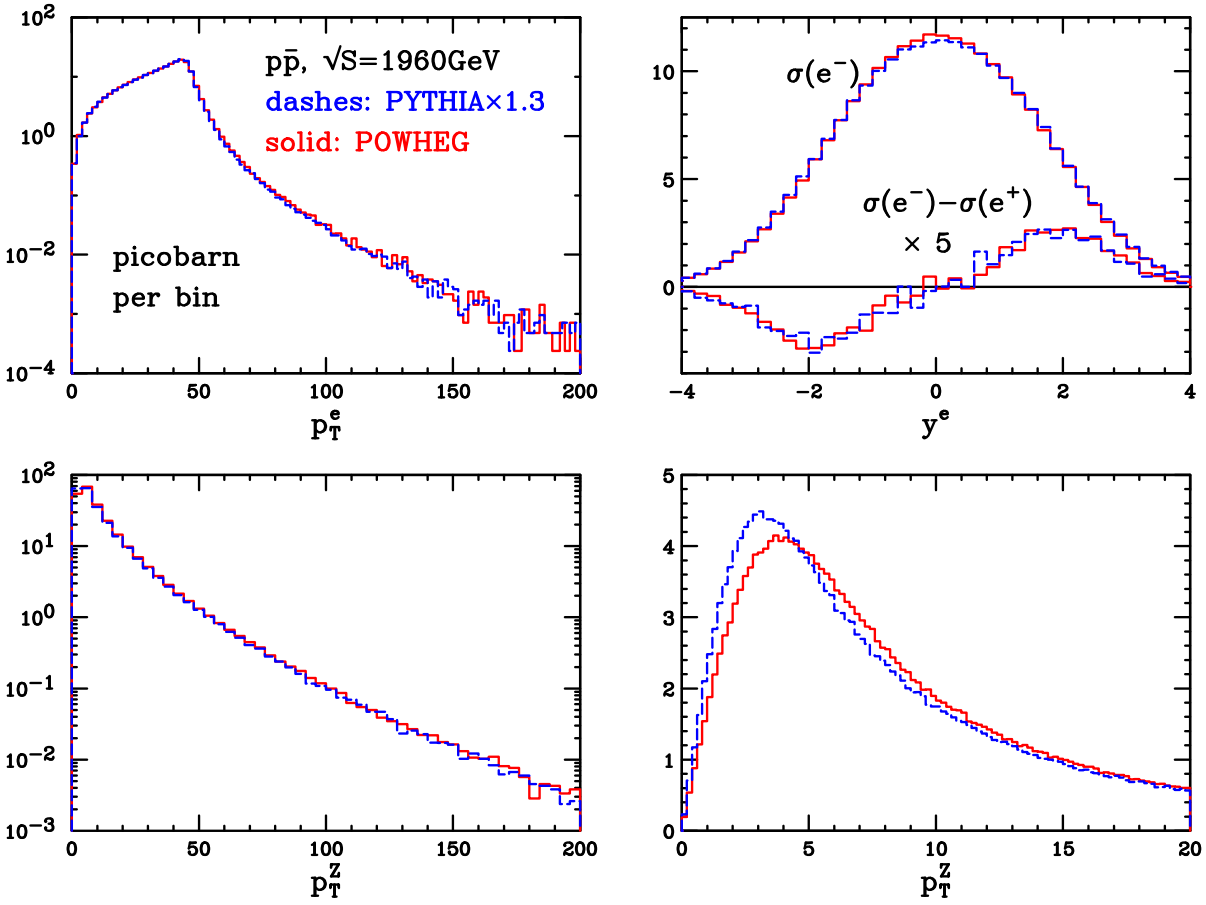

Figure 3.7: Same as fig. 3.1 for a PYTHIA and POWHEG comparison at the Tevatron.

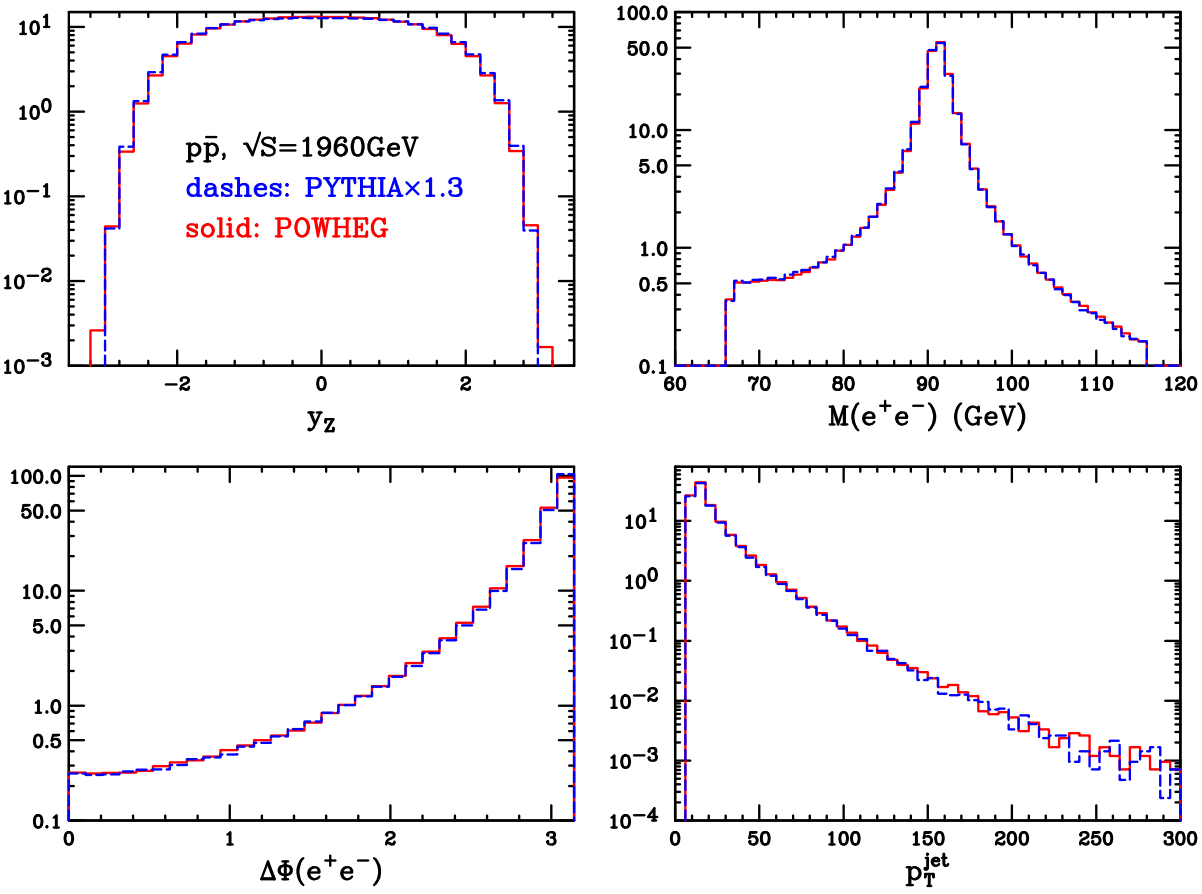

Figure 3.8: Same as fig. 3.2 for a PYTHIA and POWHEG comparison at the Tevatron.

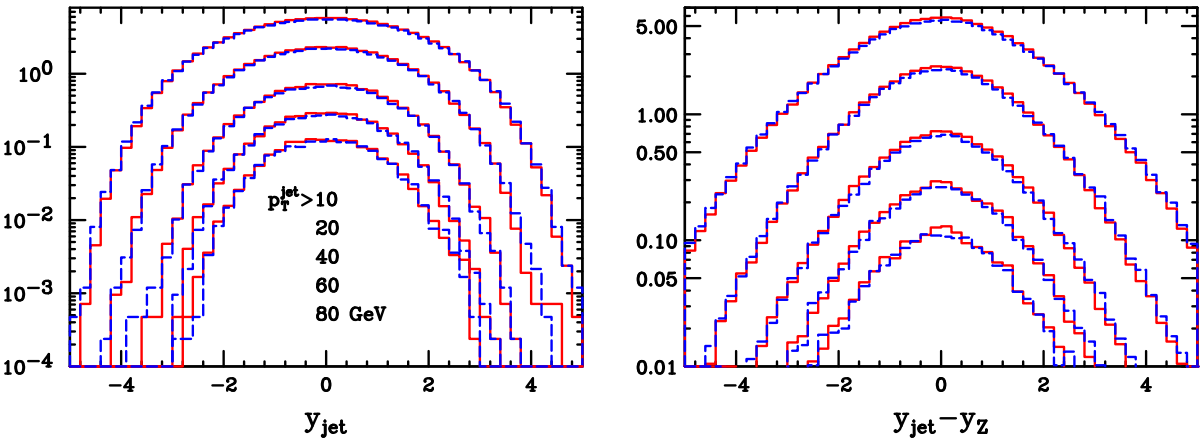

Figure 3.9: Same as fig. 3.3 for a PYTHIA and POWHEG comparison at the Tevatron.

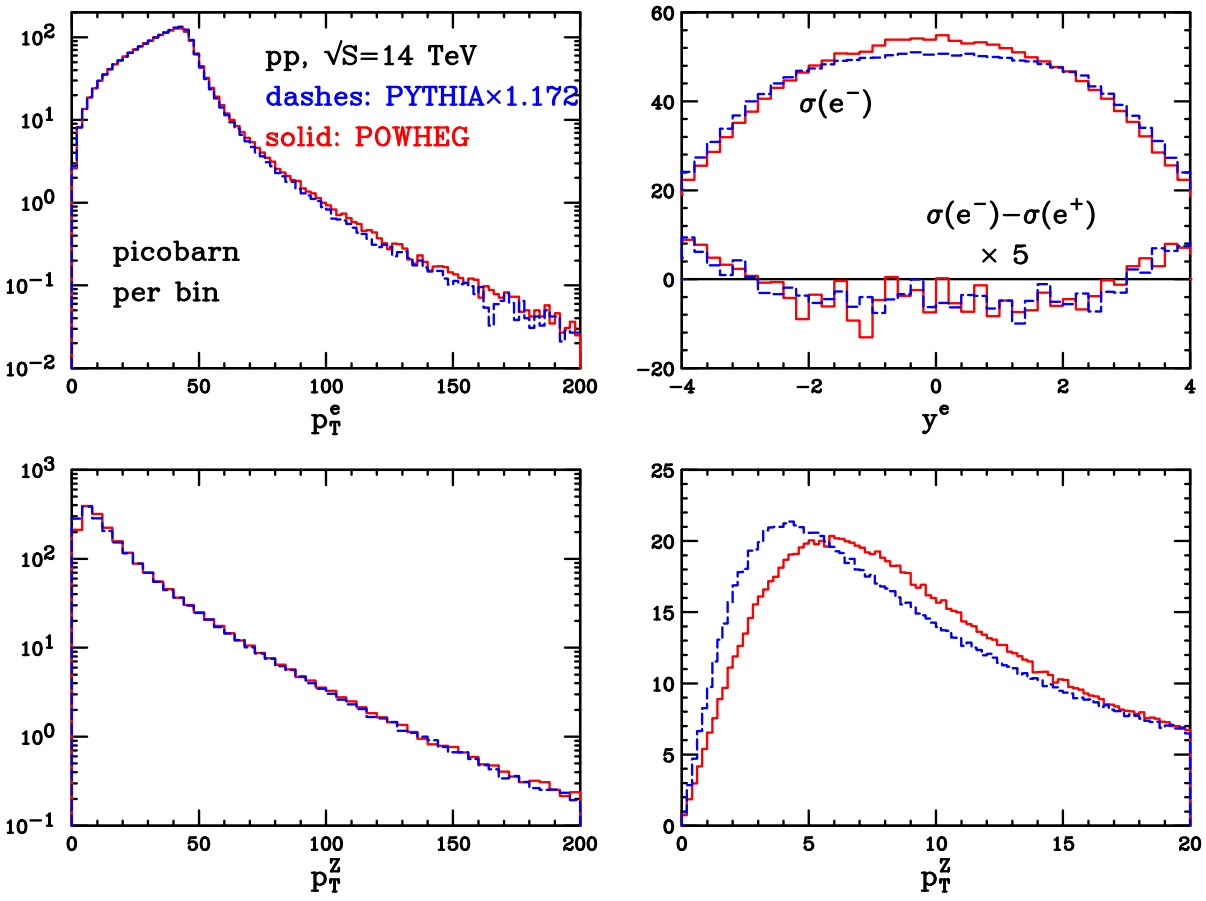

Figure 3.10: Same as fig. 3.1 for a PYTHIA and POWHEG comparison at the LHC.

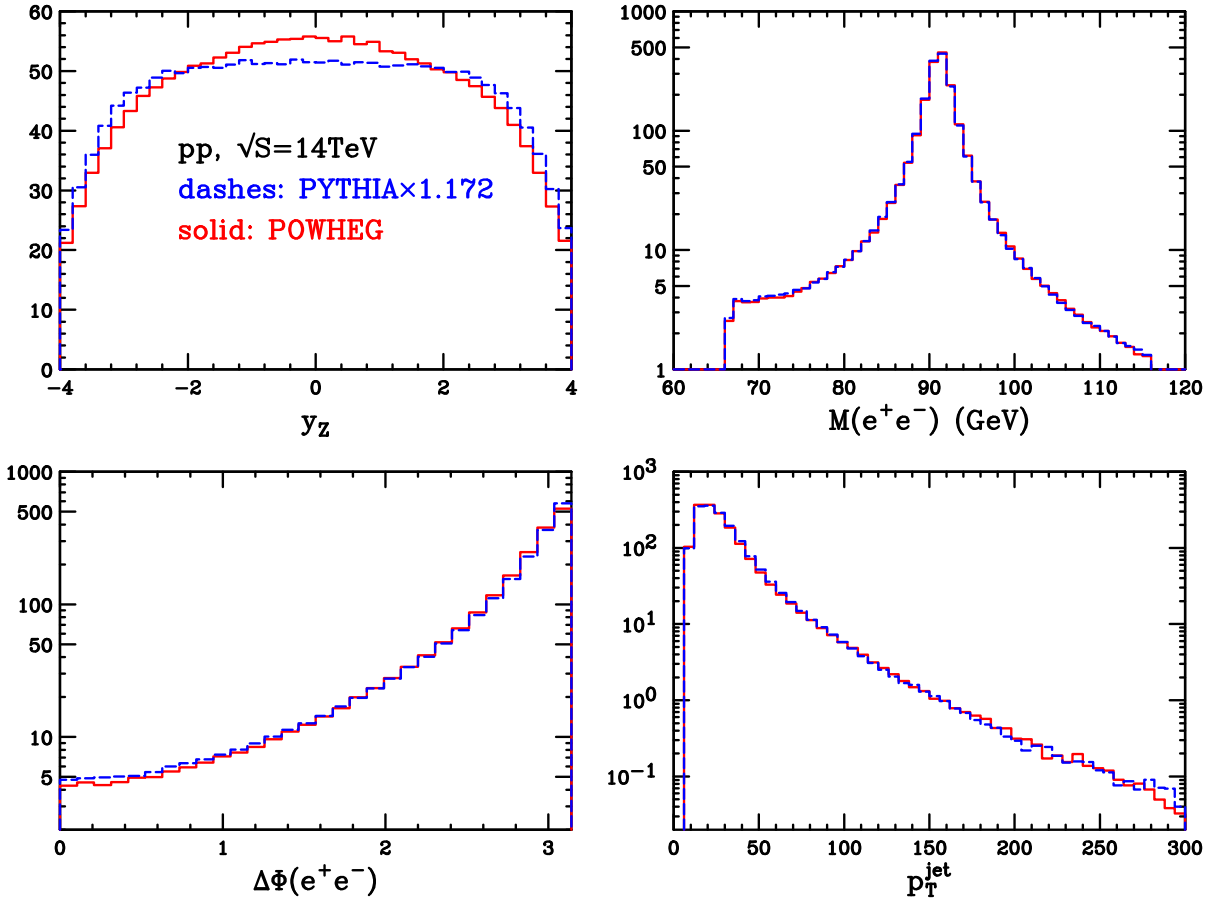

Figure 3.11: Same as fig. 3.2 for a PYTHIA and POWHEG comparison at the LHC.

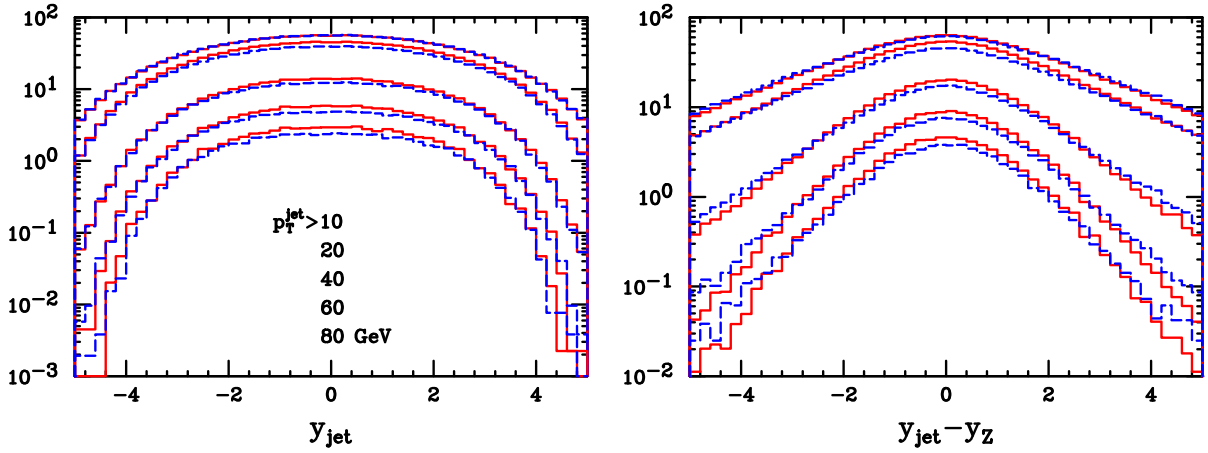

Figure 3.12: Same as fig. 3.3 for a PYTHIA and POWHEG comparison at the LHC.

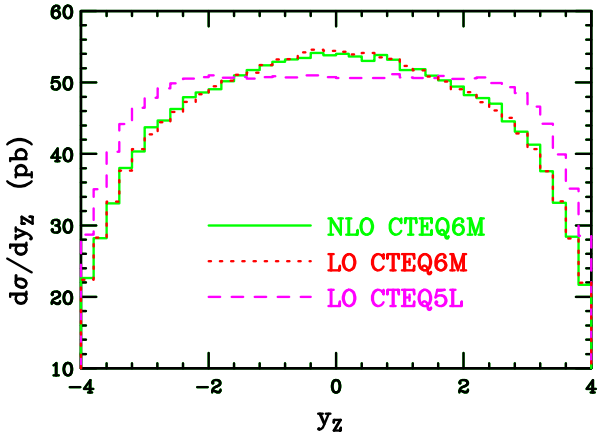

Figure 3.13: Rapidity distribution for the Z boson, computed at fixed order at LO and NLO. For the LO result, both the CTEQ6M and the CTEQ5L parton-density set were used. The plots are normalized to the NLO total cross section.

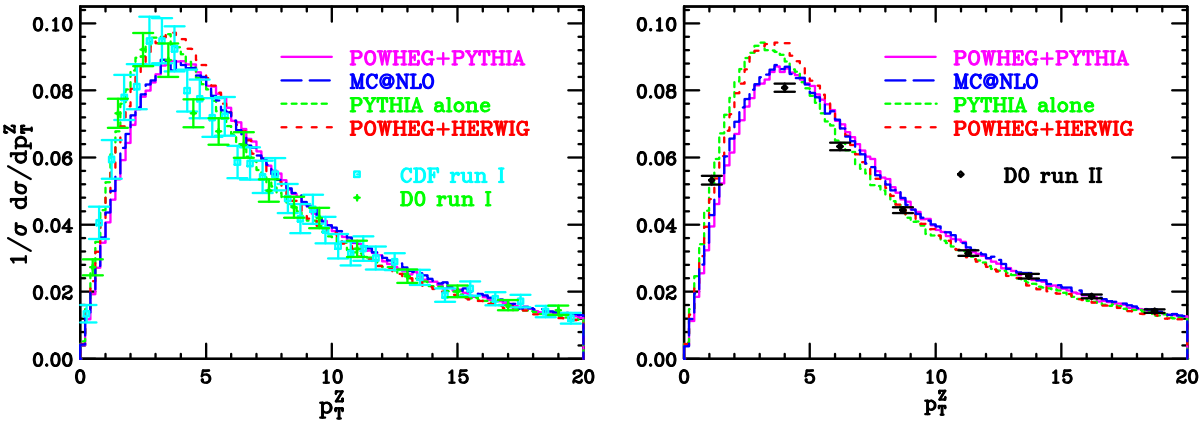

Figure 3.14: Comparison of transverse-momentum distributions of the Z bosons with data from the Tevatron.

3.3.3 Hardest-jet rapidity distribution and dips

The discrepancy of POWHEG and MC@NLO in the rapidity distribution of the hardest jet deserves further discussion. A first study of these features was performed in ref. [69], for $t\bar{t}$ production. It was shown there that the HERWIG Monte Carlo displays an even stronger dip than MC@NLO. The MC@NLO generator provides more events that partially fill the dip, thus correcting the NLO inaccuracies of the Shower Monte Carlo.

In the present case we found no dip in the rapidity distribution of the hardest jet in V production (see fig. 3.3). We found instead a dip in the distribution in the rapidity difference between the jet and the vector boson.[6]

Since both MC@NLO and POWHEG are accurate at the NLO, in order to understand the origin of this discrepancy it is natural to look for possible mismatching between the two methods at the NNLO. Moreover, since the POWHEG program, as well as matrix-element generators, generate themselves the full NLO result, and since stronger dips were found by running HERWIG alone, one can guess that, in the NNLO mismatch, something related to the HERWIG shower has to be found. In the following we illustrate a more quantitative explanation, which leads exactly to what we expect qualitatively.[7]

In sec. 2.2.2, eq. (2.9), we introduced the MC@NLO generating functional. The generating functional $\mathcal{F}_{\rm SMC}$ is the HERWIG one, so that, as it stands, eq. (2.9) can not be easily used to estimate the hardest emission cross section of MC@NLO, because the HERWIG shower is ordered in angle: initial emissions do not necessairly coincide with the harder ones. Nevertheless, we can schematically represent the MC@NLO cross section for the hardest emission with the following formula, where we use a notation similar to the one used for POWHEG:

$$\begin{aligned} d\sigma \;=\; & \underbrace{\bar{B}^{\rm MC}(\bar{\mathbf{\Phi}}_n)\, d\bar{\mathbf{\Phi}}_n}_{\mathbb{S}\text{ event}} \underbrace{\left[\Delta^{\rm veto}(\bar{\mathbf{\Phi}}_n, t_0) + \Delta^{\rm veto}(\bar{\mathbf{\Phi}}_n, t)\, \frac{R^{\rm MC}(\mathbf{\Phi}_{n+1})}{B(\bar{\mathbf{\Phi}}_n)}\, d\Phi^{\rm MC}_{\rm rad}\right]}_{\text{MC shower}} \\ & + \underbrace{\Big[R(\mathbf{\Phi}_{n+1}) - R^{\rm MC}(\mathbf{\Phi}_{n+1})\Big]\, d\bar{\mathbf{\Phi}}_n\, d\Phi_{\rm rad}}_{\mathbb{H}\text{ event}}\,. \end{aligned} \tag{3.51}$$

The terminology "$\mathbb{S}$" and "$\mathbb{H}$ events" has been already introduced, and we do not repeat

[6] The distribution in the pseudorapidity difference of the hardest jet with respect to the vector boson was considered in ref. [75], in the context of a comparison of several matrix-element programs. Although noticeable differences are found among the generators considered there, none of them exhibit a dip at zero pseudorapidity.

[7] This possible explanation of the presence of dips in the MC@NLO results has been first proposed in the talks [76–78]. In ref. [79], in the framework of Higgs production, this problem and its Shower Monte Carlo origin was accurately studied too.

it here. We have

$$\bar{B}^{\rm MC}(\bar{\mathbf{\Phi}}_n) = B(\bar{\mathbf{\Phi}}_n) + V(\bar{\mathbf{\Phi}}_n) + \int d\Phi_{\rm rad}\ [R^{\rm MC}(\mathbf{\Phi}_{n+1}) - C(\mathbf{\Phi}_{n+1})]\ , \tag{3.52}$$

$$R^{\rm MC}(\mathbf{\Phi}_{n+1}) = B(\bar{\mathbf{\Phi}}_n)\ \frac{\alpha_{\rm S}(t)}{2\pi}\frac{1}{t}\ P(z)\,, \tag{3.53}$$

$$\Delta^{\rm veto}(\bar{\mathbf{\Phi}}_n, t) = \exp\left\{-\int d\Phi^{\rm MC}_{\rm rad}\ \frac{\alpha_{\rm S}(t)}{2\pi}\frac{1}{t}\ P(z)\,\theta\left(k_{\rm T}(\mathbf{\Phi}_{n+1}) - t\right)\right\}\ , \tag{3.54}$$

where $P(z)$ are the Altarelli-Parisi splitting kernels and $d\Phi_{\rm rad} = d\Phi^{\rm MC}_{\rm rad} \equiv dz\,dt\,d\phi/(2\pi)$.

The "MC shower" factor in eq. (3.51) shows that, for $\mathbb{S}$ events, the hardest emission is produced by running the HERWIG shower Monte Carlo, starting with the event kinematics $\bar{\mathbf{\Phi}}_n$. Despite the fact that an angular-ordered Monte Carlo may not generate the hardest radiation as its first emission, thanks to the presence of $p_{\rm T}$-vetoed Sudakov form factors formula (3.51) does correctly represent the hardest emission probability up to subleading effects, that we here assume to be irrelevant for our argument.[8]

In the production of a high-$p_{\rm T}$ parton, formula (3.51) yields

$$\begin{aligned} d\sigma &\approx \bar{B}^{\rm MC}(\bar{\mathbf{\Phi}}_n)\,\frac{R^{\rm MC}(\mathbf{\Phi}_{n+1})}{B(\bar{\mathbf{\Phi}}_n)}\ d\bar{\mathbf{\Phi}}_n\,d\Phi^{\rm MC}_{\rm rad} + \Big[R(\mathbf{\Phi}_{n+1}) - R^{\rm MC}(\mathbf{\Phi}_{n+1})\Big]\,d\bar{\mathbf{\Phi}}_n\,d\Phi_{\rm rad} \\ &\approx R(\mathbf{\Phi}_{n+1})\,d\bar{\mathbf{\Phi}}_n\,d\Phi_{\rm rad} + \underbrace{\left(\frac{\bar{B}^{\rm MC}(\bar{\mathbf{\Phi}}_n)}{B(\bar{\mathbf{\Phi}}_n)} - 1\right)}_{\mathcal{O}(\alpha_{\rm S})} R^{\rm MC}(\mathbf{\Phi}_{n+1})\,d\bar{\mathbf{\Phi}}_n\,d\Phi^{\rm MC}_{\rm rad}\,, \end{aligned} \tag{3.55}$$

where we have used the fact that $\Delta^{\rm veto}(\bar{\mathbf{\Phi}}_n, t) \approx 1$ in this limit. The first term correctly describes the hard radiation in the whole phase space. The second term is responsible for the dip. In fact, according to our approximation, the dip present in HERWIG comes from the term $R^{\rm MC}(\mathbf{\Phi}_{n+1})\,d\bar{\mathbf{\Phi}}_n\,d\Phi^{\rm MC}_{\rm rad}$, that propagates here with a weight proportional to $(\bar{B}^{\rm MC}/B - 1)$. Although formally subleading in $\alpha_{\rm S}$, this term can be significant for processes with large K factors.

According to this argument, the observed mismatch is expected in the present case, since NLO corrections are found to be non negligible for single vector-boson production.

We also reconsider Z pair production and $t\bar{t}$ production at the Tevatron, and compare POWHEG and MC@NLO results for the rapidity distribution of the hardest jet, and for the distribution in the rapidity difference.[9] The results are shown in figs. 3.15 and 3.16.

[8] More details can be found in ref. [1], where it was shown how to reorganize an angular-ordered shower to generate the hardest emission as the first one.

[9] In fact, it is reasonable to assume that a dip in the rapidity distribution of the jet may be inherited from the dip in the rapidity difference, if the kinematics production regime is forced to be central, like in

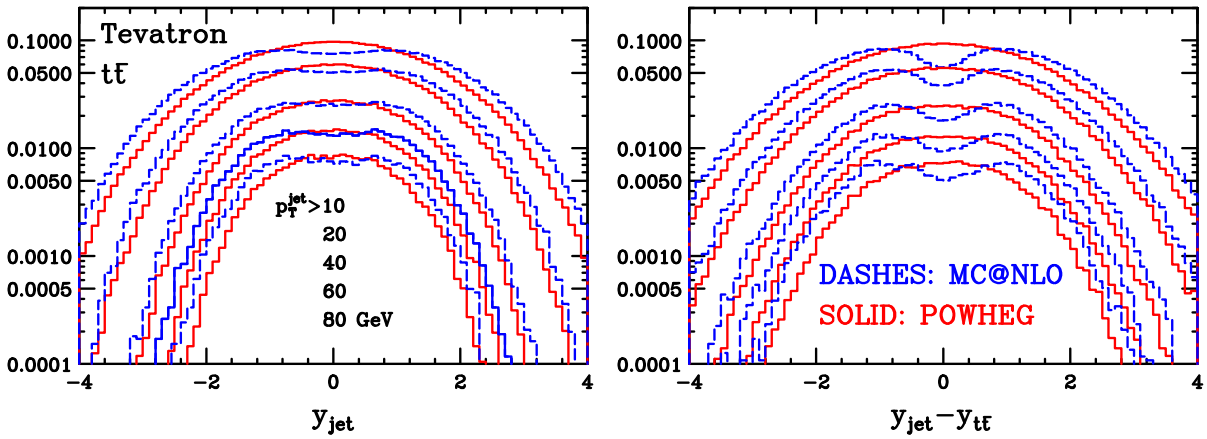

Figure 3.15: Rapidity distribution of the hardest jet and of the rapidity difference between the hardest jet and the $t\bar{t}$ system at Tevatron energies.

From fig. 3.15 we see that the dip present in the $y_{\rm jet}-y_{t\bar{t}}$ distribution is even deeper than the dip observed in the $y_{\rm jet}$ distribution. Furthermore, in fig. 3.16, we see no particular features in the $y_{\rm jet}$ distribution. The $y_{\rm jet}-y_{ZZ}$ distribution displays instead a tiny tower and a dip, depending upon the transverse-momentum cut on the jet.

Finally, for reference, we report also one figure taken from [80], where NLO corrections to the process $gg \to H$ were matched with shower in the POWHEG scheme. In that case, the K factor was very big, and dips effects were more pronounced, as it can be seen in fig. 3.17. From this plot, one can also notice that HERWIG shower is responsible for dips, and that MC@NLO partially fills them.

Finally, we notice that a similar mechanism (i.e. via a large $\bar{B}/B$ factor) for generating large NNLO terms operates also in POWHEG, and has been discussed in ref. [80] in the framework of Higgs production, as being responsible for a hard Higgs boson $p_{\rm T}$ spectrum. In POWHEG, however, this mechanism cannot generate any dip, since here HERWIG has no role in the generation of the hardest radiation.

In chapter 4, we will come back on rapidity dips in sec. 4.3.4. We will see that for processes with small K factors, such as single-top production, dips are less pronounced, or even absent, as the above argument suggests.

the case of top-pair production at the Tevatron.

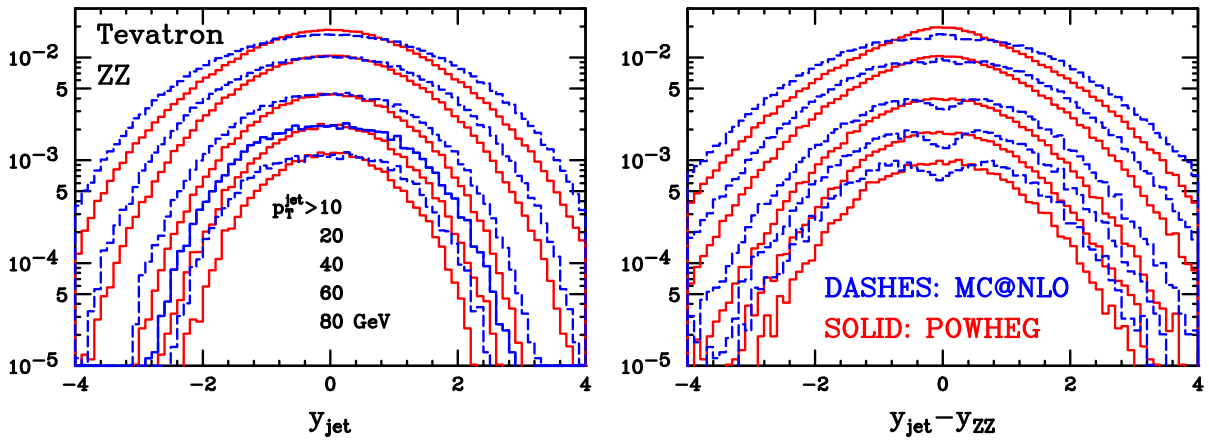

Figure 3.16: Rapidity distribution of the hardest jet and of the rapidity difference between the hardest jet and the ZZ system at Tevatron energies.

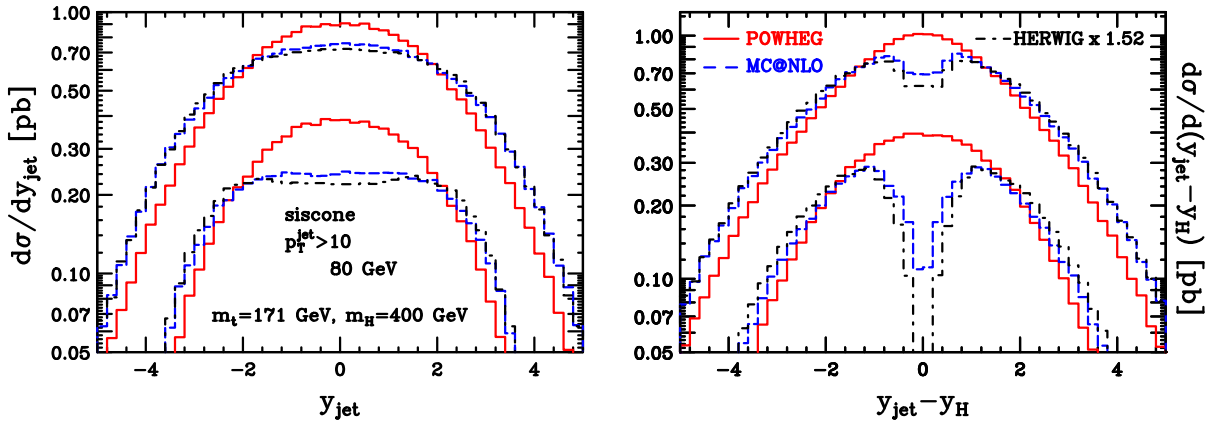

Figure 3.17: Comparison of `POWHEG`, `MC@NLO` and `HERWIG` (without matrix-element corrections), for the rapidity of the leading jet and the rapidity difference of the Higgs boson and the leading jet, defined according to the `SISCONE` algorithm, with different jet cuts.

3.3.4 *W* production at the Tevatron and LHC

All results presented so far are relative to Z boson production. In the case of W production we find similar features and the comparison between MC@NLO and PYTHIA presents very similar characteristics. For the sake of completeness, we present in fig. 3.18 through 3.35 plots of observables for W^- production at the Tevatron, and W^- and W^+ production at the LHC, comparing again the POWHEG output with MC@NLO and PYTHIA, and the observables for W^+ production at the LHC. We find again that MC@NLO displays dips in the rapidity distribution of the hardest jet at Tevatron energy. The comparison of the transverse-momentum distribution of the W shows the same differences found in the Z case. Furthermore, the rapidity distribution of the $W^\pm$ at the LHC differs in PYTHIA, showing a very marked difference in the W^+ case (see fig. 3.34), probably (as in the Z case) a consequence of the different pdf set.

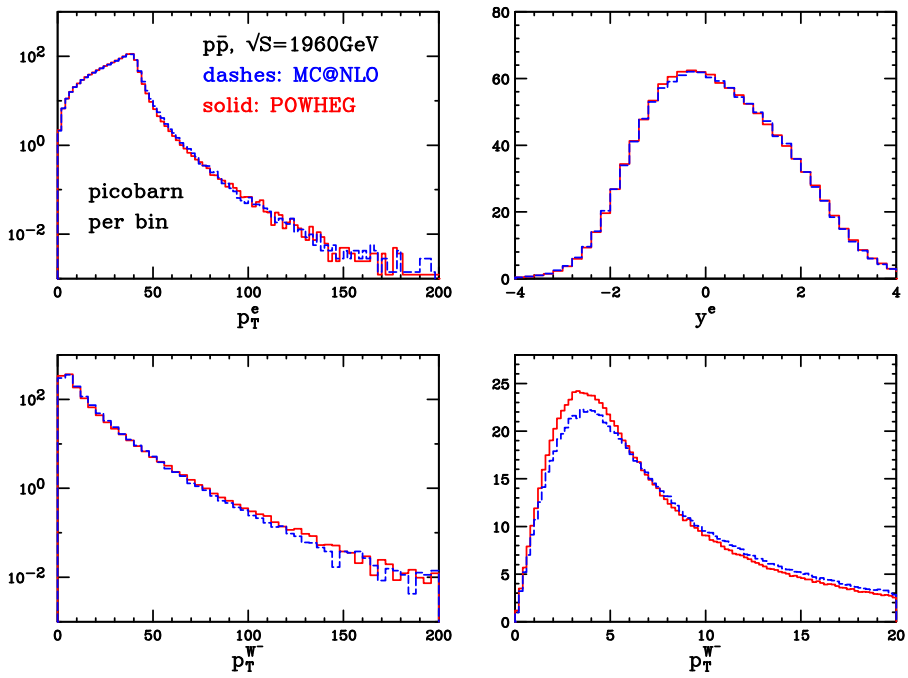

Figure 3.18: Comparison of POWHEG and MC@NLO results for the transverse momentum and rapidity of the lepton coming from the decay of the W^- boson and for the transverse momentum of the W^-, as reconstructed from its decay product.

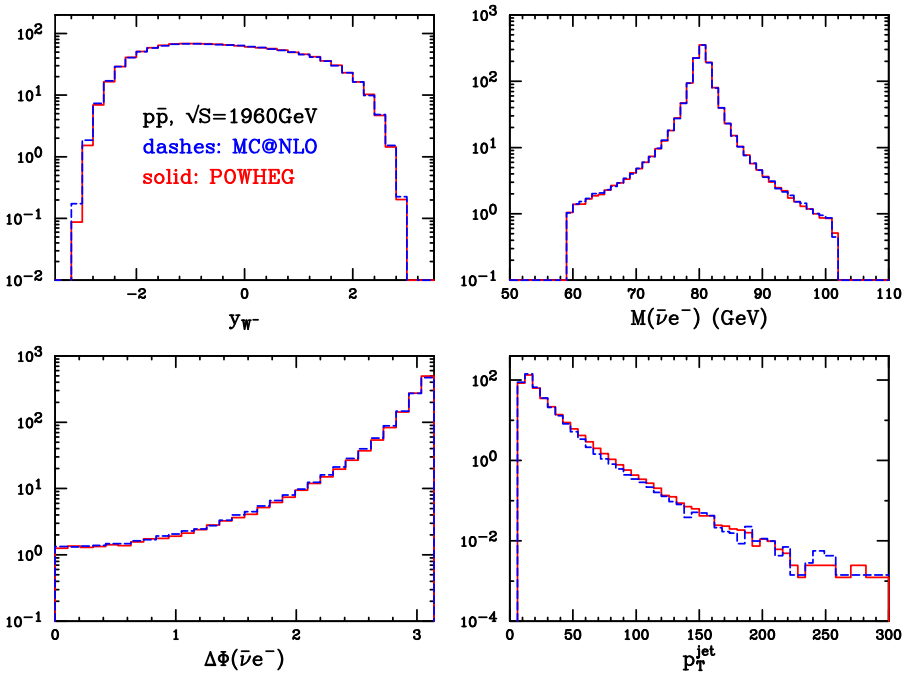

Figure 3.19: Comparison of POWHEG and MC@NLO for the reconstructed W^- rapidity, its invariant mass, the lepton-pair azimuthal distance and the transverse momentum of the reconstructed jet, above a 10 GeV minimum value.

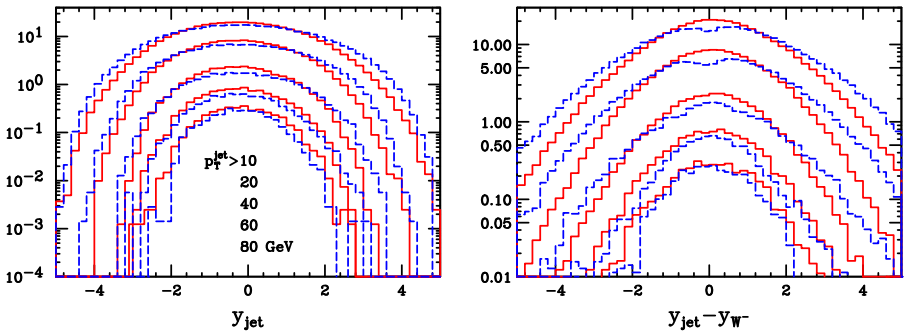

Figure 3.20: Rapidity distribution of the hardest jet with different transverse-momentum cuts, and the rapidity distance between the hardest jet and the reconstructed W^- boson for POWHEG and MC@NLO at the Tevatron.

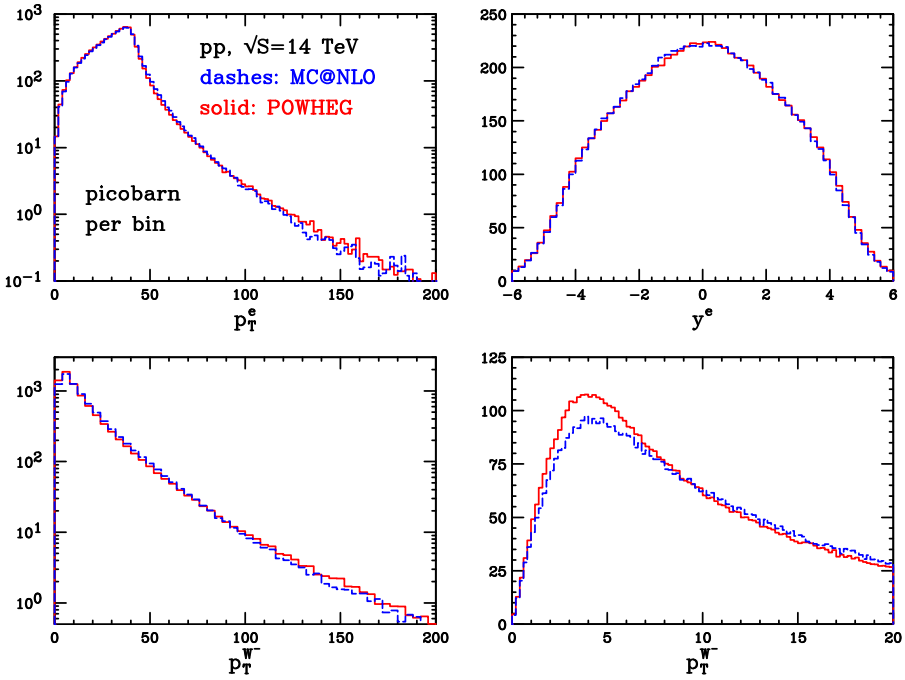

Figure 3.21: Same as fig. 3.18 for the LHC at 14 TeV.

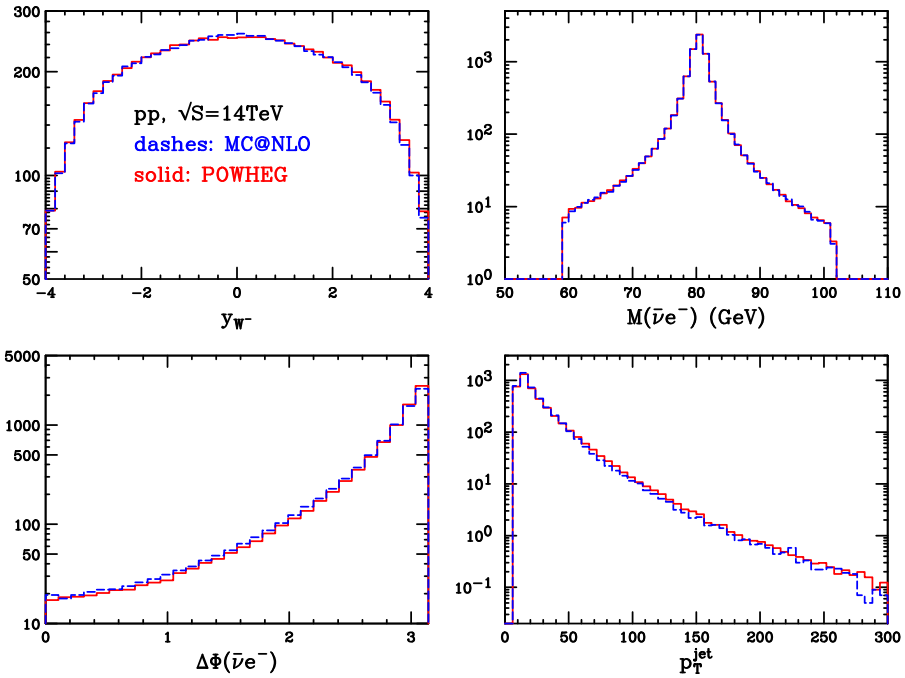

Figure 3.22: Same as fig. 3.19 for the LHC at 14 TeV.

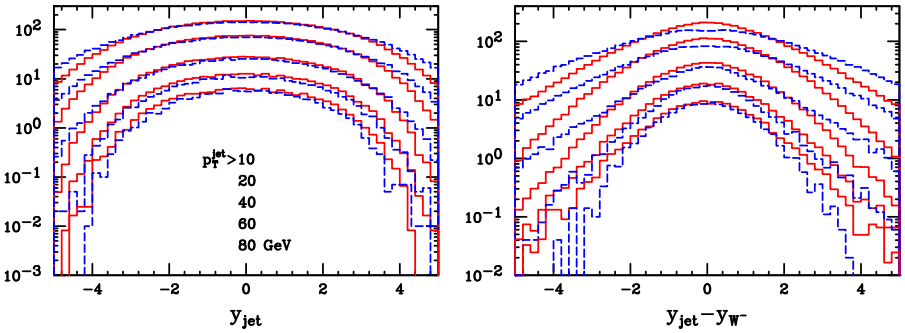

Figure 3.23: Same as fig. 3.20 at the LHC at 14 TeV.

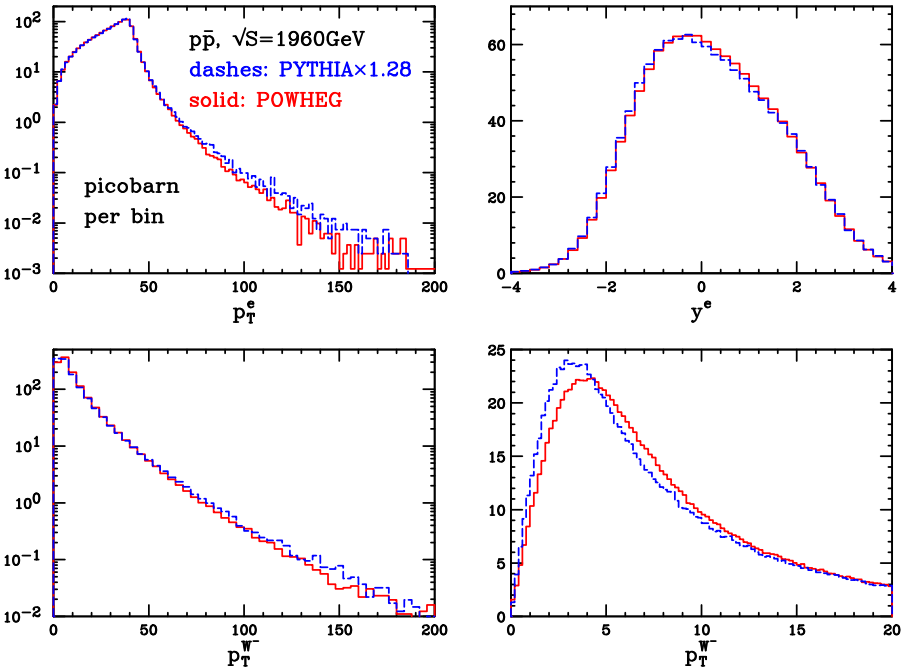

Figure 3.24: Same as fig. 3.18 for a PYTHIA and POWHEG comparison at the Tevatron.

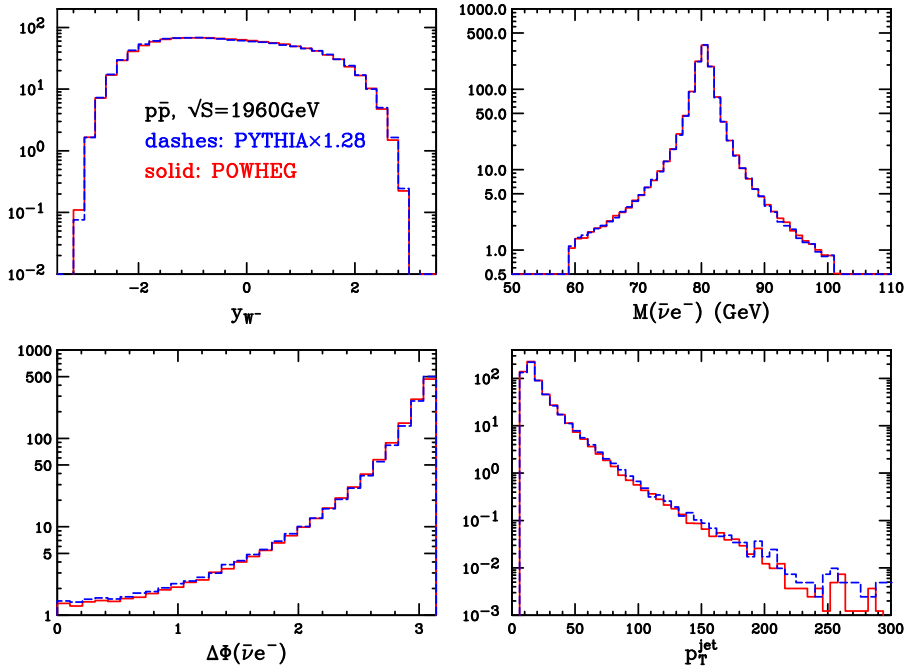

Figure 3.25: Same as fig. 3.19 for a PYTHIA and POWHEG comparison at the Tevatron.

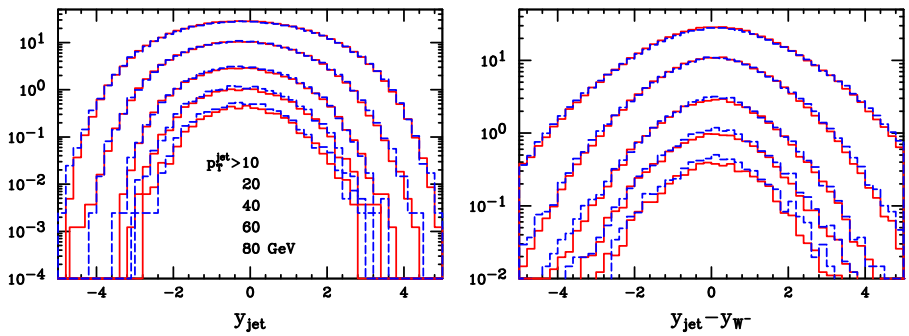

Figure 3.26: Same as fig. 3.20 for a PYTHIA and POWHEG comparison at the Tevatron.

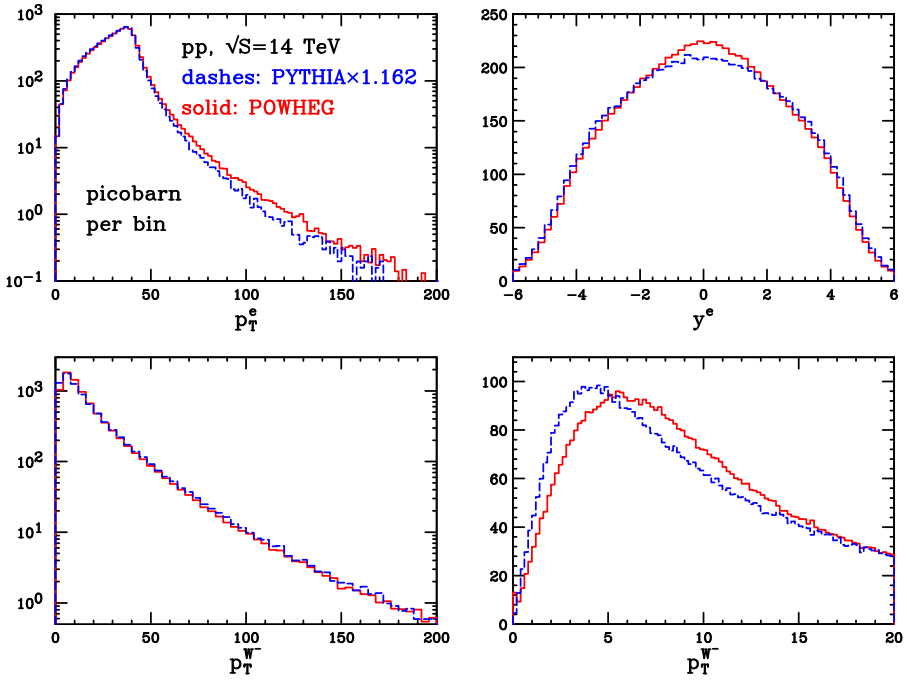

Figure 3.27: Same as fig. 3.18 for a PYTHIA and POWHEG comparison at the LHC.

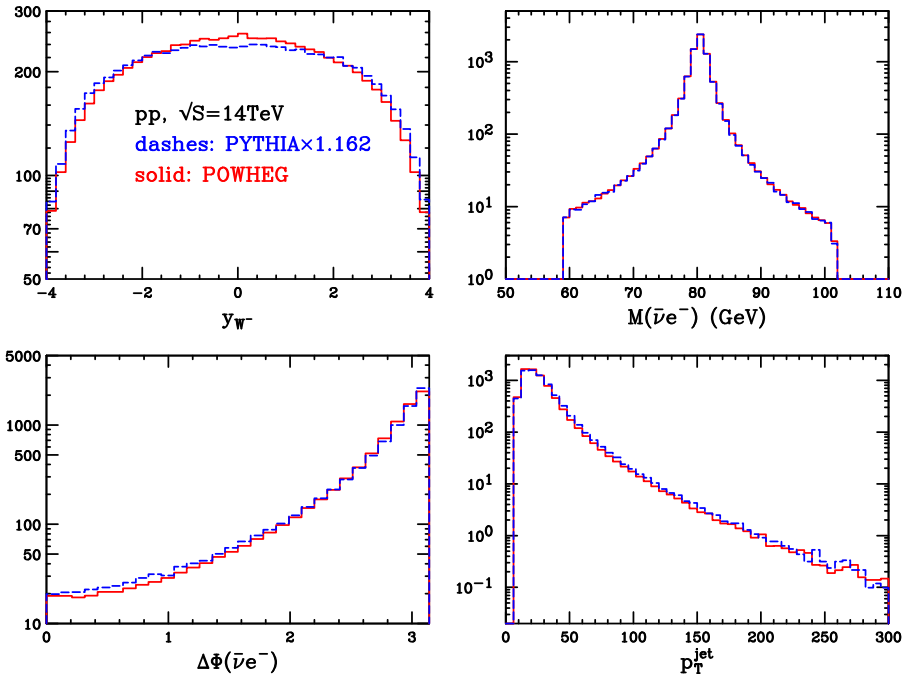

Figure 3.28: Same as fig. 3.19 for a PYTHIA and POWHEG comparison at the LHC.

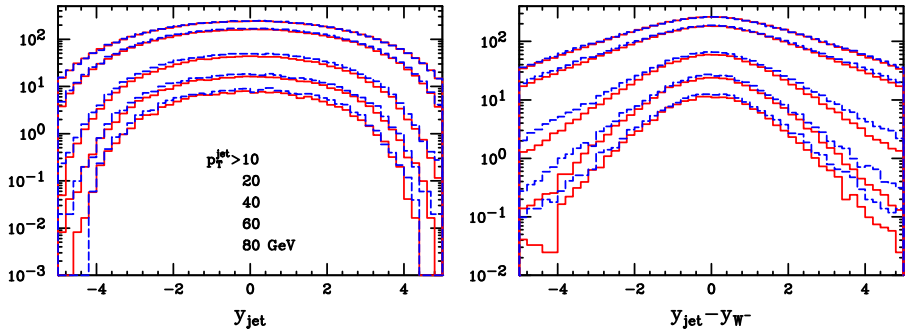

Figure 3.29: Same as fig. 3.20 for a PYTHIA and POWHEG comparison at the LHC.

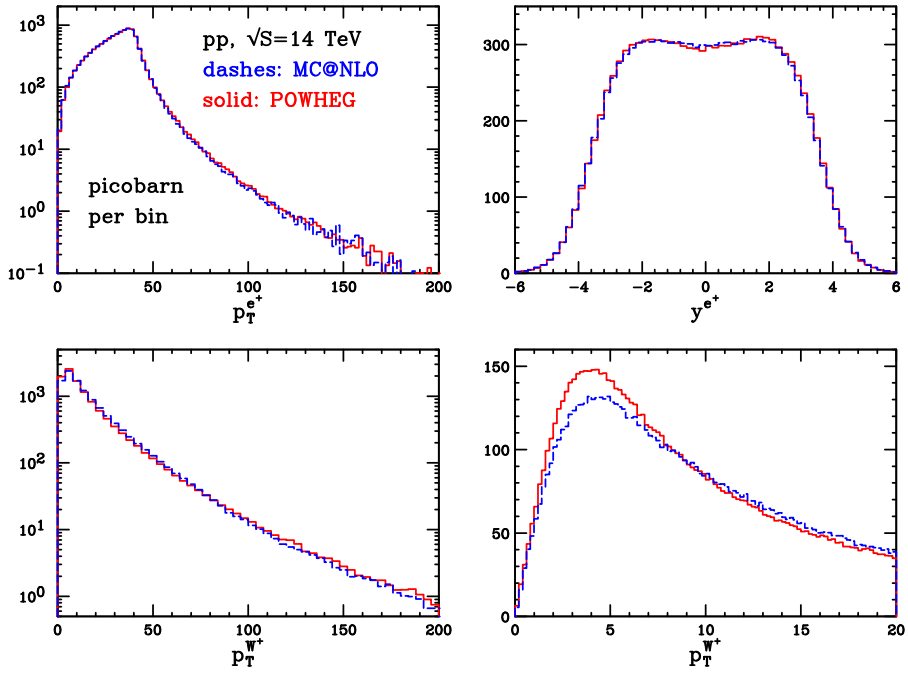

Figure 3.30: Same as fig. 3.21 for W^+ production at the LHC.

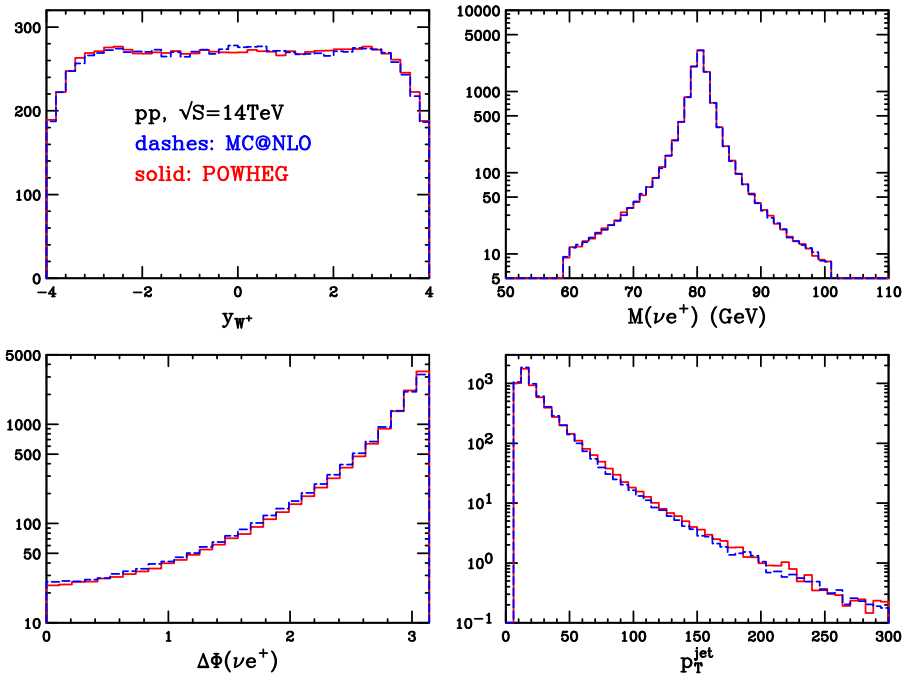

Figure 3.31: Same as fig. 3.22 for W^+ production at the LHC.

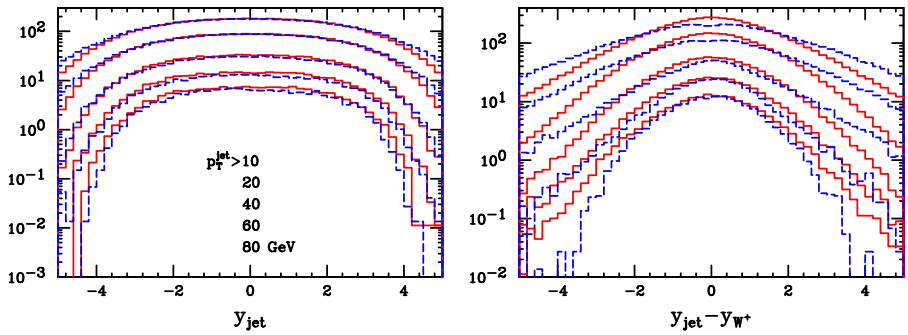

Figure 3.32: Same as fig. 3.23 for W^+ production at the LHC.

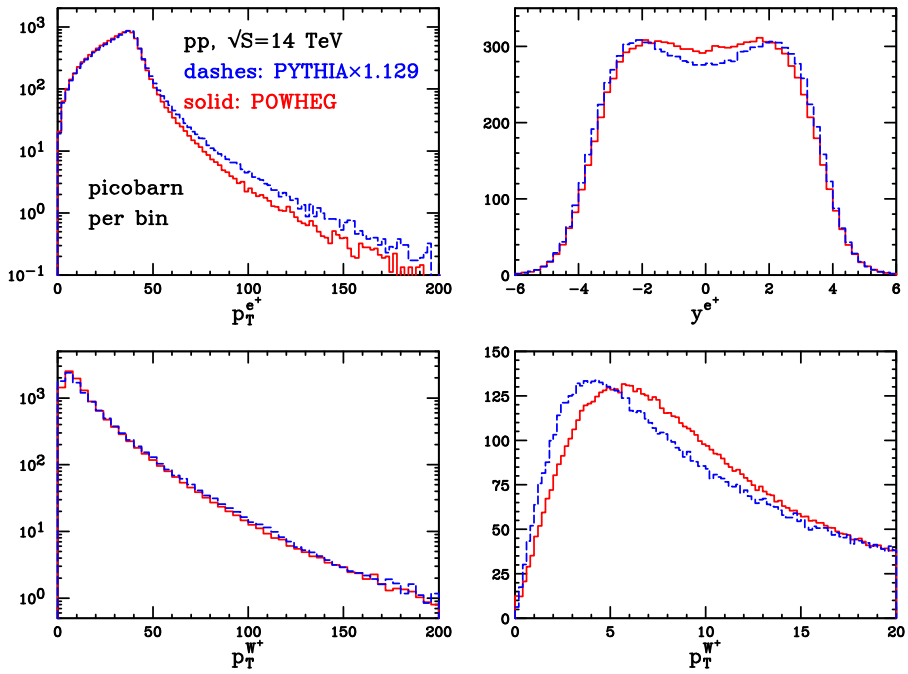

Figure 3.33: Same as fig. 3.27 for W^+ production at the LHC.

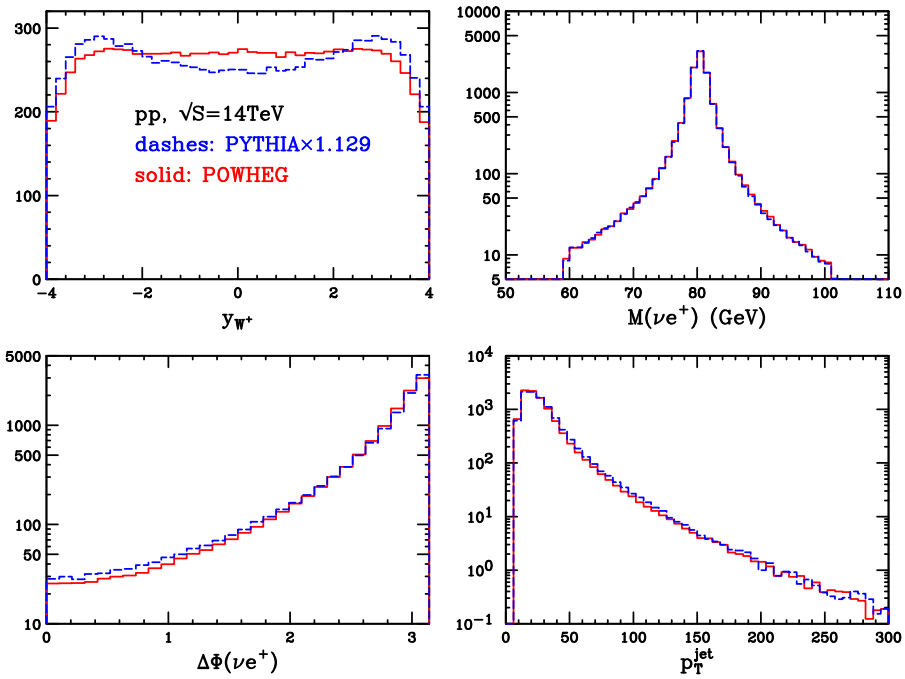

Figure 3.34: Same as fig. 3.28 for W^+ production at the LHC.

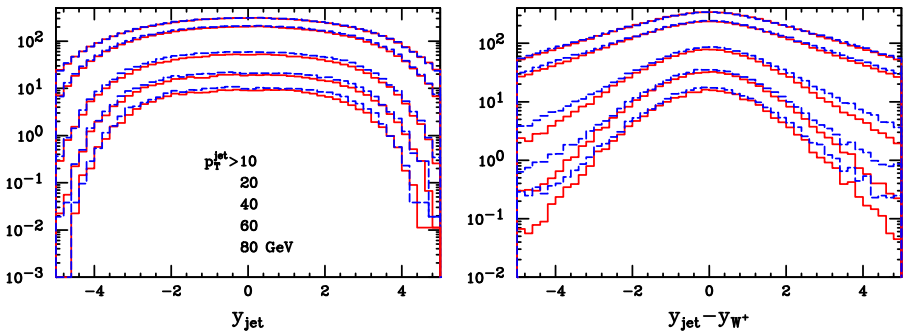

Figure 3.35: Same as fig. 3.29 for W^+ production at the LHC.

3.4 Conclusions

In this chapter we have described a complete implementation of vector-boson production at NLO in the POWHEG framework. The calculation was performed using the Catani-Seymour [64] dipole approach, and thus this is the first POWHEG implementation within the Catani-Seymour framework at a hadronic collider. We have found that, at variance with what was proposed in sec. 7.3 of ref. [2], it is better to define the transverse momentum as the true transverse momentum for the initial-state singular region. Furthermore, we have shown how to perform a POWHEG implementation when the Born term vanishes.

The results of our work have been compare extensively with MC@NLO and PYTHIA. The PYTHIA result, rescaled to the full NLO cross section, is in good agreement with POWHEG, except for differences in the rapidity distribution of the vector boson, that may be ascribed to the use of a LO parton density in PYTHIA. The MC@NLO result is in fair agreement with POWHEG, except for the distribution of the hardest jet in the process, the MC@NLO distribution being generally wider. We carefully examined also the distributions in the difference of the hardest jet and the vector-boson rapidity. We have found that the MC@NLO distributions exhibit dips at zero rapidity, that seem to be a general feature of the MC@NLO approach.

We also gave an explanation for these dips by using an approximate formula for the hardest radiation generated by MC@NLO. We found that these effects are formally subleading, but that, in general, possible dips are more and more pronounced as long as the K factor increases. This explanation seems to be confirmed by analogous distributions obtained with MC@NLO for other processes.

Chapter 4

NLO single-top production matched with shower in POWHEG: s- and t-channel subprocesses

Top-quark production in hadronic collisions has been one of the most studied signal in the last twenty years. Up to recent times, $t\bar{t}$ pair production has been the only observed top-quark source at the Tevatron collider, due to its large, QCD-dominated, cross section. Processes where only one top quark appears in the final state are known in literature as single-top processes. Their cross sections are smaller than the $t\bar{t}$ pair one, due to their weak nature. This fact, together with the presence of large W + jet and $t\bar{t}$ backgrounds, makes the single-top observation very challenging, so that this signal has been observed only recently by the CDF [81] and D0 [82] collaborations.

In spite of its relative small cross section, single-top production is an important signal for several reasons (see also refs. [83, 84] and references therein). Within the Standard Model, the single-top signal allows a direct measurement of the Cabibbo-Kobayashi-Maskawa (CKM) matrix element V_{tb} [85] and of the b parton density. Furthermore, the V-A structure of weak interactions can be directly probed in these processes, since the top quark decays before hadronizing, and its polarization can be directly observed in the angular correlations of its decay products [86, 87]. Finally, single-top processes are expected to be sensitive to several kinds of new physics effects and, in some cases, are the best channels to observe them [88–90]. For all the above reasons, single-top is an important Standard Model processes to be studied at the LHC, where the statistics limitation due to the small cross section is less severe and differential distributions can also be studied.

In order to include a reliable description of both short- and long-distance effects into the simulation of hadronic processes, it is important to consistently match fixed order

results with parton showers. Radiative corrections for single-top production have been known for years [84, 91–98], while the implementation of these results into a next-to-leading-order Shower Monte Carlo (SMC), namely MC@NLO [42,52], is more recent [18,53].

In this chapter, we present a next-to-leading-order (NLO) calculation of s- and t-channel single-top production, interfaced to Shower Monte Carlo programs, according to the POWHEG method. Due to the structure of the Born subprocesses, this is the first POWHEG implementation of a process that has both initial and final state singularities.

This chapter is organized as follows.

In sec. 4.1 we collect the next-to-leading-order cross section formulae and describe the kinematics and the structure of the singularities.

In sec. 4.2 we discuss the POWHEG implementation and how we have included the generation of top-decay products.

In sec. 4.3 we show our results for several kinematic variables. Most of this phenomenological section is devoted to study the comparison of our results with those of MC@NLO. We find fair agreement for almost all the distributions and give some explanations about the differences we found. Some comparisons are carried out also with respect to PYTHIA 6.4, showing that some distributions are strongly affected by the inclusion of NLO effects. Top-decay effects are also discussed. We also studied the problem of rapidity dips in this case. The obtained results, although more difficult to be interpreted with respect to the single vector-boson case, are in agreement with the explanation of their origin that we gave in the previous chapter.

Finally, in sec. 4.4, we give our conclusions.

The content of this chapter is mainly based on the work published in [63].[1]

4.1 Description of the calculation

In this section we present some technical details of the calculation, including the kinematic notation we are going to use throughout the chapter, the relevant differential cross sections up to next-to-leading-order in the strong coupling $\alpha_{\rm S}$ and the subtraction formalism we have used to regularize initial- and final-state singularities. In this chapter, we always refer to top-quark production, since anti-top production is obtained simply by charge conjugation.

[1] A mismatch between the text and the plots relevant for angular correlations in top decay has been found in [63]. In particular, plots presented in [63] were obtained without acceptance cuts. Here we correct that mismatch and we include an updated plot with cuts corresponding to those described in the text.

Single-top production processes are usually divided into three classes, depending on the virtuality of the W boson involved at the leading order:

1. Quark-antiquark annihilation processes, such as

$$u + \bar{d} \to t + \bar{b}\,, \tag{4.1}$$

   are called s-channel processes since the W-boson virtuality is timelike.

2. Processes where the top quark is produced with an exchange of a spacelike W boson, such as

$$b + u \to t + d\,, \tag{4.2}$$

   are called t-channel processes.

3. Processes in which the top quark is produced in association with a real W boson, such as

$$b + g \to t + W\,. \tag{4.3}$$

   These Wt processes have a negligible cross section at the Tevatron, while at the LHC their impact is phenomenologically relevant. The calculation of NLO corrections to Wt processes is also interesting from the theoretical point of view, since the definition of real corrections is not unambiguous [53].

The implementation described in this chapter includes only s- and t-channel processes. In these cases, the `POWHEG` implementation needs to deal with both initial- and final-state singularities, and is thus more involved than in processes previously considered. In this respect, the associated Wt production has only initial-state singularities and is thus analogous to previous `POWHEG` implementations.

In the calculation, all quark masses have been set to zero (except, of course, the top-quark mass) and the full Cabibbo-Kobayashi-Maskawa (CKM) matrix has been taken into account. However, for sake of illustration, we set the CKM matrix equal to the identity in this section.

We refer to chapter 2 (and to ref. [2]) for the notation and for a deeper description of the `POWHEG` method. Here we just recall that with $\mathcal{B}$, $\mathcal{V}$, $\mathcal{R}$ and $\mathcal{G}$ we indicate the Born, virtual, real and collinear contributions respectively, divided by the corresponding flux factor. The same letters, capitalized, are used for quantities multiplied by the luminosity factor. The explicit formulae for these quantities are collected in sec. 4.1.3.

4.1.1 Contributing subprocesses

In the following, we organize and label all the Born and real subprocesses, keeping the distinction between the s- and t-channel contributions. This distinction holds also when real corrections are considered, since, due to color flow, interferences do not arise between real corrections to s- and t-channel Born processes.

1) In the s-channel case, there are only Born processes of the type $qq' \to t\bar{b}$, where q and q' run over all possible different quark and antiquark flavours compatible with the final state. We denote with $\mathcal{B}_{qq'}$ the (summed and averaged) squared amplitude, divided by the flux factor. The corresponding real correction contributions include processes with an outgoing or an incoming gluon, i.e. processes of type $qq' \to t\bar{b}g$, $gq \to t\bar{b}q'$ and $qg \to t\bar{b}q'$. We denote these contributions with $\mathcal{R}_{qq'}$, $\mathcal{R}_{gq,(s)}$ and $\mathcal{R}_{qg,(s)}$. Summarizing, we have

process	notation	contributing subprocesses
$qq' \to t\bar{b}$	$\mathcal{B}_{qq'}$	$u\bar{d} \to t\bar{b}$, $\bar{d}u \to t\bar{b}$
$qq' \to t\bar{b}g$	$\mathcal{R}_{qq'}$	$u\bar{d} \to t\bar{b}g$, $\bar{d}u \to t\bar{b}g$
$gq \to t\bar{b}q'$	$\mathcal{R}_{gq,(s)}$	$gu \to t\bar{b}d$, $g\bar{d} \to t\bar{b}\bar{u}$
$qg \to t\bar{b}q'$	$\mathcal{R}_{qg,(s)}$	$ug \to t\bar{b}d$, $\bar{d}g \to t\bar{b}\bar{u}$

where u and d stand for a generic up- or down-type light quark.

2) In the t-channel case, there are only Born processes of the type $qb \to tq'$ (and $bq \to tq'$), where q and q' run over all possible flavours and anti-flavours. Their contributions are denoted $\mathcal{B}_{qb}$ ($\mathcal{B}_{bq}$). We use this notation since we want to keep track of the down-type quark connected to the top quark. The structure of real corrections is more complex in this case. Contributions obtained from the previous processes by simply adding an outgoing gluon, $qb \to tq'g$, will be denoted as $\mathcal{R}_{qb}$. The subprocesses generated by an initial-state gluon splitting into a quark-antiquark pair are designated by $\mathcal{R}_{qg,(t)}$ for $qg \to tq'\bar{b}$ $\left(\mathcal{R}_{gq,(t)} \text{ for } gq \to tq'\bar{b}\right)$ and $\mathcal{R}_{gb}$ for $gb \to t\bar{q}q'$ $\left(\mathcal{R}_{bg} \text{ for } bg \to t\bar{q}q'\right)$. In the former case q and q' are connected via a Wqq' vertex, while the gluon splits into a $b\bar{b}$ pair, so the top quark is color connected with the incoming gluon. In the latter case the situation is opposite, since the gluon splits into a $q\bar{q}$ pair, while the incoming b is directly CKM-connected to the top quark. This gives rise to a different singularities structure, which we take into account in dealing with the $qg \to tq'\bar{b}$ ($gq \to tq'\bar{b}$) and $gb \to t\bar{q}q'$ ($bg \to t\bar{q}q'$) processes separately. Summarizing

process	notation	contributing subprocesses
$bq \to tq'$	$\mathcal{B}_{bq}$	$bu \to td$, $b\bar{d} \to t\bar{u}$
$qb \to tq'$	$\mathcal{B}_{qb}$	$ub \to td$, $\bar{d}b \to t\bar{u}$
$bq \to tq'g$	$\mathcal{R}_{bq}$	$bu \to tdg$, $b\bar{d} \to t\bar{u}g$
$qb \to tq'g$	$\mathcal{R}_{qb}$	$ub \to tdg$, $\bar{d}b \to t\bar{u}g$
$gq \to tq'\bar{b}$	$\mathcal{R}_{gq,(t)}$	$gu \to td\bar{b}$, $g\bar{d} \to t\bar{u}\bar{b}$
$qg \to tq'\bar{b}$	$\mathcal{R}_{qg,(t)}$	$ug \to td\bar{b}$, $\bar{d}g \to t\bar{u}\bar{b}$
$gb \to t\bar{q}q'$	$\mathcal{R}_{gb}$	$gb \to t\bar{u}d$
$bg \to t\bar{q}q'$	$\mathcal{R}_{bg}$	$bg \to t\bar{u}d$

where u and d stand for a generic up- or down-type light quark.

In order to distinguish s- and t-channel real processes with the same flavour structure, we have used the subscript (s) and (t) on the $\mathcal{R}_{gq}$ and $\mathcal{R}_{qg}$ contributions. As already stated, these contributions do not interfere owing to different color structures, so we can keep them distinct. We have drawn a sample of Feynman diagrams for s- and t-channel $gu \to td\bar{b}$ scattering in fig. 4.1.

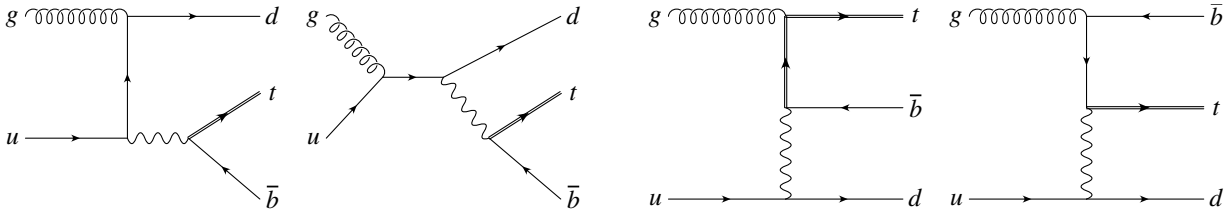

(a) s-channel (b) t-channel

Figure 4.1: Graphs corresponding to s- and t-channel contributions to the real scattering $gu \to td\bar{b}$.

4.1.2 Kinematics and singularities structure

Born kinematics

At variance with the notation used in chapter 2 and 3, for sake of simplicity, in this chapter we will not distinguish between Born and underlying-Born kinematics. Hence, Born variables will be indicated with barred symbols from the beginning, and the identification with the underlying-Born variables will be total.

We denote with $\bar{k}_\oplus$ and $\bar{k}_\ominus$ the incoming quark momenta, aligned along the plus and minus direction of the z axis, by $\bar{k}_1$ the outgoing top-quark momentum and by $\bar{k}_2$ the other outgoing light-parton momentum. The final-state top-quark virtuality will be denoted by M^2, so that $\bar{k}_1^2 = M^2$. The top quark on-shell condition is $M^2 = m_t^2$, where m_t is the top-quark mass. If $K_\oplus$ and $K_\ominus$ are the momenta of the incoming hadrons, then we have

$$\bar{k}_{\circledast} = \bar{x}_{\circledast} K_{\circledast} \,, \tag{4.4}$$

where $\bar{x}_{\circledast}$ are the momentum fractions, and momentum conservation reads

$$\bar{k}_\oplus + \bar{k}_\ominus = \bar{k}_1 + \bar{k}_2 \,. \tag{4.5}$$

We introduce the variables

$$\bar{s} = (\bar{k}_\oplus + \bar{k}_\ominus)^2, \qquad \bar{Y} = \frac{1}{2} \log \frac{(\bar{k}_\oplus + \bar{k}_\ominus)^0 + (\bar{k}_\oplus + \bar{k}_\ominus)^3}{(\bar{k}_\oplus + \bar{k}_\ominus)^0 - (\bar{k}_\oplus + \bar{k}_\ominus)^3} \,, \tag{4.6}$$

and $\bar{\theta}_1$, the angle between the outgoing top quark and the $\bar{k}_\oplus$ momentum, in the partonic center-of-mass (CM) frame. We denote with $\bar{\phi}_1$ the azimuthal angle of the outgoing top quark in the same reference frame. Since the differential cross sections do not depend on the overall azimuthal orientation of the outgoing partons, we set this angle to zero. At the end of the generation of an event, we perform a uniform, random azimuthal rotation of the whole event, in order to cover the whole final-state phase space. The set of variables $\bar{\mathbf{\Phi}}_2 \equiv \left\{\bar{s}, \bar{Y}, \bar{\theta}_1, \bar{\phi}_1\right\}$ fully parametrizes the Born kinematics. From them, we can reconstruct the momentum fractions

$$\bar{x}_\oplus = \sqrt{\frac{\bar{s}}{S}}\, e^{\bar{Y}}, \qquad \bar{x}_\ominus = \sqrt{\frac{\bar{s}}{S}}\, e^{-\bar{Y}} \,, \tag{4.7}$$

where $S = (K_\oplus + K_\ominus)^2$ is the squared CM energy of the hadronic collider. The outgoing momenta are first reconstructed in their longitudinal rest frame, where $\bar{Y} = 0$. In this frame, their energies are

$$\bar{k}_1^0|_{\bar{Y}=0} = \sqrt{\left(\frac{\bar{s} - M^2}{2\sqrt{\bar{s}}}\right)^2 + M^2} \qquad \text{and} \qquad \bar{k}_2^0|_{\bar{Y}=0} = \frac{\bar{s} - M^2}{2\sqrt{\bar{s}}}. \tag{4.8}$$

The two spatial momenta are obviously opposite and both have modulus equal to $\bar{k}_2^0|_{\bar{Y}=0}$. We fix the top-quark momentum to form an angle $\bar{\theta}_1$ with the $\oplus$ direction and to have zero azimuth (i.e. it lies in the xz plane and has positive x component). Both $\bar{k}_1$ and $\bar{k}_2$

are then boosted back in the laboratory frame, with boost rapidity $\bar{Y}$. The Born phase space, in terms of these variables, can be written as

$$\begin{aligned} d\bar{\mathbf{\Phi}}_2 &= d\bar{x}_\oplus\, d\bar{x}_\ominus (2\pi)^4 \delta^4\big(\bar{k}_\oplus + \bar{k}_\ominus - \bar{k}_1 - \bar{k}_2\big)\, \frac{d^3\bar{k}_1}{(2\pi)^3 2\bar{k}_1^0}\, \frac{d^3\bar{k}_2}{(2\pi)^3 2\bar{k}_2^0} \\ &= \frac{1}{S}\frac{\beta}{16\pi}\, d\bar{s}\; d\bar{Y}\; d\cos\bar{\theta}_1\; \frac{d\bar{\phi}_1}{2\pi}\,, \end{aligned} \tag{4.9}$$

where

$$\beta = 1 - \frac{M^2}{\bar{s}}\,. \tag{4.10}$$

We generate the top quark with virtuality M^2 and decay it with a method analogous to the one adopted in ref. [99], that will be described in sec. 4.2.3. We take into account the top finite width by first introducing a trivial integration $\int dM^2\; \delta(M^2 - m_t^2)$ in eq. (4.9) and then by performing the replacement

$$\delta\big(M^2 - m_t^2\big) \;\to\; \frac{1}{\pi}\frac{m_t\,\Gamma_t}{\big(M^2 - m_t^2\big)^2 + \big(m_t^2\,\Gamma_t^2\big)}\,. \tag{4.11}$$

With this substitution, the final expression for the Born phase space reads

$$d\bar{\mathbf{\Phi}}_2 = \frac{1}{S}\frac{\beta}{16\pi^2}\, \frac{m_t\,\Gamma_t}{\big(M^2 - m_t^2\big)^2 + m_t^2\,\Gamma_t^2}\, dM^2\, d\bar{s}\, d\bar{Y}\, d\cos\bar{\theta}_1\, \frac{d\bar{\phi}_1}{2\pi}\,. \tag{4.12}$$

Real-emission kinematics

Real-emission processes have an additional final-state parton that can be emitted from an incoming leg only ($\mathcal{R}_{gq,(s)}$, $\mathcal{R}_{qg,(s)}$, $\mathcal{R}_{gq,(t)}$, $\mathcal{R}_{qg,(t)}$, $\mathcal{R}_{gb}$, $\mathcal{R}_{bg}$) or from both an initial- and final-state leg ($\mathcal{R}_{qq'}$, $\mathcal{R}_{bq}$, $\mathcal{R}_{qb}$). We need then to use two different parametrizations of the real phase space, one to deal with initial-state singularities and one for final-state ones. We treat the radiation kinematics according to the variant of the Frixione, Kunszt and Signer (FKS) subtraction scheme [16, 17] illustrated in ref. [2]. Before giving all the technical details, we summarize briefly how the procedure works:

- We split each real squared amplitude into contributions that have at most one collinear (and/or one soft) singularity.

- We build the collinear (and soft) subtraction terms needed to deal with that singularity.

- We choose the emission phase-space parametrization suited for the singularity we integrate on.

In the FKS method, the singular regions associated with the $\oplus$ and $\ominus$ legs are treated with the same kinematics. Nevertheless, we have decided to split these two different contributions in order to gain a clear subtraction structure.

We now describe the procedure used to split real squared amplitudes and the corresponding phase-space parametrizations. Subtraction terms will then be given in sec. 4.1.3. We proceed as follows:

1. We start by considering real processes that have both initial- and final-state emissions, namely the $\mathcal{R}_{qq'}$, $\mathcal{R}_{bq}$ and $\mathcal{R}_{qb}$ contributions. In this case, the FKS parton is the outgoing gluon and we choose it to be the last particle. We denote its momentum by k_3, so that momentum conservation reads

$$k_\oplus + k_\ominus = k_1 + k_2 + k_3, \tag{4.13}$$

where $k_\oplus$, $k_\ominus$, k_1 and k_2 label the same particles of the underlying Born process. The FKS parton can become collinear to one of the incoming legs or to the other massless final-state leg, so we need to introduce a set of functions to project out these different singular regions. The general properties these functions have to satisfy were given in sec. 1.2.3. In this `POWHEG` implementation, we use[2]

$$\mathcal{S}^{3,\oplus} = \mathcal{D}^{-1}\,\frac{1}{d_{3,\oplus}}\,, \qquad \mathcal{S}^{3,\ominus} = \mathcal{D}^{-1}\,\frac{1}{d_{3,\ominus}}\,, \qquad \mathcal{S}^{3,2} = \mathcal{D}^{-1}\,\frac{1}{d_{3,2}}\,, \tag{4.14}$$

where

$$\mathcal{D} = \frac{1}{d_{3,\oplus}} + \frac{1}{d_{3,\ominus}} + \frac{1}{d_{3,2}} \qquad \text{and} \qquad d_{i,j} = k_i \cdot k_j\,. \tag{4.15}$$

For any given kinematic configuration, these functions satisfy

$$\mathcal{S}^{3,\oplus} + \mathcal{S}^{3,\ominus} + \mathcal{S}^{3,2} = 1. \tag{4.16}$$

The separation among different singular regions is performed multiplying each real contribution with the corresponding $\mathcal{S}$ function. For example, for the s-channel $\mathcal{R}_{qq'}$

[2]Note that our choice corresponds to the one described in sec. 2.4 of ref. [2], with the choice $a = b = 1$.

case, we have

$$\begin{aligned}\mathcal{R}^{3,\oplus}_{qq'} &= \mathcal{R}_{qq'}\,\mathcal{S}^{3,\oplus},\\ \mathcal{R}^{3,\ominus}_{qq'} &= \mathcal{R}_{qq'}\,\mathcal{S}^{3,\ominus},\\ \mathcal{R}^{3,2}_{qq'} &= \mathcal{R}_{qq'}\,\mathcal{S}^{3,2}.\end{aligned} \tag{4.17}$$

These contributions are now singular only when the FKS parton becomes collinear to $k_\oplus$, $k_\ominus$ and k_2 respectively, or soft. Analogous relations hold for $\mathcal{R}_{bq}$ and $\mathcal{R}_{qb}$.

2. Next we consider the real process $gb \to t\bar{q}q'$. It is singular when $\bar{q}$ or q' become collinear to the incoming gluon, so that the FKS parton can be respectively $\bar{q}$ or q' and we need again a set of functions to project out the different singular regions. Recalling the labeling of the momenta

$$g\,(k_\oplus)\,b\,(k_\ominus) \to\; t\,(k_1)\,\bar{q}\,(k_2)\,q'\,(k_3)\,,$$

we introduce the projecting functions

$$\begin{aligned}\mathcal{S}^{2,\oplus} &= \left(\frac{1}{d_{2,\oplus}}+\frac{1}{d_{3,\oplus}}\right)^{-1}\frac{1}{d_{2,\oplus}}\,,\\ \mathcal{S}^{3,\oplus} &= \left(\frac{1}{d_{2,\oplus}}+\frac{1}{d_{3,\oplus}}\right)^{-1}\frac{1}{d_{3,\oplus}}\,,\end{aligned} \tag{4.18}$$

to isolate the region where $k_2\cdot k_\oplus \to 0$ or $k_3\cdot k_\oplus \to 0$. We have then the two contributions

$$\begin{aligned}\mathcal{R}^{3,\oplus}_{gb} &= \mathcal{R}_{gb}\,\mathcal{S}^{3,\oplus}\,,\\ \mathcal{R}^{2,\oplus}_{gb} &= \mathcal{R}_{gb}\,\mathcal{S}^{2,\oplus}\,,\end{aligned} \tag{4.19}$$

coming from $\mathcal{R}_{gb}$. For $bg \to t\bar{q}q'$, analogous contributions can be obtained from eqs. (4.18) and (4.19) with the substitutions $\mathcal{R}_{gb} \to \mathcal{R}_{bg}$ and $\oplus \to \ominus$.

3. To deal with the remaining real contributions we do not need to introduce any other $\mathcal{S}$ function, since each of them is singular in one region only (the $\oplus$ one for $\mathcal{R}_{gq,(s)}$ and $\mathcal{R}_{qq,(t)}$, the $\ominus$ one for $\mathcal{R}_{qg,(s)}$ and $\mathcal{R}_{qg,(t)}$).

Having split all real contributions in such a way that each term has at most one singularity, we can associate with each of them a particular phase-space parametrization, suitable to handle that singularity structure. In the following we summarize the reconstruction

procedure (or inverse construction) needed to build the real-emission kinematics, given the underlying Born one, and a set of three radiation variables. For all the details, we refer to sec. 5 of ref. [2].

Parametrization of the initial-state radiation (ISR) phase space

The FKS method uses the same phase-space parametrization for describing both the $\oplus$ and $\ominus$ singular regions. The set of radiation variables

$$\Phi_{\rm rad}^{\rm ISR} = \{\xi,\ y,\ \phi\}\,, \tag{4.20}$$

together with the Born ones, completely reconstruct the real-event kinematics: $\mathbf{\Phi}_3 \equiv \left\{\bar{s}, \bar{Y}, \bar{\theta}_1, \xi, y, \phi\right\}$. Using eq. (4.7), we can compute the underlying Born momentum fractions $\bar{x}_{\oplus}$ and, from them, we obtain

$$x_{\oplus} = \frac{\bar{x}_{\oplus}}{\sqrt{1-\xi}}\sqrt{\frac{2-\xi(1-y)}{2-\xi(1+y)}}, \qquad x_{\ominus} = \frac{\bar{x}_{\ominus}}{\sqrt{1-\xi}}\sqrt{\frac{2-\xi(1+y)}{2-\xi(1-y)}}, \tag{4.21}$$

with the kinematics constraints

$$0 \le \xi \le \xi_{\rm M}(y)\,, \tag{4.22}$$

where

$$\xi_{\rm M}(y) = 1 - \max\left\{\frac{2(1+y)\,\bar{x}_{\oplus}^2}{\sqrt{(1+\bar{x}_{\oplus}^2)^2(1-y)^2 + 16\,y\,\bar{x}_{\oplus}^2} + (1-y)(1-\bar{x}_{\oplus}^2)}, \frac{2(1-y)\,\bar{x}_{\ominus}^2}{\sqrt{(1+\bar{x}_{\ominus}^2)^2(1+y)^2 - 16\,y\,\bar{x}_{\ominus}^2} + (1+y)(1-\bar{x}_{\ominus}^2)}\right\}. \tag{4.23}$$

In the laboratory frame, the incoming momenta are given by

$$k_{\circledast} = x_{\circledast} K_{\circledast}\,. \tag{4.24}$$

In the partonic center-of-mass frame, we define the FKS parton to have momentum

$$k_3' = k_3'^0\ (1, \sin\theta\sin\phi, \sin\theta\cos\phi, \cos\theta), \tag{4.25}$$

where

$$k_3'^0 = \frac{\sqrt{s}}{2}\xi, \qquad \cos\theta = y\,, \tag{4.26}$$

and

$$s = (k_\oplus + k_\ominus)^2 = \frac{\bar{s}}{1-\xi}. \tag{4.27}$$

From eqs. (4.25) and (4.26), we see that the soft limit is approached when $\xi \to 0$, while the collinear limits are characterized by $y \to 1$ (k_3 parallel to the $\oplus$ direction) or $y \to -1$ (k_3 parallel to the $\ominus$ direction).

Boosting k_3' back in the laboratory frame with longitudinal velocity $(x_\oplus - x_\ominus)/(x_\oplus + x_\ominus)$ we obtain k_3. Having computed k_3 and $k_{\oplus}$, we can construct $k_{\rm tot} = k_\oplus + k_\ominus - k_3$, while from the underlying Born momenta we have $\bar{k}_{\rm tot} = \bar{k}_1 + \bar{k}_2$. We construct then the longitudinal boost $\mathbb{B}_L$, with boost velocity $\vec{\beta}_L = (0, 0, \beta_L)$, where

$$\beta_L = -\frac{\bar{x}_\oplus - \bar{x}_\ominus}{\bar{x}_\oplus + \bar{x}_\ominus}\,, \tag{4.28}$$

so that the boosted momentum $k''_{\rm tot} = \mathbb{B}_L k_{\rm tot}$ has zero longitudinal component. In addition we define

$$\vec{\beta}_T = -\frac{\vec{k}''_{\rm tot}}{k''^{\,0}_{\rm tot}} \tag{4.29}$$

and the corresponding (transverse) boost $\mathbb{B}_T$, so that $\mathbb{B}_T k''_{\rm tot}$ has zero transverse momentum. The final-state momenta k_1 and k_2 in the laboratory frame are obtained with the following boost sequence

$$k_i = \mathbb{B}_L^{-1}\, \mathbb{B}_T^{-1}\, \mathbb{B}_L\, \bar{k}_i\,, \qquad i = 1, 2\,. \tag{4.30}$$

Finally, the three-body phase space can be written, in a factorized form, in terms of the Born and radiation phase space

$$d\mathbf{\Phi}_3 = dx_\oplus\, dx_\ominus (2\pi)^4 \delta^4(k_\oplus + k_\ominus - k_1 - k_2 - k_3) \frac{d^3k_1}{(2\pi)^3 2k_1^0} \frac{d^3k_2}{(2\pi)^3 2k_2^0} \frac{d^3k_3}{(2\pi)^3 2k_3^0} = d\bar{\mathbf{\Phi}}_2\, d\Phi_{\rm rad}^{\rm ISR}\,, \tag{4.31}$$

where

$$d\Phi_{\rm rad}^{\rm ISR} = \frac{s}{(4\pi)^3}\, \frac{\xi}{1-\xi}\, d\xi\, dy\, d\phi \equiv J_{\rm rad}^{\rm ISR}\big(\bar{\mathbf{\Phi}}_2, \Phi_{\rm rad}^{\rm ISR}\big)\; d\xi\, dy\, d\phi\,, \tag{4.32}$$

that defines the Jacobian $J_{\rm rad}^{\rm ISR}$ of the change of variables.

Parametrization of the final-state radiation (FSR) phase space

For the FSR phase-space parametrization $\Phi_{\rm rad}^{\rm FSR}$, we use the same notation as for the initial-state case $\Phi_{\rm rad}^{\rm ISR}$ (see eq. (4.20)). We define, in the partonic center-of-mass frame,

$$\xi = \frac{2k_3^0}{q^0}\,, \qquad y = \frac{\vec{k}_3\cdot\vec{k}_2}{\underline{k}_3\,\underline{k}_2}\,, \qquad \phi = \phi\left(\vec{\eta}\times\vec{k},\ \vec{k}_3\times\vec{k}\right), \tag{4.33}$$

where

$$q = k_\oplus + k_\ominus\,, \qquad k = k_2 + k_3\,, \tag{4.34}$$

and the notation $\underline{p}$ stands for $|\vec{p}|$. We denote with $\vec{\eta}$ an arbitrary direction that serves as origin for the azimuthal angle of $\vec{k}_3$ around $\vec{k}$, while "$\times$" is the cross vector product. The notation $\phi(\vec{v}_1,\vec{v}_2)$ indicates the angle between $\vec{v}_1$ and $\vec{v}_2$, so that ϕ is the azimuth of the vector $\vec{k}_3$ around the direction $\vec{k}$.[3]

From eq. (4.33) we see that the soft limit is approached when $\xi\to 0$, while the collinear limit is characterized by $y\to 1$ (k_3 parallel to k_2).

Given the set of variables $\mathbf{\Phi}_3 \equiv \left\{\bar{s},\bar{Y},\bar{\theta}_1,\xi,y,\phi\right\}$ we can reconstruct the full real-event kinematics. The momentum fractions $x_{\circledast}$ are the same as the underlying Born ones, since the emission from a final-state leg does not affect them, so that

$$x_\oplus = \bar{x}_\oplus\,, \qquad x_\ominus = \bar{x}_\ominus \qquad \text{and} \qquad s = \bar{s}\,. \tag{4.35}$$

Inverting the first identity in eq. (4.33), we immediately have

$$k_3^0 = \underline{k}_3 = \xi\frac{q^0}{2}\,, \tag{4.36}$$

where ξ is limited by

$$0 \le \xi \le \xi_{\rm M} \equiv \frac{q^2 - M_{\rm rec}^2}{q^2}\,, \tag{4.37}$$

with

$$M_{\rm rec}^2 = (q-\bar{k}_2)^2 = k_1^2\,. \tag{4.38}$$

The energy (and the modulus) of the other light outgoing parton, always in the partonic center-of-mass frame, is given by

$$k_2^0 = \underline{k}_2 = \frac{q^2 - M_{\rm rec}^2 - 2q^0\underline{k}_3}{2\left[q^0 - \underline{k}_3\,(1-y)\right]}\,. \tag{4.39}$$

[3]The FKS variant that we use (see ref. [2]) has a slightly different definition of ϕ than the one introduced in the original FKS papers.

Given $\underline{k}_2$ and $\underline{k}_3$ we construct the corresponding vectors $\vec{k}_2$ and $\vec{k}_3$ such that their vector sum $\vec{k}$ is parallel to $\vec{\bar{k}}_2$ and the azimuth of $\vec{k}_3$ relative to $\vec{k}$ (the given reference direction) is ϕ. Having fully defined k_2 and k_3, we can reconstruct the vector k of eq. (4.34) and find $k_{\rm rec} = q - k$. Finally, k_1 can be obtained boosting $\bar{k}_1$ along the $k_{\rm rec}$ direction with boost velocity

$$\vec{\beta} = -\left(\frac{q^2 - (k^0_{\rm rec} + \underline{k}_{\rm rec})^2}{q^2 + (k^0_{\rm rec} + \underline{k}_{\rm rec})^2}\right)\frac{\vec{k}_{\rm rec}}{\underline{k}_{\rm rec}}\,, \tag{4.40}$$

or, alternatively, exploiting momentum conservation of eq. (4.13). To obtain the momenta in the laboratory frame we need to boost back all the outgoing momenta computed in the center-of-mass frame.

In this case too, the three-body phase space can be written in a factorized form in terms of the Born and radiation phase space

$$d\mathbf{\Phi}_3 = dx_\oplus\, dx_\ominus (2\pi)^4 \delta^4(k_\oplus + k_\ominus - k_1 - k_2 - k_3)\frac{d^3k_1}{(2\pi)^3 2k_1^0}\frac{d^3k_2}{(2\pi)^3 2k_2^0}\frac{d^3k_3}{(2\pi)^3 2k_3^0} = d\bar{\mathbf{\Phi}}_2\, d\Phi^{\rm FSR}_{\rm rad}\,, \tag{4.41}$$

where

$$\begin{aligned} d\Phi^{\rm FSR}_{\rm rad} &= \frac{q^2\,\xi}{(4\pi)^3}\frac{\underline{k}_2^2}{\bar{\underline{k}}_2}\left(\underline{k}_2 - \frac{k^2}{2q^0}\right)^{-1} d\xi\, dy\, d\phi \\ &= \frac{s}{(4\pi)^3}\frac{4\,\xi}{\left[2 - \xi\,(1-y)\right]^2}\left(1 - \frac{s\,\xi}{s - M^2_{\rm rec}}\right) d\xi\, dy\, d\phi \equiv J^{\rm FSR}_{\rm rad}\left(\bar{\mathbf{\Phi}}_2, \Phi^{\rm FSR}_{\rm rad}\right)\, d\xi\, dy\, d\phi\,. \end{aligned} \tag{4.42}$$

4.1.3 Squared amplitudes

In order to apply the POWHEG method, we need the Born, real and soft-virtual contributions to the differential cross section, i.e. the squared amplitudes, summed (averaged) over colors and helicities of the outgoing (incoming) partons, and multiplied by the appropriate flux factor. We have taken the Born, real and soft-virtual contributions from the MC@NLO code, testing, where possible, our implementation against MadGraph subroutines [100]. All the matrix elements have been evaluated in the zero-width approximation, i.e. Γ_t and Γ_W are set equal to zero in all the propagators. As already mentioned, to recover finite-width effects in top-decay, the top mass M is generated according to a Breit-Wigner distribution, centered in m_t and with width Γ_t (see eq. (4.11)).

In the following, we give explicit expressions for the Born and collinear remnant contributions. Real and soft-virtual matrix elements are more complicated, and we do not report them explicitly. Nevertheless, we give the soft and collinear limits of the real

amplitude, since these expressions are needed in the FKS subtraction formalism.

Born and virtual contributions

We denote the s-channel squared matrix element for the lowest-order contribution, averaged over color and helicities of the incoming particles, and multiplied by the flux factor $1/(2\bar{s})$, as $\mathcal{B}_{qq'}$. For example, for the $u\bar{d} \to t\bar{b}$ subprocess, we have

$$\mathcal{B}_{u\bar{d}} = \frac{1}{2\bar{s}} \frac{g^4}{4} \bar{u}(\bar{u} - M^2) \left| \frac{1}{\bar{s} - m_W^2} \right|^2 |V_{ud}|^2 |V_{tb}|^2, \tag{4.43}$$

where $\bar{u} = (\bar{k}_\oplus - \bar{k}_2)^2$ is the usual Mandelstam variable, g is the weak coupling ($e = g \sin\theta_W^{\text{eff}}$) and V_{ij}'s are the CKM matrix elements. Crossing eq. (4.43) we have, for the $\bar{d}u$ initiated process,

$$\mathcal{B}_{\bar{d}u} = \frac{1}{2\bar{s}} \frac{g^4}{4} \bar{t}(\bar{t} - M^2) \left| \frac{1}{\bar{s} - m_W^2} \right|^2 |V_{ud}|^2 |V_{tb}|^2, \tag{4.44}$$

and for the t-channel contributions ($\mathcal{B}_{bq}$ and $\mathcal{B}_{qb}$) of the $bu \to td$ and $ub \to td$ subprocesses

$$\begin{aligned} \mathcal{B}_{bu} &= \frac{1}{2\bar{s}} \frac{g^4}{4} \bar{s}(\bar{s} - M^2) \left| \frac{1}{\bar{t} - m_W^2} \right|^2 |V_{ud}|^2 |V_{tb}|^2, \\ \mathcal{B}_{ub} &= \frac{1}{2\bar{s}} \frac{g^4}{4} \bar{s}(\bar{s} - M^2) \left| \frac{1}{\bar{u} - m_W^2} \right|^2 |V_{ud}|^2 |V_{tb}|^2, \end{aligned} \tag{4.45}$$

where $\bar{t} = (\bar{k}_\oplus - \bar{k}_1)^2$. The corresponding expressions for $b\bar{d} \to t\bar{u}$ and $\bar{d}b \to t\bar{u}$ can be obtained from the latter again by crossing. They are given by

$$\begin{aligned} \mathcal{B}_{b\bar{d}} &= \frac{1}{2\bar{s}} \frac{g^4}{4} \bar{u}(\bar{u} - M^2) \left| \frac{1}{\bar{t} - m_W^2} \right|^2 |V_{ud}|^2 |V_{tb}|^2, \\ \mathcal{B}_{\bar{d}b} &= \frac{1}{2\bar{s}} \frac{g^4}{4} \bar{t}(\bar{t} - M^2) \left| \frac{1}{\bar{u} - m_W^2} \right|^2 |V_{ud}|^2 |V_{tb}|^2. \end{aligned} \tag{4.46}$$

The finite soft-virtual contributions, obtained according to the FKS method, have been taken from the `MC@NLO` code. We included them in our NLO calculation and tested the correct behaviour of our program by comparing our NLO results with the MCFM code [101], both for the full NLO cross section and for typical differential distributions. Some comparisons have also been carried out with the program ZTOP [102].

Collinear remnants

The collinear remnants can be obtained by using the formula reported in sec. 1.2.3, eq. (1.117). Here we limit ourselves to list all the contributions, giving only a couple of explicit examples to clarify the notation.
For the s-channel processes, the collinear remnants are

$$\mathcal{G}^{qq'}_{\scriptscriptstyle\oplus\!\!\!\!\ominus}(\mathbf{\Phi}_{2,\scriptscriptstyle\oplus\!\!\!\!\ominus})\,, \qquad \mathcal{G}^{gq}_{\oplus}(\mathbf{\Phi}_{2,\oplus}) \qquad \text{and} \qquad \mathcal{G}^{qg}_{\ominus}(\mathbf{\Phi}_{2,\ominus})\,, \tag{4.47}$$

where the $\mathbf{\Phi}_{2,\oplus}$ notation represents the set of variables

$$\mathbf{\Phi}_{2,\oplus} = \{x_\oplus, x_\ominus, z, k_1, k_2\}, \qquad \text{with} \qquad z\,x_\oplus K_\oplus + x_\ominus K_\ominus = k_1 + k_2\,. \tag{4.48}$$

The underlying Born configuration $\bar{\mathbf{\Phi}}_2$, associated with the $\mathbf{\Phi}_{2,\oplus}$ kinematics, is defined by

$$\bar{k}_\oplus = z\,x_\oplus K_\oplus, \qquad \bar{k}_\ominus = x_\ominus K_\ominus, \qquad \bar{k}_1 = k_1, \quad \bar{k}_2 = k_2\,. \tag{4.49}$$

Similar formulae hold for $\mathbf{\Phi}_{2,\ominus}$. Among the contributions listed in (4.47), only the real process $qq' \to t\bar{b}g$ is singular in both the $\oplus$ and the $\ominus$ region. It thus needs the two collinear remnants

$$\begin{aligned}\mathcal{G}^{qq'}_{\scriptscriptstyle\oplus\!\!\!\!\ominus}(\mathbf{\Phi}_{2,\scriptscriptstyle\oplus\!\!\!\!\ominus}) \;=\; & \frac{\alpha_{\rm S}}{2\pi} C_{\rm F} \Bigg\{ (1+z^2) \left[\left(\frac{1}{1-z} \right)_+ \log \frac{\bar{s}}{z\mu_{\rm F}^2} + 2 \left(\frac{\log(1-z)}{1-z} \right)_+ \right] \\ & + (1-z) \Bigg\} \mathcal{B}_{qq'}(\bar{s}, \bar{Y}, \bar{\theta}_1)\,.\end{aligned} \tag{4.50}$$

For the t-channel processes, the collinear remnants are

$$\mathcal{G}^{bq}_{\scriptscriptstyle\oplus\!\!\!\!\ominus}(\mathbf{\Phi}_{2,\scriptscriptstyle\oplus\!\!\!\!\ominus})\,, \quad \mathcal{G}^{qb}_{\scriptscriptstyle\oplus\!\!\!\!\ominus}(\mathbf{\Phi}_{2,\scriptscriptstyle\oplus\!\!\!\!\ominus})\,, \quad \mathcal{G}^{gq}_{\oplus}(\mathbf{\Phi}_{2,\oplus})\,, \quad \mathcal{G}^{qg}_{\ominus}(\mathbf{\Phi}_{2,\ominus})\,, \quad \mathcal{G}^{gb}_{\oplus}(\mathbf{\Phi}_{2,\oplus}) \quad \text{and} \quad \mathcal{G}^{bg}_{\ominus}(\mathbf{\Phi}_{2,\ominus})\,. \tag{4.51}$$

In this case, $\mathcal{G}^{gb}_{\oplus}(\mathbf{\Phi}_{2,\oplus})$ contains two terms, since in the scattering $gb \to t\bar{q}q'$ both the two outgoing massless partons $\bar{q}$ and q' can become collinear to the incoming gluon. We have

$$\begin{aligned}\mathcal{G}^{gb}_{\oplus}(\mathbf{\Phi}_{2,\oplus}) \;=\; & \frac{\alpha_{\rm S}}{2\pi} T_{\rm F} \Bigg\{ (1-z)\left(1-2z+2z^2\right) \left[\left(\frac{1}{1-z} \right)_+ \log \frac{\bar{s}}{z\mu_{\rm F}^2} + 2 \left(\frac{\log(1-z)}{1-z} \right)_+ \right] \\ & + 2z\,(1-z) \Bigg\} \left[\mathcal{B}_{\bar{q}'b}(\bar{s}, \bar{Y}, \bar{\theta}_1) + \mathcal{B}_{qb}(\bar{s}, \bar{Y}, \bar{\theta}_1) \right]\,,\end{aligned} \tag{4.52}$$

where $\mathcal{B}_{\bar{q}'b}$ and $\mathcal{B}_{qb}$ are the corresponding underlying Born processes. All the other contributions can be obtained in a similar way.

Soft and collinear limits of the real contributions

In the FKS formalism, phase-space singular regions are approached when the radiation variables $\xi \to 0$ and/or $y \to \pm 1$. The corresponding singularities are subtracted from the real cross section using the plus distributions, as we discussed in sec. 1.2.3. One needs to express the singular limits in terms of suitable radiation variables and of the corresponding underlying Born contributions. In this section we compute these limits and give explicitly their expressions.

We start by considering the singular limits of the processes that have both ISR and FSR singularities, namely $\mathcal{R}_{qq'}$, $\mathcal{R}_{bq}$ and $\mathcal{R}_{qb}$. These processes are the most subtle, being both soft and collinear divergent for initial- and final-state radiation. As an example, we study the limits for the s-channel scattering $qq' \to t\bar{b}g$. We can deal with ISR and FSR separately, having defined the contributions $\mathcal{R}^{3,\oplus}_{qq'}$, $\mathcal{R}^{3,\ominus}_{qq'}$ and $\mathcal{R}^{3,2}_{qq'}$.

For ISR singularities, we use the set $\Phi^{\text{ISR}}_{\text{rad}}$ to parametrize the kinematics. When $y \to \pm 1$, the momentum k_3 is aligned along the $\circledpm$ direction and $k_3 = \xi\, k_{\circledpm}$, in the CM frame. The real squared amplitude factorizes and we have

$$\left[\mathcal{R}^{3,\circledpm}_{qq'}\right]_{y\to\pm1} = \frac{4\pi\alpha_{\text{S}}}{k_{\circledpm}\cdot k_3}\, P^{qq}(z)\, \mathcal{B}_{qq'} = C_{\text{F}} \frac{1}{\xi^2(1\mp y)} \frac{16\pi\alpha_{\text{S}}}{s} \left(1+z^2\right) \mathcal{B}_{qq'}\,, \tag{4.53}$$

where $z = (1-\xi)$, $P^{qq}(z)$ is the usual Altarelli-Parisi (AP) splitting kernel and we have included the real flux factor $1/(2s)$ and a $1/z$ factor into the $\mathcal{B}$ term, as its definition requires. In the FKS approach, one needs the finite quantity $\xi^2(1\mp y)\mathcal{R}^{3,\circledpm}_{qq'}$ to perform the subtraction of the singularities. In the collinear limit, we have

$$\left[\xi^2(1\mp y)\mathcal{R}^{3,\circledpm}_{qq'}\right]_{y=\pm1} = C_{\text{F}} \frac{16\pi\alpha_{\text{S}}}{s} \left(1+z^2\right) \mathcal{B}_{qq'}\,. \tag{4.54}$$

In the FSR case, the collinear limit is reached when $y \to 1$. The outgoing momenta k_3 and k_2 become parallel and aligned along their sum, denoted by k. Momentum conservation reads

$$k = k_2 + k_3\,, \tag{4.55}$$

and, in the partonic CM frame, one has

$$k_2 = z\, k \tag{4.56}$$

where $z = 1 - \xi s/(s - M_{\rm rec}^2)$. A factorized expression holds in this case too

$$\left[\mathcal{R}^{3,2}_{qq'}\right]_{y\to 1} = \frac{4\pi\alpha_{\rm S}}{k_2\cdot k_3}\, P^{qq}(z)\, \mathcal{B}_{qq'} = C_{\rm F}\frac{1}{\xi^2(1-y)}\frac{16\pi\alpha_{\rm S}}{zs}\left(1+z^2\right)\mathcal{B}_{qq'}\,. \tag{4.57}$$

The finite quantity needed in the application of the subtraction method is now $\xi^2(1-y)\,\mathcal{R}^{3,2}_{qq'}$, that is given by

$$\left[\xi^2(1-y)\mathcal{R}^{3,2}_{qq'}\right]_{y=1} = C_{\rm F}\frac{16\pi\alpha_{\rm S}}{zs}\left(1+z^2\right)\mathcal{B}_{qq'}\,. \tag{4.58}$$

The contribution $\mathcal{R}_{qq'}$ is also singular when the outgoing gluon becomes soft, i.e. when $k_3 \to 0$. In both the two phase-space parametrizations ($\Phi^{\rm ISR}_{\rm rad}$ and $\Phi^{\rm FSR}_{\rm rad}$), this limit is approached when $\xi \to 0$. The Born process has more than 3 colored particles, so that, in general, one may expect that soft singularities factorize in terms of the color ordered Born amplitudes [2]. However, in this case, the color algebra simplifies, because of the exchange of an intermediate colorless particle, and we have complete factorization on the Born squared amplitude. The $\mathcal{R}_{qq'}$ contribution in the soft limit (eikonal approximation) is given by

$$\left[\mathcal{R}_{qq'}\right]_{\xi\to 0} = 8\pi\alpha_{\rm S}C_{\rm F}\left\{\frac{k_\oplus\cdot k_\ominus}{(k_\oplus\cdot k_3)(k_\ominus\cdot k_3)} + \frac{k_1\cdot k_2}{(k_1\cdot k_3)(k_2\cdot k_3)} - \frac{M^2}{2(k_1\cdot k_3)^2}\right\}\mathcal{B}_{qq'}\,. \tag{4.59}$$

The radiation variable y assumes different meaning in the case of ISR or FSR (see sec. 4.1.2). In the ISR case, we have the finite contributions

$$\left[\xi^2(1\mp y)\mathcal{R}^{3,\oplus}_{qq'}\right]_{\xi=0} = 4\pi\alpha_{\rm S}C_{\rm F}\left\{\frac{16}{s(1\pm y)} + \frac{(s-M^2)(1\mp y)}{(k_1\cdot\hat{k}_3)(k_2\cdot\hat{k}_3)} - \frac{M^2(1\mp y)}{(k_1\cdot\hat{k}_3)^2}\right\}\mathcal{S}^{3,\oplus}\,\mathcal{B}_{qq'}\,, \tag{4.60}$$

where $\hat{k}_3 = k_3/\xi$ identifies the direction of the soft gluon. In the FSR case we have instead

$$\left[\xi^2(1-y)\mathcal{R}^{3,2}_{qq'}\right]_{\xi=0} = 4\pi\alpha_{\rm S}C_{\rm F}\left\{\frac{s(1-y)}{(k_\oplus\cdot\hat{k}_3)(k_\ominus\cdot\hat{k}_3)} + \frac{4(s-M^2)}{(k_1\cdot\hat{k}_3)s\xi_2} - \frac{M^2(1-y)}{(k_1\cdot\hat{k}_3)^2}\right\}\mathcal{S}^{3,2}\,\mathcal{B}_{qq'}\,, \tag{4.61}$$

with $\xi_2 = 2k_2^0/\sqrt{s}$, defined in the partonic CM frame.

The t-channel processes $\mathcal{R}_{bq}$ and $\mathcal{R}_{qb}$ are dealt in an analogous way, either for the collinear and the soft limits.

All the other processes have only ISR collinear singularities: the corresponding limits can be obtained from eq. (4.53), substituting the appropriate AP splitting kernel and the Born term.

4.2 POWHEG implementation

4.2.1 Generation of the Born variables

In the POWHEG method, we first generate the Born kinematics according to the $\bar{B}$ function, which is the integral of the full NLO cross section at a given value of the underlying Born kinematics. It is defined as follows:

$$\bar{B} = \bar{B}_{(s)} + \bar{B}_{(t)}\,, \tag{4.62}$$

where

$$\bar{B}_{(s)} = \sum_{qq'} \bar{B}_{qq'}\,, \tag{4.63}$$

with

$$\begin{aligned}
\bar{B}_{qq'}\left(\bar{\mathbf{\Phi}}_2\right) &= B_{qq'}\left(\bar{\mathbf{\Phi}}_2\right) + V_{qq'}\left(\bar{\mathbf{\Phi}}_2\right) + \int d\Phi_{\rm rad}^{\rm FSR}\ \hat{R}_{qq'}^{3,2}\left(\bar{\mathbf{\Phi}}_2, \Phi_{\rm rad}^{\rm FSR}\right) \\
&\quad + \int d\Phi_{\rm rad}^{\rm ISR}\ \left[\sum_{\substack{\oplus \\ \ominus}} \hat{R}_{qq'}^{3,\substack{\oplus \\ \ominus}}\left(\bar{\mathbf{\Phi}}_2, \Phi_{\rm rad}^{\rm ISR}\right) + \hat{R}_{gq,(s)}\left(\bar{\mathbf{\Phi}}_2, \Phi_{\rm rad}^{\rm ISR}\right) + \hat{R}_{qg,(s)}\left(\bar{\mathbf{\Phi}}_2, \Phi_{\rm rad}^{\rm ISR}\right)\right] \\
&\quad + \int_{\bar{x}_\oplus}^1 \frac{dz}{z}\left[G_\oplus^{qq'}\left(\mathbf{\Phi}_{2,\oplus}\right) + G_\oplus^{gq}\left(\mathbf{\Phi}_{2,\oplus}\right)\right] + \int_{\bar{x}_\ominus}^1 \frac{dz}{z}\left[G_\ominus^{qq'}\left(\mathbf{\Phi}_{2,\ominus}\right) + G_\ominus^{qg}\left(\mathbf{\Phi}_{2,\ominus}\right)\right],
\end{aligned} \tag{4.64}$$

and where

$$\bar{B}_{(t)} = \sum_{q} \left[\bar{B}_{qb} + \bar{B}_{bq}\right], \tag{4.65}$$

with

$$\begin{aligned}
\bar{B}_{qb}\left(\bar{\mathbf{\Phi}}_2\right) &= B_{qb}\left(\bar{\mathbf{\Phi}}_2\right) + V_{qb}\left(\bar{\mathbf{\Phi}}_2\right) + \int d\Phi_{\rm rad}^{\rm FSR}\ \hat{R}_{qb}^{3,2}\left(\bar{\mathbf{\Phi}}_2, \Phi_{\rm rad}^{\rm FSR}\right) \\
&\quad + \int d\Phi_{\rm rad}^{\rm ISR}\ \left[\sum_{\substack{\oplus \\ \ominus}} \hat{R}_{qb}^{3,\substack{\oplus \\ \ominus}}\left(\bar{\mathbf{\Phi}}_2, \Phi_{\rm rad}^{\rm ISR}\right) + \hat{R}_{qg,(t)}\left(\bar{\mathbf{\Phi}}_2, \Phi_{\rm rad}^{\rm ISR}\right)\right. \\
&\quad \left. + \hat{R}_{gb}^{3,\oplus}\left(\bar{\mathbf{\Phi}}_2, \Phi_{\rm rad}^{\rm ISR}\right) + \hat{R}_{gb}^{2,\oplus}\left(\bar{\mathbf{\Phi}}_2, \Phi_{\rm rad}^{\rm ISR}\right)\right] \\
&\quad + \int_{\bar{x}_\oplus}^1 \frac{dz}{z}\left[G_\oplus^{qb}\left(\mathbf{\Phi}_{2,\oplus}\right) + G_\oplus^{gb}\left(\mathbf{\Phi}_{2,\oplus}\right)\right] + \int_{\bar{x}_\ominus}^1 \frac{dz}{z}\left[G_\ominus^{qb}\left(\mathbf{\Phi}_{2,\ominus}\right) + G_\ominus^{qg}\left(\mathbf{\Phi}_{2,\ominus}\right)\right]
\end{aligned} \tag{4.66}$$

The $\bar{B}_{bq}$ contribution can be obtained from eq. (4.66) by simply exchanging all flavour indexes and substituting $\oplus \leftrightarrow \ominus$. Note that, in the previous formula, in the collinear contribution $G^{gb}_{\oplus}$, only the term with underlying-Born that matches the $\bar{B}$ labels is included. In this way, when summing all the $\bar{B}_{qb}$ contributions,[4] both the two terms in eq. (4.52) are correctly included, each one ending in the appropriate $\bar{B}$ function.

According to the POWHEG notation, in eqs. (4.64) and (4.66) we have traded the $\mathcal{B}$, $\mathcal{V}$, $\mathcal{R}$ and $\mathcal{G}$ quantities with the corresponding capital letters, obtained by multiplying them with the appropriate luminosity $\mathcal{L}$, defined in terms of the parton distribution functions (PDF) $f_f^{\circledast}(x_{\circledast}, \mu_{\rm F}^2)$ as

$$\mathcal{L}_{ff'}(x_\oplus, x_\ominus) = f_f^{\oplus}(x_\oplus, \mu_{\rm F}^2)\; f_{f'}^{\ominus}(x_\ominus, \mu_{\rm F}^2)\,. \tag{4.67}$$

All the integrals appearing in the above equations are now finite. In fact, following the FKS subtraction scheme, the hatted functions

$$\hat{\mathcal{R}}^{\circledast}_{ij} = \frac{1}{\xi}\left\{\left(\frac{1}{\xi}\right)_+ \left(\frac{1}{1\mp y}\right)_+\right\}\left[(1\mp y)\;\xi^2\,\mathcal{R}^{\circledast}_{ij}\right] \tag{4.68}$$

and

$$\hat{\mathcal{R}}^{\rm FSR}_{ij} = \frac{1}{\xi}\left\{\left(\frac{1}{\xi}\right)_+ \left(\frac{1}{1- y}\right)_+\right\}\left[(1- y)\;\xi^2\,\mathcal{R}^{\rm FSR}_{ij}\right] \tag{4.69}$$

have only integrable divergences when integrated over $\Phi^{\rm ISR}_{\rm rad}$ and $\Phi^{\rm FSR}_{\rm rad}$ respectively.[5] Some care should still be taken when dealing with the plus distributions. In Appendix C more details on this point are given.

Following sec. 2.3.6, we introduce the $\tilde{B}$ function, defined such that its integral over the radiation variables, mapped onto a unit cube $\left(\{\xi, y, \phi\} \to \left\{X^{(1)}_{\rm rad}, X^{(2)}_{\rm rad}, X^{(3)}_{\rm rad}\right\}\right)$, gives

$$\bar{B} = \int_0^1 d^3X_{\rm rad}\,\tilde{B}\,. \tag{4.70}$$

The generation of the Born variables $\bar{\mathbf{\Phi}}_2$ is performed by using the integrator-unweighter

[4] We recall that, in the sum of eq. (4.65), the index q runs both on quark and antiquark admitted flavours.

[5] In our case, for both the s- and t-channels,

$$\begin{aligned}
\hat{\mathcal{R}}^{\oplus}_{ij} &= \left\{\hat{R}^{3,\oplus}_{qq'}, \hat{R}_{qq,(s)}, \hat{R}^{3,\oplus}_{qb}, \hat{R}^{3,\oplus}_{gb}, \hat{R}^{2,\oplus}_{gb}, \hat{R}^{3,\oplus}_{bq}, \hat{R}_{gq,(t)}\right\},\\
\hat{\mathcal{R}}^{\ominus}_{ij} &= \left\{\hat{R}^{3,\ominus}_{qq'}, \hat{R}_{qg,(s)}, \hat{R}^{3,\ominus}_{qb}, \hat{R}^{3,\ominus}_{bg}, \hat{R}^{2,\ominus}_{bg}, \hat{R}^{3,\ominus}_{bq}, \hat{R}_{qg,(t)}\right\},\\
\hat{\mathcal{R}}^{\rm FSR}_{ij} &= \left\{\hat{R}^{3,2}_{qq'}, \hat{R}^{3,2}_{qb}, \hat{R}^{3,2}_{bq}\right\}.
\end{aligned}$$

program MINT [61] that, after a single integration of the function $\tilde{B}$ over the Born and radiation variables, can generate random values for the variables $\{\bar{\mathbf{\Phi}}_2, X_{\rm rad}\}$, distributed according to the weight $\tilde{B}\left(\bar{\mathbf{\Phi}}_2, X_{\rm rad}\right)$. We then keep the $\bar{\mathbf{\Phi}}_2$ generated values only, and neglect all the others, which corresponds to integrate over them. At this stage, we also need to choose a Born flavour structure (a value for f_b in the notation introduced in sec. 2.3.3) with a probability proportional to its relative weight in the $\bar{B}$ function (see eqs. (4.63) and (4.65)). The event is then further processed, to generate the radiation variables, as illustrated in the following section.

4.2.2 Generation of the hardest-radiation variables

Radiation kinematics is generated using the POWHEG Sudakov form factor. For a given underlying Born kinematics ($\bar{\mathbf{\Phi}}_2$) and flavour structure (f_b), the Sudakov form factor can be expressed as

$$\Delta^{f_b}(\bar{\mathbf{\Phi}}_2, p_{\rm T}) = \prod_{\alpha_{\rm r}\in\{\alpha_{\rm r}|f_b\}} \Delta^{f_b}_{\alpha_{\rm r}}(\bar{\mathbf{\Phi}}_2, p_{\rm T})\,, \tag{4.71}$$

where one needs to include in the product all the projected real contributions that have, as singular limit, the generated underlying Born. In our case, for the s-channel, we can write

$$\Delta^{qq'}(\bar{\mathbf{\Phi}}_2, p_{\rm T}) = \Delta^{qq'}_{\rm ISR}(\bar{\mathbf{\Phi}}_2, p_{\rm T})\ \Delta^{qq'}_{\rm FSR}(\bar{\mathbf{\Phi}}_2, p_{\rm T})\,, \tag{4.72}$$

where

$$\begin{aligned}\Delta^{qq'}_{\rm ISR}(\bar{\mathbf{\Phi}}_2, p_{\rm T}) \;=\; \exp\Bigg\{ -\int d\Phi^{\rm ISR}_{\rm rad} \frac{\sum_{\circledast} R^{3,\circledast}_{qq'}(\mathbf{\Phi_3}) + R_{gq',(s)}(\mathbf{\Phi_3}) + R_{qg,(s)}(\mathbf{\Phi_3})}{B_{qq'}(\bar{\mathbf{\Phi}}_2)} \\ \times\,\theta(k_{\rm T,ISR}(\mathbf{\Phi_3}) - p_{\rm T})\Bigg\}\end{aligned} \tag{4.73}$$

and

$$\Delta^{qq'}_{\rm FSR}(\bar{\mathbf{\Phi}}_2, p_{\rm T}) \;=\; \exp\left\{ -\int d\Phi^{\rm FSR}_{\rm rad} \frac{R^{3,2}_{qq'}(\mathbf{\Phi_3})}{B_{qq'}(\bar{\mathbf{\Phi}}_2)}\,\theta(k_{\rm T,FSR}(\mathbf{\Phi_3}) - p_{\rm T})\right\}. \tag{4.74}$$

For clarity, here we indicate with $R_{gq',(s)}$ the real contribution of gq type that corresponds to the underlying Born qq'. The functions $k_{\rm T,ISR}(\mathbf{\Phi_3})$ and $k_{\rm T,FSR}(\mathbf{\Phi_3})$ measure the hardness of the radiation in the real event. In case of ISR singular processes, we chose as hardness variable the exact transverse momentum of the emitted parton with respect to the beam

axis. In terms of $\Phi_{\rm rad}^{\rm ISR}$, this is given by

$$k_{\rm T,ISR}^2 = \frac{s}{4}\,\xi^2\left(1-y^2\right) = \frac{\bar{s}}{4(1-\xi)}\,\xi^2\left(1-y^2\right). \tag{4.75}$$

For the FSR singular processes, instead, we use as hardness variable the exact transverse momentum of the FKS parton with respect to the other light outgoing parton, evaluated in the center-of-mass frame. In terms of $\Phi_{\rm rad}^{\rm FSR}$, this is given by[6]

$$k_{\rm T,FSR}^2 = \frac{\bar{s}}{4}\xi^2\,\left(1-y^2\right). \tag{4.77}$$

The generation of the hardest radiation is performed individually for $\Delta_{\rm ISR}^{q\bar{q}}$ and $\Delta_{\rm FSR}^{q\bar{q}}$, and the highest generated $k_{\rm T}$ is retained. This corresponds to generate according to eq. (4.72), as shown in Appendix B of ref. [2]. If $k_{\rm T}$ is below a given cut, $p_{\rm T}^{\rm min}$, no radiation is generated, and a Born event is returned.

As explained in sec. 2.3.6, to generate radiation according to the POWHEG Sudakov form factors (4.73)-(4.74), we need to use a veto technique. The upper bounding functions for the application of the veto method have been chosen in the following way:

$$\frac{\sum_{\circledast} R_{qq'}^{3,\circledast}\left(\mathbf{\Phi_3}\right) + R_{gq',(s)}\left(\mathbf{\Phi_3}\right) + R_{qg,(s)}\left(\mathbf{\Phi_3}\right)}{B_{qq'}(\bar{\mathbf{\Phi}}_2)}\, J_{\rm rad}^{\rm ISR}(\bar{\mathbf{\Phi}}_2, \Phi_{\rm rad}^{\rm ISR}) \leq N_{qq'}^{\rm ISR}\,\frac{\alpha_{\rm S}(k_{\rm T,ISR}^2)}{\xi\,(1-y^2)} \tag{4.78}$$

for ISR, and

$$\frac{R_{qq'}^{3,2}\left(\mathbf{\Phi_3}\right)}{B_{qq'}(\bar{\mathbf{\Phi}}_2)}\, J_{\rm rad}^{\rm FSR}(\bar{\mathbf{\Phi}}_2, \Phi_{\rm rad}^{\rm FSR}) \leq N_{qq'}^{\rm FSR}\,\frac{\alpha_{\rm S}(k_{\rm T,FSR}^2)}{\xi\,(1-y^2)} \tag{4.79}$$

for FSR.

The same procedures holds also for the t-channel case, with appropriate modifications in formulae (4.72)–(4.79).

The method used to generate radiation events according to these upper bounding functions is analogous to the one described in Appendix D of ref. [103], and we do not repeat it here. Some details can also be found in the Examples section of ref. [2].

After the generation of the hardest radiation, only the kinematics is fixed. In case of FSR, only one flavor choice is possible. For ISR, instead, the flavour structure is

[6] Since for $y \to -1$ no singularities arise in the FSR case, another possible choice for $k_{\rm T,FSR}$ would be

$$k_{\rm T,FSR}^2 = \frac{\bar{s}}{2}\,\xi^2(1-y)\,, \tag{4.76}$$

that has the same behaviour of eq. (4.77) in the collinear limit but has a simpler functional form. We have checked that no sizable differences arise if one uses eq. (4.76) instead of eq. (4.77).

chosen according to the relative weight of the real contributions in the Sudakov exponent of eq. (4.73). At this stage, events are passed to a SMC program, after assigning a planar color structure for each of them. In the single-top case, if a Born-like event is generated, the planar color structure is trivial, since there are always two independent quark currents, connected by a W exchange. Hence, only one choice is possible. For real processes with a gluon in the initial state, the choice for color connections is again forced: the quark line which is not color connected to the gluon will keep its own color flow, while the other outgoing quark-antiquark pair is color connected to the incoming gluon. The only case where a choice is really needed is for processes with an outgoing gluon: in this case, we used the procedure outlined in sec. 2.3.3. In particular, the FKS parton has been connected to the emitter, that is fully specified by $\alpha_{\rm r}$, the label of the singular region. For example, for s-channel processes, the outgoing gluon is linked to the outgoing heavy current in case of FSR, and to the incoming quark-antiquark line for ISR. In the t-channel case, instead, the situation is slightly different. Taking the scattering $qb \to tq'g$ as reference, the gluon is connected to the incoming b-quark for emission in the $\ominus$ region, whereas for FSR, and for ISR in the $\oplus$ region, g is linked to the light-quark line, i.e. the line that does not contain the top quark.

As a final remark, we also point out that single-top s- and t-channel Born cross sections vanish at some points in the Born phase space, as one can argue by looking at eqs. (4.43)–(4.46). For this reason, special care has to be taken during the radiation generation procedure. In this case, the problem has been handled with the same method described in sec. 3.2.3.

4.2.3 Top-quark decay

The calculation we have described so far leads to the generation of events with an undecayed top quark. We include the decay kinematics effects in an approximate way, by requiring that the decay products are distributed with a probability proportional to the tree-level cross section for the full production and decay process. This procedure was first suggested in ref. [99]. In the following we describe our implementation, focusing upon the decay $t \to bW^+ \to b\bar{\ell}\nu$.

We first generate a Born-like or real-like event according to the `POWHEG` method. In both cases we denote the set of variables that parametrize the undecayed momenta as $\Phi_{\rm POW}$ and the corresponding flavour structure as f. As described at the end of sec. 4.1.2, at this stage the top virtuality M^2 is distributed according to a Breit-Wigner function.

We write the tree-level cross section for production and decay in the following form

$$d\sigma^f_{\rm dec} = \frac{1}{2s}\,\mathcal{L}\,|\mathcal{M}^f_{\rm dec}(\Phi_{\rm POW},\Phi_{t\to b\bar\ell\nu})|^2\,d\Phi_{\rm dec}\,, \tag{4.80}$$

where $\mathcal{L}$ is the luminosity factor and $|\mathcal{M}^f_{\rm dec}|^2$ is the squared amplitude corresponding to the full decayed process that originates from the undecayed process f.[7] For consistency, the squared amplitude $|\mathcal{M}^f_{\rm dec}|^2$ must include only resonant graphs (i.e. graphs where the top momentum equals the sum of the b, $\bar\ell$ and ν momenta). We write the full phase space, including the decay, in the factorized form

$$d\Phi_{\rm dec} = d\Phi_{\rm POW}\,d\Phi_{t\to b\bar\ell\nu}\,, \tag{4.81}$$

where $\Phi_{\rm POW}$ is the undecayed (POWHEG) phase space and $\Phi_{t\to b\bar\ell\nu}$ is defined implicitly by this equation. We notice that

$$|\mathcal{M}^f_{\rm undec}|^2\times{\rm BR}(t\to b\bar\ell\nu) = \int|\mathcal{M}^f_{\rm dec}|^2\,d\Phi_{t\to b\bar\ell\nu}\,, \tag{4.82}$$

where $\mathcal{M}^f_{\rm undec}$ is the undecayed amplitude, i.e. the Born or real amplitude that we used throughout the computation. Thus, the differential probability $dP(\Phi_{t\to b\bar\ell\nu}|\Phi_{\rm POW})$ for the generation of $\Phi_{t\to b\bar\ell\nu}$ from a given undecayed kinematics $\Phi_{\rm POW}$ is

$$dP(\Phi_{t\to b\bar\ell\nu}|\Phi_{\rm POW}) = \frac{1}{{\rm BR}(t\to b\bar\ell\nu)}\,\frac{|\mathcal{M}^f_{\rm dec}(\Phi_{\rm POW},\Phi_{t\to b\bar\ell\nu})|^2}{|\mathcal{M}^f_{\rm undec}(\Phi_{\rm POW})|^2}\,d\Phi_{t\to b\bar\ell\nu}\,. \tag{4.83}$$

To generate efficiently $\Phi_{t\to b\bar\ell\nu}$ distributed according to (4.83) we use the hit-and-miss technique and so we need to find an upper bounding function for dP. This bound can be guessed from the structure of the top decay. In our case, we use as upper bound for the ratio $|\mathcal{M}^f_{\rm dec}(\Phi_{\rm POW},\Phi_{t\to b\bar\ell\nu})|^2/|\mathcal{M}^f_{\rm undec}(\Phi_{\rm POW})|^2$, the expression

$$U_{\rm dec}(M^2,\Phi_{t\to b\bar\ell\nu}) = N_{\rm dec}\,\frac{|\mathcal{M}_{t\to bW}(M^2,M^2_{\bar\ell\nu})|^2}{(M^2-m_t^2)^2+m_t^2\,\Gamma_t^2}\,\frac{|\mathcal{M}_{W\to\bar\ell\nu}(M^2_{\bar\ell\nu})|^2}{(M^2_{\bar\ell\nu}-m_W^2)^2+m_W^2\,\Gamma_W^2}\,, \tag{4.84}$$

where $M^2_{\bar\ell\nu}=(k_{\bar\ell}+k_\nu)^2$ and $\mathcal{M}_{t\to bW}$ and $\mathcal{M}_{W\to\bar\ell\nu}$ are the decay amplitudes corresponding to the subprocesses in their subscripts. In the previous formula, as well as in $\mathcal{M}^f_{\rm dec}$, finite-width effects have been fully taken into account. One can predict the appropriate value for the normalization factor $N_{\rm dec}$ as explained in ref. [99] or compute it by sampling the

[7] The full tree-level squared amplitudes $|\mathcal{M}^f_{\rm dec}|^2$ have been obtained using MadGraph.

decay phase space $\Phi_{t\to b\bar{\ell}\nu}$ and comparing $U_{\rm dec}$ with the exact expression, in such a way that the inequality

$$|\mathcal{M}^f_{\rm dec}(\Phi_{\rm POW},\Phi_{t\to b\bar{\ell}\nu})|^2 \leq |\mathcal{M}^f_{\rm undec}(\Phi_{\rm POW})|^2\; U_{\rm dec}(M^2,\Phi_{t\to b\bar{\ell}\nu}) \tag{4.85}$$

holds. In this work, we used this last procedure. The veto algorithm is then applied:

1. First one generates a point in the phase space $\Phi_{t\to b\bar{\ell}\nu}$.
2. Then a random number r in the range $[0, U_{\rm dec}(M^2,\Phi_{t\to b\bar{\ell}\nu})]$ is generated.
3. If $r < |\mathcal{M}^f_{\rm dec}(\Phi_{\rm POW},\Phi_{t\to b\bar{\ell}\nu})|^2/|\mathcal{M}^f_{\rm undec}(\Phi_{\rm POW})|^2$, keep the decay kinematics and generate the event. Otherwise go back to step 1.

4.3 Results

In this section we present our results and comparisons with the fixed order (next-to-leading) calculation and with the `MC@NLO` 3.3 and `PYTHIA` 6.4.21 Shower Monte Carlo (SMC) programs.[8] We have used the CTEQ6M [10] set for the parton distribution functions and the associated value of $\Lambda^{(5)}_{\overline{\rm MS}} = 0.226$ GeV. Furthermore, as discussed in refs. [2, 103], we use a rescaled value $\Lambda_{\rm MC} = 1.569\,\Lambda^{(5)}_{\overline{\rm MS}}$ in the expression for $\alpha_{\rm S}$ appearing in the Sudakov form factors, in order to achieve next-to-leading logarithmic accuracy.

Although the matrix-element calculation has been performed in the massless-quark limit (except, of course, for the top quark), the lower cutoff in the generation of the radiation has been fixed according to the mass of the emitting quark. The lower bound on the transverse momentum for the emission off a massless emitter (u, d, s) has been set to the value $p_{\rm T}^{\rm min} = \sqrt{5}\,\Lambda_{\rm MC}$. We instead choose $p_{\rm T}^{\rm min}$ equal to m_c or m_b when the gluon is emitted by a charm or a bottom quark, respectively. We set $m_c = 1.55$ GeV and $m_b = 4.95$ GeV.

The renormalization and factorization scales have been taken equal to the radiated transverse momentum during the generation of radiation (see eqs. (4.75) and (4.77)), as the `POWHEG` method requires. We have also taken into account properly the heavy-flavour thresholds in the running of $\alpha_{\rm S}$ and in the PDF's, by changing the number of active flavours when the renormalization or factorization scales cross a mass threshold. In the $\bar{B}$ calculation, instead, μ_R and μ_F have been chosen equal to the top-quark mass, whose value has been fixed to $m_t = 175$ GeV. In all the comparisons, we have kept the top-quark

[8] This newest update of `PYTHIA` yields more consistent results when multiple interactions are turned on in user-initiated processes (see the release notes in `http://projects.hepforge.org/pythia6/`).

virtuality M^2 fixed to m_t^2, so that matrix elements have been evaluated assuming $\Gamma_t = 0$. We have also set $\Gamma_W = 0$ in all the propagators. The other relevant parameters are

$$M_W = 80.4 \text{ GeV}\,, \qquad \sin^2\theta_W^{\text{eff}} = 0.23113\,, \qquad \alpha_{\text{em}}^{-1}(m_t) = 127.011989\,. \tag{4.86}$$

From the above values, the weak coupling has been computed as $g = \sqrt{4\pi\alpha_{\text{em}}}/\sin\theta_W^{\text{eff}}$. In addition, for sake of comparison,[9] we fixed the CKM matrix elements equal to

$$V_{\text{CKM}} = \begin{array}{c} \\ u \\ c \\ t \end{array} \begin{array}{c} \begin{array}{ccc} d & s & b \end{array} \\ \begin{pmatrix} 0.9740 & 0.2225 & 0.0000 \\ 0.2225 & 0.9740 & 0.0000 \\ 0.0000 & 0.0000 & 1.0000 \end{pmatrix} \end{array}. \tag{4.87}$$

In order to minimize effects due to differences in the shower and hadronization algorithms, we have interfaced `POWHEG` with the `HERWIG` angular-ordered shower when comparing with `MC@NLO` and with the p_{T}-ordered `PYTHIA` shower when comparisons with `PYTHIA` have been carried out.

All the following results have been obtained assuming that the top decays semileptonically ($t \to b\,\bar{\ell}\,\nu$), as explained in sec. 4.2.3, but removing the branching ratio, so that plots are normalized to the total cross section.

We present a few distributions, done mainly for comparison with `MC@NLO` and with the NLO calculation. Some of them are "unphysical", i.e., for example, when talking of the top-quark momentum p^t, we refer to the exact p^t taken directly from the MC shower history, right before the top decay. For sake of simplicity, we also force the lightest b-flavoured hadrons to be stable after the hadronization stage of SMC programs.

Jets have been defined according to the k_{T} algorithm [104], as implemented in the `FASTJET` package [68], setting $R = 1$ and imposing a lower 10 GeV cut on jet transverse momenta. We call "top jet" the jet that contains the hardest b-flavoured hadron,[10] which will, most of the time, come from the top-quark decay. The other reconstructed jets will come from the shower of massless partons, and we call them "light jets".[11] In this way, the momentum p^t of the top quark and the momentum of the top jet are different, since the last may or may not include all the particles from the top decay and shower.

[9] In particular, intermediate comparisons with MCFM required this choice, since in MCFM $V_{tb} = 1$.

[10] Here we mean precisely b-flavoured, i.e. not $\bar{b}$-flavoured, that arises in the production process.

[11] In the fixed-order calculation, instead, the top quark is not decayed, and the top jet corresponds to the jet that contains the top quark.

4.3.1 Tevatron results

We start comparing various kinematical variables for single-top s-channel production at the Tevatron $p\bar{p}$ collider. In fig. 4.2 we have collected the following distributions:

- In panels (a) and (b) we show the transverse momentum p_{T}^t and the pseudorapidity η^t of the top quark and in panel (c) we show the hardest jet transverse momentum $p_{\mathrm{T}}^{j_1}$. The agreement with the fixed-order calculation and with the `MC@NLO` results is very good. Only the top transverse-momentum distribution shows a tiny mismatch, our result being slightly softer than the NLO and the `MC@NLO` ones. When interfacing `POWHEG` with `PYTHIA`, we instead find full overlapping with the NLO result. It is thus likely that this small feature may be attributed to shower effects.

- In panel (d), we plot $p_{\mathrm{T}}^{\mathrm{rel},j_1}$, the relative transverse momentum of all the particles clustered inside the hardest jet. This is defined as follows:

  - We perform a longitudinal boost to a frame where the hardest-jet rapidity is zero.
  - In this frame, we compute the quantity

$$p_{\mathrm{T}}^{\mathrm{rel},j_1} = \sum_{i \in j_1} \frac{|\vec{k}^i \times \vec{p}^{j_1}|}{|\vec{p}^{j_1}|}\,, \tag{4.88}$$

    where k^i's are the momenta of the particles that belong to the hardest jet that, in this frame, has momentum p^{j_1}.

  This quantity is thus the sum of the absolute values of the transverse momenta, taken with respect to the jet axis, of the particles inside the hardest jet, in the frame specified above. The plot shows a marked disagreement between fixed order calculation and showered results. This disagreement is well understood, since the observable we are considering is a measure of the spreading of the hardest jet. Thus, its shape is strongly affected by the Sudakov form factor and it is well described by SMC programs. The NLO calculation cannot give, instead, a reliable estimate, since when $p_{\mathrm{T}}^{\mathrm{rel},j_1} \to 0$ the differential cross section diverges.

- In plots (e) and (f), the next-to-hardest jet transverse momentum $p_{\mathrm{T}}^{j_2}$, and the transverse momentum of the system made by the top quark and the hardest jet, $p_{\mathrm{T}}^{(tj_1)}$, are shown. We see a remarkable good agreement between our program and `MC@NLO`, while sensible differences with respect to the NLO results are present. At

the NLO parton level, $p_{\mathrm{T}}^{j_2}$ and $p_{\mathrm{T}}^{(tj_1)}$ balance against each other, so that the two distributions coincide down to the minimum p_{T} cut present in the first plot.

In plot (e), we see an enhancement of the showered results at intermediate values of p_{T}, while in plot (f) we see a low-p_{T} suppression and an enhancement at intermediate and high p_{T}.[12] The low-p_{T} suppression is clearly a Sudakov effect. The high-p_{T} enhancement comes instead from events in which the hardest parton is well balanced against the top quark, but where many hadrons, coming from the hardest parton, end up in the top jet, and are thus removed, or they end up out of the jet cluster. This creates an artificial imbalance, and thus an effective p_{T} for the (tj_1) system. These effects are so pronounced because the cross section for a balanced top-quark–hardest-jet system is much higher, since it does not require the production of an additional hard parton. We have verified this hypothesis by analyzing `POWHEG` outputs before the showering stage, either clustering or not the b quark coming from the top decay. In the case where the b quark is included in the analysis (and the jet containing the b is removed from the jet sample), we see a marked rise of the p_{T} tail. A further rise is observed when the shower is turned on, and may be attributed to energy lost out of the hardest jet cluster due to showering. We see no such effect for the next-to-hardest jet spectrum in plot (e). There, the raise at medium p_{T} may be attributed to the shower p_{T} smearing.

- Finally, in plots (g) and (h), the pseudorapidity $\eta^{(tj_1)}$ of the top-quark–hardest-jet system and the azimuthal difference $\Delta\phi_{t\text{-}j_1} = |\phi_t - \phi_{j_1}|$ are shown. The pseudorapidity of the (tj_1) system shows an expected discrepancy between the showered results and the fixed order one: radiation near the beam axis is suppressed by the Sudakov form factor but not in the NLO result, giving rise to the higher tails at large $|\eta^{(tj_1)}|$. In plot (h), `MC@NLO` and `POWHEG` differ instead from the fixed order result for a kinematical reason: at the parton level, having at most three particles, there is no phase space for the next-to-hardest jet to recoil against the (tj_1) system when $\Delta\phi_{t\text{-}j_1} < \pi/2$.

[12] We note that a similar result has been shown in the `MC@NLO` reference paper for single-top production, ref. [18]

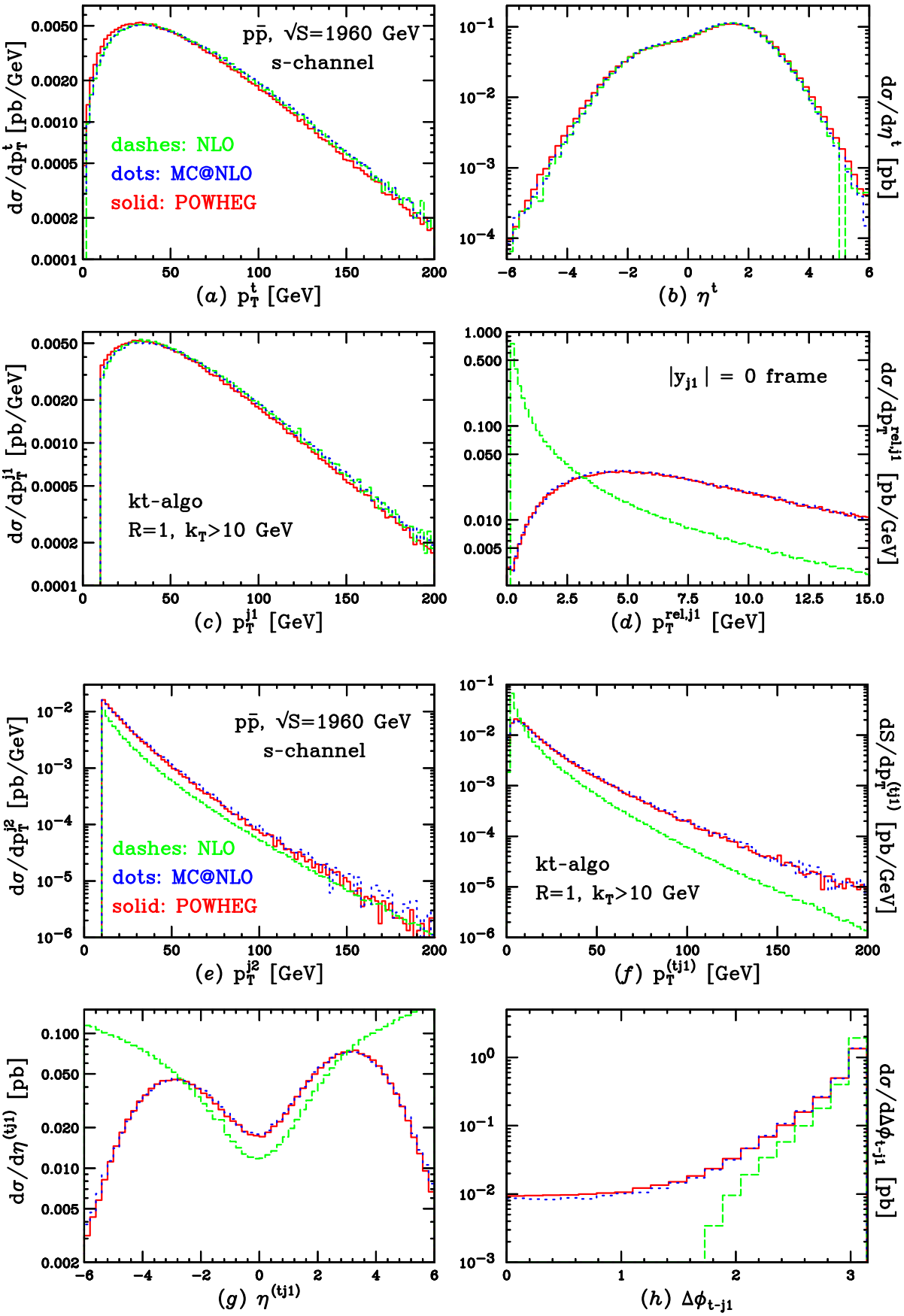

Figure 4.2: Comparisons between POWHEG, MC@NLO and NLO results for s-channel top production at the Tevatron $p\bar{p}$ collider.

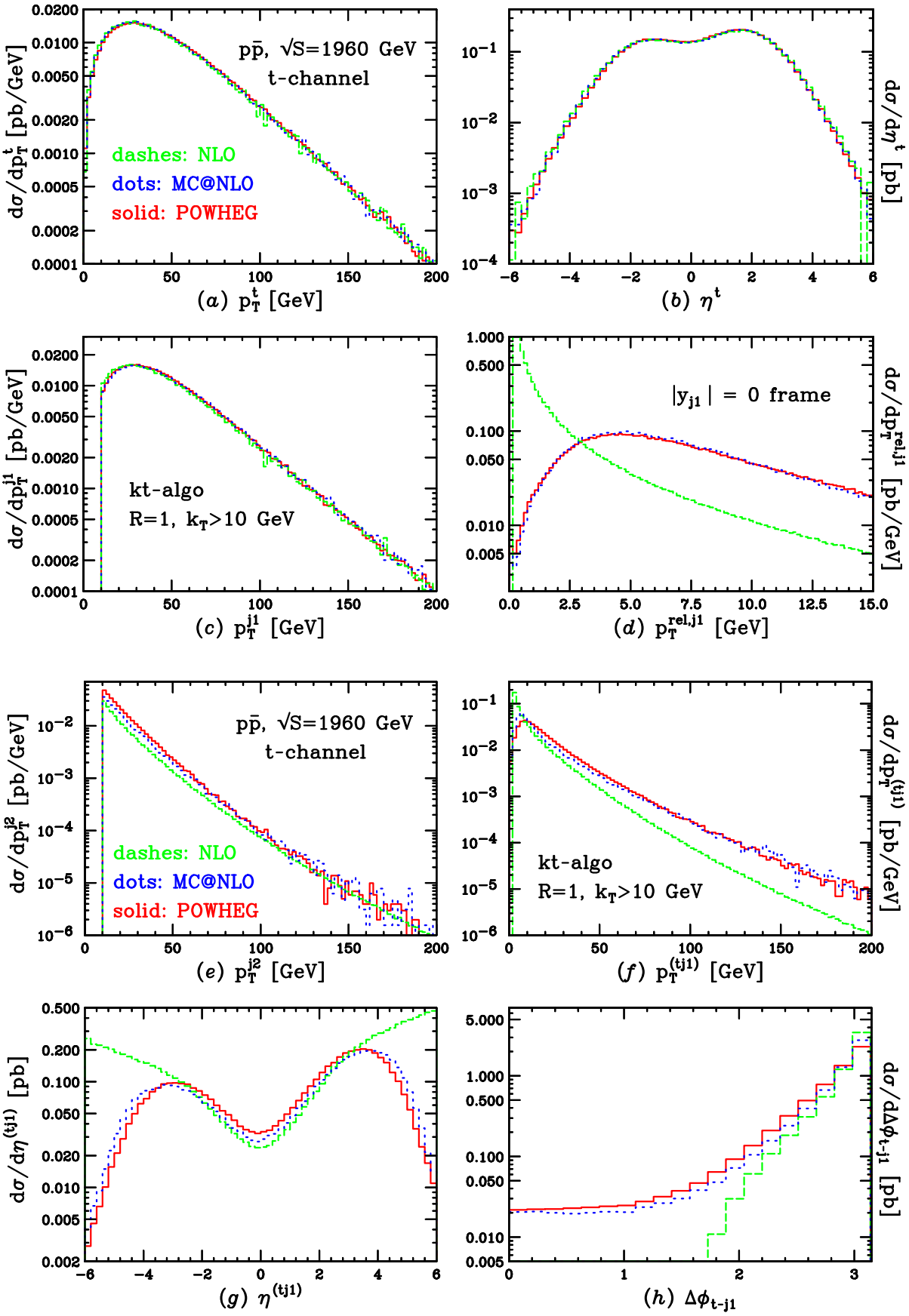

Figure 4.3: Comparisons between POWHEG, MC@NLO and NLO results for t-channel top production at the Tevatron $p\bar{p}$ collider.

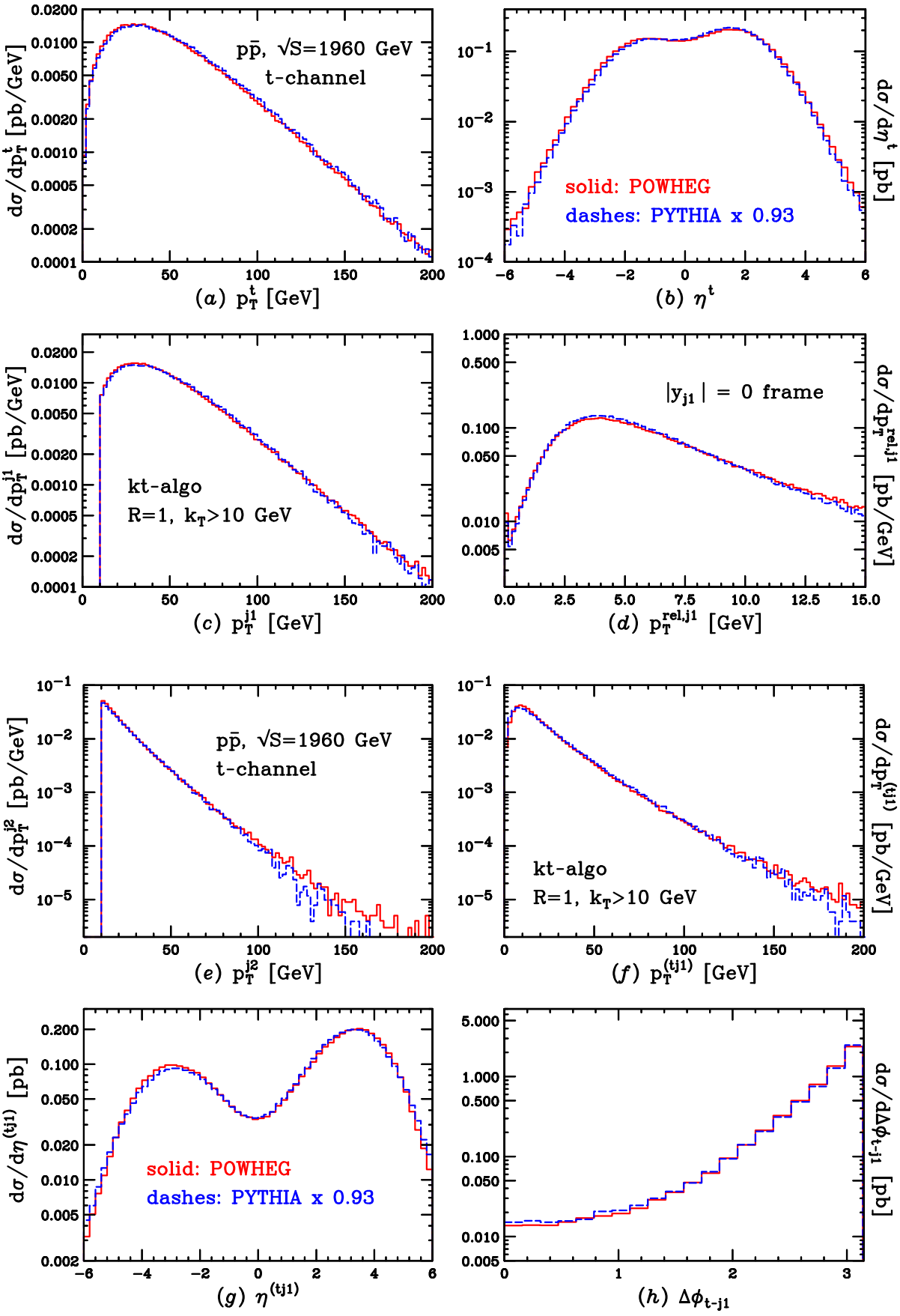

Figure 4.4: Comparisons between POWHEG and PYTHIA results for t-channel top production at the Tevatron $p\bar{p}$ collider.

A similar set of comparisons is presented in fig. 4.3 for the t-channel production mechanism, always at the Tevatron. The agreement between POWHEG and MC@NLO is as good as before for inclusive quantities, or even better. In particular, the slight mismatch in the top transverse-momentum distribution completely disappears, as one can see in plot (a). For all the other plots, considerations similar to the s-channel case remain valid.

In fig. 4.4 the same set of plots are shown, comparing POWHEG and PYTHIA. We have good agreement for most distributions, after applying an appropriate K factor to the PYTHIA results. Only minor differences are present in the high-$p_{\rm T}$ tail of distributions in panels (e) and (f).

As a final comparison, in the left panel of fig. 4.5, we show $p_{\rm T}^{\bar{B}}$, the transverse-momentum spectrum of the hardest $\bar{b}$-flavoured hadron, after imposing the rapidity cut $|y_{\bar{B}}| < 3$. In the t-channel, this hadron will come most probably from an initial-state gluon undergoing a $b\bar{b}$ splitting. The b quark is then turned into a t while the $\bar{b}$ quark is showered and hadronized. We see that, while POWHEG and MC@NLO are in a fair agreement in the medium- and high-$p_{\rm T}$ range, sizable differences are present at low $p_{\rm T}$. These discrepancies are most probably due to the disagreement that one can notice in the $y_{\bar{B}}$ distribution (right panel of fig. 4.5), and to a smaller extent to a different implementation of the inclusion of b-mass effects by both programs (just before the showering stage).

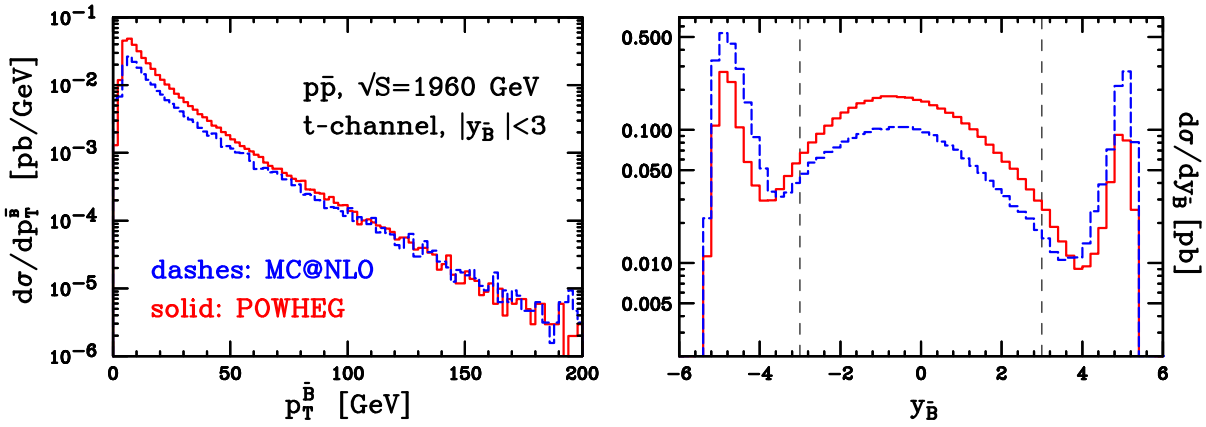

Figure 4.5: Comparisons between POWHEG and MC@NLO results for the hardest $\bar{b}$-flavoured hadron transverse momentum (left) and rapidity (right), for t-channel top production at the Tevatron $p\bar{p}$ collider. Rapidity cuts are highlighted.

We also plot in fig. 4.6 the same quantities comparing POWHEG interfaced to PYTHIA with respect to PYTHIA alone. A large mismatch in the high-$p_{\rm T}^{\bar{B}}$ spectrum is clearly visible in the left panel. This observable is particularly sensitive to real matrix-element effects, not present in PYTHIA. Concerning the low-$p_{\rm T}^{\bar{B}}$ behaviour, we see that here the difference

is much less pronounced than in fig. 4.5. Furthermore, the aforementioned mismatch in the $y_{\bar{B}}$ distribution is no longer present, as one can see in the right panel.

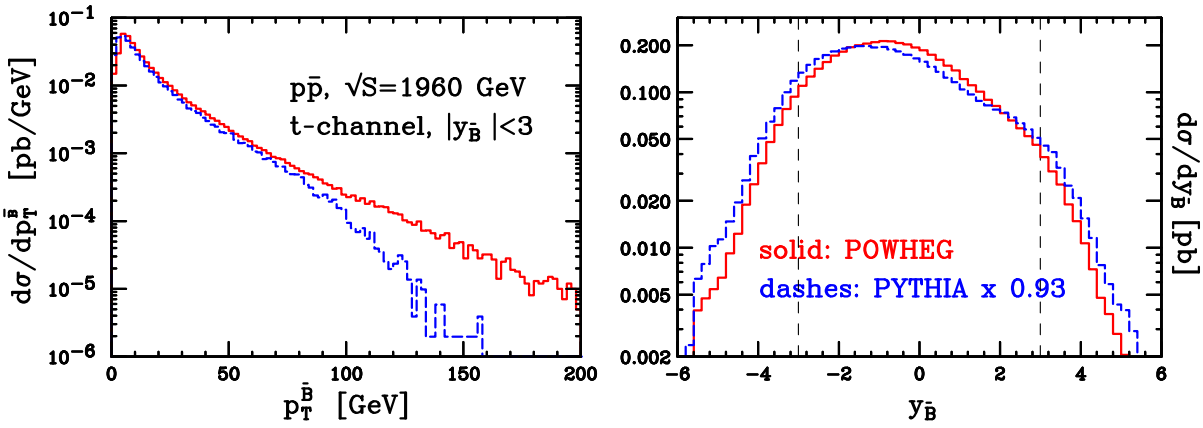

Figure 4.6: Comparisons between POWHEG and PYTHIA results for the hardest $\bar{b}$-flavoured hadron transverse momentum (left) and rapidity (right), for t-channel top production at the Tevatron $p\bar{p}$ collider. Rapidity cuts are highlighted.

By comparing figs. 4.5 and 4.6, one immediately notices the different behaviours of the two Monte Carlo programs that we are interfacing to. We observe that the HERWIG shower and hadronization create an enhancement at large values of $|y_{\bar{B}}|$, which is not present in PYTHIA. This feature is known to the HERWIG authors,[13] and is traced back to a mismatch of the scale at which backward evolution is switched off, with the scale at which the b-quark density is turned on in the pdf's. The effect is more pronounced in MC@NLO, probably due to the fact that POWHEG does not rely on HERWIG for the generation of the hardest splitting.

4.3.2 LHC results

In figs. 4.7 and 4.8 similar results are reported for the LHC pp collider. Only plots for the t-channel production are shown, the s-channel process having a negligible impact at the LHC.

Figure 4.7 contains comparisons between POWHEG, MC@NLO and NLO results. No significant differences with respect to what we observed at the Tevatron arise in any plot, so that we refer to the previous section for comments.

In the PYTHIA and POWHEG comparisons shown in fig. 4.8, we immediately notice that the POWHEG enhancement of high-$p_{\rm T}$ tails in panels (e) and (f) is here more marked, even if

[13] See for example M. Seymour's talk in `http://bwhcphysics.lbl.gov/vplusjets.html`.

still small. This may again be related to the lack of matrix-element corrections in PYTHIA, resulting in larger discrepancies at the LHC with respect to the Tevatron case.

In panels (c) and (e), one can also notice different low-p_{T} shapes with respect to the same plots showing the POWHEG+HERWIG results of fig. 4.7. We have verified that these differences are due to the inclusion of multiple interactions (MI) in the default PYTHIA.[14] If we limit ourselves to the results without MI (i.e. setting MSTP(81)=0 in PYTHIA), the agreement is much better.

[14]These account for events where more than one parton pair in the same incoming hadrons give rise to hard interactions.

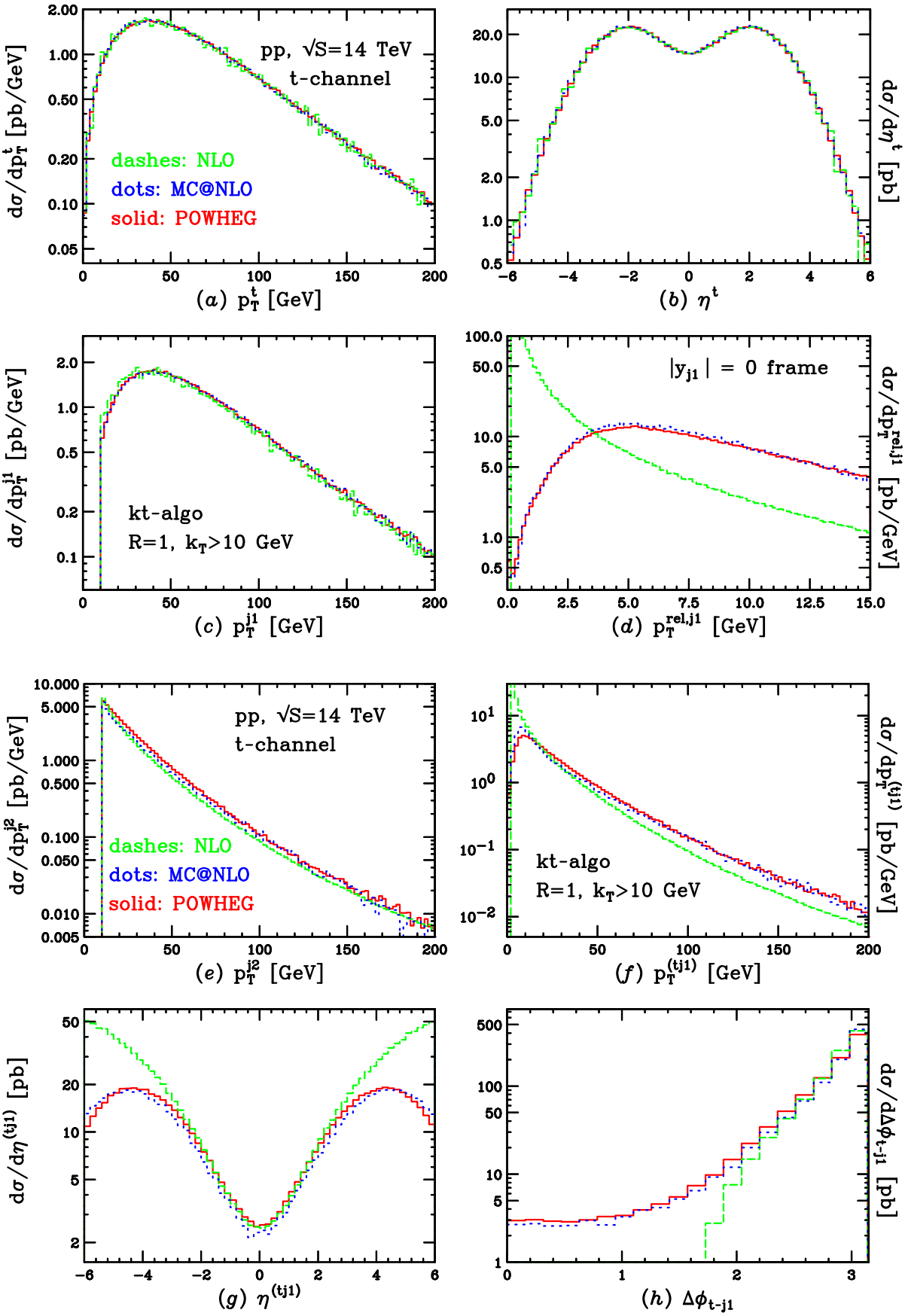

Figure 4.7: Comparisons between POWHEG, MC@NLO and NLO results for t-channel top production at the LHC pp collider.

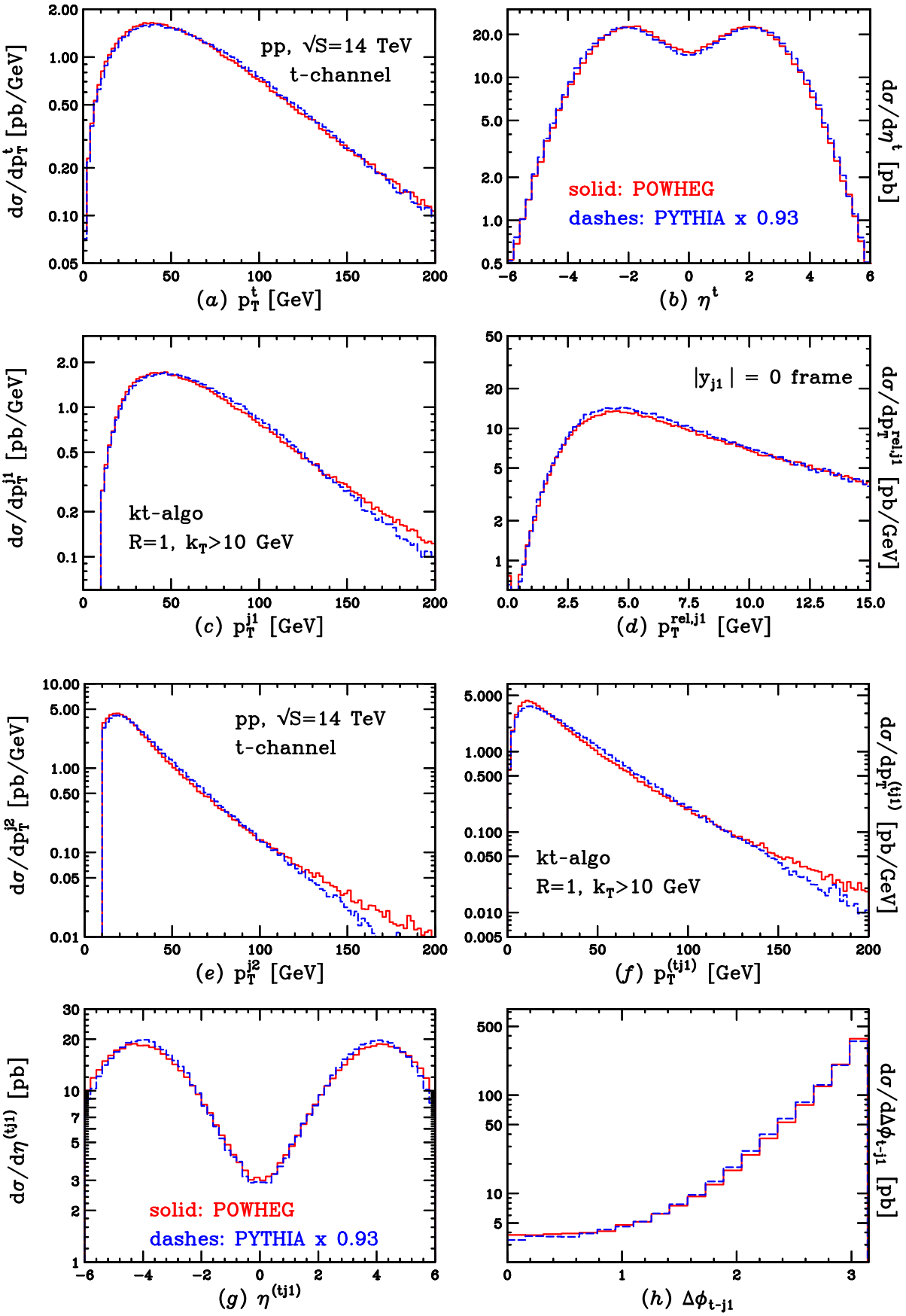

Figure 4.8: Comparisons between POWHEG and PYTHIA results for t-channel top production at the LHC pp collider.

4.3.3 Top-quark decay

As explained in sec. 4.2.3, in our calculation we have implemented spin correlations in top decay. Sizable effects are thus visible when comparing our results with SMC programs that do not implement them. `MC@NLO` accounts for these effects with approximately the same method that we use. Hence, we expect to have good agreement with `MC@NLO` and visible discrepancies when comparing with `PYTHIA`.

Due to the V-A structure of the weak current, the best observables to highlight eventual discrepancies are those involving the angle between the charged lepton $\bar{\ell}$ coming from top decay and the direction of the down-type quark entering the W vertex involved in top production, as shown in fig. 4.9.

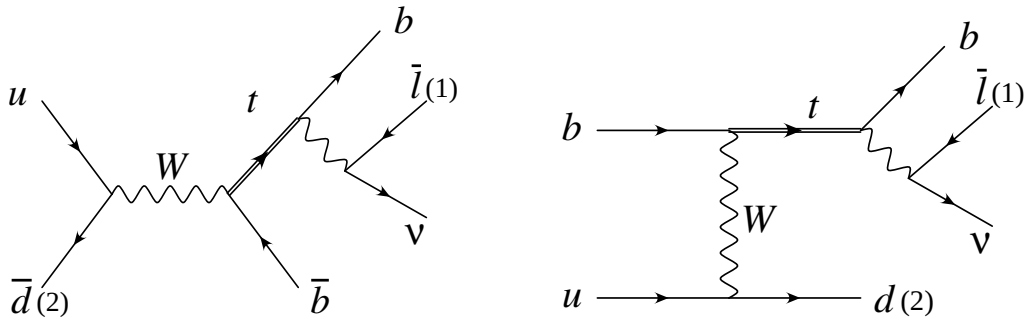

(a) s-channel (b) t-channel

Figure 4.9: Lepton (1) and down-type quark (2) used to study spin correlations in top decay.

At the Born level, the down-type quark direction is possibly identified with the beam axis for s-channel production, while, for t-channel production, it often corresponds to the hardest jet axis (see ref. [105] for further details).

For sake of comparison, we have set the top virtuality $M^2 = m_t^2$ and we have taken the values $\Gamma_t = 1.7$ GeV and $\Gamma_W = 2.141$ GeV in the evaluation of upper bounds of the decay amplitudes in eq. (4.84) and in the decayed matrix element $\mathcal{M}^f_{\rm dec}$.

In fig. 4.10 we show comparisons for the Tevatron $p\bar{p}$ collider. On the left panel, we plot the s-channel differential cross section as a function of $\cos\chi$, where χ is the angle between the hardest charged lepton $\bar{\ell}$, which we assume coming from top decay, and the direction of the incoming parton with negative rapidity (the $\ominus$ direction of the z axis), as seen in the top rest frame. Such angle is sensitive to the spin correlation between $\bar{\ell}$ and the incoming $\bar{d}$ quark, which, at the Tevatron, is pulled out mostly from the antiproton traveling in the negative direction. On the right panel, we plot the t-channel differential cross section as a function of $\cos\theta$, where θ is the angle between $\bar{\ell}$ and the hardest jet,

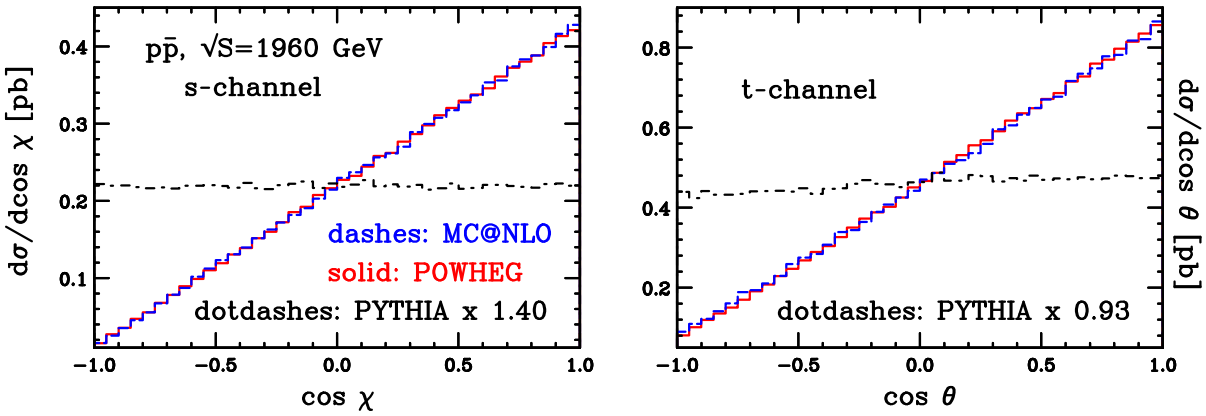

Figure 4.10: Comparisons between POWHEG, MC@NLO and PYTHIA angular correlations for s- (left) and t-channel (right) top production at the Tevatron $p\bar{p}$ collider.

always evaluated in the top rest frame. In both plots, we observe a remarkable good agreement with MC@NLO and the expected discrepancy with PYTHIA, that only performs a spin-averaged top decay.

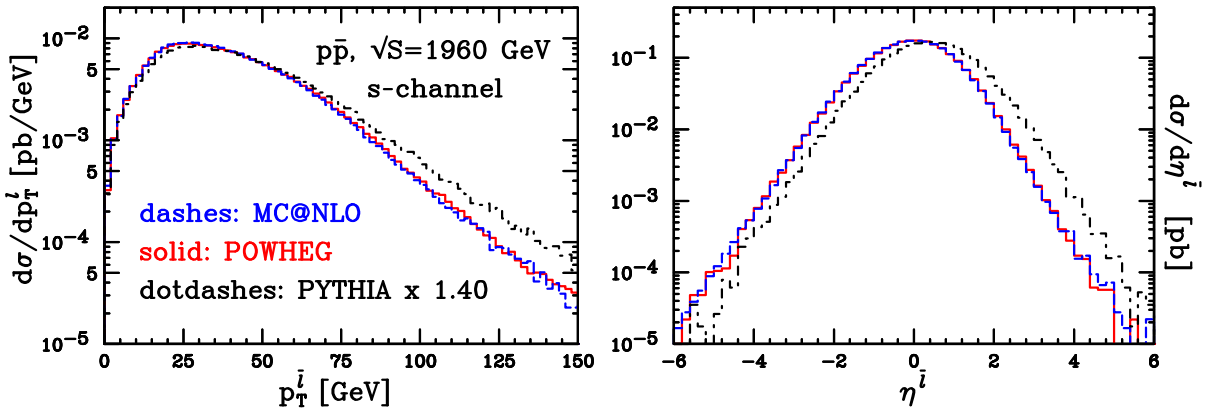

Figure 4.11: Comparisons between POWHEG, MC@NLO and PYTHIA transverse momentum and pseudorapidity of the lepton coming from the top decay, for s-channel top production at the Tevatron $p\bar{p}$ collider.

In fig. 4.11 we plot the transverse momentum and pseudorapidity of the hardest charged lepton, for s-channel production at Tevatron. The difference between PYTHIA and POWHEG (or MC@NLO) can be shown to arise because of spin-correlation effects. To test this, we run POWHEG with an undecayed top in the final state, leaving PYTHIA to perform the decay: after rescaling the plots with the appropriate K factor, we obtain the same behaviour as PYTHIA standalone.

In fig. 4.12, the same distributions of fig. 4.10 are shown for the LHC collider. The same considerations done for the Tevatron apply for the LHC results.

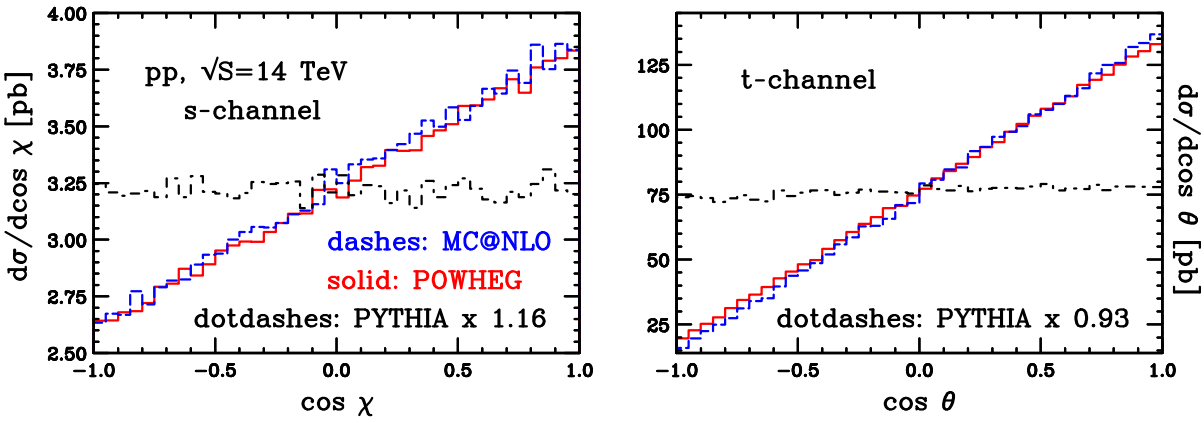

Figure 4.12: Comparisons between POWHEG, MC@NLO and PYTHIA angular correlations for *s*- (left) and *t*-channel (right) top production at the LHC *pp* collider.

We also tried to apply cuts similar to those used in ref. [99], namely

$$p_{\mathrm{T}}^{B} \geq 20 \text{ GeV}\,, \qquad |\eta^{B}| \leq 2\,, \tag{4.89}$$

$$p_{\mathrm{T}}^{\bar{\ell}} \geq 10 \text{ GeV}\,, \qquad |\eta^{\bar{\ell}}| \leq 2.5\,, \tag{4.90}$$

$$p_{\mathrm{T}}^{\nu} \geq 20 \text{ GeV}\,. \tag{4.91}$$

We denote with the superscript B the top jet, i.e. the jet that contains the hardest b-flavoured hadron (not the $\bar{b}$). In single-top processes, this comes almost exclusively from the bottom quark emerging from top decay. In t-channel production, in order to isolate a central hardest light jet, we apply the further cuts

$$p_{\mathrm{T}}^{j_1} \geq 20 \text{ GeV}\,, \qquad |\eta^{j_1}| \leq 2.5\,. \tag{4.92}$$

Results for the Tevatron collider are reported in fig. 4.13.

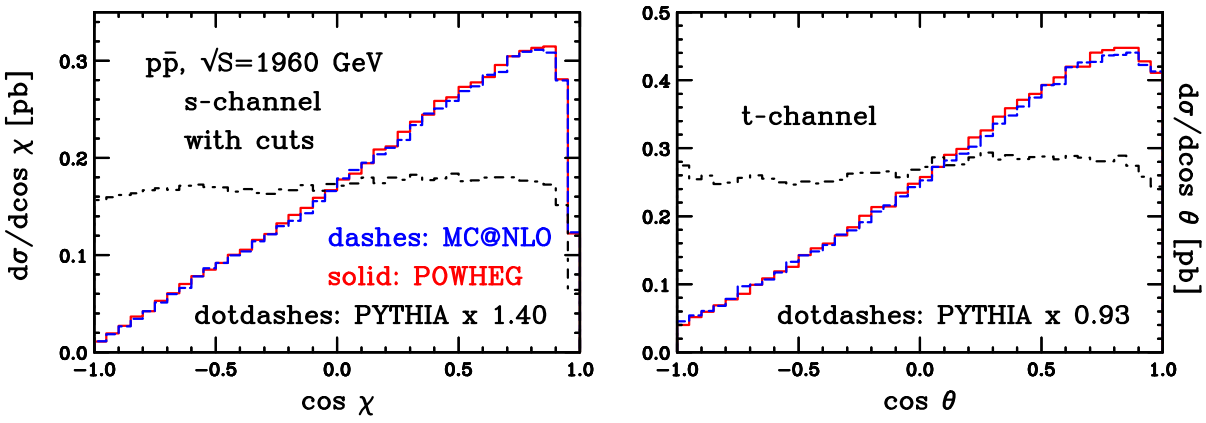

Figure 4.13: Comparisons between POWHEG, MC@NLO and PYTHIA angular correlations for s- (left) and t-channel (right) top production at the Tevatron $p\bar{p}$ collider. Results are obtained with the cuts described in the text.

4.3.4 Dips in the rapidity distributions

In the previous chapter, we extensively discussed the problem of rapidity dips. In particular, we have seen that the presence of sizable mismatches between POWHEG and MC@NLO results in the rapidity difference between the hardest jet and the heavy system recoiling against it can be reasonably explained by expanding an approximate estimate of the MC@NLO hardest emission formula. In particular, we found that for processes where the K factor is small, that mismatch is expected to be reduced.

In single-top production, the suitable quantity where to observe this mismatch is the rapidity difference between the top-quark–hardest-jet system and the next-to-hardest jet. As one can see in fig. 4.14, in this case a dip in the central rapidity region is already present at the next-to-leading-order. This feature may mask an eventual dip in MC@NLO. However, the two showered results are fairly similar, with the dip being slightly more pronounced in MC@NLO.

This result agrees with the explanation that we gave in the previous chapter. In fact, for t-channel single-top production, the K factor is close to one. Therefore, in eq. (3.55) one has $\bar{B}^{\rm MC}/B \approx 1$, and no effects coming from the term $R^{\rm MC}(\mathbf{\Phi}_{n+1})\, d\bar{\mathbf{\Phi}}_n\, d\Phi^{\rm MC}_{\rm rad}$ are then expected. This, together with the fact that the fixed NLO result already presents a central dip for $y^{(t\,j_1)} - y^{j_2}$, results in the small discrepancies between MC@NLO and POWHEG that can be seen in fig. 4.14.

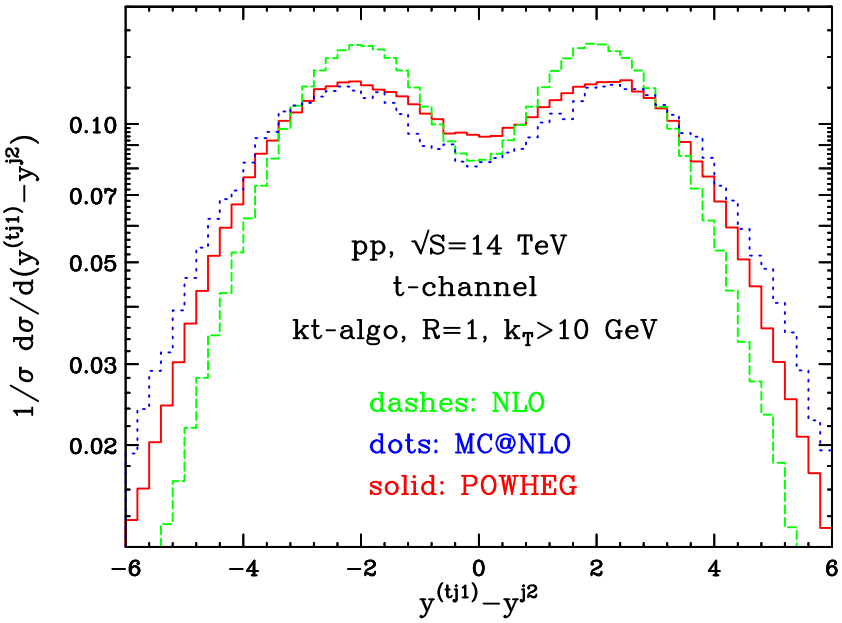

Figure 4.14: Comparison between POWHEG, MC@NLO and NLO results for the rapidity difference between the rapidity of the top-quark–hardest-jet system and the rapidity of the next-to-hardest jet, for t-channel top production at the LHC pp collider. Plots are normalized to the total cross section.

4.4 Conclusions

In this chapter, we have described a complete implementation of s- and t-channel single-top production at next-to-leading-order in QCD, in the POWHEG framework. This is the first POWHEG implementation of a process where both initial- and final-state radiation is present. The calculation for top production has been performed within the Frixione-Kunszt-Signer subtraction approach [16,17], modified according to ref. [2]. We accounted for spin-correlation effects in top-quark decay with a method analogous to the one proposed in ref. [99]. The results of our work have been extensively compared with the MC@NLO and PYTHIA Shower Monte Carlo programs, together with the fixed next-to-leading-order calculation, both for the Tevatron and for the LHC.

The MC@NLO results are in good agreement with POWHEG, also for quantities sensitive to angular correlations in top decay.

The PYTHIA results, normalized to the total NLO cross section, show fair agreement with ours for inclusive quantities that do not involve the top-decay products. As expected, we have found sizable mismatches with PYTHIA when considering distributions involving top-decay products, such as angular-correlation measurements and charged-lepton trans-

verse momentum and pseudorapidity. We have also found differences between our results and the MC@NLO and PYTHIA ones in the hardest $\bar{b}$-flavoured hadron transverse momentum and rapidity. The high-$p_{\rm T}$ mismatch with PYTHIA may be a consequence of the lack of matrix-element corrections in the latter, while we attribute the low-$p_{\rm T}$ disagreement with MC@NLO to the sizable difference that we observe in the rapidity distribution.

We also tried to study the problem of rapidity dips for this process. Despite the fact that in this case the variable suited to study these effects is not obvious, we find results that are in qualitative agreement with the explanation that we gave in sec. 3.3.3.

Conclusions

In recent years, the merging of NLO QCD calculations with parton showers has been one of the main research topic in the development of available event generators. The main reason to go in this direction is that high-precision QCD calculations are important as well as Shower Monte Carlo event generators for the phenomenology of collider physics. Therefore, by merging the benefits of the two approaches, the experimental community would have the possibility to easily perform simulations with event generators more accurate than the traditional ones, improving in this way the reliability of the results.

From a theoretical point of view, the inclusion of NLO corrections in shower Monte Carlo programs is a non-trivial task, because a parton shower already includes approximate NLO corrections. Therefore the main problem is to avoid the double-counting of emissions from the NLO calculation with emissions due to the parton shower.

In this thesis we described in detail how this problem is solved with the POWHEG method, and we then showed results for single vector boson production and single-top (s- and t-channel) production in hadronic collisions.

In chapter 1 we started by describing how fixed order calculations are performed and by summarizing the relevant results for the Catani-Seymour and the Frixione-Kunszt-Signer subtraction methods. We also gave a review on SMC programs, mainly focused on the description of the parton shower algorithm.

Next, in chapter 2 we illustrated the drawbacks and benefits of NLO calculations and parton showers, highlighting the features that a matching procedure has to preserve. We also showed how the problem of double-counting typically arises. After a brief description of MC@NLO, we then described in detail the POWHEG method, which was used to produce the results of this thesis, presented in chapter 3 and 4.

Single vector boson production has been implemented by taking in full account finite width effects, Z/γ interference and angular correlations of decay products. A generalization of the original formulation of the POWHEG method has been introduced, in order to correctly generate events whose leading-order cross section vanishes in some phase-space regions. Furthermore, to implement single vector-boson production, the Catani-Seymour

subtraction scheme was used for the first time in the POWHEG framework.

Results have been extensively compared with those obtained with other Monte Carlo generators. In particular, good agreement has been observed with the MC@NLO results and with the available Tevatron data. Differences have been discussed, and their origin traced back.

Single-top hadroproduction has been implemented for the s- and t-channel production mechanisms. In this case, the subtraction scheme used to deal with infrared divergences has been the one by Frixione, Kunszt and Signer. Matrix elements for on-shell, undecayed top quarks have been used for the NLO calculation. In order to produce events where angular correlations are retained, spin correlation effects have been included by generating top-decay products with tree-level accuracy, according to a method already present in literature.

We presented results for various observables, both for the Tevatron and the LHC, for s and t-channel production. We find fair agreement with MC@NLO for almost all the distributions and give some explanations about the differences we found. Some comparisons are carried out also with respect to PYTHIA, showing that some distributions are affected by the inclusion of NLO effects, which are not included in PYTHIA. For observables sensitive to spin correlation effects, we found agreement with MC@NLO, and the expected disagreement with PYTHIA, where these effects are not taken into account.

In summary, the good agreement between POWHEG and MC@NLO results, already observed for other processes, confirms that the former method can be considered a valid alternative to the latter.

Concerning the processes discussed in this thesis, deeper phenomenological studies can be performed with the use of the POWHEG method. In particular, as an example, the matching of a parton shower with the (recently appeared) calculation of NLO single-top t-channel production with the exact dependence on the b-quark mass can yield improvements in the accuracy of the predictions for this process, which will be studied extensively at the LHC.

Appendix A

QCD Feynman rules

In the following, we report the Feynman rules that follow from the QCD Lagrangian density given in eq. (1.16). Quarks, gluons and ghosts are indicated as usual, with solid, wrapped and dashed lines.

Propagators

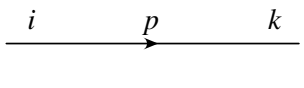

$$= \delta^{ik} \frac{i}{\not{p} - m + i\epsilon}$$

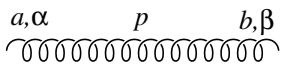

$$= \delta^{ab} \frac{i}{p^2 + i\epsilon} \left(-g^{\alpha\beta} + (1 - \xi) \frac{p^\alpha p^\beta}{p^2} \right)$$

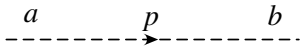

$$= \delta^{ab} \frac{i}{p^2 + i\epsilon}$$

Vertexes

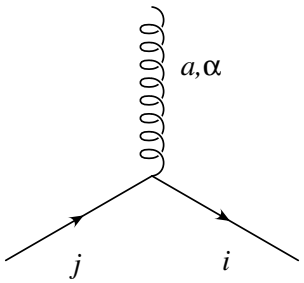

$$= -ig\gamma^\alpha t^a_{ij}$$

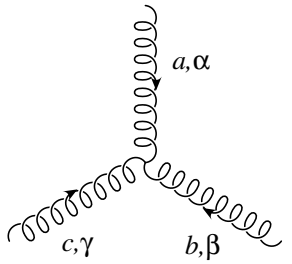

$$= -gf^{abc}\left[g^{\alpha\beta}\left(p_a - p_b\right)^{\gamma} + g^{\beta\gamma}\left(p_b - p_c\right)^{\alpha} + g^{\gamma\alpha}\left(p_c - p_a\right)^{\beta}\right]$$

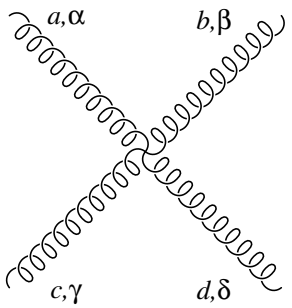

$$= -ig^2\left[f^{eac}f^{ebd}\left(g^{\alpha\beta}g^{\gamma\delta} - g^{\alpha\delta}g^{\gamma\beta}\right) + f^{ead}f^{ebc}\left(g^{\alpha\beta}g^{\gamma\delta} - g^{\alpha\gamma}g^{\beta\delta}\right) + f^{eab}f^{ecd}\left(g^{\alpha\gamma}g^{\beta\delta} - g^{\alpha\delta}g^{\beta\gamma}\right)\right]$$

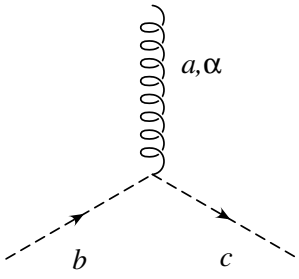

$$= gf^{abc}p_c^{\alpha}$$

Appendix B

Upper bounding functions

In this Appendix, we report the derivation of the upper bounding function used to generate the hardest radiation according to the veto technique.

Here we describe the case relevant for the single-vector boson implementation, where the Catani-Seymour radiation variables have been used. Therefore, we refer to the equations in chapter 3.

We call $\Delta_U(p_T^2)$ the Sudakov form factor obtained with the upper bounding function of eq. (3.44). Using the definitions of eqs. (3.22) and (3.17)

$$d\Phi_{\rm rad} = \frac{M^2}{16\pi^2}\,\frac{d\phi}{2\pi}\,dv\,\frac{dx}{x^2}\,\theta(v)\,\theta\!\left(1-\frac{v}{1-x}\right)\theta(x(1-x))\,\theta(x-\bar{x}_{\oplus}) \tag{B.1}$$

$$k_T^2 = \frac{M^2}{x}(1-x-v)\,v\;, \tag{B.2}$$

we write

$$\begin{aligned}\frac{\log\Delta_U(p_T^2)}{-N} &= \int_{\bar{x}}^1\frac{dx}{x^2}\int_0^{1-x}dv\,\frac{\alpha_s(k_T^2)}{2v}\frac{x^2}{1-x-v}\,\theta\big(k_T^2-p_T^2\big)\\ &= \int_{\bar{x}}^1\frac{dx}{x}\int_0^{1-x}dv\,\frac{\alpha_s(k_T^2)}{2}\,\frac{M^2}{k_T^2}\,\theta\big(k_T^2-p_T^2\big)\\ &= \int_{p_T^2}^{\infty}\frac{dk_T^2}{k_T^2}\,\frac{\alpha_s(k_T^2)}{2}\int_0^1 dv\int_{\bar{x}}^1\frac{dx}{x}\,\theta(1-x-v)\,M^2\,\delta\!\left(\frac{M^2}{x}(1-x-v)v-k_T^2\right)\;,\end{aligned}$$

where, for ease of notation, we have dropped the $\oplus$ and $q\bar{q}$ labels on N and $\bar{x}$. We perform the x integration using the δ function

$$\int\frac{dx}{x}\,M^2\,\delta\!\left(\frac{M^2}{x}(1-x-v)v-k_T^2\right)=\frac{1}{k_T^2/M^2+v},\qquad x=\frac{M^2v(1-v)}{k_T^2+M^2v}\;. \tag{B.3}$$

Notice that $x < 1$, and

$$\theta\left(1 - v - \frac{M^2 v(1-v)}{k_T^2 + M^2 v}\right) = \theta\left(1 - v\frac{k_T^2 + M^2}{k_T^2 + M^2 v}\right) = 1. \tag{B.4}$$

The only remaining condition on x is $x \geqslant \bar{x}$. We thus get

$$\frac{\log \Delta_U(p_T^2)}{-N} = \int_{p_T^2}^{\infty} \frac{dk_T^2}{k_T^2} \frac{\alpha_s(k_T^2)}{2} \int_0^1 \frac{dv}{k_T^2/M^2 + v}\, \theta\left(\frac{M^2 v(1-v)}{k_T^2 + M^2 v} - \bar{x}\right). \tag{B.5}$$

We must find the conditions implied by the theta function upon v. For

$$k_T^2 < k_{T\max}^2 = \frac{M^2(1-\bar{x})^2}{4\bar{x}}\,, \tag{B.6}$$

the θ function is satisfied if $v_- < v < v_+$, where

$$v_\pm = \frac{1 - \bar{x} \pm \sqrt{(1-\bar{x})^2 - 4\,\bar{x}\,\frac{k_T^2}{M^2}}}{2}\,. \tag{B.7}$$

We thus have

$$\frac{\log \Delta_U(p_T^2)}{-N} = \int_{p_T^2}^{k_{T\max}^2} \frac{dk_T^2}{k_T^2} \frac{\alpha_s(k_T^2)}{2} \log \frac{\frac{k_T^2}{M^2} + v_+}{\frac{k_T^2}{M^2} + v_-}\,. \tag{B.8}$$

The k_T^2 integral is still too complex to be performed analytically. We thus resort another time to the veto method, by finding an upper bound to the integrand. We have

$$\frac{\frac{k_T^2}{M^2} + v_+}{\frac{k_T^2}{M^2} + v_-} \leqslant \frac{\frac{k_T^2}{M^2} + 1}{\frac{k_T^2}{M^2}} = \frac{M^2}{k_T^2} + 1 \leqslant \frac{M^2}{k_T^2} + \frac{k_{T\max}^2}{k_T^2} = \frac{M^2(1+\bar{x})^2}{4\,\bar{x}\,k_T^2}. \tag{B.9}$$

We thus define

$$q^2 = \frac{M^2(1+\bar{x})^2}{4\,\bar{x}\,k_T^2}, \tag{B.10}$$

and introduce a new Sudakov form factor

$$\frac{\log \tilde{\Delta}_U(p_T^2)}{-N} = \int_{p_T^2}^{k_{T\max}^2} \frac{dk_T^2}{k_T^2} \frac{\alpha_U(k_T^2)}{2} \log \frac{q^2}{k_T^2}, \tag{B.11}$$

where $\alpha_U(k_T^2)$ has the form of the one-loop running coupling constant

$$\alpha_U(k_T^2) = \frac{1}{b \log \frac{k_T^2}{\Lambda_U^2}}, \tag{B.12}$$

and is required to satisfy the bound $\alpha_U(k_T^2) \geqslant \alpha_s(k_T^2)$ in the allowed range for k_T^2. The integral in eq. (B.11) is now easily performed, and we get

$$\tilde{\Delta}_U(p_T^2) = \exp\left\{ -\frac{N}{2b} \left[\log \frac{q^2}{\Lambda_U^2} \log \frac{\log \frac{k_{T\,\max}^2}{\Lambda_U^2}}{\log \frac{p_T^2}{\Lambda_U^2}} - \log \frac{k_{T\,\max}^2}{p_T^2} \right] \right\}. \tag{B.13}$$

The generation of the radiation variables is then performed starting with $\tilde{\Delta}_U(p_T^2)$, using the veto procedure to obtain the $\Delta_U(p_T^2)$ distribution. Further vetoing is then used to obtain the correct R/B generated distribution.

Appendix C

Integration of FKS plus distributions

In this Appendix we describe how the integration of the real terms present in the single-top cross section has been performed. Since the subtraction scheme used is the FKS one, divergences are subtracted with plus distributions. In particular, here we explicitly show how to deal with the action of two plus distributions in presence of integration variables which are not independent.

In the following, we describe the manipulations needed to integrate over the ISR phase space, which, from this point of view, is more complicated with respect to the FSR one. In fact, we can notice that, in the FSR case, the ξ variable does not span the whole range $[0, 1]$, but its maximum value does not depend on the value of y.[1] Therefore, in this case the action of plus distributions is simpler with respect to ISR, and we do not report it here. Moreover, plus distributions are present also in the collinear remnants. With the change of variable $z = 1 - \xi$, and with manipulations similar to those described in the following, one can obtain explicit results also in that case.

We now describe the integration over the ISR phase space.

From eq. (4.23), we can see that the FKS parameterization of the real phase space for ISR is such that the maximum value for ξ is a function of y. Therefore, after having separated real terms on different singular regions by means of the $\mathcal{S}$ functions, we are left with integrals of the form[2]

$$I(\bar{\mathbf{\Phi}}_2) = \int_0^{2\pi} d\phi \int_{-1}^{1} dy \int_0^{\xi_{\rm M}(y)} d\xi \left(\frac{1}{1-y}\right)_+ \left(\frac{1}{\xi}\right)_+ f(\bar{\mathbf{\Phi}}_2, \xi, y, \phi)\,, \tag{C.1}$$

[1] In our case, the maximum value for ξ is a function of the mass of the recoiling system (eq. (4.37)), which is equal to the top-quark virtuality.

[2] Here we are assuming to look to terms projected onto the $\oplus$ region. Therefore we write the $1/(1-y)_+$ distribution. For the $\ominus$ region, manipulations are similar, with obvious modifications.

where

$$f(\bar{\mathbf{\Phi}}_2, \xi, y, \phi) = \left[(1-y)\ \xi^2\, R(\bar{\mathbf{\Phi}}_2, \xi, y, \phi)\right] \frac{J^{\rm ISR}_{\rm rad}\left(\bar{\mathbf{\Phi}}_2, \xi, y, \phi\right)}{\xi}\,. \tag{C.2}$$

With R, we denote, generically, a real squared amplitude, divided by the flux factor, multiplied for the corresponding luminosity function and, if needed, for the proper $\mathcal{S}$ function. Observe that all the terms integrated over the $\Phi^{\rm ISR}_{\rm rad}$ phase space in eq. (4.64) and (4.66) have this form.

First of all, we rescale ξ, by performing the change of variable

$$\xi = \xi_{\rm M}(y)\ \tilde{\xi}\,. \tag{C.3}$$

Now, in the integration over ξ, we make use of the following identity

$$\int_0^{\xi_{\rm M}(y)} d\xi \left(\frac{1}{\xi}\right)_+ F(\xi, y) = \int_0^1 d\tilde{\xi} \left[\left(\frac{1}{\tilde{\xi}}\right)_+ + \log \xi_{\rm M}(y)\ \delta(\tilde{\xi})\right] F(\xi_{\rm M}(y)\tilde{\xi}, y)\,, \tag{C.4}$$

where F denotes a generic function of ξ and y.

Using the previous identity in eq. (C.1), we get:

$$\begin{aligned} I(\bar{\mathbf{\Phi}}_2) &= \int_0^{2\pi} d\phi \int_{-1}^1 dy \frac{1}{(1-y)_+} \int_0^1 d\tilde{\xi} \left[\frac{f(\tilde{\xi}\xi_{\rm M}(y), y, \phi) - f(0, y, \phi)}{\tilde{\xi}} + \log \xi_{\rm M}(y) f(0, y, \phi)\right] \\ &= \int_0^{2\pi} d\phi \int_{-1}^1 dy \int_0^1 d\tilde{\xi} \frac{1}{(1-y)} \left[\frac{f(\tilde{\xi}\xi_{\rm M}(y), y, \phi) - f(0, y, \phi)}{\tilde{\xi}}\right. \\ &\quad \left. - \frac{f(\tilde{\xi}\xi_{\rm M}(1), 1, \phi) - f(0, 1, \phi)}{\tilde{\xi}} + \Big(\log \xi_{\rm M}(y) f(0, y, \phi) - \log \xi_{\rm M}(1) f(0, 1, \phi)\Big)\right], \end{aligned} \tag{C.5}$$

where, for ease of notation, we have omitted the dependence of f on the $\bar{\mathbf{\Phi}}_2$ phase space.

Now $\tilde{\xi}$ lives in the range $[0, 1]$. Therefore, by mapping the variables y and ϕ onto a unit cube, and inserting the proper jacobians, we obtain an expression suited to define the contribution of a generic (ISR-projected) real subprocess, that we named here R, to the function $\tilde{B}$ (see eq. (4.70)).

Since the f function is evaluated in $\xi = 0$ and/or $y = 1$, it is apparent that we need to calculate expressions for the soft and collinear limits in terms of the FKS variables. More precisely, we need to evaluate analytically the limits of the expression $\left[(1-y)\ \xi^2\, R(\bar{\mathbf{\Phi}}_2, \xi, y, \phi)\right]$, as we did in sec. (4.1.3).

As already stated, an analogous manipulation is used to handle the plus distributions

needed to subtract FSR singularities and the soft singularities of collinear remnants.

Bibliography

[1] P. Nason, *A new method for combining NLO QCD with shower Monte Carlo algorithms*, *JHEP* **11** (2004) 040, [hep-ph/0409146].

[2] S. Frixione, P. Nason, and C. Oleari, *Matching NLO QCD computations with Parton Shower simulations: the POWHEG method*, *JHEP* **11** (2007) 070, [arXiv:0709.2092].

[3] F. Ambroglini *et al.*, *Proceedings of the Workshop on Monte Carlo's, Physics and Simulations at the LHC PART I*, 0902.0293.

[4] M. E. Peskin and D. V. Schroeder, *An Introduction to quantum field theory*, . Reading, USA: Addison-Wesley (1995) 842 p.

[5] R. K. Ellis, W. J. Stirling, and B. R. Webber, *QCD and collider physics*, *Camb. Monogr. Part. Phys. Nucl. Phys. Cosmol.* **8** (1996) 1–435.

[6] T. Muta, *Foundations of quantum chromodynamics: An Introduction to perturbative methods in gauge theories*, *World Sci. Lect. Notes Phys.* **5** (1987) 1–409.

[7] G. Dissertori, I. G. Knowles, and M. Schmelling, *Quantum Chromodynamics: High energy experiments and theory*, . Oxford, UK: Clarendon (2003) 538 p.

[8] P. Nason, *Introduction to QCD*, . Prepared for The 1997 European School of High-Energy Physics, Menstrup, Denmark, 25 May - 7 Jun 1997.

[9] M. L. Mangano, *Introduction to QCD*, . Prepared for 1998 European School of High-Energy Physics, St. Andrews, Scotland, 23 Aug - 5 Sep 1998.

[10] J. Pumplin *et al.*, *New generation of parton distributions with uncertainties from global QCD analysis*, *JHEP* **07** (2002) 012, [hep-ph/0201195].

[11] S. Catani and M. H. Seymour, *A general algorithm for calculating jet cross sections in NLO QCD*, *Nucl. Phys.* **B485** (1997) 291–419, [hep-ph/9605323].

[12] S. Catani, S. Dittmaier, M. H. Seymour, and Z. Trocsanyi, *The dipole formalism for next-to-leading order QCD calculations with massive partons*, *Nucl. Phys.* **B627** (2002) 189–265, [hep-ph/0201036].

[13] T. Kinoshita, *Mass singularities of feynman amplitudes*, *J. Math. Phys.* **3** (1962) 650–677.

[14] T. D. Lee and M. Nauenberg, *Degenerate systems and mass singularities*, *Phys. Rev.* **133** (1964) B1549–B1562.

[15] R. K. Ellis, D. A. Ross, and A. E. Terrano, *The perturbative calculation of jet structure in e+ e- annihilation*, *Nucl. Phys.* **B178** (1981) 421.

[16] S. Frixione, Z. Kunszt, and A. Signer, *Three-jet cross sections to next-to-leading order*, *Nucl. Phys.* **B467** (1996) 399–442, [hep-ph/9512328].

[17] S. Frixione, *A general approach to jet cross sections in QCD*, *Nucl. Phys.* **B507** (1997) 295–314, [hep-ph/9706545].

[18] S. Frixione, E. Laenen, P. Motylinski, and B. R. Webber, *Single-top production in MC@NLO*, *JHEP* **03** (2006) 092, [hep-ph/0512250].

[19] T. Sjostrand, *A model for initial state parton showers*, *Phys. Lett.* **B157** (1985) 321.

[20] G. Marchesini and B. R. Webber, *Monte carlo simulation of general hard processes with coherent qcd radiation*, *Nucl. Phys.* **B310** (1988) 461.

[21] G. Altarelli and G. Parisi, *Asymptotic freedom in parton language*, *Nucl. Phys.* **B126** (1977) 298.

[22] Y. L. Dokshitzer, *Calculation of the Structure Functions for Deep Inelastic Scattering and e^+e^- Annihilation by Perturbation Theory in Quantum Chromodynamics. (In Russian)*, *Sov. Phys. JETP* **46** (1977) 641–653.

[23] L. N. Lipatov, *The parton model and perturbation theory*, *Sov. J. Nucl. Phys.* **20** (1975) 94–102.

[24] V. N. Gribov and L. N. Lipatov, *e^+e^- pair annihilation and deep inelastic ep scattering in perturbation theory*, *Sov. J. Nucl. Phys.* **15** (1972) 675–684.

[25] A. H. Mueller, *On the Multiplicity of Hadrons in QCD Jets*, *Phys. Lett.* **B104** (1981) 161–164.

[26] B. I. Ermolaev and V. S. Fadin, *Log - Log Asymptotic Form of Exclusive Cross-Sections in Quantum Chromodynamics*, *JETP Lett.* **33** (1981) 269–272.

[27] Y. L. Dokshitzer, V. S. Fadin, and V. A. Khoze, *Coherent Effects in the Perturbative QCD Parton Jets*, *Phys. Lett.* **B115** (1982) 242–246.

[28] A. Bassetto, M. Ciafaloni, G. Marchesini, and A. H. Mueller, *Jet Multiplicity and Soft Gluon Factorization*, *Nucl. Phys.* **B207** (1982) 189.

[29] A. Bassetto, M. Ciafaloni, and G. Marchesini, *Jet Structure and Infrared Sensitive Quantities in Perturbative QCD*, *Phys. Rept.* **100** (1983) 201–272.

[30] G. Marchesini and B. R. Webber, *Simulation of qcd jets including soft gluon interference*, *Nucl. Phys.* **B238** (1984) 1.

[31] B. R. Webber, *A QCD Model for Jet Fragmentation Including Soft Gluon Interference*, *Nucl. Phys.* **B238** (1984) 492.

[32] M. Bahr *et al.*, *Herwig++ Physics and Manual*, *Eur. Phys. J.* **C58** (2008) 639–707, [0803.0883].

[33] S. Catani, B. R. Webber, and G. Marchesini, *QCD coherent branching and semiinclusive processes at large x*, *Nucl. Phys.* **B349** (1991) 635–654.

[34] G. Corcella *et al.*, *HERWIG 6: An event generator for hadron emission reactions with interfering gluons (including supersymmetric processes)*, *JHEP* **01** (2001) 010, [hep-ph/0011363].

[35] T. Sjostrand, S. Mrenna, and P. Skands, *Pythia 6.4 physics and manual*, *JHEP* **05** (2006) 026, [hep-ph/0603175].

[36] T. Gleisberg *et al.*, *Sherpa 1.alpha, a proof-of-concept version*, *JHEP* **02** (2004) 056, [hep-ph/0311263].

[37] T. Gleisberg *et al.*, *Event generation with SHERPA 1.1*, *JHEP* **02** (2009) 007, [0811.4622].

[38] G. Marchesini and B. R. Webber, *Monte carlo simulation of general hard processes with coherent qcd radiation*, *Nucl. Phys.* **B310** (1988) 461.

[39] **CDF** Collaboration, F. Abe *et al.*, *Evidence for color coherence in $p\bar{p}$ collisions at $\sqrt{s} = 1.8$ TeV*, *Phys. Rev.* **D50** (1994) 5562–5579.

[40] T. Sjostrand and P. Z. Skands, *Transverse-momentum-ordered showers and interleaved multiple interactions*, *Eur. Phys. J.* **C39** (2005) 129–154, [hep-ph/0408302].

[41] L. Lonnblad, *Ariadne version 4: A program for simulation of qcd cascades implementing the color dipole model*, *Comput. Phys. Commun.* **71** (1992) 15–31.

[42] S. Frixione and B. R. Webber, *Matching NLO QCD computations and parton shower simulations*, *JHEP* **06** (2002) 029, [hep-ph/0204244].

[43] G. Corcella *et al.*, *Herwig 6.5 release note*, hep-ph/0210213.

[44] T. Sjostrand, L. Lonnblad, S. Mrenna, and P. Skands, *Pythia 6.3: Physics and manual*, hep-ph/0308153.

[45] M. Bengtsson and T. Sjostrand, *Coherent Parton Showers Versus Matrix Elements: Implications of PETRA - PEP Data*, *Phys. Lett.* **B185** (1987) 435.

[46] M. H. Seymour, *Matrix element corrections to parton shower algorithms*, *Comp. Phys. Commun.* **90** (1995) 95–101, [hep-ph/9410414].

[47] S. Catani, F. Krauss, R. Kuhn, and B. R. Webber, *Qcd matrix elements + parton showers*, *JHEP* **11** (2001) 063, [hep-ph/0109231].

[48] F. Krauss, *Matrix elements and parton showers in hadronic interactions*, *JHEP* **08** (2002) 015, [hep-ph/0205283].

[49] F. Caravaglios, M. L. Mangano, M. Moretti, and R. Pittau, *A new approach to multi-jet calculations in hadron collisions*, *Nucl. Phys.* **B539** (1999) 215–232, [hep-ph/9807570].

[50] M. L. Mangano, M. Moretti, and R. Pittau, *Multijet matrix elements and shower evolution in hadronic collisions: W b anti-b + (n)jets as a case study*, *Nucl. Phys.* **B632** (2002) 343–362, [hep-ph/0108069].

[51] M. L. Mangano, M. Moretti, F. Piccinini, R. Pittau, and A. D. Polosa, *Alpgen, a generator for hard multiparton processes in hadronic collisions*, *JHEP* **07** (2003) 001, [hep-ph/0206293].

[52] S. Frixione, P. Nason, and B. R. Webber, *Matching NLO QCD and parton showers in heavy flavour production*, *JHEP* **08** (2003) 007, [hep-ph/0305252].

[53] S. Frixione, E. Laenen, P. Motylinski, B. R. Webber, and C. D. White, *Single-top hadroproduction in association with a W boson*, *JHEP* **07** (2008) 029, [arXiv:0805.3067].

[54] O. Latunde-Dada, *Herwig Monte Carlo At Next-To-Leading Order for e^+e^- annihilation and lepton pair production*, *JHEP* **11** (2007) 040, [0708.4390].

[55] A. Papaefstathiou and O. Latunde-Dada, *NLO production of W' bosons at hadron colliders using the MC@NLO and POWHEG methods*, arXiv:0901.3685.

[56] T. Sjostrand, *Monte Carlo generators*, hep-ph/0611247.

[57] E. Boos *et al.*, *Generic user process interface for event generators*, hep-ph/0109068.

[58] P. Nason and G. Ridolfi, *A positive-weight next-to-leading-order Monte Carlo for Z pair hadroproduction*, *JHEP* **08** (2006) 077, [hep-ph/0606275].

[59] Y. L. Dokshitzer, D. Diakonov, and S. I. Troian, *Hard Processes in Quantum Chromodynamics*, *Phys. Rept.* **58** (1980) 269–395.

[60] S. Kawabata, *A New version of the multidimensional integration and event generation package BASES/SPRING*, *Comp. Phys. Commun.* **88** (1995) 309–326.

[61] P. Nason, *MINT: a Computer Program for Adaptive Monte Carlo Integration and Generation of Unweighted Distributions*, arXiv:0709.2085.

[62] S. Alioli, P. Nason, C. Oleari, and E. Re, *NLO vector-boson production matched with shower in POWHEG*, *JHEP* **07** (2008) 060, [arXiv:0805.4802].

[63] S. Alioli, P. Nason, C. Oleari, and E. Re, *NLO single-top production matched with shower in POWHEG: s- and t-channel contributions*, *JHEP* **09** (2009) 111, [0907.4076].

[64] S. Catani and M. H. Seymour, *A general algorithm for calculating jet cross sections in NLO QCD*, *Nucl. Phys.* **B485** (1997) 291–419, [hep-ph/9605323].

[65] K. Hagiwara and D. Zeppenfeld, *Helicity Amplitudes for Heavy Lepton Production in e^+e^- Annihilation*, *Nucl. Phys.* **B274** (1986) 1.

[66] K. Hagiwara and D. Zeppenfeld, *Amplitudes for Multiparton Processes Involving a Current at e^+e^-, $e^\pm p$, and Hadron Colliders*, *Nucl. Phys.* **B313** (1989) 560.

[67] G. P. Salam and G. Soyez, *A practical Seedless Infrared-Safe Cone jet algorithm*, *JHEP* **05** (2007) 086, [arXiv:0704.0292].

[68] M. Cacciari and G. P. Salam, *Dispelling the N^3 myth for the k_T jet-finder*, *Phys. Lett.* **B641** (2006) 57–61, [hep-ph/0512210].

[69] M. L. Mangano, M. Moretti, F. Piccinini, and M. Treccani, *Matching matrix elements and shower evolution for top-quark production in hadronic collisions*, *JHEP* **01** (2007) 013, [hep-ph/0611129].

[70] C. Anastasiou, L. J. Dixon, K. Melnikov, and F. Petriello, *High-precision QCD at hadron colliders: Electroweak gauge boson rapidity distributions at NNLO*, *Phys. Rev.* **D69** (2004) 094008, [hep-ph/0312266].

[71] **D0** Collaboration, V. M. Abazov *et al.*, *Measurement of the shape of the boson transverse momentum distribution in $p\bar{p} \to Z/\gamma^* \to e^+e^- + X$ events produced at $\sqrt{s} = 1.96$ TeV*, *Phys. Rev. Lett.* **100** (2008) 102002, [arXiv:0712.0803 [hep-ex]].

[72] **CDF** Collaboration, A. A. Affolder *et al.*, *The transverse momentum and total cross section of e^+e^- pairs in the Z boson region from $p\bar{p}$ collisions at $\sqrt{s} = 1.8$ TeV*, *Phys. Rev. Lett.* **84** (2000) 845–850, [hep-ex/0001021].

[73] **D0** Collaboration, B. Abbott *et al.*, *Measurement of the inclusive differential cross section for Z bosons as a function of transverse momentum in $\bar{p}p$ collisions at $\sqrt{s} = 1.8$ TeV*, *Phys. Rev.* **D61** (2000) 032004, [hep-ex/9907009].

[74] **D0** Collaboration, B. Abbott *et al.*, *Differential production cross section of Z bosons as a function of transverse momentum at $\sqrt{s} = 1.8$ TeV*, *Phys. Rev. Lett.* **84** (2000) 2792–2797, [hep-ex/9909020].

[75] J. Alwall *et al.*, *Comparative study of various algorithms for the merging of parton showers and matrix elements in hadronic collisions*, *Eur. Phys. J.* **C53** (2008) 473–500, [arXiv:0706.2569].

[76] P. Nason, *Shower Monte Carlo at Next-to-Leading Order*, http://theory.fi.infn.it/research/nason.pdf.
Talk given at the Università degli Studi di Firenze, Florence, Italy, 2009.

[77] P. Nason, *MC at NLO tools*,
`http://indico.cern.ch/getFile.py/access?contribId=2&resId=0&materialId=slides&confId=49675`.
Talk given at *MC4LHC Meeting*, CERN, Switzerland, 2009.

[78] P. Nason, *POWHEG*,
`http://agenda.hep.wisc.edu/materialDisplay.py?contribId=13&materialId=slides&confId=189`.
Talk given at *LoopFest Symposium*, Madison, WI, USA, 2009.

[79] K. Hamilton, P. Richardson, and J. Tully, *A Positive-Weight Next-to-Leading Order Monte Carlo Simulation for Higgs Boson Production*, *JHEP* **04** (2009) 116, [arXiv:0903.4345].

[80] S. Alioli, P. Nason, C. Oleari, and E. Re, *NLO Higgs boson production via gluon fusion matched with shower in POWHEG*, *JHEP* **04** (2009) 002, [arXiv:0812.0578].

[81] **CDF** Collaboration, T. Aaltonen *et al.*, *First Observation of Electroweak Single Top Quark Production*, arXiv:0903.0885.

[82] **D0** Collaboration, V. M. Abazov *et al.*, *Observation of Single Top Quark Production*, arXiv:0903.0850.

[83] M. Beneke *et al.*, *Top quark physics*, hep-ph/0003033.

[84] B. W. Harris, E. Laenen, L. Phaf, Z. Sullivan, and S. Weinzierl, *The Fully differential single top quark cross-section in next to leading order QCD*, *Phys. Rev.* **D66** (2002) 054024, [hep-ph/0207055].

[85] J. Alwall *et al.*, *Is $V_{tb} = 1$?*, *Eur. Phys. J.* **C49** (2007) 791–801, [hep-ph/0607115].

[86] G. Mahlon and S. J. Parke, *Improved spin basis for angular correlation studies in single top quark production at the Tevatron*, *Phys. Rev.* **D55** (1997) 7249–7254, [hep-ph/9611367].

[87] G. Mahlon and S. J. Parke, *Single top quark production at the LHC: Understanding spin*, *Phys. Lett.* **B476** (2000) 323–330, [hep-ph/9912458].

[88] T. M. P. Tait and C. P. Yuan, *Single top quark production as a window to physics beyond the standard model*, *Phys. Rev.* **D63** (2001) 014018, [hep-ph/0007298].

[89] Q.-H. Cao, J. Wudka, and C. P. Yuan, *Search for New Physics via Single Top Production at the LHC*, *Phys. Lett.* **B658** (2007) 50–56, [arXiv:0704.2809].

[90] T. Plehn, M. Rauch, and M. Spannowsky, *Understanding Single Tops using Jets*, arXiv:0906.1803.

[91] G. Bordes and B. van Eijk, *Calculating QCD corrections to single top production in hadronic interactions*, *Nucl. Phys.* **B435** (1995) 23–58.

[92] T. Stelzer, Z. Sullivan, and S. Willenbrock, *Single top quark production via W-gluon fusion at next-to-leading order*, *Phys. Rev.* **D56** (1997) 5919–5927, [hep-ph/9705398].

[93] Z. Sullivan, *Understanding single-top-quark production and jets at hadron colliders*, *Phys. Rev.* **D70** (2004) 114012, [hep-ph/0408049].

[94] J. M. Campbell, R. K. Ellis, and F. Tramontano, *Single top production and decay at next-to-leading order*, *Phys. Rev.* **D70** (2004) 094012, [hep-ph/0408158].

[95] J. M. Campbell and F. Tramontano, *Next-to-leading order corrections to Wt production and decay*, *Nucl. Phys.* **B726** (2005) 109–130, [hep-ph/0506289].

[96] Q.-H. Cao, R. Schwienhorst, and C. P. Yuan, *Next-to-leading order corrections to single top quark production and decay at Tevatron. 1. s-channel process*, *Phys. Rev.* **D71** (2005) 054023, [hep-ph/0409040].

[97] Q.-H. Cao, R. Schwienhorst, J. A. Benitez, R. Brock, and C. P. Yuan, *Next-to-leading order corrections to single top quark production and decay at the Tevatron: 2. t-channel process*, *Phys. Rev.* **D72** (2005) 094027, [hep-ph/0504230].

[98] J. M. Campbell, R. Frederix, F. Maltoni, and F. Tramontano, *t-channel single-top production at hadron colliders*, arXiv:0903.0005.

[99] S. Frixione, E. Laenen, P. Motylinski, and B. R. Webber, *Angular correlations of lepton pairs from vector boson and top quark decays in Monte Carlo simulations*, *JHEP* **04** (2007) 081, [hep-ph/0702198].

[100] J. Alwall *et al.*, *MadGraph/MadEvent v4: The New Web Generation*, *JHEP* **09** (2007) 028, [arXiv:0706.2334].

[101] http://mcfm.fnal.gov.

[102] `http://home.fnal.gov/~zack/ZTOP/ZTOP.html`.

[103] P. Nason and G. Ridolfi, *A positive-weight next-to-leading-order Monte Carlo for Z pair hadroproduction*, *JHEP* **08** (2006) 077, [hep-ph/0606275].

[104] S. Catani, Y. L. Dokshitzer, M. H. Seymour, and B. R. Webber, *Longitudinally invariant k_T clustering algorithms for hadron-hadron collisions*, *Nucl. Phys.* **B406** (1993) 187–224.

[105] Z. Sullivan, *Angular correlations in single-top-quark and Wjj production at next-to-leading order*, *Phys. Rev.* **D72** (2005) 094034, [hep-ph/0510224].